DIFFRACTIVE PROCESSES IN 200 GEV/C

$\pi^- N \rightarrow \pi^- \pi^- \pi^+ N$

INTERACTIONS

A Dissertation

Submitted to the Graduate School

of the University of Notre Dame

in Partial Fulfillment of the Requirements

for the Degree of

Doctor of Philosophy

by

Rex W. Joyner, B.S.,M.S.

Director

Department of Physics

Notre Dame, Indiana

August, 1987

DIFFRACTIVE PROCCESSES IN 200 GEV/C

$\pi^- N \rightarrow \pi^- \pi^- \pi^+ N$

INTERACTIONS

FERMILAB LIBRARY

Abstract

by

Rex W. Joyner

This paper analyzes $\pi^- N \rightarrow \pi^- \pi^- \pi^+ N$ events from Fermilab experiment E580, which ran at the Multi-Particle Spectrometer facility in 1980, using 200 GeV/c π^- particles on a segmented plastic scintillator target. Starting with 48657 triggers of this type, data quality cuts and a cut on (missing mass)^2 < 16 (GeV/c^2)^2 lead to a final sample of 7205 events. Acceptances are calculated on an event-by-event basis using a computer model of the MPS. The overall cross section is 244 ± 71 μb. The x_F distribution of the 3π system shows almost all events in a peak at +1, suggesting the presence of pion diffraction into three pions. In the $\pi^- \pi^+$ effective mass spectrum, the $\rho^o(770)$ and $f^o(1270)$ are observed, and their cross sections are calculated. The t′ distribution, where t′ is the effective momentum transfer from the beam π^- to the 3π system, is the sum of three exponential decays, for coherent diffraction off of carbon nuclei from the plastic target, diffraction off of individual nucleons, and background. The exponential slope for diffraction is observed to decrease with increasing 3π effective mass. The fraction of coherent carbon diffraction in the total cross section is observed to decrease with increasing 3π effective mass.

Dedicated to the memory of

Dr. Leslie Gordon Joyner,

who inspired me to come

this far in my education,

and to

Mrs. Yvonne Calhoun Joyner,

who has done, and is doing,

a wonderful job of being

my mother.

TABLE OF CONTENTS

	Page
LIST OF TABLES	v
LIST OF FIGURES	vii
PREFACE: E580 HISTORY	xvi
CHAPTER 1 : INTRODUCTION	1
1.1 Diffraction	1
1.2 $\pi^- N \rightarrow \pi^- \pi^- \pi^+ N$ Interactions	2
CHAPTER 2 : EXPERIMENTAL DETAILS	5
2.1 Fermilab Accelerator	5
2.1.1 Cockcroft-Walton Pre-Accelerator	5
2.1.2 Linear Accelerator	6
2.1.3 Booster Accelerator	6
2.1.4 Main-Ring Accelerator	7
2.2 M6W Beamline and E580 Beam	8
2.3 Fermilab Multi-Particle Spectrometer	10
2.3.1 Scintillators	10
2.3.2 Smart Target	12
2.3.3 Proportional Wire Chambers	14
2.3.4 Decay Region	15
2.3.5 Magnet	17
2.3.6 Cerenkov Counter Hodoscope	17
2.3.7 Spark Chambers	18
2.4 E580 Trigger	19
2.4.1 Two V^0 Triggers	21
2.4.2 3π Trigger	23
CHAPTER 3 : DATA PROCESSING AND PRELIMINARY ANALYSIS	25
3.1 TEARS	25
3.2 KLEENX	29
3.3 Shared Legs	32
3.4 Data Quality Cuts	64
3.5 Missing Mass	74
3.6 Effective Beam	82
3.7 Trigger Efficiency	84

3.8 Software Efficiency..... 88
3.9 Geometrical Acceptance..... 89
3.9.1 $\pi^-\pi^-\pi^+$ Acceptance..... 89
3.9.2 Fiducial Cut on Veto 1x1..... 92
3.9.3 Results of Geometrical Model..... 93
3.9.4 Acceptance of Other E580 Samples..... 94
3.9.5 A-station Correction..... 97
3.9.6 Event-by-Event Acceptance Corrections. 107
3.10 Sensitivity and Cross Sections..... 107
3.11 Resolutions..... 112
3.11.1 Momentum Resolution..... 112
3.11.2 Resolution of Invariant Quantities... 113
3.11.3 Decay Angle Resolutions..... 125

CHAPTER 4 : PHYSICS ANALYSIS..... 129

4.1 Diffraction..... 129
4.2 Two Pion Data Sample..... 146
4.2.1 $\pi^-\pi^-$ Mass Spectrum..... 146
4.2.2 $\pi^-\pi^+$ Mass Spectrum..... 148
4.2.3 $\pi^-\pi^+$ Spin Analysis..... 151
4.2.4 ρ^0 and f^0 Cuts..... 160
4.3 Three Pion Data Sample..... 163
4.3.1 $M(3\pi)$ Spectrum with f^0 Cut..... 167
4.3.2 $M(3\pi)$ Spectrum..... 170
4.3.3 3π Spin Analysis..... 173
4.4 Conclusions and Summary..... 191

APPENDIX A : Spherical Harmonic Moments..... 195

APPENDIX B : Histogram Plotting Package..... 196

APPENDIX C : Breit-Wigner Resonance Functions..... 202

REFERENCES..... 203

LIST OF TABLES

2.1 Smart Target Composition..... 13

2.2 Proportional Wire Chamber Vital Statistics..... 16

2.3 Spark Chamber Positions..... 19

3.1 Cuts for Defining Shared Legs..... 42

3.2 Minimum Requirements For Number of Sparks to Reprieve a Track..... 56

3.3 Differences in Number of Sparks Required to Cut a Shared Leg Track..... 57

3.4 Degrees of Freedom in Each View..... 58

3.5 Progressive Effects of Cuts..... 73

3.6 Effective Beam By Run..... 84

3.7 Trigger Efficiencies..... 88

3.8 PIACPT Simulation Parameters..... 91

3.9 A-Station Correcrions..... 104

3.10 Results of Geometrical Acceptance Calculations... 106

3.11 Sensitivity by Mass Region..... 111

3.12 Resolutions of Invariant Quantities..... 117

4.1 Results of t′ Fits by Mass Region..... 136

LIST OF FIGURES

2.1 MPS Layout for E580..... 11

3.1(a) Δ(slope) for Downstream x tracks,
before shared leg cut..... 34

3.1(b) Δ(slope) for Downstream y tracks,
before shared leg cut..... 35

3.1(c) Δ(slope) for Upstream x tracks,
before shared leg cut..... 36

3.1(d) Δ(slope) for Upstream y tracks,
before shared leg cut..... 37

3.2(a) Δ(intercept) for Downstream x tracks,
before shared leg cut..... 38

3.2(b) Δ(intercept) for Downstream y tracks,
before shared leg cut..... 39

3.2(c) Δ(intercept) for Upstream x tracks,
before shared leg cut..... 40

3.2(d) Δ(intercept) for Upstream y tracks,
before shared leg cut..... 41

3.3(a) Δ(slope) for Downstream x tracks,
after shared leg cut..... 44

3.3(b) Δ(slope) for Downstream y tracks,
after shared leg cut..... 45

3.3(c) Δ(slope) for Upstream x tracks, after shared leg cut..... 46

3.3(d) Δ(slope) for Upstream y tracks, after shared leg cut..... 47

3.4(a) Δ(intercept) for Downstream x tracks, after shared leg cut..... 48

3.4(b) Δ(intercept) for Downstream y tracks, after shared leg cut..... 49

3.4(c) Δ(intercept) for Upstream x tracks, after shared leg cut..... 50

3.4(d) Δ(intercept) for Upstream y tracks, after shared leg cut..... 51

3.5(a) Number of sparks for Downstream x tracks..... 52

3.5(b) Number of sparks for Downstream y tracks..... 53

3.5(c) Number of sparks for Upstream x tracks..... 54

3.5(d) Number of sparks for Upstream y tracks..... 55

3.6(a) Number of sparks for good tracks, of pairs of tracks having shared legs..... 60

3.6(b) Number of sparks for bad tracks, of pairs of tracks having shared legs..... 61

3.7(a) χ^2/(Degree of Freedom) for good tracks, of pairs of tracks having shared legs..... 62

3.7(b) χ^2/(Degree of Freedom) for bad tracks, of pairs of tracks having shared legs..... 63

3.8(a) χ^2/(Degree of Freedom), x view, of tracks passing KLEENX..... 66

3.8(b) χ^2/(Degree of Freedom), y view, of tracks passing KLEENX..... 67

3.9 Distance of closest approach to target vertex of outgoing tracks..... 69

3.10 Uncertainty of distance of closest approach to target vertex of outgoing tracks..... 70

3.11 Number of standard deviations of distance of closest approach to target vertex of outgoing tracks..... 71

3.12 Total energy of events..... 72

3.13 Missing mass squared, assuming target has proton mass, with beam momentum scaled up to 202 GeV/c..... 77

3.14(a) Missing mass squared, assuming target has proton mass, with beam momentum scaled up to 201 GeV/c..... 79

3.14(b) Missing mass squared, assuming target has proton mass, with beam momentum scaled up to 203 GeV/c..... 80

3.15 Resolution of missing mass squared, with $MM^2 < 16\ (GeV/c^2)^2$..... 81

3.24 Resolution of Mass($\pi^-\pi^-\pi^+$), for
1.10 < Mass($\pi^-\pi^-\pi^+$) < 1.40 GeV/c^2..... 120

3.25 Resolution of Mass($\pi^-\pi^+$), for
0.67 < Mass($\pi^-\pi^+$) < 0.87 GeV/c^2..... 121

3.26 Resolution of missing mass squared, for
MM^2 < 16 (GeV/c^2)^2..... 122

3.27 Resolution of effective momentum transfer t',
for all values of t'..... 123

3.28 Resolution of effective momentum transfer t',
for t' < 0.02 (GeV/c)$^{-2}$..... 124

3.29 Definition of θ_J..... 126

3.30 Definition of θ_2..... 127

4.1 Feynman x (x_F) for the $\pi^-\pi^-\pi^+$ system..... 130

4.2 Momentum transfer t, for all data..... 132

4.3 Effective momentum transfer t', for all data..... 134

4.4 Effective momentum transfer t', for
Mass($\pi^-\pi^-\pi^+$) < 1.10 GeV/c^2..... 138

4.5 Effective momentum transfer t', for
1.10 < Mass($\pi^-\pi^-\pi^+$) < 1.40 GeV/c^2..... 139

4.6 Effective momentum transfer t', for
1.40 < Mass($\pi^-\pi^-\pi^+$) < 1.55 GeV/c^2..... 140

4.7 Effective momentum transfer t′, for
1.55 < Mass($\pi^-\pi^-\pi^+$) < 1.80 GeV/c^2..... 141

4.8 Effective momentum transfer t′, for
1.80 GeV/c^2 < Mass($\pi^-\pi^-\pi^+$)..... 142

4.9 Scatterplot of Mass($\pi^-\pi^-\pi^+$) vs. t,
for 0 < t < 1.0 (GeV/c)^2..... 144

4.10 Effective mass of all $\pi^-\pi^-$ pairs,
one entry per event..... 147

4.11 Effective mass of all $\pi^-\pi^+$ pairs,
two entries per event..... 149

4.12(a) Moments of spherical harmonic Y_1^0 vs.
Mass($\pi^-\pi^+$). Two entries per event..... 152

4.12(b) Moments of spherical harmonic Y_2^0 vs.
Mass($\pi^-\pi^+$). Two entries per event..... 153

4.12(c) Moments of spherical harmonic Y_3^0 vs.
Mass($\pi^-\pi^+$). Two entries per event..... 154

4.12(d) Moments of spherical harmonic Y_4^0 vs.
Mass($\pi^-\pi^+$). Two entries per event..... 155

4.12(e) Moments of spherical harmonic Y_5^0 vs.
Mass($\pi^-\pi^+$). Two entries per event..... 156

4.12(f) Moments of spherical harmonic Y_6^0 vs.
Mass($\pi^-\pi^+$). Two entries per event..... 157

4.12(g) Moments of spherical harmonic Y_7^0 vs.
Mass($\pi^-\pi^+$). Two entries per event..... 158

4.12(h) Moments of spherical harmonic Y_8^0 vs. Mass($\pi^-\pi^+$). Two entries per event..... 159

4.13 Dalitz plot of Mass(π^-(fast)) vs. Mass(π^-(slow))..... 162

4.14(a) Effective mass of π^-(fast)π^+ combinations. One entry per event..... 164

4.14(b) Effective mass of π^-(slow)π^+ combinations. One entry per event..... 165

4.15 Effective Mass of $\pi^-\pi^-\pi^+$ combinations. One entry per event..... 166

4.16 Effective Mass of $\pi^-\pi^-\pi^+$ combinations, with 1.14 < Mass($\pi^-\pi^+$) < 1.36 GeV/c^2 (f^o cut). One entry per event..... 168

4.17 Scatterplot of Mass($\pi^-\pi^-\pi^+$) vs. Mass($\pi^-\pi^+$)..... 171

4.18 Effective Mass of $\pi^-\pi^-\pi^+$ combinations, with 0.67 < Mass($\pi^-\pi^+$) < 0.87 GeV/c^2 (ρ^o cut). One entry per event..... 172

4.19(a) Moments of spherical harmonic Y_1^0 vs. Mass($\pi^-\pi^-\pi^+$). Two entries per event... 174

4.19(b) Moments of spherical harmonic Y_2^0 vs. Mass($\pi^-\pi^-\pi^+$). Two entries per event... 175

4.19(c) Moments of spherical harmonic Y_3^0 vs. Mass($\pi^-\pi^-\pi^+$). Two entries per event... 176

4.19(d) Moments of spherical harmonic Y_4^0 vs. Mass($\pi^-\pi^-\pi^+$). Two entries per event... 177

4.19(e) Moments of spherical harmonic Y_5^0 vs. Mass($\pi^-\pi^-\pi^+$). Two entries per event... 178

4.19(f) Moments of spherical harmonic Y_6^0 vs. Mass($\pi^-\pi^-\pi^+$). Two entries per event... 179

4.19(g) Moments of spherical harmonic Y_7^0 vs. Mass($\pi^-\pi^-\pi^+$). Two entries per event... 180

4.19(h) Moments of spherical harmonic Y_8^0 vs. Mass($\pi^-\pi^-\pi^+$). Two entries per event... 181

4.20(a) Moments of spherical harmonic Y_1^0 vs. Mass($\pi^-\pi^-\pi^+$), with $0.67 < \text{Mass}(\pi^-\pi^+) < 0.87$ GeV/c^2. One entry per event..... 182

4.20(b) Moments of spherical harmonic Y_2^0 vs. Mass($\pi^-\pi^-\pi^+$), with $0.67 < \text{Mass}(\pi^-\pi^+) < 0.87$ GeV/c^2. One entry per event..... 183

4.20(c) Moments of spherical harmonic Y_3^0 vs. Mass($\pi^-\pi^-\pi^+$), with $0.67 < \text{Mass}(\pi^-\pi^+) < 0.87$ GeV/c^2. One entry per event..... 184

4.20(d) Moments of spherical harmonic Y_4^0 vs. Mass($\pi^-\pi^-\pi^+$), with $0.67 < \text{Mass}(\pi^-\pi^+) < 0.87$ GeV/c^2. One entry per event..... 185

4.20(e) Moments of spherical harmonic Y_5^0 vs. Mass($\pi^-\pi^-\pi^+$), with $0.67 < \text{Mass}(\pi^-\pi^+) < 0.87$ GeV/c^2. One entry per event..... 186

4.20(f) Moments of spherical harmonic Y_6^0 vs. Mass($\pi^-\pi^-\pi^+$), with 0.67 < Mass($\pi^-\pi^+$) < 0.87 GeV/c^2. One entry per event..... 187

4.20(g) Moments of spherical harmonic Y_7^0 vs. Mass($\pi^-\pi^-\pi^+$), with 0.67 < Mass($\pi^-\pi^+$) < 0.87 GeV/c^2. One entry per event..... 188

4.20(h) Moments of spherical harmonic Y_8^0 vs. Mass($\pi^-\pi^-\pi^+$), with 0.67 < Mass($\pi^-\pi^+$) < 0.87 GeV/c^2. One entry per event..... 189

PREFACE: E580 HISTORY

The inspiration for E580 came from Fermilab E110, which ran in March 1977 with a 200 GeV/c π^- beam. E110 had as one of its nine triggers a $2V^0+n$, n=0,1,2 trigger, which garnered a small handful of events. Deciding that final states with two neutral strange particles (K^0_s, Λ, or $\bar{\Lambda}$, collectively known as V^0's), Kwan-Wu Lai of Brookhaven National Lab proposed P548 to use this trigger exclusively, again with 200 GeV/c π^-.

In January 1978 P580 was proposed with a similar trigger, using a 300 GeV/c π^- beam. The collaborators on the proposal were Arizona, Brookhaven, Florida State, Notre Dame, Tufts, Vanderbilt, and Virginia Tech. The presentation before the Fermilab PAC was made in May 1978, and approval for 800 hours came on June 19, 1978, with Joe Lannutti of Florida State as spokesman. By this time Georgia Tech and Michigan State had joined the collaboration.

Several modifications to the existing MultiParticle Spectrometer were made. Horace Ma of Michigan State rebuilt the Cerenkov counter to have 30 cells, with better segmentation in the center region. John Poirier of Notre Dame proposed and then built the segmented "smart target",

allowing more precise determination of the target vertex and helping in reconstruction of events. Several new PWC's were built and installed, and a helium bag for the decay region was made at Argonne by Notre Dame.

Sometime before actual running of the experiment began, Georgia Tech and Michigan State left the collaboration, as did Brookhaven when Kwan-Wu Lai went to Arizona. Also, Dan Green of Fermilab joined the experiment as MPS liason, bringing the group to its final state.

On Dec. 18, 1979, Run 1 of E580 began. Running continued until Jan. 17, 1980. This test run was successful in diagnosing the equipment for problems, and beam momenta of both 200 GeV/c and 250 GeV/c were tested. During the test run many trigger configurations were tested, with the final conclusion being that $N \rightarrow N + 4\pm1$, $N=0,1,2,3,4,5$ would work best.

On March 16, 1980, data taking resumed with a 250 GeV/c π^- beam. By the time the experiment finished on May 6, 1,708,871 triggers had been taken in 408 runs over 545.1 hours (combining the two running periods).

Analysis commenced forthwith. Pattern recognition processing using the program TEARS took place at Fermilab, followed by fitting and production of Data Summary Tapes (DSTs) at Vanderbilt and Arizona. The first publication

was a talk by John Poirier of Notre Dame at the 12th International Conference on Multiparticle Dynamics, held at Notre Dame in June, 1981 (Poirier 1982).

Next came a paper on the $K_s^o K_s^o \pi^-$ final state, with first author T.Y. Chen of Arizona (Chen 1983) published in Physical Review D in 1983.

In 1984 came several more papers. $K_s^o K_s^o \pi^- \pi^- \pi^+$ final states were covered in a paper with first author C.C. Chang of Notre Dame, published in Phys. Rev. D (Chang 1984). ΛK_s^o and $\bar{\Lambda} K_s^o$ inclusive final states were covered in another Phys. Rev. D paper with first author H.C. Fenker of Fermilab (Fenker 1984). $K_s^o K_s^o$ inclusive states were dealt with in a paper in Phys. Rev. D with first author E.G.H. Williams of Vanderbilt (Williams 1984). And finally K_s^o inclusive states were covered in a Physics Letters paper with first author A. Napier of Tufts (Napier 1984a). Also, J. Piper of Florida State wrote a doctoral dissertation on $1V^o$ events in 1984.

In 1985 S. Mikocki of Virginia Tech wrote his doctoral dissertation on events with one V^o, for which there was a separate trigger during the latter part of the E580 spring run (Mikocki 1985a). A version of this has been submitted to Phys. Rev. D for publication (Mikocki 1985b).

In 1986 a paper concerning high mass states in the topology $\Lambda K^{o}_{s}\pi^{+}\pi^{+}\pi^{-}\pi^{-}$ was published with first author M. Arenton of Arizona, in Nuclear Physics B (Arenton 1986).

Along with a study of $\bar{\Lambda}\Lambda$ currently being prepared at Virginia Tech, this paper forms the conclusion of work on E580.

CHAPTER 1

INTRODUCTION

1.1 Diffraction

"Diffraction" in high-energy physics refers to a class of interactions bearing some common characteristics. The name "diffraction" comes from the fact that some features of the interactions collectively known as diffractive may be explained by an adaptation of the formulations used in classical optical diffraction to the realm of high-energy matter waves interacting (Kaidalov 1979). However, it is entirely possible to formulate theories pertaining to high-energy diffraction without reference to any sort of optical model (Abarbanel 1976, Kaidalov 1979, Zachariasen 1971) In general, there seems to be no complete agreement as to all the features which are necessary in diffractive processes, although there is an overall consensus as to what processes are diffractive and what are not.

Some features of high-energy diffractive interactions are as follows:

1) Cross-sections are independent of energy, up to log powers (Abarbanel 1976, Zachariasen 1971).

2) Differential cross sections $d\sigma/dt$ have sharp forward peaks (Abarbanel 1976, Zachariasen 1971) which tend to decrease with invariant mass of the system (Alberi 1981, Zotov 1978)

3) In the reaction $A + B \rightarrow A' + B'$, there is an empirical rule that

$$P_A = P_{A'} * (-1)^{(J_A - J_{A'})}$$

(Abarbanel 1976, Berger 1979, Zachariasen 1971), where P_A is the intrinsic parity of particle A, and J_A is the spin. This rule, however, has known exceptions (Berger 1979, Bosetti 1975, Daum 1981, Kaidalov 1979).

4) Cross sections are such that $\sigma_{diff}(AB) = \sigma_{diff}(\bar{A}B)$ (Abarbanel 1976).

1.2 $\pi^- N \rightarrow \pi^- \pi^- \pi^+ N$ Interactions

One interaction which is generally agreed to be diffractive, or at least to have a diffractive component, is $\pi^- N \rightarrow \pi^- \pi^- \pi^+ N$. This reaction has been extensively studied at a wide variety of energies (Aaron 1981, Antipov 1973a, Antipov 1973b, Ascoli 1973, Azimov 1982, Brick 1980, Brick 1983, Chabaud 1981, Daum 1981, Gaidos 1979, Kitagaki

1982, Pernegr 1978, Pernegr 1982, Saleem 1984, Zielinski 1984), including a small amount at the E580 energy of 200 GeV/c (Azimov 1982, Zielinski 1984). Further, the closely-related reaction $\pi^+N \rightarrow \pi^+\pi^-\pi^+N$ has been extensively studied (Baltay 1977, Baltay 1978, Beketov 1978, Otter 1974, Thompson 1974a, Thompson 1974b)

The main feature of interest in the $(3\pi)^-$ system is a set of three enhancements in the invariant mass distribution, which are known as the A_1^-, A_2^-, and A_3^-. These enhancements have spin-parity J^P of 1^+, 2^+, and 2^-, respectively (PDG 1986). Of these, the A_1^- and A_3^- obey Rule 3 above, since the incident π^- has $J^P = 0^-$, and expected diffractive resonances would therefore have $J^P = 1^+, 2^-, 3^+$, etc. The A_2^- is one of the exceptions to this rule, as it gives every indication of also being produced diffractively (Daum 1981, Kaidalov 1979).

A further interesting feature of these enhancements is that, while the A_2^- can be established as being purely Breit-Wigner in form (Berger 1979, Daum 1981), the A_1^- and A_3^- are not, but rather Breit-Wigner resonances interfering with a background according to the Drell-Hiida-Deck model (Antipov 1973b, Chabaud 1981, Daum 1981). Further, the A_2^- sits, mass-wise, directly on top of the A_1^-, making its extraction difficult. The best way to understand what is happening in the 3π spectrum is by doing a Partial-Wave

Analysis (PWA) on the data (Ascoli 1973, Bonesini 1981, Chabaud 1981, Daum 1981, Otter 1974), which requires a large number of events.

The data sample in this paper is too small to do a PWA, but every attempt will be made to extract as much information as can possibly be gleaned.

CHAPTER 2

EXPERIMENTAL DETAILS

2.1 Fermilab Accelerator

The Fermilab Accelerator at the time of E580 was designed to accelerate protons from rest to a final energy of 400 Gev. This was accomplished in four steps:

1) Cockcroft-Walton pre-acceleration to 750 keV.

2) Linear acceleration to 200 MeV.

3) Booster acceleration to 10 GeV.

4) Main-ring acceleration to 400 GeV.

We shall examine each stage in the process briefly.

2.1.1 Cockcroft-Walton Pre-Accelerator

An electrical arc is passed through hydrogen gas at the high-voltage electrode of the Cockcroft-Walton voltage supply, producing H^- ions (protons with two electrons). These are accelerated to the ground electrode, where they

pass into the Linear Accelerator with an energy of 750 keV (URA 1968).

2.1.2 Linear Accelerator

The Fermilab Linear Accelerator is 475 feet long. It has 286 drift tubes along which the H^- ions are accelerated. The drift tubes provide shielding from radio-frequency electric fields while inside the tube. Between each pair of tubes is an electric potential, timed to provide maximum acceleration to the ions. The tubes are arranged into nine cavities, each about 50 feet long and 3 feet in diameter. At the end of the Linear Accelerator the ions have an energy of 200 MeV, and pass into the Booster Accelerator (URA 1968).

2.1.3 Booster Accelerator

The Booster is a rapid-cycling synchrotron 495 feet in diameter. It is a combined-function machine, meaning that the the magnet poles are designed to both bend and focus the beam. At injection, the H^- ions are stripped of their electrons by passing through carbon foil, leaving bare protons. The Booster goes through 15 acceleration cycles per second, injecting 13 pulses to the Main Ring in 0.8

seconds, distributing these pulses fairly evenly about the Main Ring, which has a diameter 13.25 times that of the Booster. There are 24 identical cells distributed about the Booster ring, with guiding magnetic fields ranging from 0.5 kG at injection to 8.4 kG at extraction. Protons emerge from the Booster with an energy of 10GeV, and are injected into the Main Ring (URA 1968).

2.1.4 Main-Ring Accelerator

The Main Ring is 2 km in diameter (6562 feet). It is a separated-function synchrotron, meaning that separate magnets are used for bending the beam (dipoles) and focusing the beam (quadrupoles). It is not perfectly circular, but is divided into six arcs of 60° each. Within each arc is a 50 foot straight section, and between each arc is a 170 foot straight section. These straight sections provide regions for injection, extraction, targeting, testing, and the radio-frequency accelerating system. Quadrupole magnets are approximately 7 feet long and weigh 3 tons, and are spaced 100 feet apart. The dipoles are 20 feet long and weigh 10 tons, and are placed with four between each quadrupole (less for the straight sections). The Main Ring as a whole contains 216 quadrupoles and 774 dipoles. The strength of the dipole magnetic fields ranges from 0.5 kG at injection (10 GeV) to

17.9 kG at a final energy of 400 GeV (URA 1968).

As for timing, injection takes about 1.2 seconds, acceleration about 3.2 seconds, and extraction a variable period of time up to about 2 seconds. In E580, the extraction ("spill") was about 1 second. After beam is extracted, the guiding field falls to its injection value in about 1.2 seconds. Finally there is a dead time between cycles. For E580 the total cycle time ranged from 10 to 15 seconds (URA 1968).

Please note that these numbers apply to the Main Ring in Spring of 1980, when E580 data was taken. More recent upgrades due to the Tevatron project are irrelevant to consideration here. It also must be noted that maximum beam energy during the E580 run was 350 GeV (Poirier 1982).

After acceleration to final energy, the beam is extracted and sent to various experimental areas.

2.2 M6W Beamline and E580 Beam

After extraction from the Main Ring, protons are sent to the Meson Area. The maximum energy of the protons was 350 GeV during E580 (Poirier 1982). Those intended for the M6 beam line strike a beryllium target 0.04 in x 0.04 in x 8.00 in long (Stampke 1982). The production angle is 3 mr,

meaning that particles are collected at an angle of 3 mr from the incident beam (Malamud 1977). This produces pions (among other things) which are selected by sign and momentum and delivered to one of three branches, East, West, or Far West. The MultiParticle Spectrometer lay at the end of the M6 West line, the only one of the three to extend beyond the detector building. Momentum resolution is very good, better than 1% (Malamud 1977).

Each of the three lines has several stages, during which the beam is focussed to a point, allowed to separate, and again focussed. All three lines have their third focus in the detector building, and M6W has a fourth focus near the target in the MPS. The total length of M6W is 6070 ft.

The cycle time between spills was 10 to 15 seconds, with the actual spill lasting about 1 second. The beam had an rf structure, with beam buckets spaced 18.8 nanoseconds apart (Stampke 1982). A typical spill contained 500,000 pions, meaning less than 1% of the buckets were populated.

10% of the data was taken with a pion energy of 250 GeV, and the rest at 200 GeV. This paper concerns itself only with the 200 GeV data.

2.3 Fermilab Multi-Particle Spectrometer

The Multi-particle Spectrometer (MPS) at Fermilab qualifies as a Fermilab-supported Facility, along with the 15-foot Bubble Chamber. Figure 2.1 shows the basic layout of the MPS. Its components are described in the following sections:

2.3.1 Scintillators

2.3.2 Smart Target

2.3.3 Proportional Wire Chambers

2.3.4 Decay Region

2.3.5 Magnet

2.3.6 Cerenkov Counter Hodoscope

2.3.7 Spark Chambers

2.3.1 Scintillators

There were three plastic scintillator paddles in front of the BA PWC station. SA and SB were both 1 5/8 in x 1 3/16 x 1/16 in thick, directly in front of the nominal beam. SC was 6 in square and 1/4 in thick, with a hole in the beam spot 1 5/8 in in diameter. These were used to detect the presence of beam.

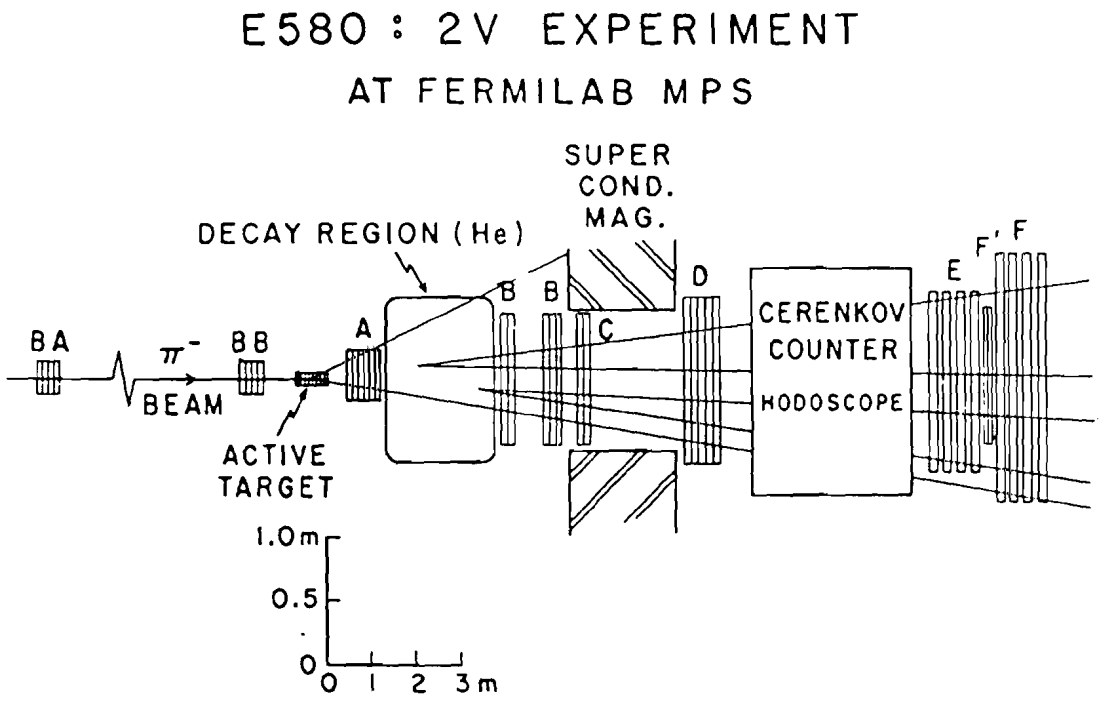

Figure 2.1: MPS Layout for E580.

A plastic scintillator counter dubbed "1x1" was located between the Cerenkov counter and the E station spark chambers. It was 1 in square and 1/4 in thick. It was positioned such that a non-interacting beam particle (i.e., a 200 GeV π^-) would strike it, thus providing a veto for the trigger. It was located at z = 6.0066 m from the front magnet face, y = 0 m vertically, and x = 0.0165 m horizontally from beam center.

2.3.2 Smart Target

The target in E-580 consisted of 20 layers of plastic scintillator, each approximately 1/4 inch thick, with a 1/4 inch separation between each layer. This provided good determination of the z-position of the interaction: by examining the pulse heights of the counters, it was possible to pinpoint the location of the interaction to within a layer. This precise determination of the z-vertex helped greatly later in the mass resolution of particles emerging from the vertex. This target was built at Notre Dame.

The target was located between z = -4.856 m and z = -4.600 m, measured from the front of the magnet face.

Each layer measured approximately 1.25" x 1.25" x .25", and was wrapped with thin layers of aluminum and black tape, assuring electromagnetic shielding and light-tightness. Four counters were measured in detail, and averaged.

Table 2.1 contains numerical information on the composition of the smart target.

TABLE 2.1

SMART TARGET COMPOSITION

Material	Interaction Length(a) (g/cm^2)	Density (g/cm^3)	Thickness (cm)	Density-Thickness (g/cm^2)	Interaction Lengths
Scintillator	82.0	1.032	0.621	0.640	0.00781
Aluminum	106.4	2.70	0.010	0.027	0.000258
Black Tape(b)	78.8	1.046	0.107	0.112	0.00142
Air	90.0	0.00129	0.584	0.0008	0.00000837
				---	---
Total for one layer				0.780	0.00950

(a) Source: Particle Data Group

(b) Polyolefin, assumed same chemically as polyethylene

Total density thickness = 0.780 g/cm^2 x 20 layers = 15.60 g/cm^2

Total interaction length = .00950/layer x 20 layers = 0.190

Thus it was a 19% target, allowing interactions a good fraction of the time, but making multiple interactions within the target fairly unlikely.

2.3.3 Proportional Wire Chambers

There were a total of 29 planes of proportional wire chambers in the MPS, divided into several stations.

The BA station was in two sections well upstream of the target, totalling five chambers. First was an xy module, then came an xyu module further downstream.

The BB station was just upstream of the target, and had three planes at angles of 0°, 45°, and 90° to the horizontal (x, u, and y).

The A station was immediately downstream of the target, and had six planes: two x, two y, and one each of u and v (at ±45° to the horizontal).

The B station was immediately after the decay volume, and had five planes, four x and one y. Two of the x chambers, named BU and BV for historical reasons, were built at Notre Dame.

The C station sat inside the magnet, and had one plane each of x and y. These spent a good fraction of the experiment off-line, as there was great trouble getting them to work correctly.

The D-station was after the magnet, with five planes (x, y, u, v, and x') (Malamud 1977).

Finally, the F' station, with four planes, sat between the spark chamber groups E and F. Of the four F' planes, only three were active (x, y, and u). F'Y sat inside spark chamber group F.

Numerical details on the various chambers are in Table 2.2.

2.3.4 Decay Region

Between the A and B stations of PWC's was a region of 2.10 m in which strange particles could decay. This region was mostly filled with a plastic bag containing atmospheric pressure helium. Notre Dame constructed the bag at Argonne National Lab, and also the circuit to maintain proper (just above atmospheric) pressure.

TABLE 2.2

PROPORTIONAL WIRE CHAMBER VITAL STATISTICS

Chamber Name	z-position (meters)	Number Wires	Spacing (mm)	Rotation (degrees) (x=0)
BAX1	-33.249	64(a)	1.954(b)	0
BAY1	-33.249	64(a)	1.954	90
BAU	-21.031	64(a)	1.954	-45
BAX2	-21.184	64(a)	1.954	0
BAY2	-21.184	64(a)	1.954	90
BBX	-5.726	64	1.000	0
BBY	-5.739	64	1.000	90
BBU	-5.733	64	1.000	45
AX1	-4.024	256	1.000	0
AX2	-4.018	256	1.000	0
AY1	-4.013	256	1.000	90
AY2	-4.007	256	1.000	90
AU	-3.940	256	1.000	45
AV	-3.934	256	1.000	-45
BU	-1.834	512	1.954	0(c)
BV	-1.564	512	1.954	0(c)
BX	-0.316	448	1.954	0
BY	-0.238	256	1.954	90
BX'	-0.060	384	1.954	0
CX	0.610	512	1.954	0
CY	0.686	320	1.954	90
DX	2.978	992	1.954	0
DU	3.086	864	1.954	15
DY	3.213	605	1.954	90
DV	3.339	864	1.954	-15
DX'	3.447	992	1.954	0
F'X	6.866	320	1.954	0
F'V	6.949	320	1.954	-45
F'Y	7.194	320	1.954	90

(a) Only 56 wires were active in each of the BA chambers.

(b) Wire spacing of 1.954 mm corresponds to 13 wires/inch.

(c) BU and BV, despite their names, were actually x chambers.

2.3.5 Magnet

The Magnet at the MultiParticle Spectrometer is superconducting, kept cold with liquid helium. The aperture is 4 feet wide by 34 inches tall. The magnet is 8 feet long. In the center 4 feet of the magnet is the pole tip, where the vertical aperture narrows to 28 inches.

Operating current was 180 A for E580, producing a magnetic induction of 1.657 T at the center of the magnet, giving a transverse momentum kick of 676 MeV.

The front face of the magnet was used as the reference point for the defined geometry of the MPS, and defined as z=0, where the z-axis is the nominal beam direction. y was then defined as up, with x horizontal and to the left as one looks downstream.

2.3.6 Cerenkov Counter Hodoscope

There was a Cerenkov counter hodoscope between the D-station of PWC's and the spark chambers. It had an active area of 4 m x 2 m, originally segmented into 16 cells, with a radiator length of 5.7 m (Dzierba 1977). It was modified by Z. Ma of Michigan State into 30 cells.

The Cenrenkov counter was filled with nitrogen at atmospheric pressure, and used to separate pions from protons. Threshold momentum for pions was 5.78 GeV/c, and for protons was 38.7 GeV/c. The Cerenkov counter was not used for this analysis.

2.3.7 Spark Chambers

There were eight modules of magnetostrictive spark chambers in the MPS, arranged into two stations (E and F) of four modules each. The E-station had an aperture of 8 x 4 ft^2, longer horizontally. The F-station was 12 x 6 ft^2. Each module had a y-y gap and an x-u gap, and each wand had pickups at each end, giving 6 signals per module (x, y, and u). Signals were fed into Multi-Time Digitizers (Dzierba 1977). Wires were aluminum, 0.005 inch in diameter, and spaced 32/inch. The u-wires were at an angle of 5.7° to the x-wires. Gas mixture was 90% neon, 10% helium, and a trace of ethanol (Stampke 1982). Spatial resolution was around 0.7 mm, but the pair resolution was only 5.5 mm (Yung 1979).

Table 2.3 contains the positions of the spark chambers.

TABLE 2.3

SPARK CHAMBER POSITIONS

Chamber Name	z-position (meters)	Rotation (degrees) (x=0)
E1X	6.083	0
E1U	6.092	-5.7
E1Y	6.115	90
E2X	6.203	0
E2U	6.213	5.7
E2Y	6.235	90
E3X	6.330	0
E3U	6.340	-5.7
E3Y	6.362	90
E4Y	6.468	90
E4U	6.490	5.7
E4X	6.499	0
F1X	6.576	0
F1U	6.585	5.7
F1Y	6.614	90
F2X	6.750	0
F2U	6.760	5.7
F2Y	6.788	90
F3X	7.040	0
F3U	7.049	-5.7
F3Y	7.078	90
F4X	7.329	0
F4U	7.339	-5.7
F4Y	7.368	90

2.4 E580 Trigger

E580 was designed to look for cases where the $\pi^- p$ interaction resulted in two neutral strange particles (K^o_s, Λ, $\bar{\Lambda}$, generally referred to as V^o's) which decay to two charged particles inside the decay volume. Most of the triggers involved in E580 were of this type.

The events with which this paper is concerned were not of this type. Here the events of interest are of the type $\pi^- p \rightarrow \pi^+\pi^-\pi^- p$, for which there was one trigger. However, many elements of both trigger types are the same, so both shall be discussed.

The presence of beam was defined as follows:

$$BM = BMGT \cdot SA \cdot SB \cdot \overline{SC}$$

where BMGT (BeaM GaTe) is a signal from upstream that beam is coming, and SA, SB, and SC are plastic scintillators placed in the path of the beam upstream of the target. SC has a hole where the beam passes through, and acts as a veto for the presence of charged halo surrounding the beam.

Next it must be defined how it is known that the beam interacted in the target. This is defined as follows:

$$IB = BM \cdot DE/DX \cdot \overline{1x1}$$

To have interacting beam requires the presence of BM, plus a signal from DE/DX (a scintillator paddle sitting after the target) of a pulse height corresponding to at least one charged particle, plus the requirement that there not be a hit in 1x1, a one-inch square scintillator located downstream of the magnet, directly in the path of a non-interacting beam particle, which is defined as a negatively charged particle of momentum P_z=200 GeV/c, P_x=P_y=0 GeV/c. The position of the 1x1 was where such a particle would be curved by the magnet, specifically z =

6.007 m, y = 0m, and x = 0.017 m.

Now that IB is defined, it is possible to look at individual triggers. All physics triggers used the folowing chambers: AU, AV, BU, BV, CX, CY, DX, DY, and DX'. These chambers were wired to fast logic which counted the number of hits in each. In some cases, majority logic was used, meaning that only some of the chambers were required to exhibit the appropriate number of hits.

2.4.1 Two V^o Triggers

The purpose of the main physics triggeres was to detect the presence of two neutral strange particles (like K^o_s, Λ, or $\bar{\Lambda}$), each decaying to two charged particles inside the 2.10 m decay region. The desired decays are:

1) $K^o_s \rightarrow \pi^+\pi^-$
2) $\Lambda \rightarrow p\pi^-$
3) $\bar{\Lambda} \rightarrow \bar{p}\pi^+$

When both V^o's decay in the appropriate way inside the decay volume, one should observe a multiplicity increase of 4 between the A chambers and the B chambers, with the same number of particles observed in the C and D chambers as in the B.

In practice, this multiplicity change was defined as 4±1, and majority logic used. Also, interactions with more than 5 direct charged tracks were rejected as too hard to reconstruct.

Thus, the interactions of interest were, in terms of number of charged tracks, as follows:

$0 \to 4\pm1$, $1 \to 5\pm1$, $2 \to 6\pm1$, $3 \to 7\pm1$, $4 \to 8\pm1$, and $5 \to 9\pm1$.

These triggers were defined logically as:

$$
\begin{aligned}
(N \to N+4) = {} & IB \cdot ST(1) \cdot ST(2\text{-}19) \cdot \\
& \cdot AU(N) \cdot AV(N) \cdot \\
& \cdot BU(N+4\pm1) \cdot BV(N+4\pm1) \cdot \\
& \cdot [\, (CX(N+4\pm1) + CY(N+4\pm1) + DX(N+4\pm1) \\
& \qquad + DY(N+4\pm1) + DX'(N+4\pm1)) \geq 2]
\end{aligned}
$$

where ST(1) is a signal from the first smart target segment consistent with a single track, ST(2-19) is an appropriate signal from other segments of the smart target, and AU(N) refers to seeing N sparks in chamber AU, and so on.

In general, the triggers require:

1) IB
2) Signals from the smart target consistent with an interaction.
3) Exactly N hits in both AU and AV

4) N + 4±1 hits in both BU and BV

5) N + 4±1 hits in 2 out of 5 of CX, CY, DX, DY, and DX'.

6) $0 \leq N \leq 5$.

2.4.2 3π Trigger

The 3π trigger, corresponding to the physics of interest here, was as follows:

$$3\pi = IB \cdot ST(1) \cdot$$
$$\cdot [(AU(3)+AV(3)+BU(3)+BV(3)) \geq 2] \cdot$$
$$\cdot [(CX(3)+CY(3)+DX(3)+DY(3)+DX'(3)) \geq 3]$$

where ST(1) is a signal from the first smart target segment consistent with a single track, AU(N) refers to seeing N sparks in chamber AU, and so on.

In words, the 3π trigger required

1) Interacting beam (IB)

2) A signal from the smart target indicating beam

3) Two out of four of AU, AV, BU, and BV register exactly three hits.

4) Three out of five of CX, CY, DX, DY, and DX' register exactly three hits.

In practice, CX and CY were frequently not working and off-line, making these triggers more stringent that it otherwise might seem. It may be noted that no multiplicity increase in the smart target was required in the 3π trigger.

CHAPTER 3

DATA PROCESSING AND PRELIMINARY ANALYSIS

3.1 TEARS

Basic pattern recognition for E580 was done with the pattern recognition program TEARS, which stands for "Terrific Event Analysis and Reconstruction System." TEARS takes the raw data as recorded at the MPS and matches PWC and spark chamber hits into proposed tracks. It uses the approximation that the magnetic field is constant, with corrections for vertical focussing.

The following review of TEARS function is thanks to A. Napier, the caretaker of the program (Napier 1984b).

First, TEARS unpacks the raw data tapes. In the event that a chamber has several adjacent wires lit, TEARS will treat each separate wire as a unique hit, and not group several wires together into one hit with a larger error.

Next, TEARS looks at downstream tracks in the xz (bend) plane, or x view. The chambers used in the downstream x are as follows: DX, DX', F'X, and the eight spark chamber x-planes: E1X, E2X, E3X, E4X, F1X, F2X, F3X, and F4X, for 11 chambers total. It makes three passes,

looking first for tracks of very high quality ("supertracks"), then two more in search of lower-quality tracks. After finding a supertrack, TEARS will delete all sparks used in that track. This is not done on subsequent passes.

The criteria for a supertrack (first pass) in downstream x are as follows: Maximum χ^2/DF of 2.0. If between 1.5 and 2.0, may fail subsequent tests; if less than 1.5, keep without question. Also require at least five hits within a road width of 1 cm: one each in DX and DX', one in one of (E1X, E2X, E3X), and two in any of the remaining six chambers (E4X, F1X, F2X, F3X, F4X, F'X).

The second pass has requirements of five sparks anywhere, with a χ^2_{max} of 5.0 and χ^2_{ok} of 2.5. The third pass requires merely two or three sparks.

Next TEARS looks for downstream y tracks, using the chambers DY, E1Y, E2Y, E3Y, E4Y, F1Y, F2Y, F3Y, F4Y, F'Y, and the upstream chambers BY and CY. The numerical requirements are identical in all three passes to those for downstream x tracks, with the change that when looking for supertracks it requires two hits from (BY, CY, DY), one from (E1Y, E2Y, E3Y), and two from the remaining six.

Next TEARS matches the downstream x tracks with the downstream y using information from the U and V chambers.

After this, TEARS goes to the Smart Target and determines possible z-positions for the vertex. It matches these up with tracks from the BB chambers upstream of the target to determine up to three possible positions for the main vertex.

Next, TEARS looks at upstream x sparks, ignoring for the moment the A-station, looking for possible V^o tracks. This is an unnecessary thing to do for this particular data sample, but was needed for the processing of the bulk of the data. Four sparks are required from the six posibilities: the five chambers (BU, BV, BX, BX', CX), and a "mid-magnet point" extrapolated from already-found tracks downstream. Note that BU and BV, while given names of slant chambers, are in actuality x chambers. The road width for upstream x is 5 mm. $\chi^2_{max} = 2.5$, $\chi^2_{ok} = 1.5$.

After this, the program matches upstream x tracks with downstream x, assuming constant magnetic field. It calculates a preliminary momentum, and from this a vertical focussing correction.

The next step is to look for upstream y tracks, again ignoring the A-station. Three hits are required, from the chambers (BY, CY), the mid-magnet point as explained above,

and a projected point calculated from the upstream x tracks using UV information. $\chi^2_{max} = 2.5$, $\chi^2_{ok} = 1.5$.

After this, TEARS incorporates the vertex information and the A-station while looking for upstream tracks in first y, then x. In y, one hit is required from (AY1, AY2), one from (BY, CY), and one from anywhere else (including the mid-magnet point, the vertex point, and the projected point from the x and UV data). $\chi^2_{max} = 5.$, $\chi^2_{ok} = 2.5$ for y.

In x, six hits are required: one from (AX1, AX2, AU, AV) (where AU and AV data is converted to x sparks using y data), one from (BX, BX', CX), one from (BU, BV), and three from anywhere (including the mid-magnet point and the vertex). $\chi^2_{max} = 4.$, $\chi^2_{ok} = 2.5$.

Finally, TEARS outputs its predictions for the slope and intercept at the magnet face of each track, with full error information, as well as all x and y chamber hits associated with each proposed track.

TEARS will sometimes reject events if they do not meet certain low minimum standards for reconstructability. Events will fail if there are no downstream tracks found, due to insufficient information from the downstream chambers. TEARS will also fail events if the main vertex mechanism fails to produce any candidates, or if the vertex

lies well ahead of or behind the target. Finally, TEARS gives up on an event if there are more than 20 downstream tracks, making effective reconstruction improbable.

On the negative side, TEARS will frequently create tracks seemingly out of thin air. Stray sparks in the various chambers will be matched up and pass the loose cuts, giving more tracks for an event than actually exist. Most frequently this is done by matching two or more tracks in a given view with a single track in the other views, giving a situation of "shared legs". This problem will be dealt with later.

3.2 KLEENX

The next stage in 3π analysis is to process the TEARS output through a program called KLEENX (which "mops up after TEARS"). KLEENX takes the TEARS results and makes detailed fits and calculations, outputting a DST (Data Summary Tape).

One major function of KLEENX is to do a detailed spline fit of the tracks from TEARS, using a 64722-point map of the magnetic field. The map contains information on Bx, By, and Bz in a 23 (x) x 14 (y) x 67 (z) array. In using this, interpolation is done to estimate the B field at points in between those actually contained in the map.

For each track KLEENX returns momentum (actually 1/p), slope in x and y upstream, and intercept with the magnet face in x and y. A χ^2 of the fit is determined, but no cuts are made at this point. The assumption is made at this point that all tracks are either positive or negative pions. The program outputs all this information, plus mass, charge, and energy of the tracks, with appropriate error matrices.

Another thing that KLEENX does is to determine the position of the target vertex, in two ways: first by fitting together all tracks at a point, and second by taking the beam tracks from TEARS and the smart target information. Should these two methods both be successful, the weighted average of the two is used as the target vertex. If one fails, the other is used. If both fail, the center of the target is assigned as the vertex. The program returns the target vertex as determined by each method, as well as the average, with corresponding errors. A flag called IVFLAG is set which tells the success of determining the main vertex. IVFLAG is set as follows:

IVFLAG = DTFLAG + NUMINT

DTFLAG =	o00	No direct vertex
=	o10	Good direct vertex
=	o70	Vertex outside target limits

NUMINT	= 0	No smart target interactions, no beam
	= 1	One smart target interaction, no beam
	= 2	Two smart target interactions, no beam
	= 3	Three smart target interactions, no beam
	= 4	No smart target interactions, good beam
	= 5	One smart target interaction, good beam
	= 6	Two smart target interactions, good beam
	= 7	Three smart target interactions, good beam

Clearly, the best values for IVFLAG are IVFLAG = o10 (8) + 5, 6, or 7, or 13, 14, or 15. The data shows 85% with the value 13, 4% with 14, and less than 1% with 15. Thus, 89% of the data has a very well-determined main vertex.

KLEENX also returns values called DIRR and SDIRR. DIRR is the distance of closest approach in the xy plane of each track from the just-determined main vertex. SDIRR is the uncertainty on this value, determined by a very complicated calculation from the errors on both the track and the main vertex.

KLEENX was designed to find V^{o}'s, and spent considerable effort pairing up TEARS tracks to form neutral tracks which pointed to the target vertex. This function was turned off in the analysis of the 3π data.

3.3 Shared Legs

In previous E580 analysis, the problem of two tracks sharing sparks was not addressed until after KLEENX processing had been completed. It was well-known that TEARS would frequently assign the same spark or group of sparks to two or more tracks, creating extra tracks. If one waits until KLEENX has finished its work, which includes doing a spline fit to the tracks using a detailed map of the magnetic field and (in other parts of the E580 analysis) doing a constrained fit to V^0 masses, most information about shared legs has been obscured.

This analysis has the opportunity to move back one step in order to get at the root of the shared leg problem. Using TEARS output tapes, which include some (but not all) data on the original sparks, it is possible to devise cuts by which at least the worst of the tracks, possessing legs shared with other better tracks, may be marked for later removal.

There are four "views" involved in the TEARS output: downstream x, downstream y, upstream x, and upstream y. For each view, there are two parameters which describe a track leg in that view: slope and intercept at the magnet face.

In Fig. 3.1(a-d) are shown the difference in slope between pairs of tracks for each of the four views. In the downstream x and y views, the binning is chosen so that a difference of one wire spacing over the distance between the DY and the middle of the FY chambers will correspond to five bins. In the upstream x and y views, the binning is chosen so that a difference of one wire spacing over the distance between the A-station and the C-station will correspond to five or ten bins. (The A-station has half the wire spacing of the C.) As may be seen, there is a sharp rise in the first bin for all views but the downstream x. This means a large number of pairs of tracks have virtually identical legs in the upstream x and y and the downstream y views, and hence some tracks are candidates for removal. This is not expected in the downstream x, since this view is largely used by TEARS to differentiate between tracks, and so most shared legs can be attributed to pairs of tracks which differ in downstream x but are very similar otherwise.

In Fig. 3.2(a-d) are shown differences of intercepts between pairs of tracks in each of the four views. For downstream x and y, the binning is chosen so that a difference of one wire spacing in D and F will correspond to five bins. For upstream x and y, the binning is chosen so that a difference of one wire spacing will correspond to ten bins (A-station) or five bins (C-station). Again,

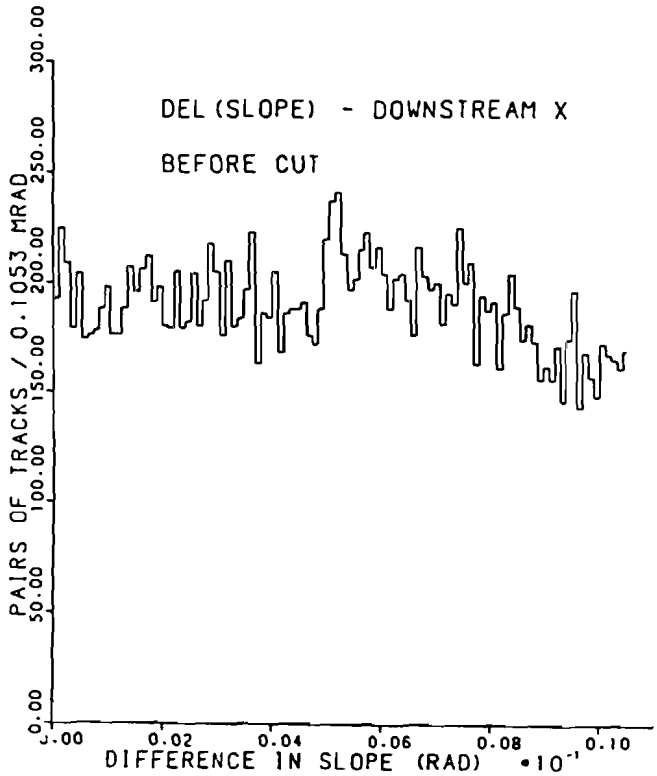

Figure 3.1(a): Δ(slope) for Downstream x tracks, before shared leg cut.

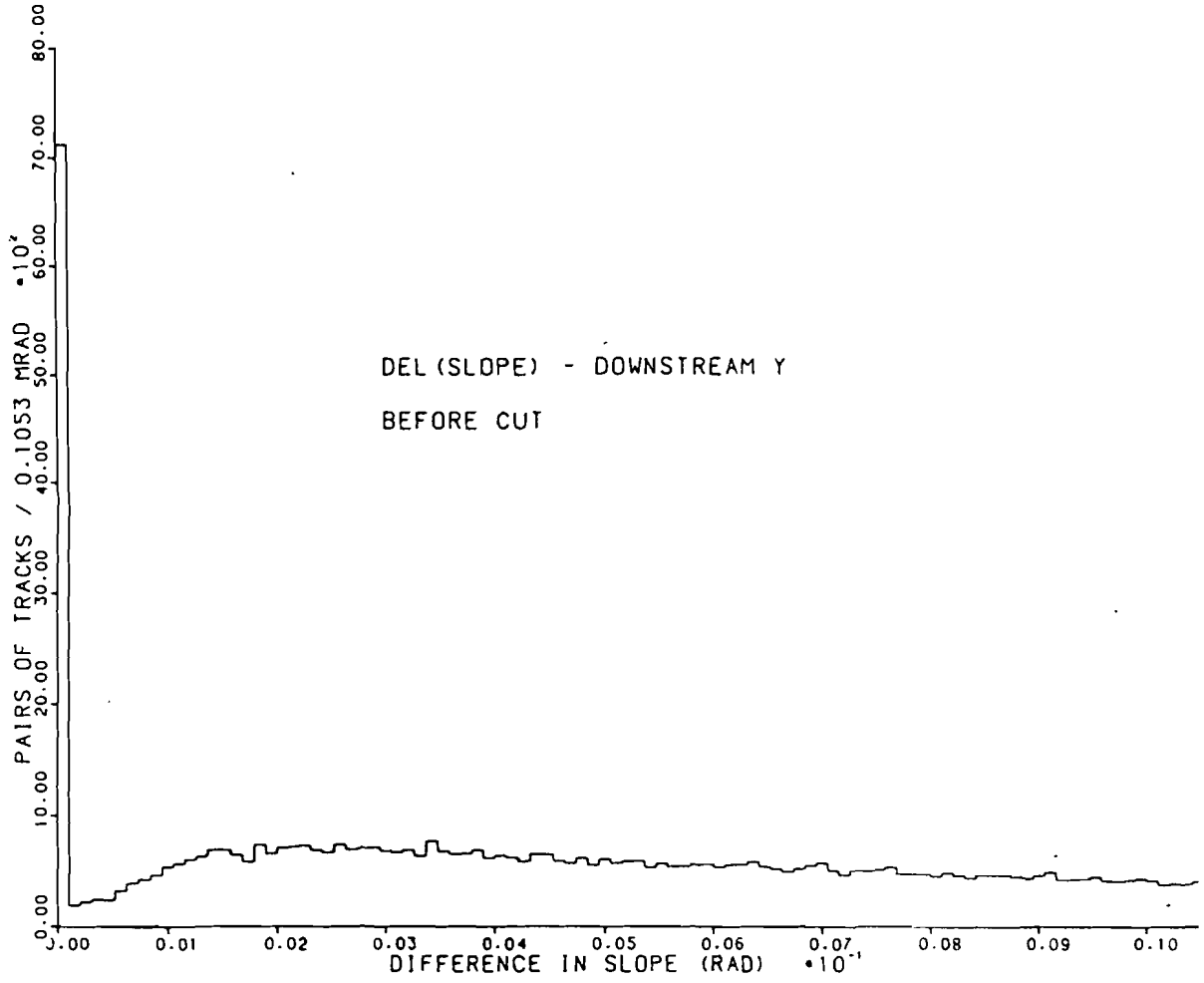

Figure 3.1(b): Δ(slope) for Downstream y tracks, before shared leg cut.

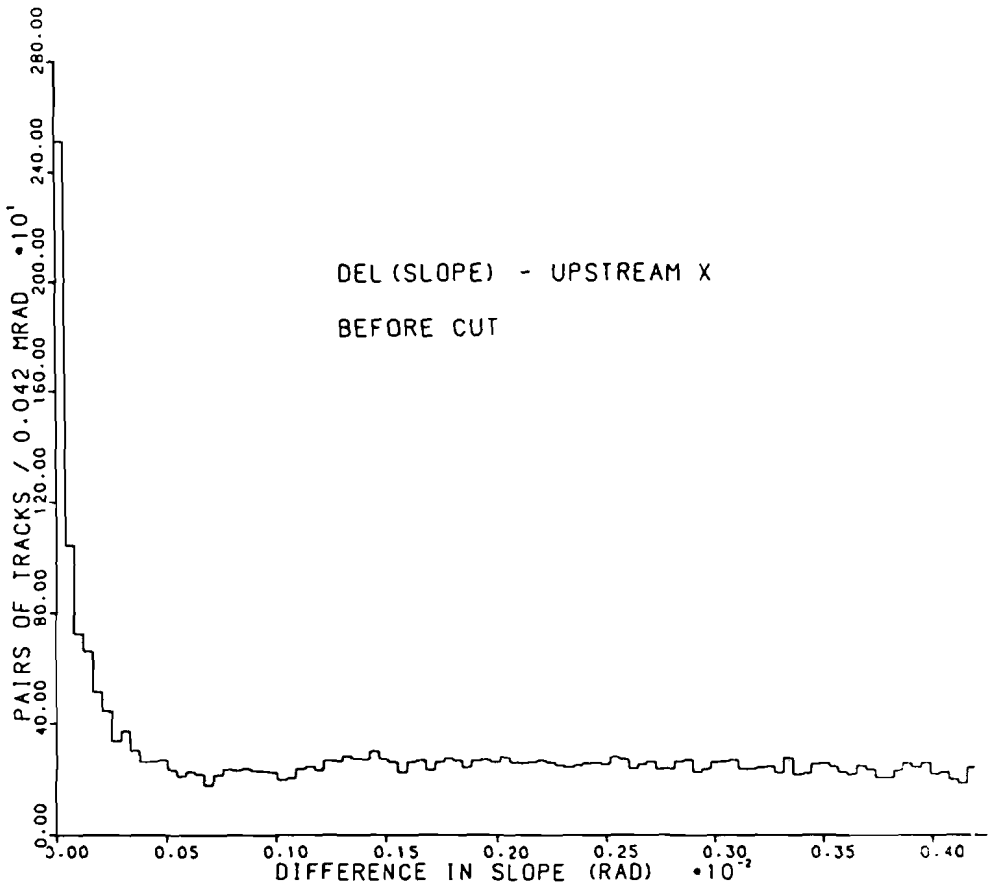

Figure 3.1(c): Δ(slope) for Upstream x tracks, before shared leg cut.

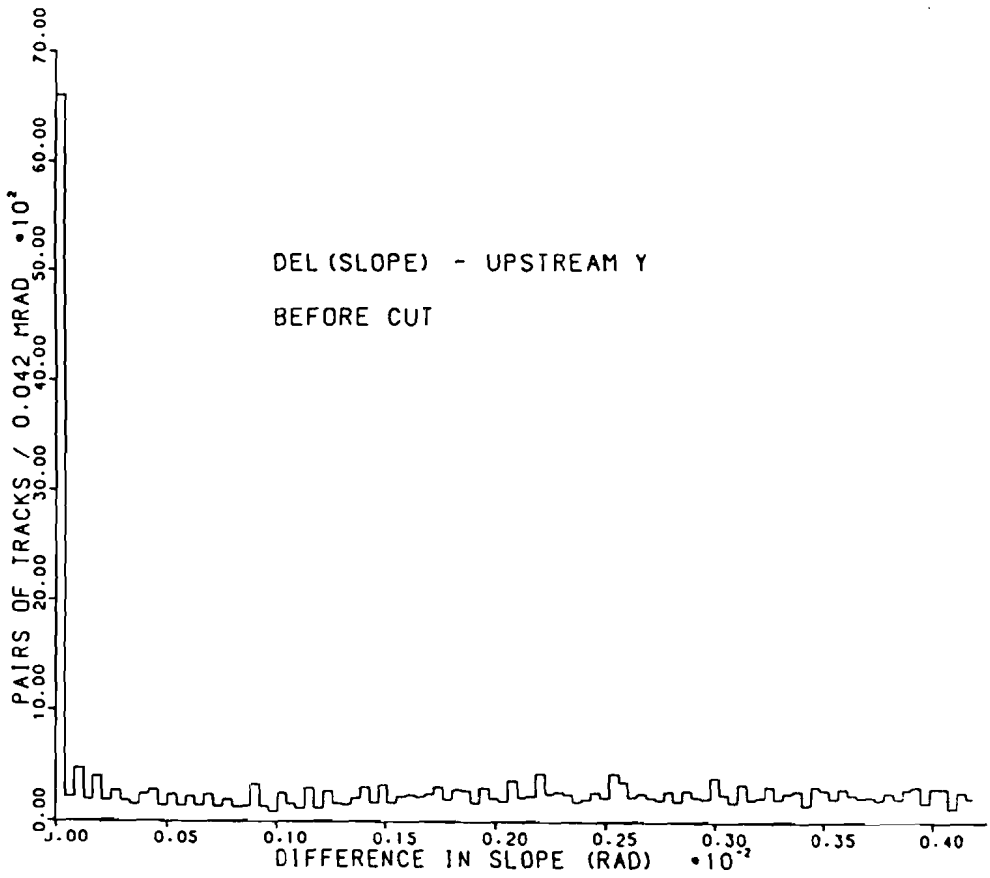

Figure 3.1(d): Δ(slope) for Upstream y tracks, before shared leg cut.

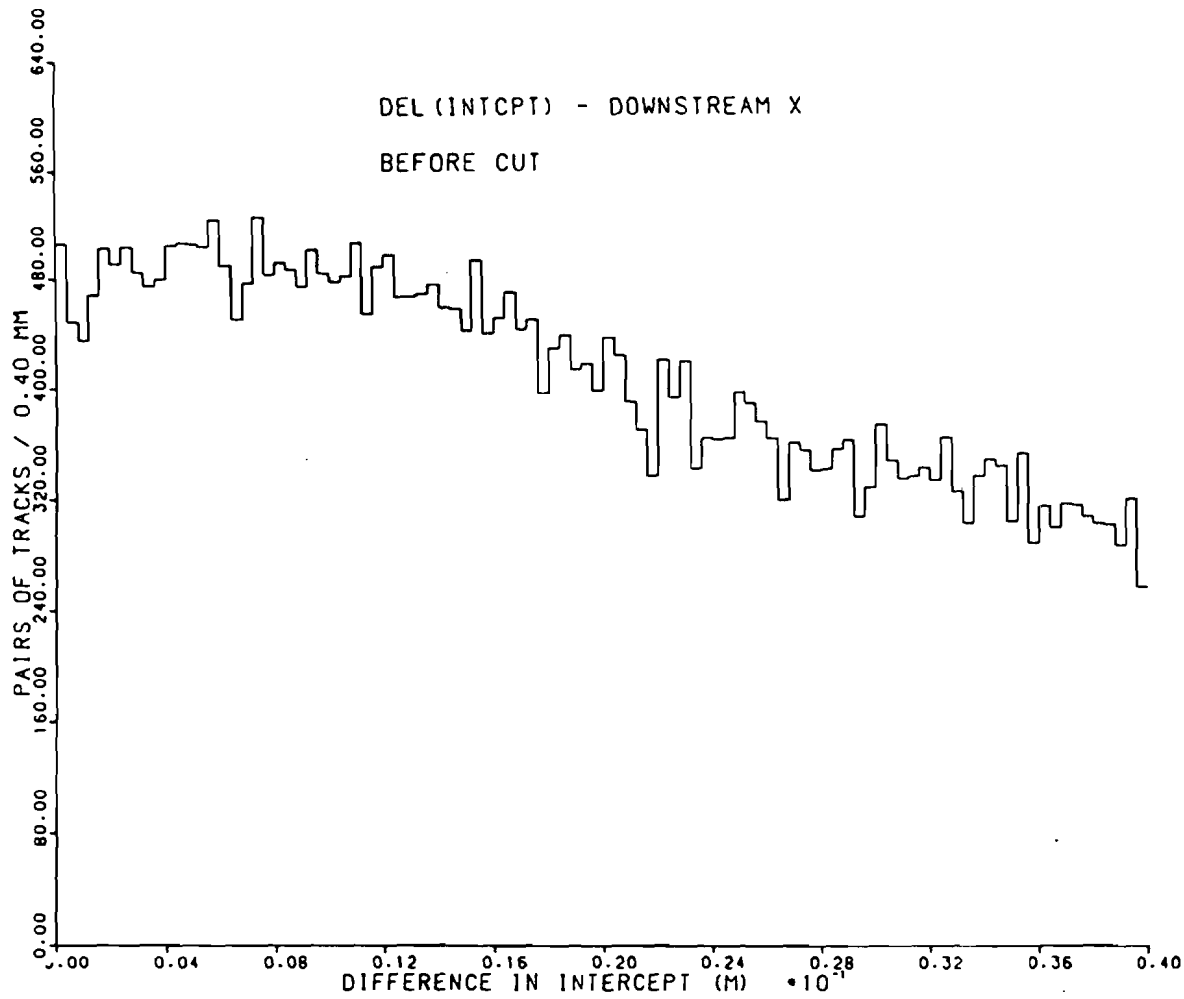

Figure 3.2(a): Δ(intercept) for Downstream x tracks, before shared leg cut.

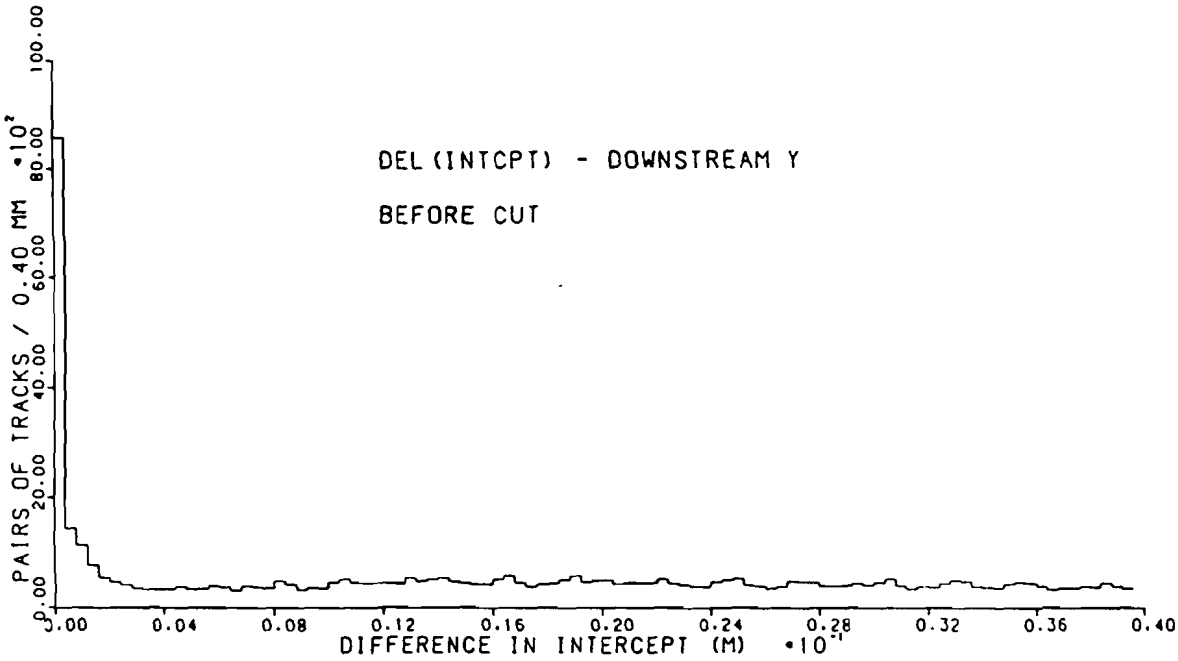

Figure 3.2(b): Δ(intercept) for Downstream y tracks, before shared leg cut.

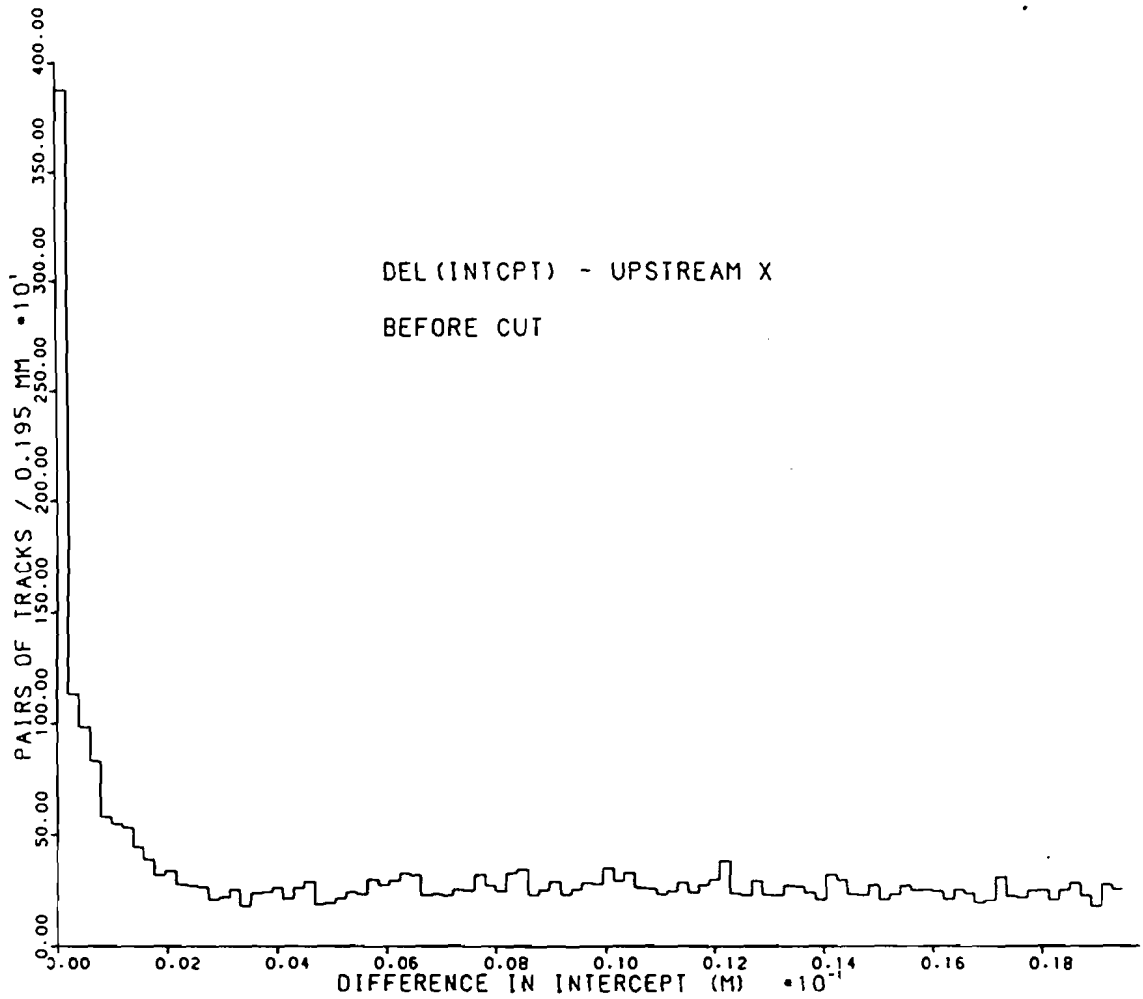

Figure 3.2(c): Δ(intercept) for Upstream x tracks, before shared leg cut.

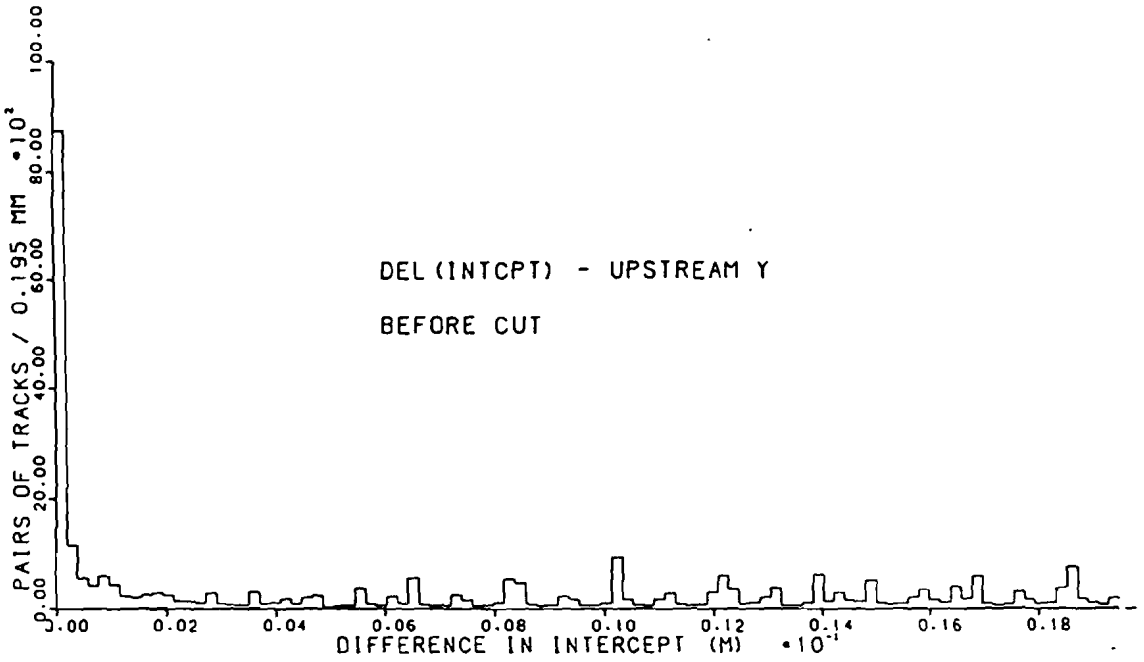

Figure 3.2(d): Δ(intercept) for Upstream y tracks, before shared leg cut.

there is a sharp rise in the first bin in all views except downstream x, meaning that overlapping is occurring in intercepts as well as slopes. This is not seen in downstream x, as the intercept is extrapolated to the front magnet face, rather than the center of the magnet, and so we would not expect downstream tracks in the xz (bend) plane to have correlating intercepts.

Based upon these plots, the assumption was made that the curves involved are smooth, and a cut was found for each view which would smooth out the first bin. These cuts are in Table 3.1.

TABLE 3.1

CUTS FOR DEFINING SHARED LEGS

View	Slope(mrad)	Intercept(mm)
Downstream x	0.00	0.00
Downstream y	0.06	0.01
Upstream x	0.18	0.03
Upstream y	0.10	0.02

Figs. 3.3(a-d) and 3.4(a-d) illustrate differences of slope and intercept with the binning shifted by the amount of the cuts above. The curves, while still not perfectly smooth, are a vast improvement.

It was required that, for a given pair of tracks, both the slope and intercept in any given view be within the parameters above, as two tracks with virtually identical slope or intercept could be mere coincidence, but an instance of both occurring meant virtual certainty of a shared leg. In fact, a very strong correlation is observed between the two.

Now that pairs of tracks with shared legs have been found, how does one decide whether and how to mark one of them as being "bad"? First shall be dealt with the matter of "reprieving" tracks, a situation in which both tracks are deemed to be good, in spite of a shared leg.

In order for both tracks in a shared-leg pair to be "good", two things are required: first, a minimum number of sparks in each view; and second, that the two tracks not completely overlap in both y-views.

Fig. 3.5 shows the observed number of sparks in each view, for all tracks. Note that in the upstream y-view some tracks actually have zero sparks, meaning that the leg was created solely out of the vertex point, the mid-magnet

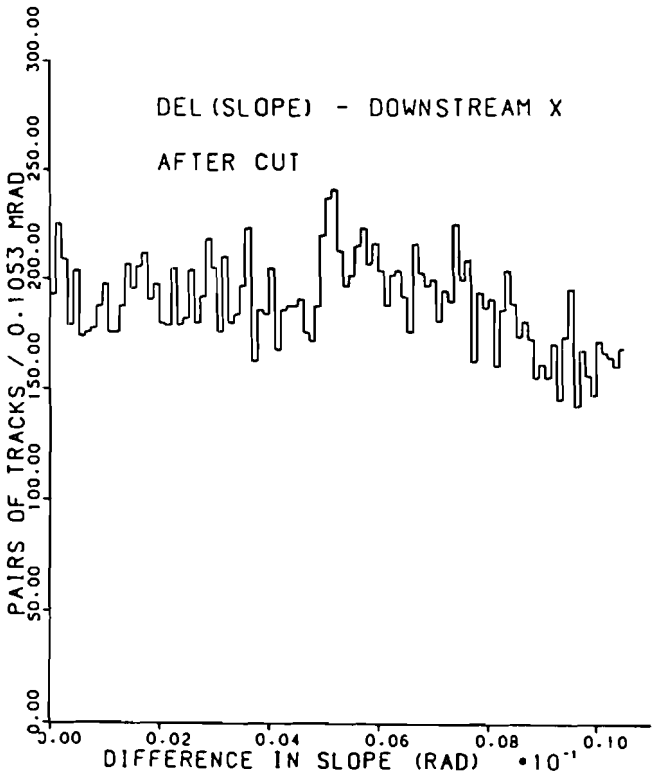

Figure 3.3(a): Δ(slope) for Downstream x tracks, after shared leg cut.

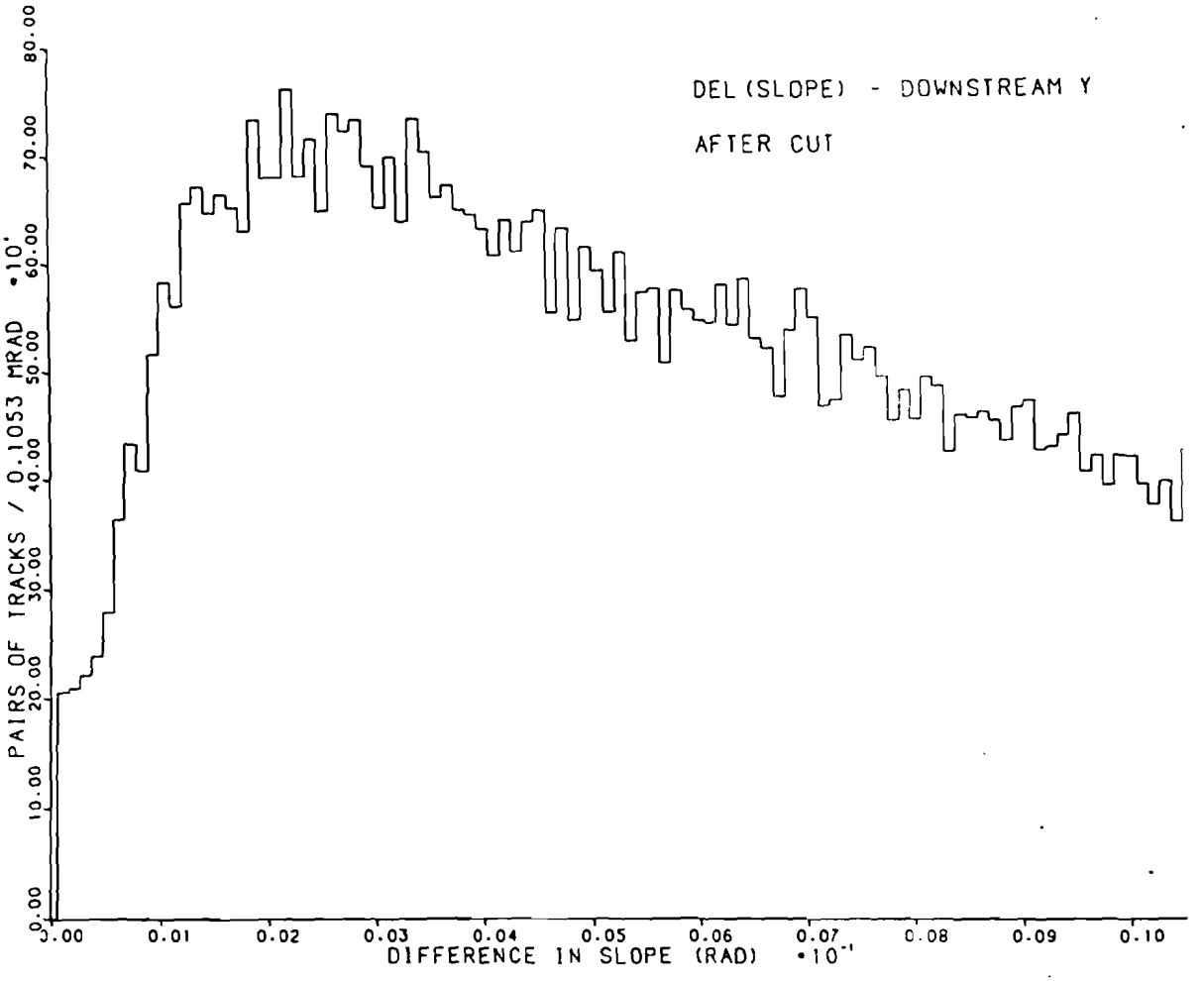

Figure 3.3(b): Δ(slope) for Downstream y tracks, after shared leg cut.

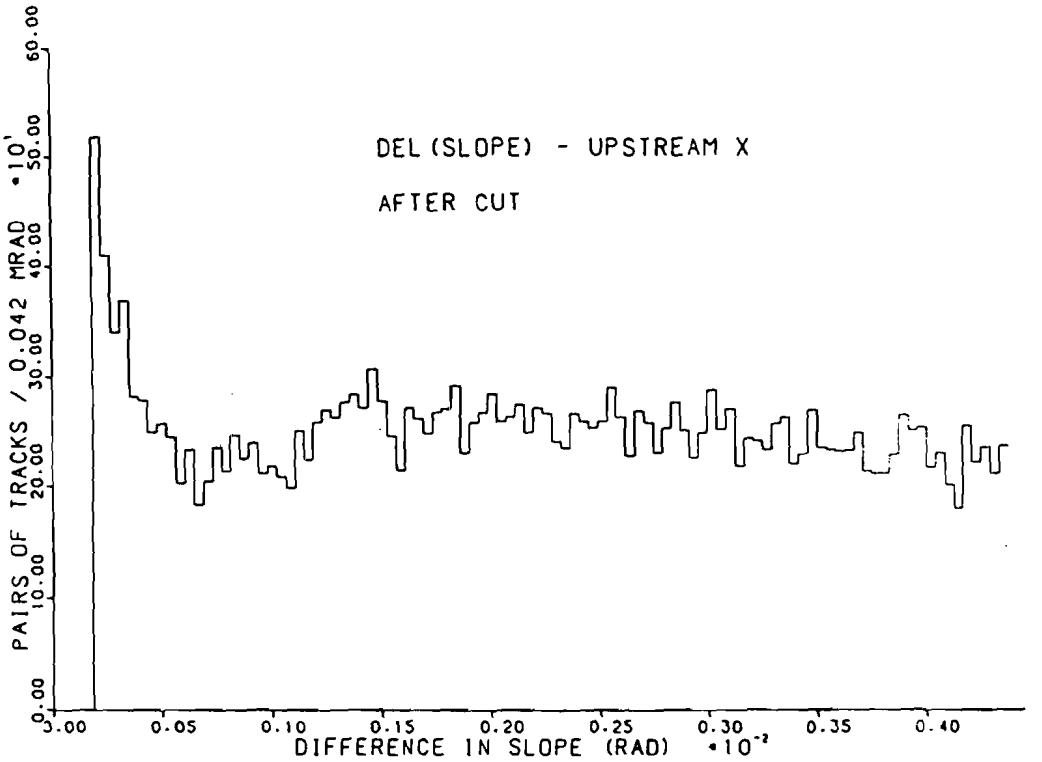

Figure 3.3(c): Δ(slope) for Upstream x tracks, after shared leg cut.

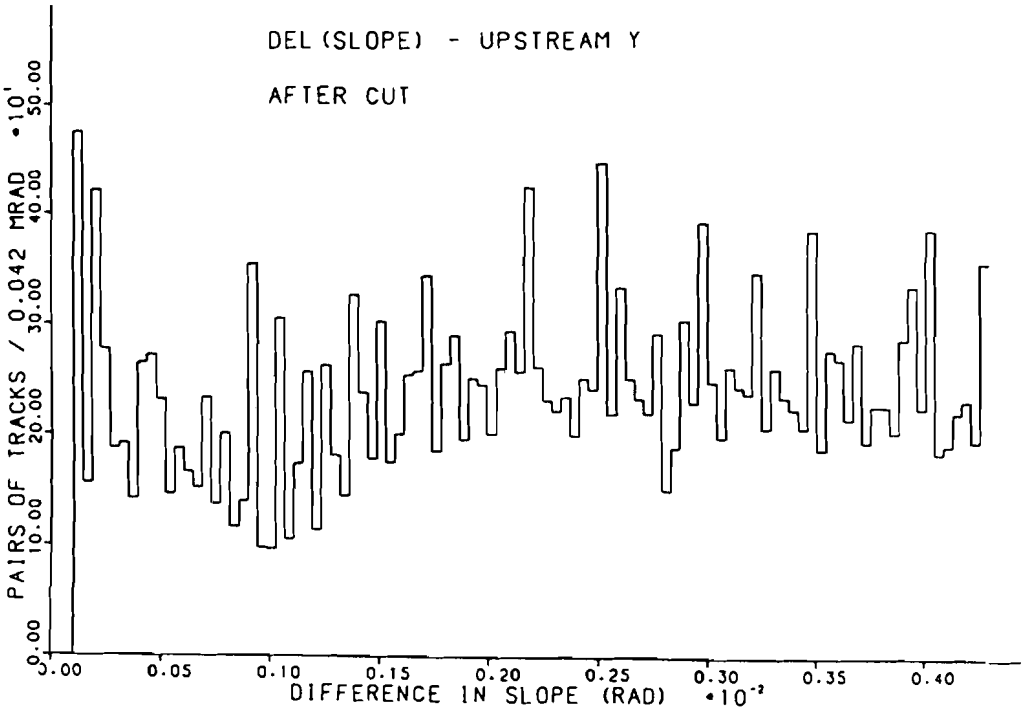

Figure 3.3(d): Δ(slope) for Upstream y tracks, after shared leg cut.

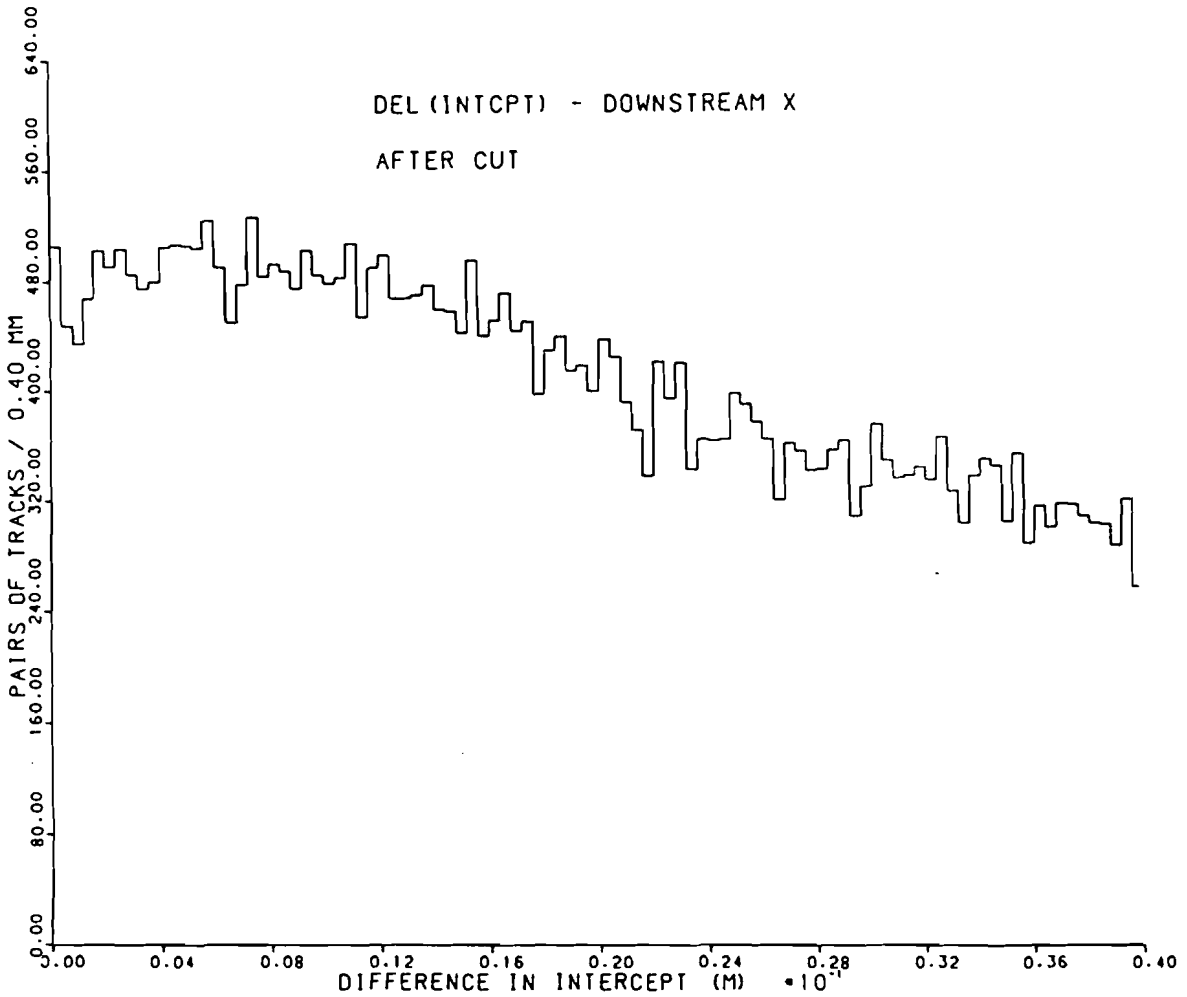

Figure 3.4(a): Δ(intercept) for Downstream x tracks, after shared leg cut.

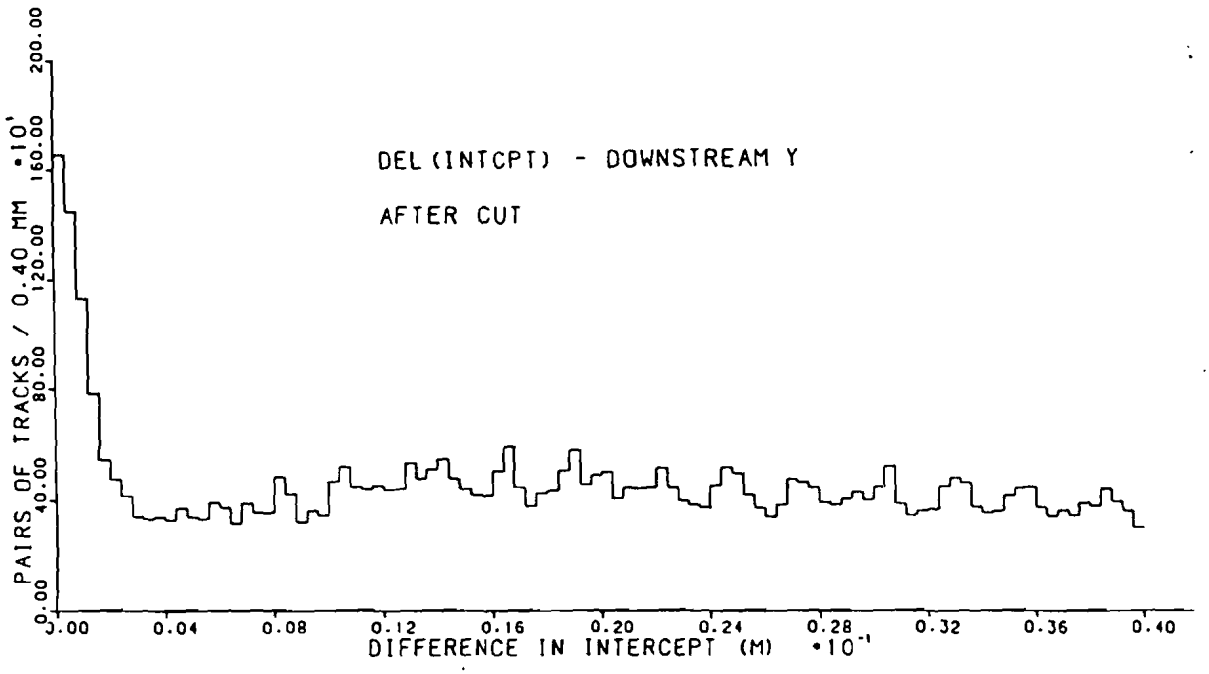

Figure 3.4(b): Δ(intercept) for Downstream y tracks, after shared leg cut.

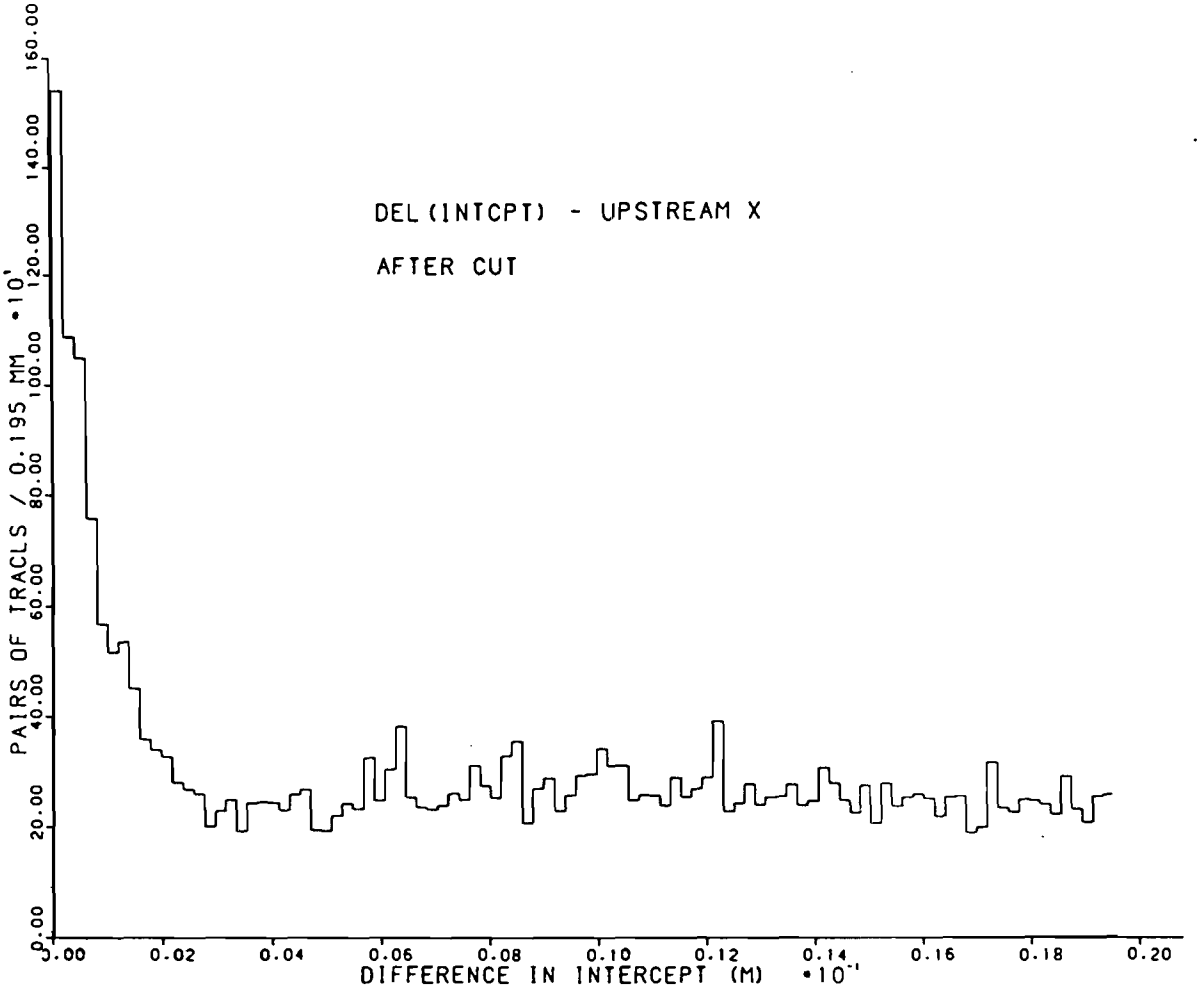

Figure 3.4(c): Δ(intercept) for Upstream x tracks, after shared leg cut.

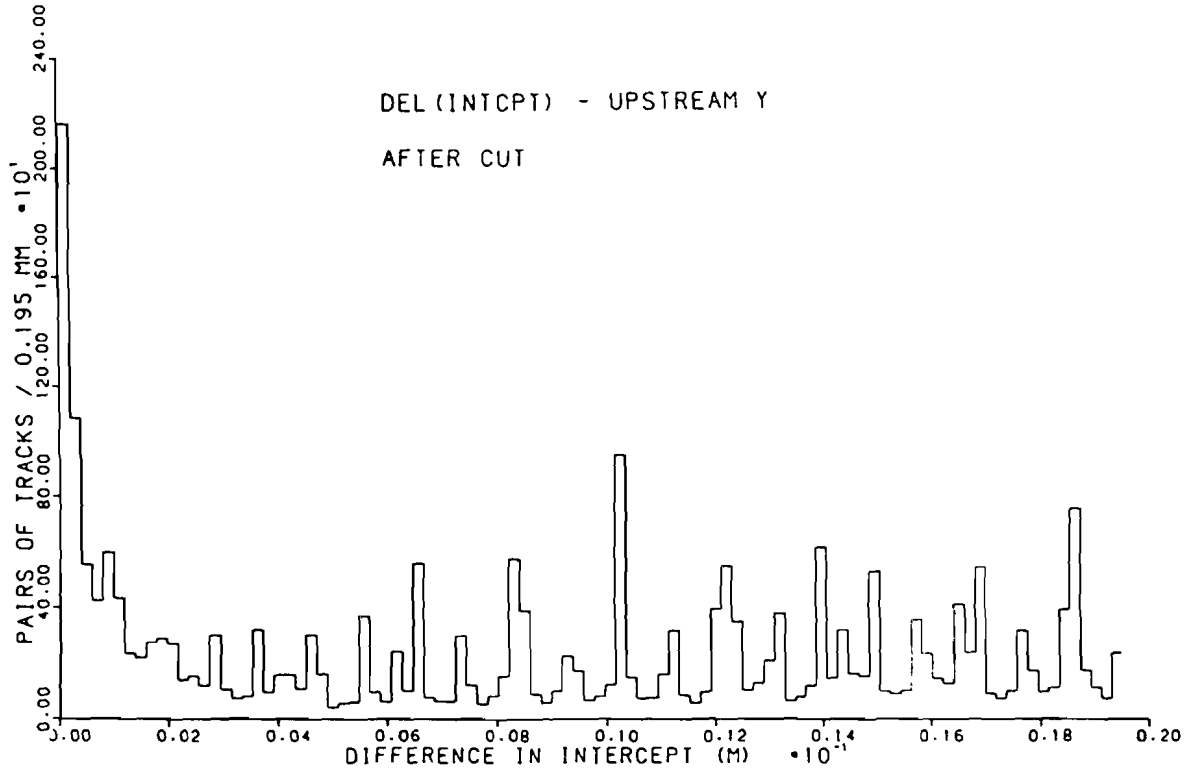

Figure 3.4(d): Δ(intercept) for Upstream y tracks, after shared leg cut.

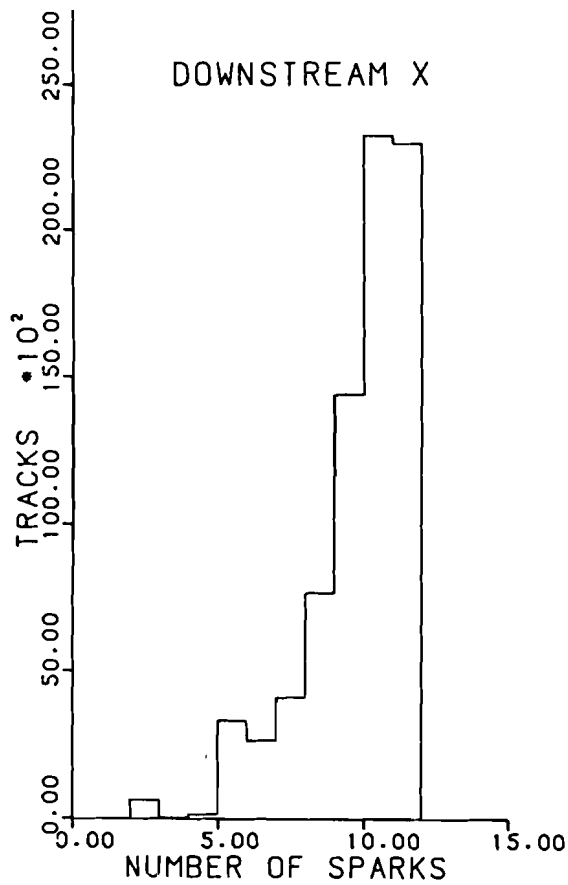

Figure 3.5(a): Number of sparks for Downstream x tracks.

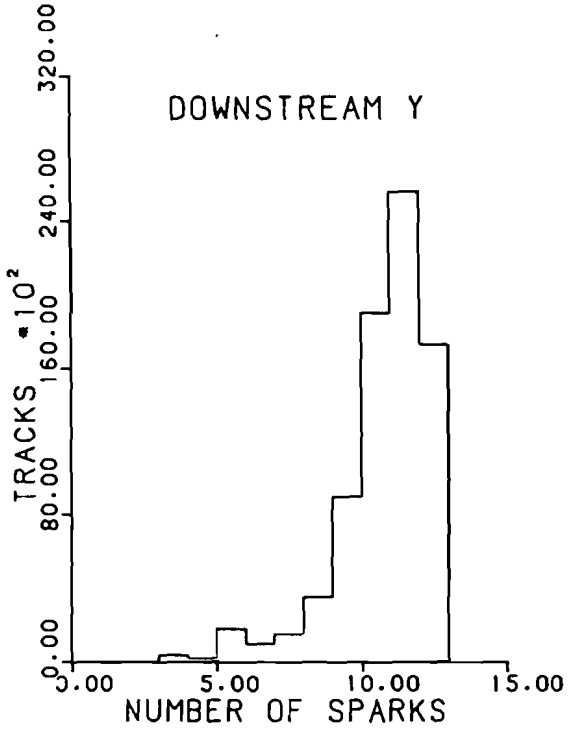

Figure 3.5(b): Number of sparks for Downstream y tracks.

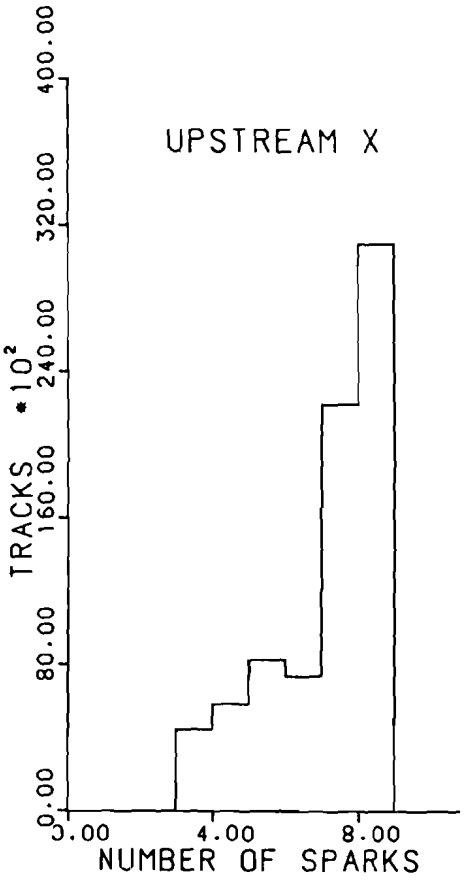

Figure 3.5(c): Number of sparks for Upstream x tracks.

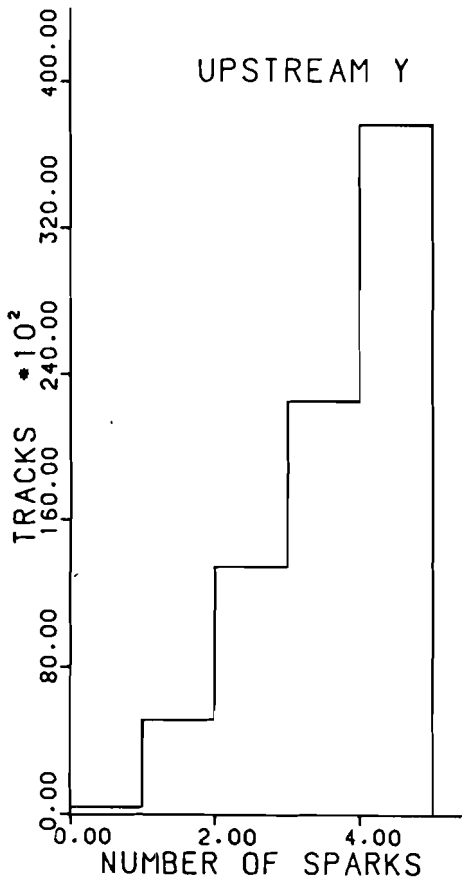

Figure 3.5(d): Number of sparks for Upstream y tracks.

point from downstream tracks, and/or the projected point from upstream x tracks using UV information.

The minimum requirements for number of sparks in each view required to reprieve a track, along with maximum number of sparks in each view, are in Table 3.2.

TABLE 3.2

MINIMUM REQUIREMENTS FOR NUMBER OF SPARKS TO REPRIEVE A TRACK

View	Maximum	Required
Downstream x	11	7
Downstream y	12	8
Upstream x	9	6
Upstream y	4	2

The requirement that both tracks not overlap in both y-views is based on the idea that, while coincidence may account for an overlap in one view, there ought to be enough separation between the two tracks as they traverse the length of the MPS that they eventually be distinct.

Next we deal with question of how to decide when one track is "better" than another. Two criteria are used: total number of sparks in the track, and χ^2/DF of the tracks.

The first test made is to determine when if one track contains "substantially" more sparks than the other. The definition of "substantially" was set at 10 percent. If track 1 has N1 sparks, track 2 has N2 sparks, and N1 > N2, then mark as bad track 2 if (N1 - N2)/ N1 > 0.10. For specific values of N1 and N2, this corresponds to the following:

TABLE 3.3

DIFFERENCES IN NUMBER OF SPARKS REQUIRED TO CUT A SHARED LEG TRACK

N1 in Range	Track 2 cut if (N1-N2) >=
10-19	2
20-29	3
30-35	4

Should one track not have substantially more sparks than the other, their χ^2/DF are compared. TEARS returns a χ^2 value for each track for each view, and the number of degrees of freedom for each view are in Table 3.4.

TABLE 3.4

DEGREES OF FREEDOM IN EACH VIEW

View	Number of Degrees of Freedom
Downstream x	(Number sparks) - 2
Downstream y	(Number sparks) - 2
Upstream x	(Number sparks) - 1
Upstream y	(Number sparks)

Nominally, the number of degrees of freedom is (Number sparks) - 2, since there are two fit parameters: slope and intercept. For the upstream views this is different, since additional points (such as the mid-magnet point and the projected point) were used. In the event of zero sparks in upstream y, the degrees of freedom was set to 1.

The χ^2/DF is calculated for each view, and these numbers are added together to give an overall value for each track. The track with the higher value is marked as bad.

Fig. 3.6(a-b) shows the distribution of number of sparks of good and bad tracks from pairs in which a decision was made. The mean number of sparks of good tracks is 30.3; of bad tracks, 26.2.

Fig 3.7(a-b) shows the distribution of sums of χ^2/DF for good and bad tracks from pairs in which a decision was made. The mean value for good tracks is 0.78; for bad tracks, 1.04.

Overall, 14481 tracks were marked as bad, from 11576 events. For comparison, the data was subjected to the same shared-leg cuts (post-KLEENX) as were used during other E580 analysis. The result was 55 tracks cut. Clearly, the approach used here is more effective than that used during other E580 analysis.

The program which performed this analysis was named SHRTRK, and the results from both KLEENX and SHRTRK were merged to give a final DST with bad shared-leg tracks marked for later use.

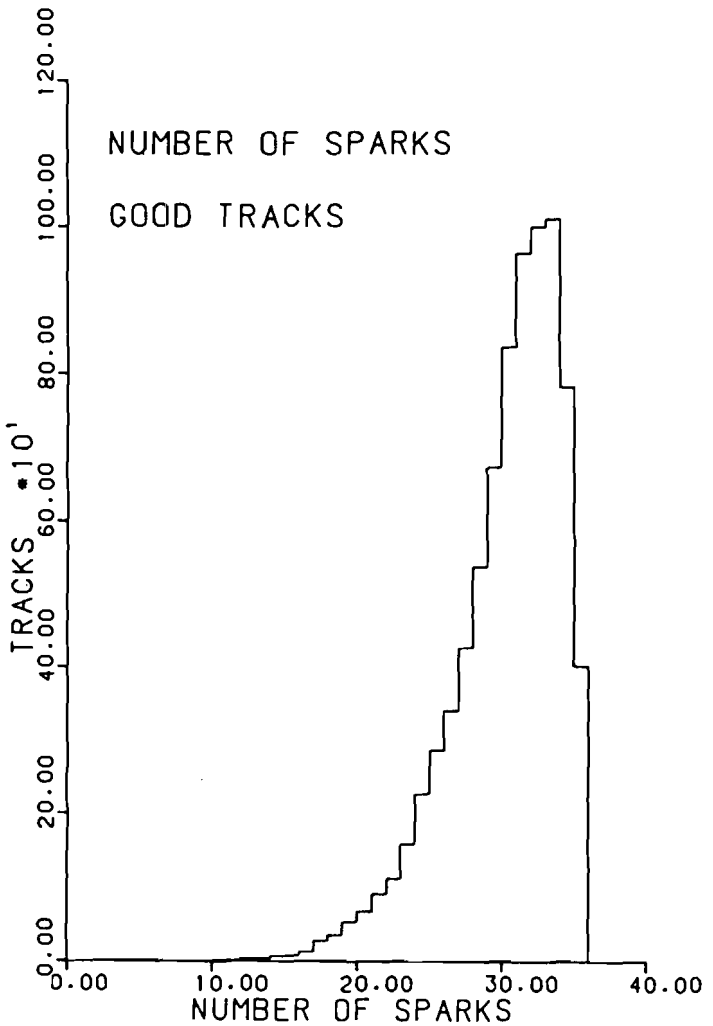

Figure 3.6(a): Number of sparks for good tracks, of pairs of tracks having shared legs.

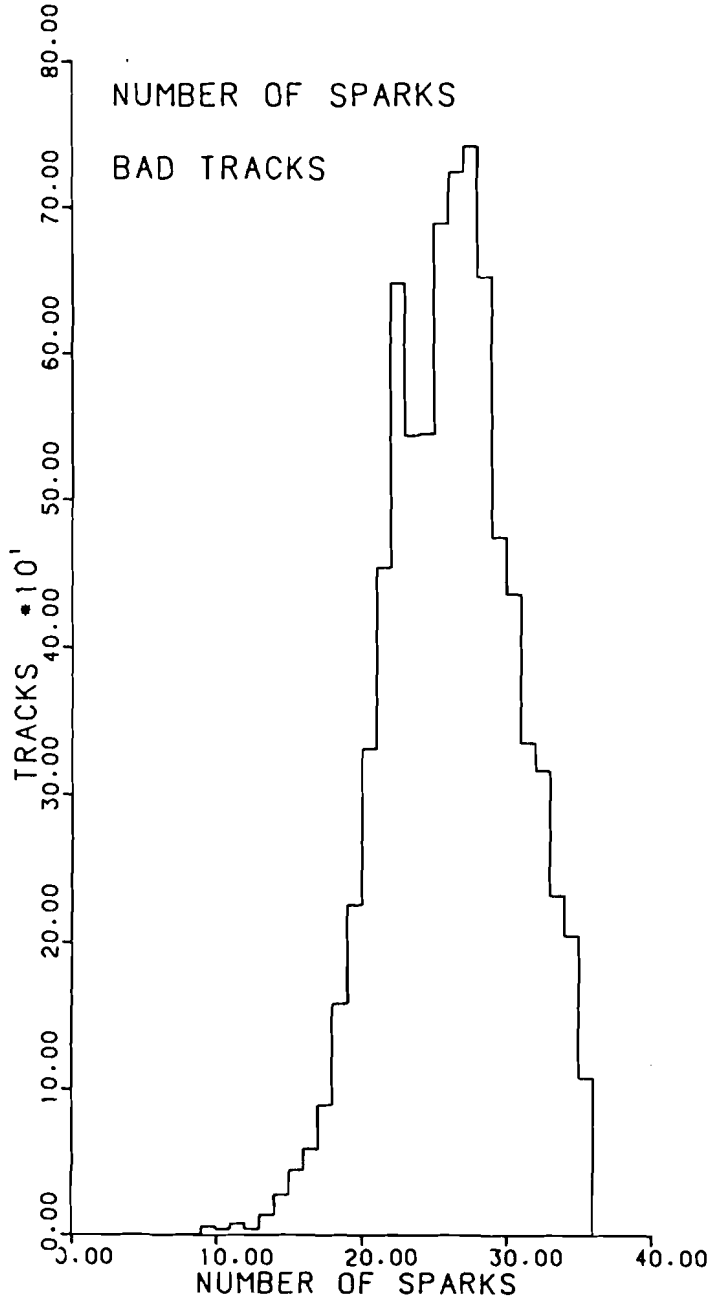

Figure 3.6(b): Number of sparks for bad tracks, of pairs of tracks having shared legs.

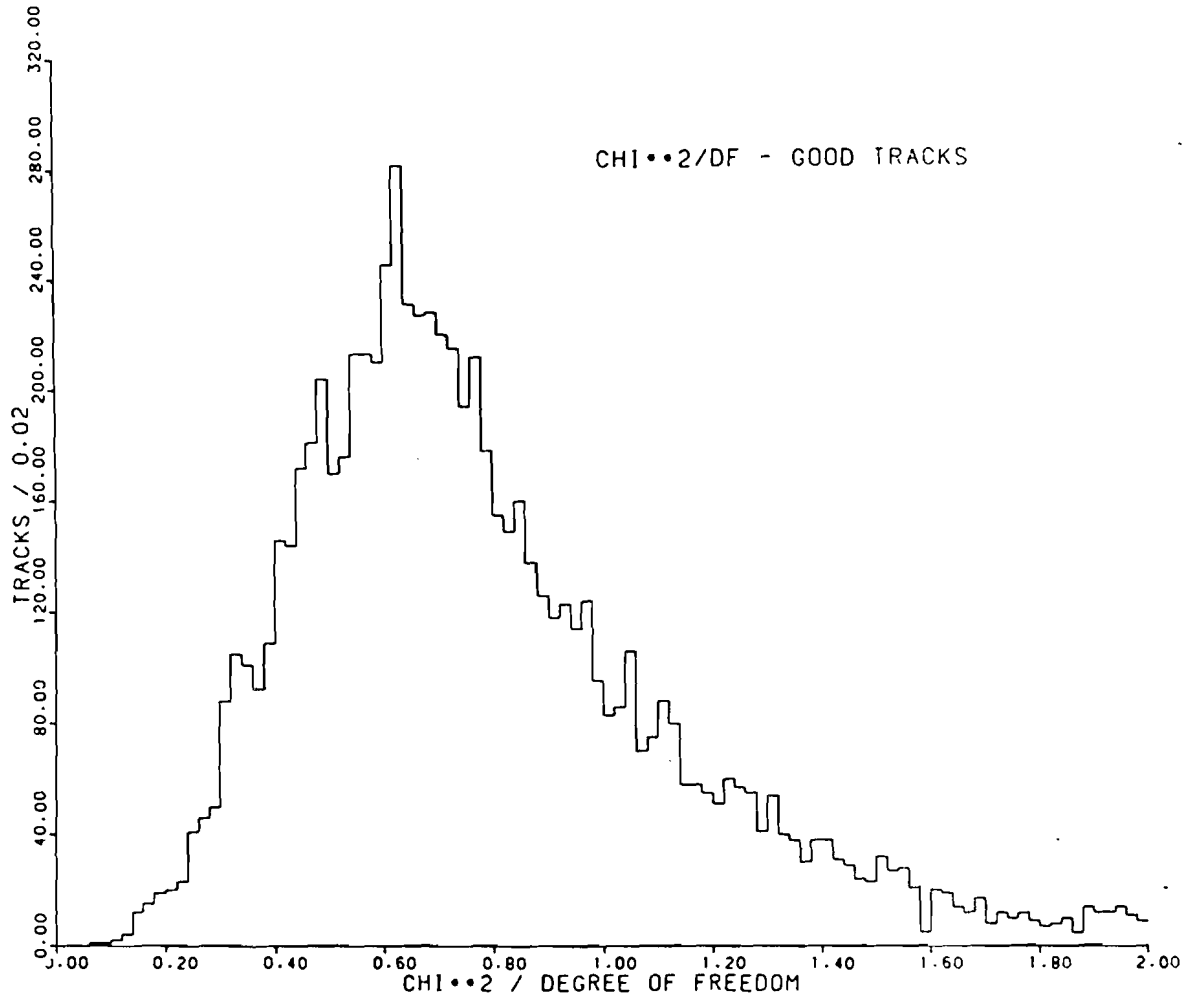

Figure 3.7(a): χ^2/(Degree of Freedom) for good tracks, of pairs of tracks having shared legs.

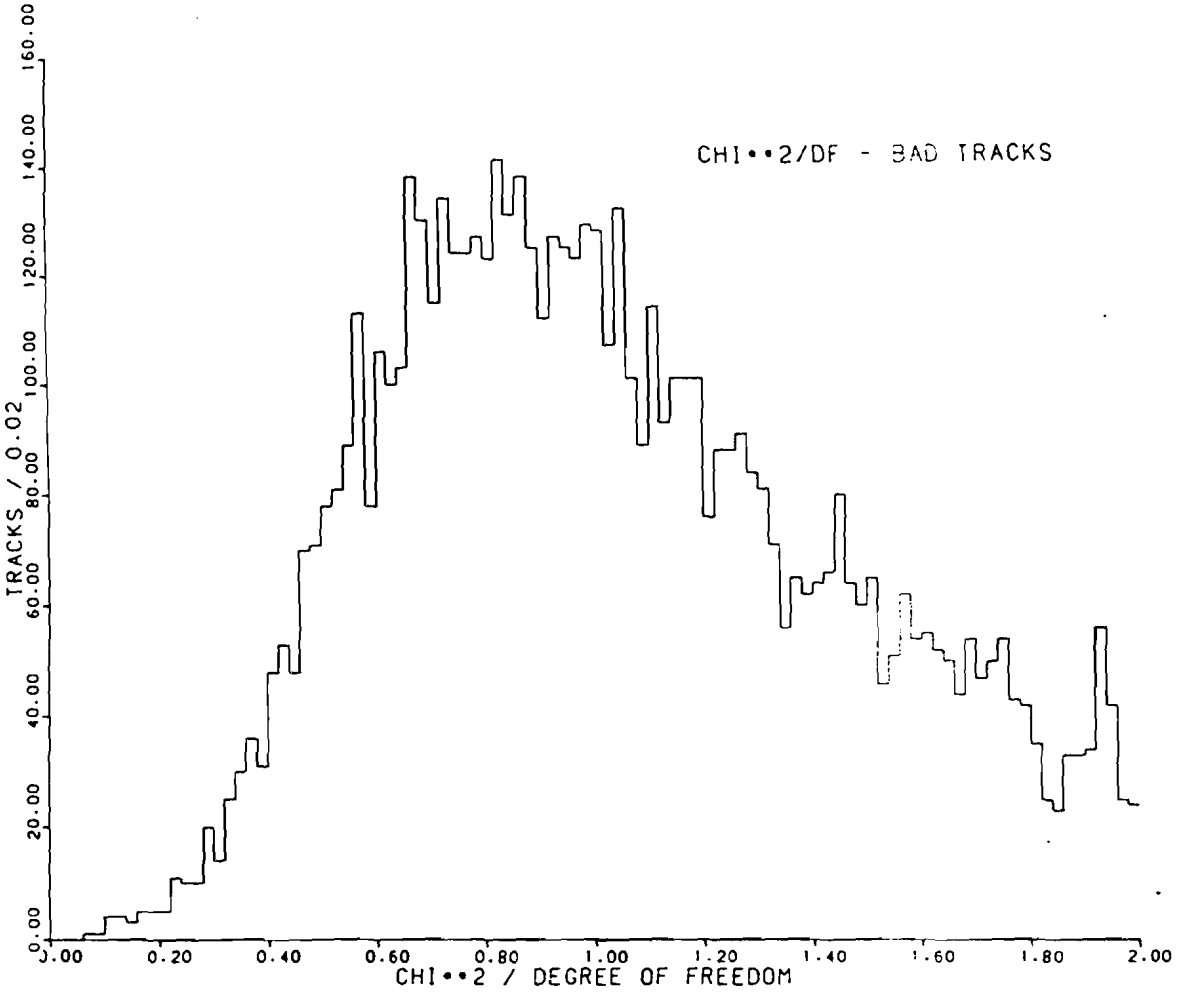

Figure 3.7(b): χ^2/(Degree of Freedom) for bad tracks, of pairs of tracks having shared legs.

3.4 Data Quality Cuts

When KLEENX analysis of the 3π data was finished, 48657 events were left. A series of cuts was made on this sample to ensure high-quality data.

The minimum requirement for candidates for events of the type $\pi^-\pi^-\pi^+$ is that there be three charged tracks, two with -1 charge and one with +1 charge. In practice, these translated to the requirement that there be four good tracks in each event (one beam plus three direct) and that the charges on the three direct tracks add up to -1. With merely these requirements, the sample of 48657 was reduced to 31274.

Next a series of cuts was made which threw out individual tracks, after which the above cuts for multiplicity and total charge were applied. Thus each cut would throw out some events which had previously passed, while at the same time making some previously-unacceptable events of higher multiplicity good by eliminating one or more tracks.

The first such cut was to eliminate tracks marked by the SHRTRK program as being duplicates of other tracks. This cut changed the number of good events to 35350. It is interesting to note that the number of good events has actually increased with this cut, but it must be remembered

that the purpose of SHRTRK, as of many of these cuts, is to cut tracks, not whole events. Thus, it turns out that with this cut, more events of initial multiplicity greater than four had the correct number of tracks cut out to bring them to four, than events with fours initial tracks had one or more cut out, eliminating the event entirely.

The next cut was to look at the χ^2 distribution of tracks as fit by the KLEENX spline fitter (Fig. 3.8(a-b). A cut of $\chi^2_x/NDF_x < 2.0$ and $\chi^2_y/NDF_y < 2.0$ was made. The reasons for the choice of 2.0 as the number upon which to cut were twofold. As may be seen from Fig. 3.8, 2.0 is out on the tails of the respective χ^2 distributions, corresponding to a probability of 0.21% for both x and y, assuming 17 hits in x and 13 in y. However, 2.0 does not occur at the same point on the tail for each. This brings us to the second reason for the choice of 2.0: historically, when the analysis of the bulk of the data from E580 was done, KLEENX contained a cut on χ^2/NDF of 2.0 in both x and y. Thus, while a different number or numbers could have been chosen, to do so would hamper efforts to compare these results with other results from the same experiment. And, since 2.0 does fulfill the desired criterion of wanting only tracks which had good fits, it was selected for this sample. After this cut, plus the ones mentioned above, there were 23200 events left in the sample.

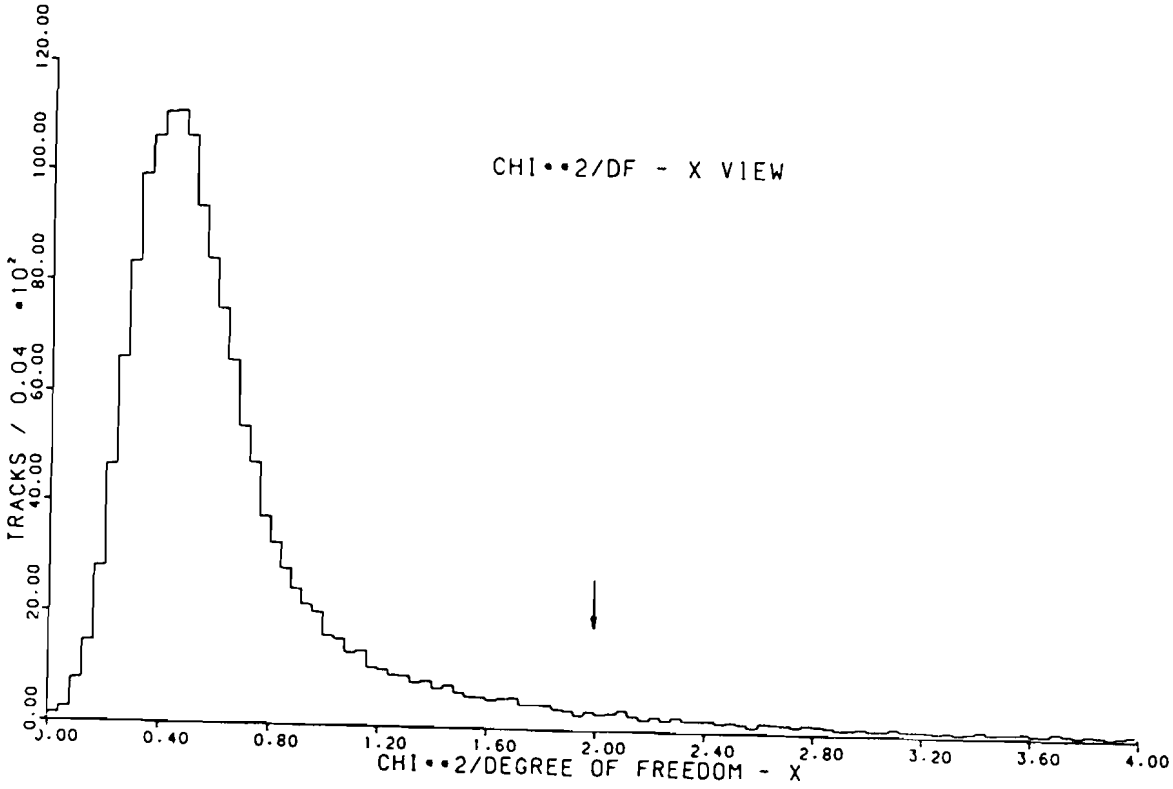

Figure 3.8(a): χ^2/(Degree of Freedom), x view, of tracks passing KLEENX. The arrow shows the position of the cut at 2.0.

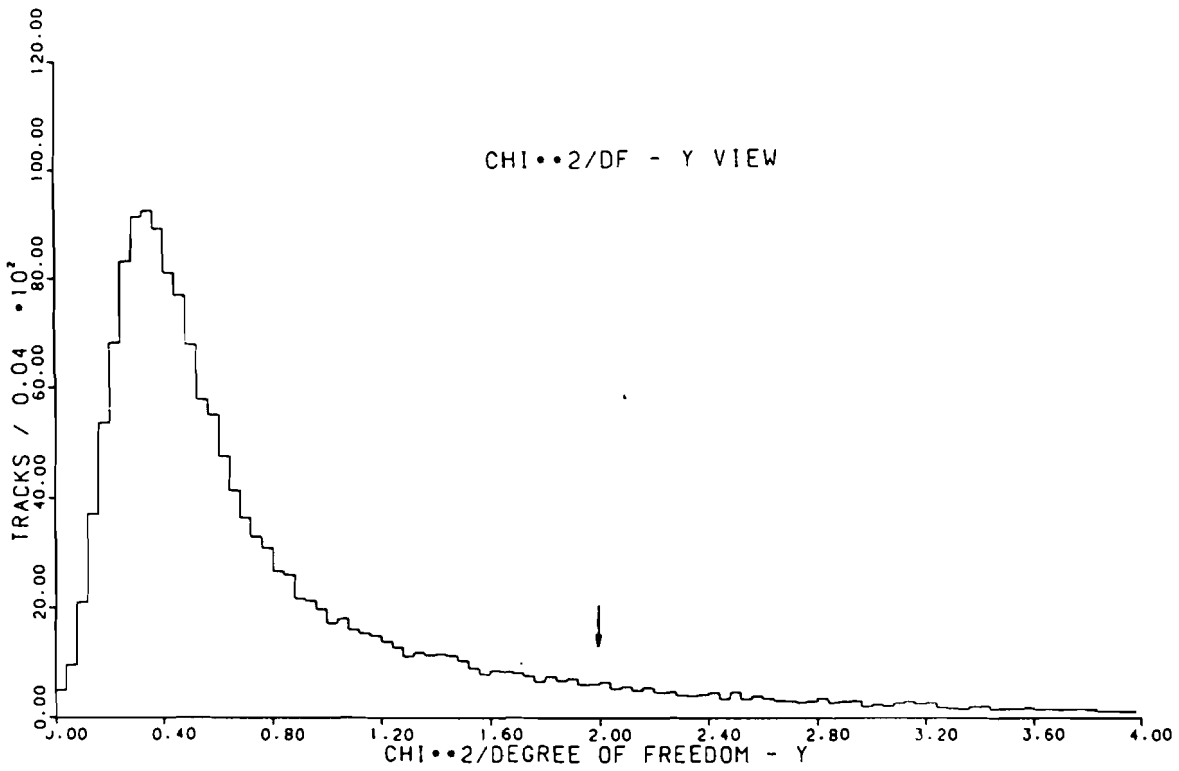

Figure 3.8(b): χ^2/(Degree of Freedom), y view, of tracks passing KLEENX. The arrow shows the position of the cut at 2.0.

The next cut was made to ensure that the tracks in the event actually came from the target, and were not the result of decays or secondary interactions. This was done by looking at the distance of closest approach of each track to the target vertex (DIRR) (Fig. 3.9) and its error (SDIRR) (Fig. 3.10), as determined by KLEENX. We define RDIRR=DIRR/SDIRR, and look at the distribution of RDIRR (Fig. 3.11). The number of events passed is not sensitive to the value of RDIRR, so the cut is chosen as RDIRR < 6.0. This is fairly loose, but does not allow in a large number of bad tracks. Basically it says that the track must be within 6σ of the target vertex. After this cut there are 19273 events left.

Finally comes the final quality cut, that upon total energy in the event (Fig. 3.12). The nominal beam momentum is 200 GeV/c. A cut of 250 GeV/c is chosen as sufficiently loose. The cut is made as follows: if the total energy of all good tracks in the event (after shared leg, χ^2, and RDIRR cuts) is greater than 250 GeV, then look first for individual tracks with energy above 250 GeV. These are thrown away, and the total energy recalculated. If no individual tracks above the limit are found, tracks are eliminated in order of decreasing RDIRR (even though RDIRR is at this point less than 6.0 for all remaining tracks). After this cut, there are 18933 events left.

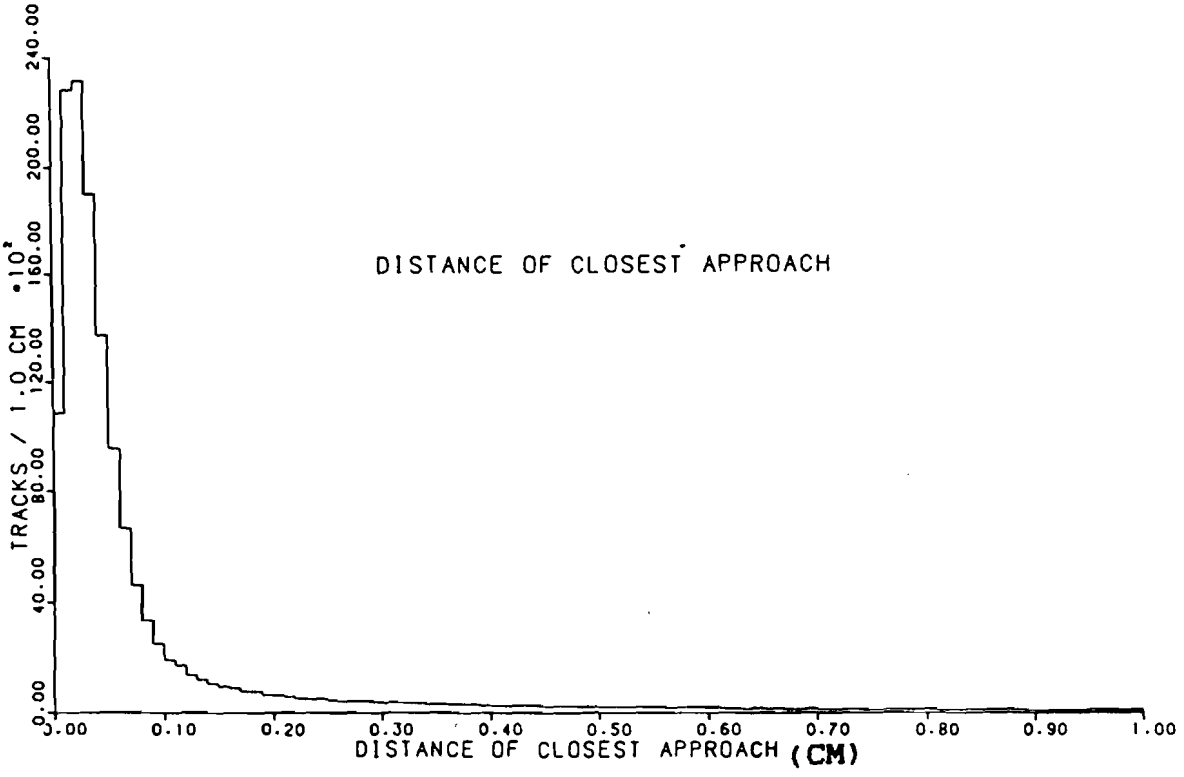

Figure 3.9: Distance of closest approach to target vertex of outgoing tracks.

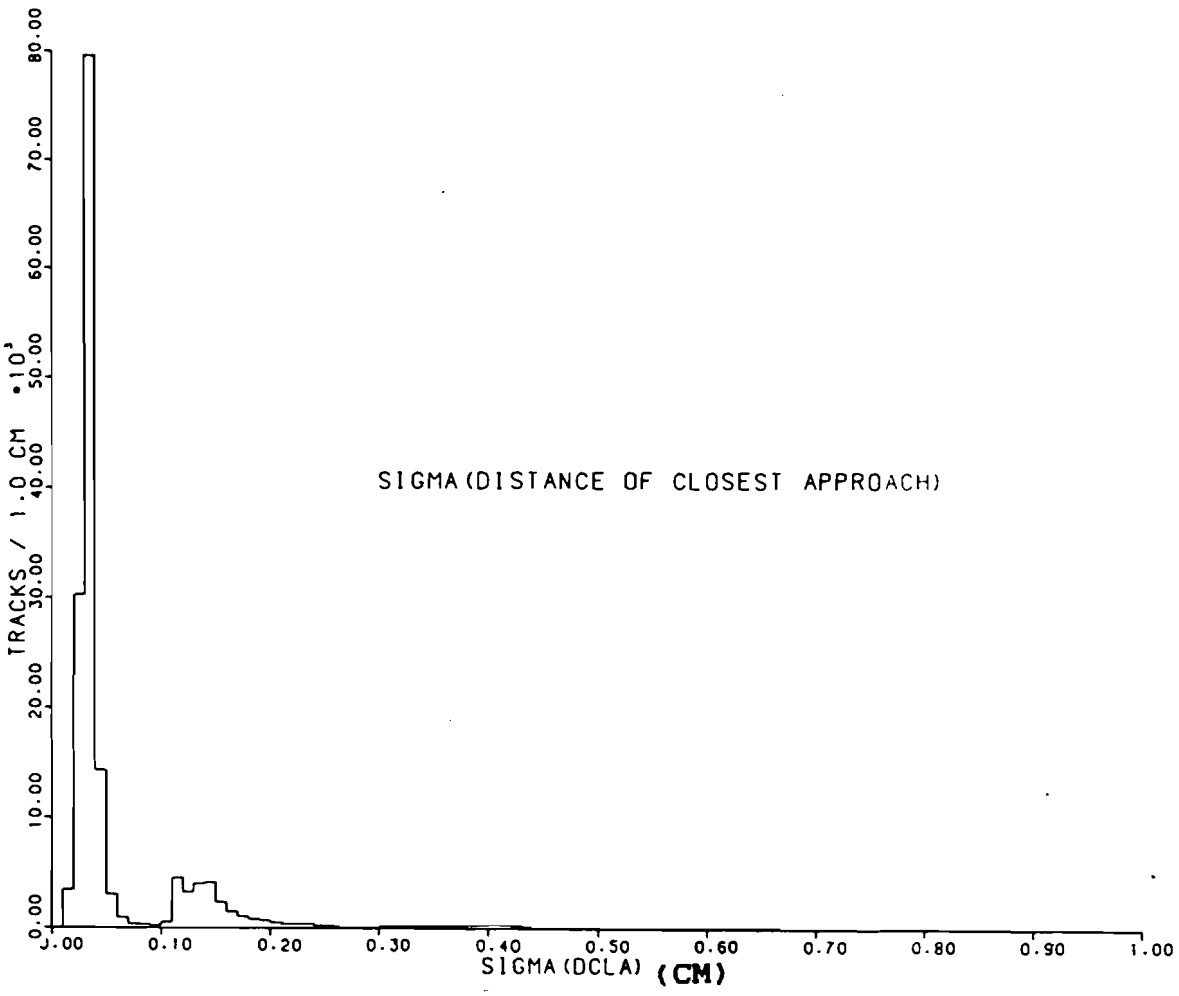

Figure 3.10: Uncertainty of distance of closest approach to target vertex of outgoing tracks.

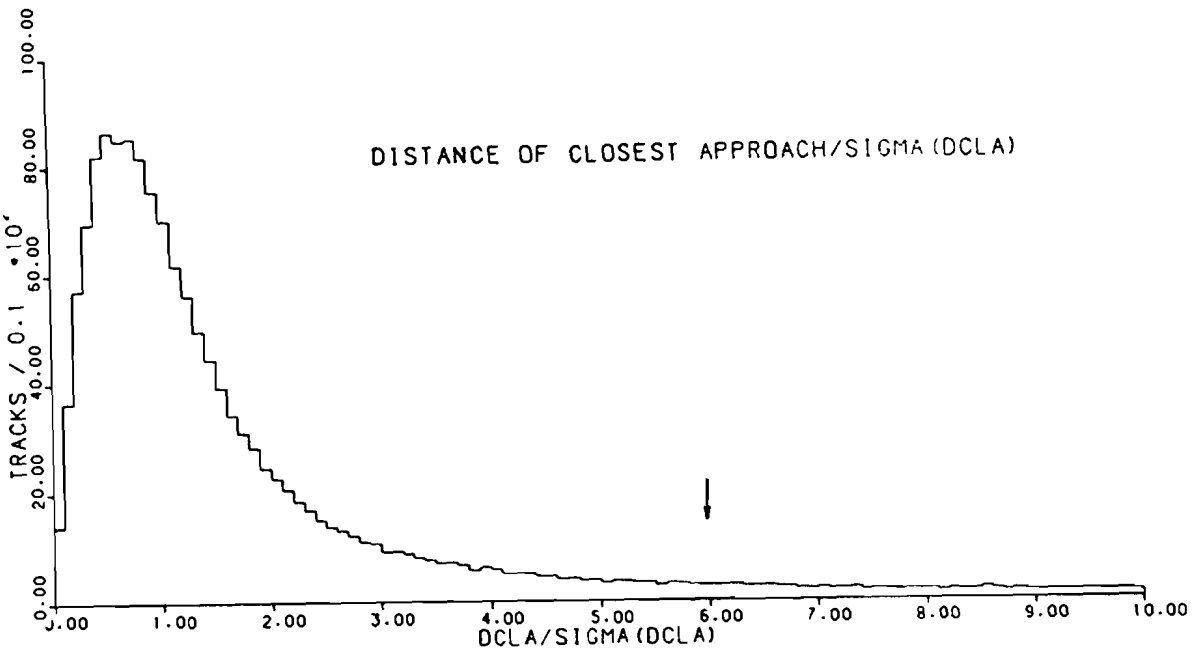

Figure 3.11: Number of standard deviations of distance of closest approach to target vertex of outgoing tracks. The arrow shows the cut at 6σ.

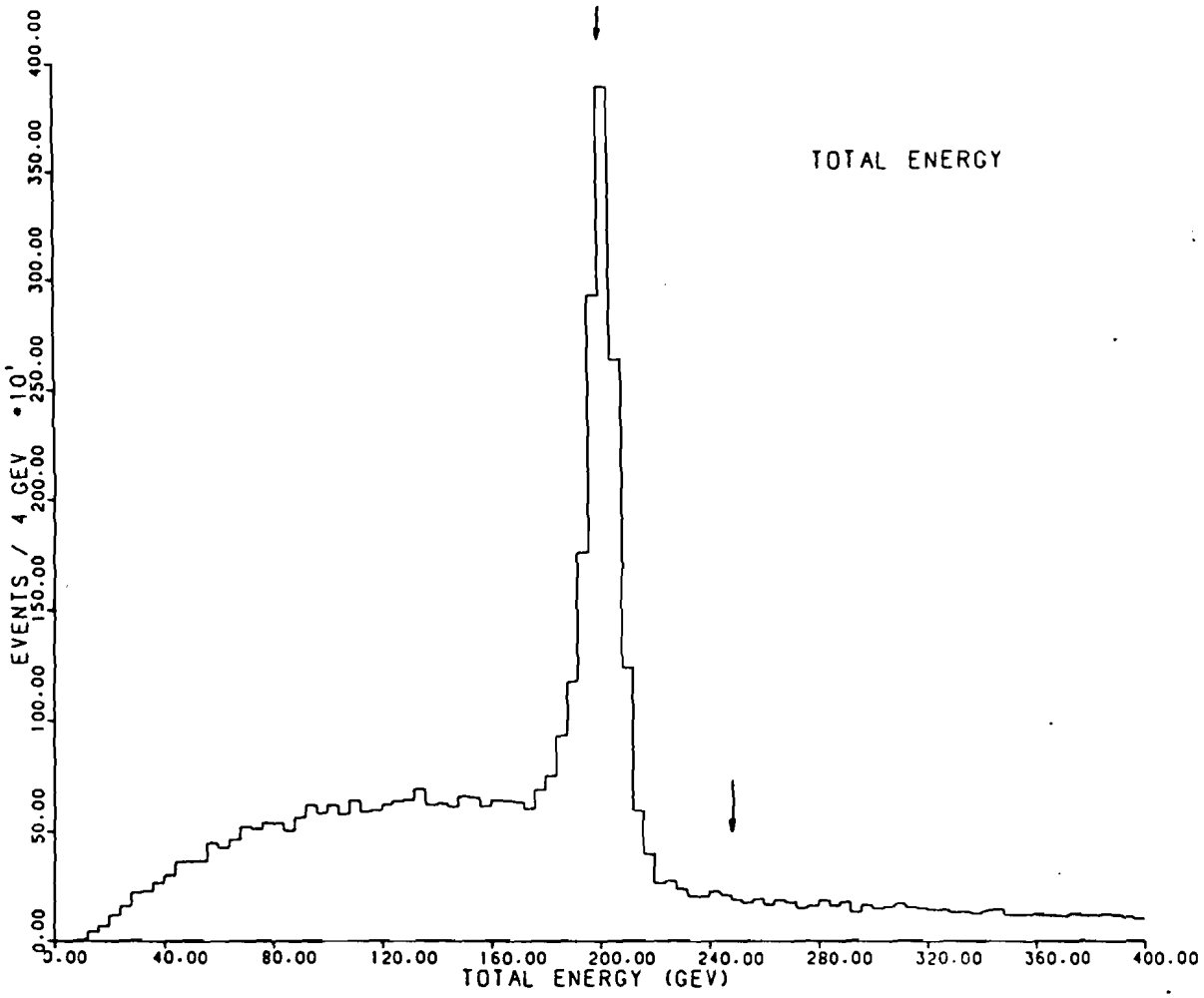

Figure 3.12: Total energy of events. One arrow shows the peak at 202 GeV, the other shows the cut at 250 GeV.

Another cut which could be made, but was not, is upon IVFLAG. As explained in the section on KLEENX, IVFLAG is a measure of the quality of the main vertex. There are two reasons for not making this cut: first, 89% of the events after KLEENX have the optimum value of IVFLAG; and second, the question of how well-determined is the main vertex is not considered a critical one in determining the overall quality of the event.

Table 3.5 gives the distribution of events with various multiplicities after each cut.

TABLE 3.5

PROGRESSIVE EFFECTS OF CUTS

CUT	No. of Original Tracks						
	4	5	6	7	8	9+	Total
NONE	33580	10692	3252	781	239	113	48657
NLDIR=4,Qtot=-1	31274	0	0	0	0	0	31274
No shared legs	29747	4627	830	119	23	4	35350
$\chi^2<2.0$	19142	3318	623	86	24	7	23200
RDIRR<6.0	16242	2550	418	51	10	2	19273
Etot<250	16111	2384	378	48	10	2	18933
$MM^2<16$	6613	851	85	12	1	1	7563
Fiducial Cut on Veto 1x1							7205

3.5 Missing Mass

Looking at the plot of total energy (Fig. 3.12), one sees that the energy actually peaks at a value of 202 GeV, not the nominal value of 200 GeV.

It is desired to show that there is in the 3π sample a diffractive component, which shall be defined as the existence of a decaying exponential pattern in the t' (momentum transfer squared) distribution. In order to see if this is the case, it is necessary to cut the sample so that what remain are events which topologically possess the capability to be diffractive. This means cutting so that events are retained in which the target particle is unchanged, and the incident pion dissociates into three charged pions.

Ideally, in events of interest, there are four final-state particles: three pions and a recoiling target particle. The MPS is capable of detecting the pions, but the target particle receives too little momentum to be detected in the MPS. Thus three particles are seen, and the hope is that what is not seen consists solely of a single particle.

To determine whether this is the case, one looks at the missing mass of the event. The momentum and mass of the incident beam are known, as are the momentum of the

target (zero) and of all detected outgoing particles. Assumptions must be made as to the identities, and hence masses of the outgoing particles. Since pions are the subject of the search, and since pions are by far the most common of all final-state particles in hadron interactions, and since no particle-identification mechanism is being used, the assumption is made that the outgoing particles are pions. The identity of the target particle is not known, but as the target was plastic (50% Hydrogen/50% Carbon), the assumption can be made that the target particle was a proton, neutron, or complete carbon nucleus. In any case, it turns out that the missing mass calculation does not depend on the identity of the target particle.

The mass of the missing particle(s) is calculated as follows:

Let

p_1 = 4-momentum of incident beam particle,

p_2 = 4-momentum of target particle,

p_3 = 4-momentum of all seen direct particles,

p_4 = 4-momentum of unseen particle(s),

where

$$p_1 + p_2 = p_3 + p_4 \ .$$

Then

$$m_4{}^2 = p_4{}^2$$

$$= (p_1 + p_2 - p_3)^2 .$$

The only element of p_1, p_2, and p_3 which is not known is m_2, the mass of the target. Make the assumption that it is the proton mass. If, and only if, the unseen component consists solely of the target particle, whatever it was, then

$$p_4{}^2 = p_2{}^2$$

by definition. Thus is obtained

$$m_4{}^2 = m_2{}^2 ,$$

and the missing mass will equal the mass that was assumed for the target particle, namely the proton mass. This holds for whatever is the actual mass of the target.

The end result of all this is that events in our sample in which the target is the only unseen particle will give a peak in the missing mass squared (MM^2) spectrum at the proton mass squared, or approximately 1 $(GeV/c^2)^2$. Figure 3.13 shows this to be the case. It is necessary to scale the beam momentum upward by 1% to reflect the facts that the average actual beam was 202 GeV/c, not 200 GeV/c, and the beam momentum three-vector has previously been

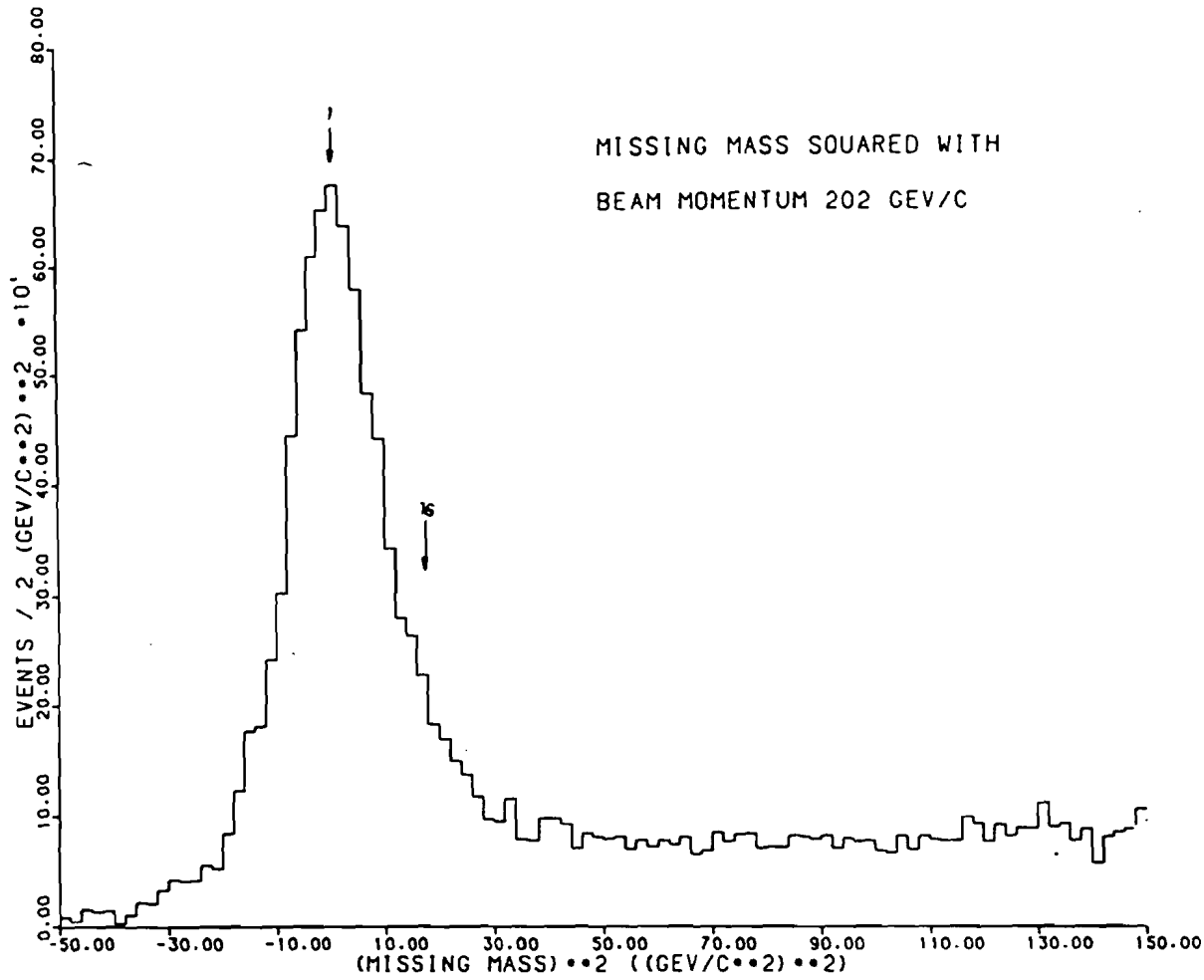

Figure 3.13: Missing mass squared, assuming target has proton mass, with beam momentum scaled up to 202 GeV/c. The arrows show the peak at 1 $(GeV/c^2)^2$, and the position of the cut at 16 $(GeV/c^2)^2$.

assumed to have magnitude of exactly 200 GeV/c, with components given by slopes as determined by the beam's traversal of the beam PWC's. Fig. 3.14(a-b) shows missing mass squared with a beam momentum of 201 GeV/c and 203 GeV/c.

The resolution of the MM^2 distribution is $\sigma = 12$ $(GeV/c^2)^2$ for events with $MM^2 < 16$ $(GeV/c^2)^2$, as determined by taking errors from individual tracks as calculated by KLEENX, calculating the errors of whole events, using these errors to generate points according to a Gaussian distribution, then looking at the width of the resulting distribution (see Fig 3.15). This number is consistent with the cut at 16 $(GeV/c^2)^2$, as that is approximately 1σ from the proton mass.

To isolate a sample which is deemed to be "diffractive", a cut is made in the MM^2 distribution to get only those events in which the sole thing missing is an object of proton mass. It is noted that there is a slight broadening of the MM^2 peak on the positive side, which may be taken as being the result of the production of nucleon resonances such as the N^* or Δ. In an attempt to cut out at least some of these unwanted events the cut is made at 16 $(GeV/c^2)^2$. This is consistent with the desired goal of taking only events which have only a recoil proton, and also with the resolution of the distribution. The value 16

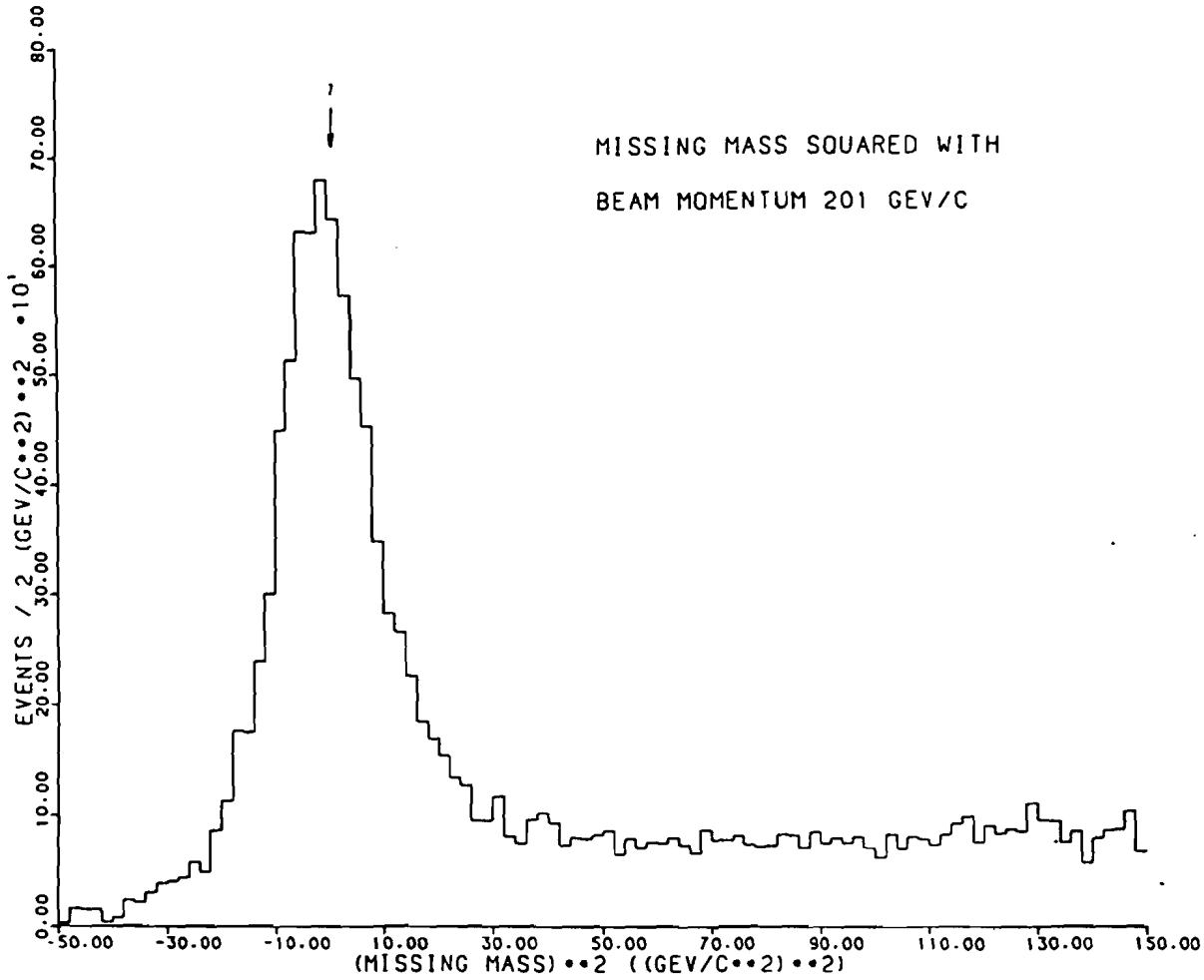

Figure 3.14(a) : Missing mass squared, assuming target has proton mass, with beam momentum scaled up to 201 GeV/c. The arrow shows the position of the proton mass.

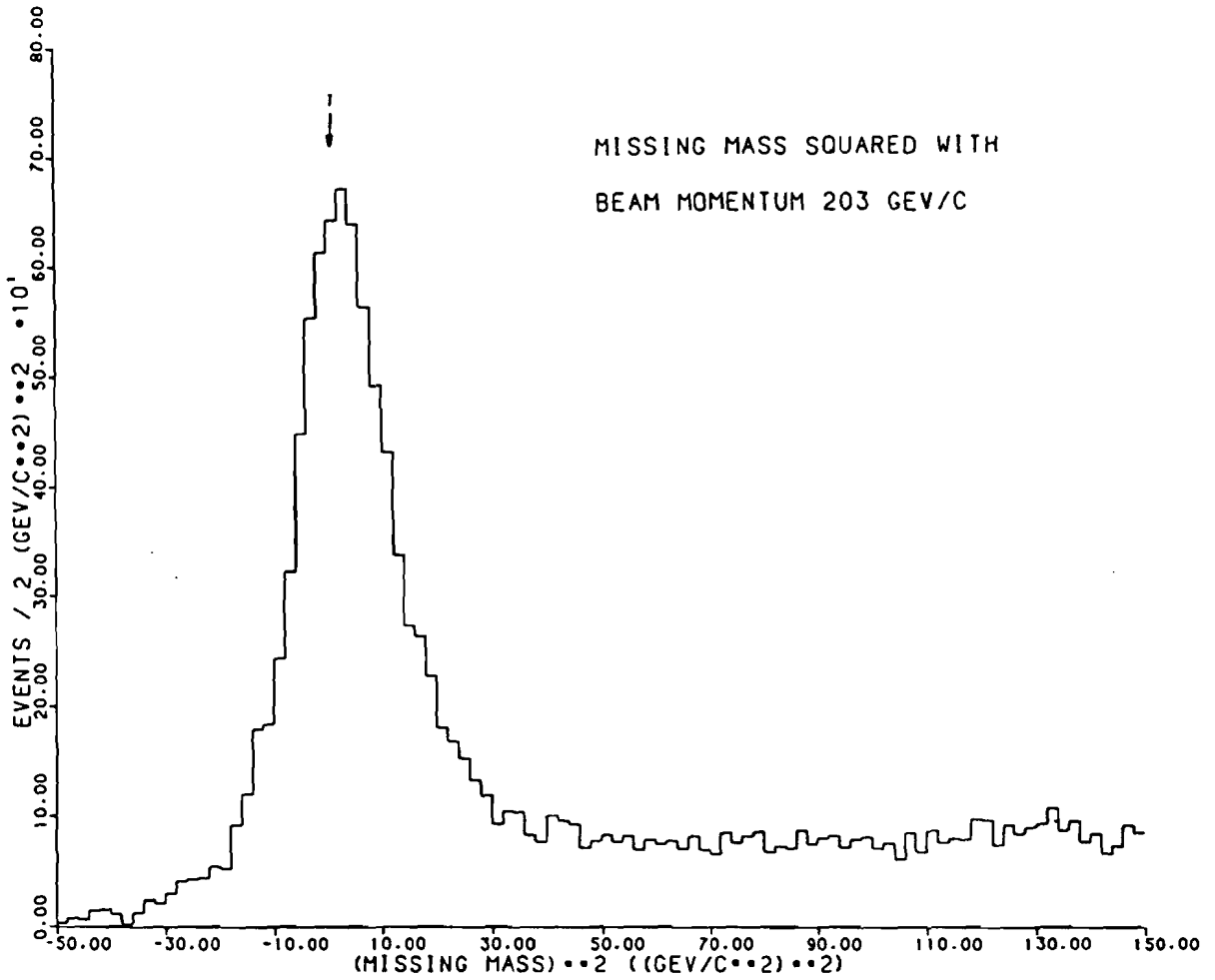

Figure 3.14(b) : Missing mass squared, assuming target has proton mass, with beam momentum scaled up to 203 GeV/c. The arrow shows the position of the proton mass.

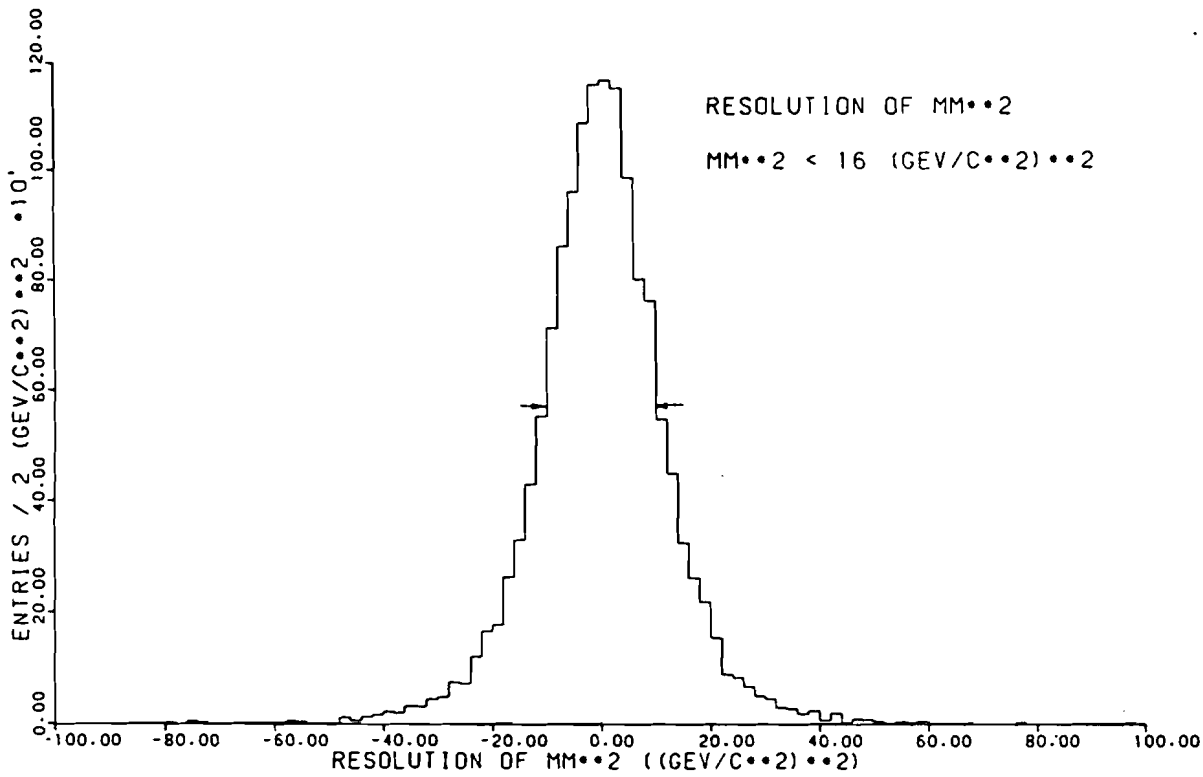

Figure 3.15: Resolution of missing mass squared, with $MM^2 < 16\ (GeV/c^2)^2$. The arrows show the FWHM of 20 $(geV/c^2)^2$.

$(GeV/c^2)^2$ also has the advantage of being the same cut used in other E580 analyses of the samples $K^o_s K^o_s \pi^-$ and $K^o_s K^o_s \pi^+ \pi^- \pi^-$ to get diffractive samples.

Starting with the 18933 events left over after the data quality cuts, the 16 $(GeV/c^2)^2$ MM^2 cut leaves a final "diffractive" sample of 7693 events. There is an undetermined amount of background in this number, due to unseen nondiffractive π^o's which survived the cut, and also due to nucleon diffraction into N^*. The seems to be no easy way to determine the amount of this double diffraction (in which both the incident pion and the target nucleon break up), except to note that another experiment at 200 GeV/c finds that it accounts for about 20% of the data in which the pion diffractively dissociates (Lamsa 1978).

A further, final cut will be explained in Section 3.9.2.

3.6 Effective Beam

In order to calculate a sensitivity for the E580 3π sample, it is necessary to know just how many "good" π^-'s were incident on the target. This means the number of beam pions which came at a time when the MPS was fully prepared to trigger, and is called "effective beam". The number of effective beam particles was recorded for each run of the

experiment.

Two difficulties next arise. First, not all runs are available for this analysis. Several tapes of data were inexplicably lost prior to the beginning of this work, specifically runs 257-282, and comprising about 15% of the total data taken during the running of E580. The solution to this is simply to not count those runs in the adding up of effective beam.

The second, and by far more serious, difficulty is that, in order to avoid flooding the data tapes with 3π data, the 3π trigger had a "÷N" circuit on it. Thus, only one out of every N 3π triggers which occurred was actually written onto tape. The complication here is that N changed several times during the running of E580. Through careful analysis, consisting of comparing logs kept during the actual running with the number of triggers recorded on tape, it has been possible to determine the value of N during the experiment.

TABLE 3.6

EFFECTIVE BEAM BY RUN

Runs(a)	Eff. Beam	N	3π Eff. Beam
208-305	7949 M	4000	1.987 M
306-307	220 M	200	1.100 M
308-408	7926 M	400	19.816 M
Total			22.90 M

(a) Excluding runs in which no physics triggers were taken, or for which data is not available (Runs 257-282).

So the final number is EB = 22.90 x 10^6 incident π^- .

3.7 Trigger Efficiency

Calculating the efficiency of the triggers used in E580 is a fairly complex task. First it is necessary to know exactly the efficiencies of the individual chambers involved in the triggers (AU, AV, BU, BV, CX, CY, DX, DY, and DXP), and also to know the probability that each chamber sparks spuriously, be that one, two, three, or four

or more times. An extensive analysis of these probabilities was performed at Notre Dame by Tom Davis, and his data was used to calculate the trigger efficiencies for various run periods.

The 3π trigger required exactly three hits in at least two out of four of the chambers AU, AV, BU, and BV, and exactly three hits in at least three out of five of the chambers CX, CY, DX, DY, and DX'. In its simplest form, ignoring the extra hit probabilities, the calculation may be done as follows:

Let the probability that a chamber fires given a single spark be e. Then the probability that it fires m times given n sparks is given by

$$p(n,m) = {}_nC_m \; e^m \; (1-e)^{(n-m)}$$

Thus, if one desires to detect 3 hits, and there are actually n particles, one may calculate the probabilty for each chamber that it did, indeed, fire the desired number of times. Let this probabilty be designated tot(ch), where ch is an index referring to which chamber is involved.

Now, the total probability involved is equal to unity. The probability that a given chamber did not fire the desired number of times is [1-tot(ch)]. Therefore, the probability that <u>none</u> of the chambers fired correctly is given by

$$P(\text{all bad}) = \prod_i [1-\text{tot}(i)]$$

Thus the probability that at least one chamber fired correctly is given by

$$P(\geq 1 \text{ good}) = 1 - P(\text{all bad})$$

Now, the probability that a single chamber (m) fired the correct number of times, but none of the others did, is given by

$$P(\text{only m good}) = \text{tot}(m) \prod_{i \neq m} [1-\text{tot}(i)]$$

So the probability that at least <u>two</u> chambers fired correctly is given by

$$P(\geq 2 \text{ good}) = 1 - P(\text{all bad}) - \sum_{i} P(\text{only i good})$$

Collecting this together, the probability that at least two of the four chambers AU, AV, BU, and BV registered three hits is

$$P(\text{A-B good}) = 1 - P(\text{A-B all bad}) - \sum_{A-B} P(\text{only i good})$$

For the CX, CY, DX, DY, and DX′ chambers, further complication is necessary. One needs to calculate the probability that any given two chambers fire correctly, but none of the others. This is given by

$$P(\text{only m,n good}) = \text{tot}(m)\ \text{tot}(n) \prod_{i \neq m,n} [1-\text{tot}(i)]$$

Now the probability that at least <u>three</u> chambers fired correctly is given by

$$P(\geq 3 \text{ good}) = 1 - P(\text{all bad}) - \sum_{i} p(\text{only i good}) - \sum_{i,j,i \neq j} P(\text{only i,j good})$$

Collecting this together, one applies this last formula to get the probability P(C-D good) that three of the five chambers CX, CY, DX, DY, and DX′ fired the desired number of times.

Finally, the probability of the trigger working correctly is given by

P(trigger) = P(A-B good) P(C-D good)

A further complication is imposed when one allows chambers to have extra spurious hits as well as not always firing on a real particle. This affects the values of the tot(ch), but not the above calculations.

It is also desirable to know the uncertainties of all these calculations, using the uncertainties of the efficiencies, and also error matrices associated with the extra hit probabilities.

Table 3.7 shows the results of the calculations.

TABLE 3.7

TRIGGER EFFICIENCIES

Runs	Trig. Eff.	Triggers	Comments
201-251	0.670 ± 0.060	1642	Normal
252-258	0.484 ± 0.034	192	CX dead
259-293	0.644 ± 0.051	266	Normal
294-301	0.559 ± 0.053	132	CY dead
302-317	0.555 ± 0.044	6044	CX,CY
dead			
318-408	0.321 ± 0.026	40381	DX' weak
---	---	---	
Overall	0.365 ± 0.029	48657	

3.8 Software Efficiency

In order to find out how effective the TEARS and KLEENX software were in reconstructing 3π events, 5000 simulated 3π events were generated by rotating real events about the beam axis. These were then run through a highly-accurate MPS simulation program at Tufts, where they generated data in format identical to that of real triggers at the MPS. This was then sent through TEARS, and 4740 events passed. Coming back to Notre Dame, 1297 of these 4740 good events were processed through KLEENX, and then

through subsequent quality and physics cuts, and 1023 passed. From this information we conclude that, with statistical errors, the reconstruction efficiency for this sample is

$$e_{recon} = 0.784 \pm 0.029$$

3.9 Geometrical Acceptance

3.9.1 $\pi^-\pi^-\pi^+$ Acceptance

In order to calculate correct cross sections per nucleon for the 3π data, it is necessary to know the precise acceptance of the experimental apparatus of E580 for events of this type. This can be readily accomplished by constructing a model of the MPS, and sending actual reconstructed events through it. If all the tracks (in this case three) from the event make it all the way through the simulation without going outside any of the given apertures (except for the veto 1x1, in which case the track should <u>miss</u> the aperture), the event is counted as accepted. The program to do this is called PIACPT.

The model consisted of the following components:

1) A magnet of given dimensions with given constant magnetic field.

2) A detector of given (x,y) aperture after the magnet.

3) A 2nd detector of given (x,y) aperture after the magnet.

4) A 1x1 veto counter to reject non-interacting events.

It was determined that all of the real chambers upstream of the magnet had sufficiently large apertures that no tracks would be lost in them that would not be lost elsewhere in the system.

The parameters of these components are in Table 3.8.

TABLE 3.8

PIACPT SIMULATION PARAMETERS

Component	z-position	x-aperture	y-aperture	Comments
Magnet	0.00 m	± 0.6096 m	± 0.4318 m	Front Face
Magnet	0.57 m	± 0.6096 m	± 0.4318 m	Start of Field
Magnet	0.66 m	± 0.6096 m	± 0.3556 m	Start of Pole Tip
Magnet	1.88 m	± 0.6096 m	± 0.3556 m	End of Pole Tip
Magnet	1.97 m	± 0.6096 m	± 0.4318 m	End of Field
Magnet	2.54 m	± 0.6096 m	± 0.4318 m	Back Face
Detector 1	3.4465 m	± 0.969 m	± 0.591 m	DX' PWC
Detector 2	6.08 m	± 1.296 m	± 0.686 m	E1X Spark Chamber
Veto 1x1	6.0066 m	± 0.01575 m	± 0.015875 m	At x=0.0165m, y=0

Magnet had constant B = 1.657 Tesla.

The idea is to take actual reconstructed events, rotate them some number of times about the beam axis, and send them through the simulation. It was decided to create 100 new events for each real event, rotated about the beam axis in even steps of 1.8°. Since neither beam nor target was polarized, there can be no bias in azimuthal angle of the events, and regularly-spaced rotations were chosen rather than random ones for the same reason. Also, due to

the total up-down symmetry of the simulation, a total covered angle of 180° was preferable than 360°, to avoid redundancies.

3.9.2 Fiducial Cut on Veto 1x1

It is found that there is a handful of events which have very poor acceptance, with some of them having 0%. These events are undesirable due to the later use of acceptance factors for event-by-event weighting in the physics analysis. Most of these events were eventually characterized as having a pion with high momentum in a very forward direction, causing them to consistently hit the 1x1 veto counter.

It was decided to cut these events out as a class, by making a fiducial cut around the 1x1. A veto counter was placed into the simulation, centered at the position of the real 1x1, but with a size of 1.25"x1.25", thus allowing for some leeway. Real (unrotated) events which struck this veto counter were deleted from the sample. 358 events were thus affected, leaving a final sample of 7205 events out of 7563. These 7205 events comprise the final data sample for analysis.

Due to this cut in the data, it is necessary to calculate the efficiency of the cut. This can be done by using the fact that 358 events are cut by the PIACPT simulation using a $(1.25")^2$ counter, whereas with a $(1.00")^2$ counter, 102 events are cut. From these numbers can be calculated the number of events/in^2 which will be cut by the simulation, which requires the assumption that the distribution of events/in^2 in the region of the 1x1 is flat. The result is that it can be estimated that 7916 events were actually present in the $(1.25")^2$ region during the experiment, of which 7205 survive the fiducial volume cut. This gives for the efficiency:

$$e_{fid\ cut} = 0.910 \pm 0.003$$

with statistical errors.

3.9.3 Results of Geometrical Model

The result of swimming 100 generated events through the model for each real event was that uncorrected geometrical efficiency was 91.27%, with statistics so high that statistical error is negligible.

As this point an important point must be made. The Veto 1x1 counter is responsible for the bulk of the events which are lost in this model, generally due to stray tracks which happen to have a trajectory which carries them

through that seemingly-tiny one square inch. Of the about 9% of the rotated events which were not accepted, 89% of them were lost due to the presence of the 1x1. This number is very sensitive to the given size of the 1x1, but not as much to position. When the size of the 1x1 is increased from 1" square to 1.25" square, the number of events lost in the 1x1 increases from 102 to 358. The rest of the non-accepted rotated events were lost by having a track hit a wall of the magnet.

3.9.4 Acceptance for Other E580 Samples

The procedure used above for calculating 3π acceptances was developed in the process of abnalyzing other data samples from E580, specifically the $K^o_s K^o_s \pi^+ \pi^- \pi^-$ sample and the $K^o_s K^o_s$ inclusive sample, so the procedure used in analyzing these other types of events will be discussed. For these, it was necessary to determine the probability that the K^o_s particles would decay within the region between the A-station and the B-station. Thus each event had an acceptance probability given by

$$P(\text{total}) = P(\text{geometry})\ P(K^o_s\text{-1 in DV})\ P(K^o_s\text{-2 in DV})$$

where the latter two factors are the

probability of decaying within the

specified decay volume.

The probability of a K_S^0 of known momentum decaying within the decay volume is not difficult to calculate. The mean lifetime of a K_S^0 at rest is known (τ = 89.17 psec). Multiplying by the speed of light, the decay length for a K_S^0 travelling at the speed of light (without time dilation) is $c\tau$ = 0.02675 m. If the particle is moving at a speed v = βc, then the undilated decay length is $\beta c\tau$. Finally, adding in the time dilation factor γ, the particle will travel a mean distance of $\beta\gamma c\tau$ in the lab frame.

Now, the position of the target vertex Z_T for each event of E580 is known, as are all the momentum components. The $\beta\gamma$ for each event is given by

$$\beta\gamma = p_{tot}/M_K \text{ for each } K_S^0, \text{ where } M_K = 0.49767 \text{ GeV}/c^2$$

The K_S^0's were not, of course, travelling in exactly the +z direction. Thus, they would actually travel a further distance through the decay volume than merely the distance between the last A-chamber and the first B-chamber. This further distance is given by a correction factor of p_{tot}/p_z.

Let Z_A be the position of the last A-chamber, and Z_B be the position of the first B-chamber. Then the minimum distance <u>along the z-axis</u> until the particle first enters the decay volume is

$$z_{min} = Z_A - Z_T,$$

and the maximum distance along the z-axis before the particle exits the decay volume is

$$z_{max} = Z_B - Z_T \ .$$

Using the above information, we find that the minimum total distance a particle will travel is

$$d_{min} = Z_{min} * p_{tot} \ / \ p_z$$

and the maximum distance is

$$d_{max} = Z_{max} * p_{tot} \ / \ p_z \ .$$

The probability of a particle surviving after a distance d when it has a mean decay length L in that frame is given by

$$P(\text{not decay}) = \exp(-d/L) \ .$$

Thus the probability of its decaying in distance d is

$$P(\text{decay}) = 1 - P(\text{not decay}) \ .$$

For these particles, $L = \beta\gamma c\tau$.

So the probability of one of these K_s^o's decaying by the end of the last A-chamber is

$$P_A = 1 - \exp(-d_{min}/\beta\gamma c\tau) \ ,$$

and the probability of decaying by the beginning of the first B-chamber is

$$P_B = 1 - \exp(-d_{max}/\beta\gamma c\tau) \ .$$

Finally, the probability of decaying <u>within</u> the dacay volume is merely the difference between these, or

$$P(K_s^o \text{ in DV}) = P_B - P_A \ .$$

This number is calculated for each K_s^o in each event, and combined with the geometrical acceptance from the MPS simulation of each event to get a total acceptance of the events in the samples mentioned.

3.9.5 A-station correction

In looking at the events from the 3π sample, it was found that the separation distribution between tracks at the z-position of the A-station, taken as z = -4.01 m (which is the midpoint of the actual A-station), showed a drop at small separations. Fig. 3.16(a-b) shows the observed minimum separation between pairs of tracks at the A-station in the x- and y-views, and Fig. 3.17 shows the

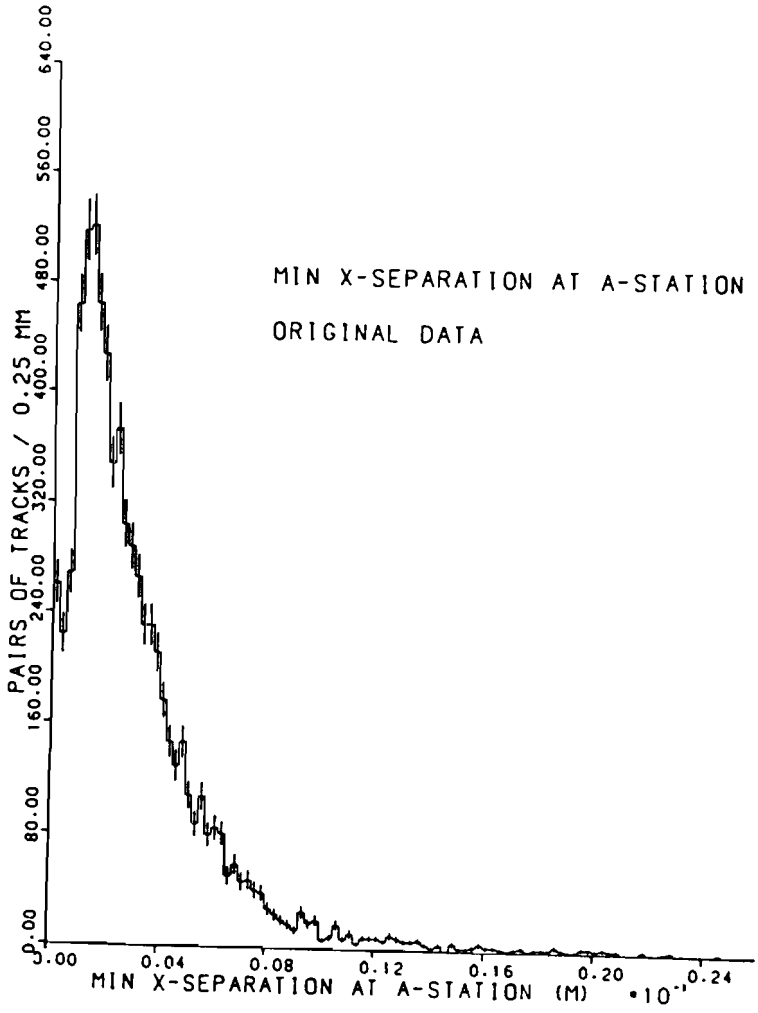

Figure 3.16(a): Minimum x-plane separation of outgoing tracks at the position of the A-station.

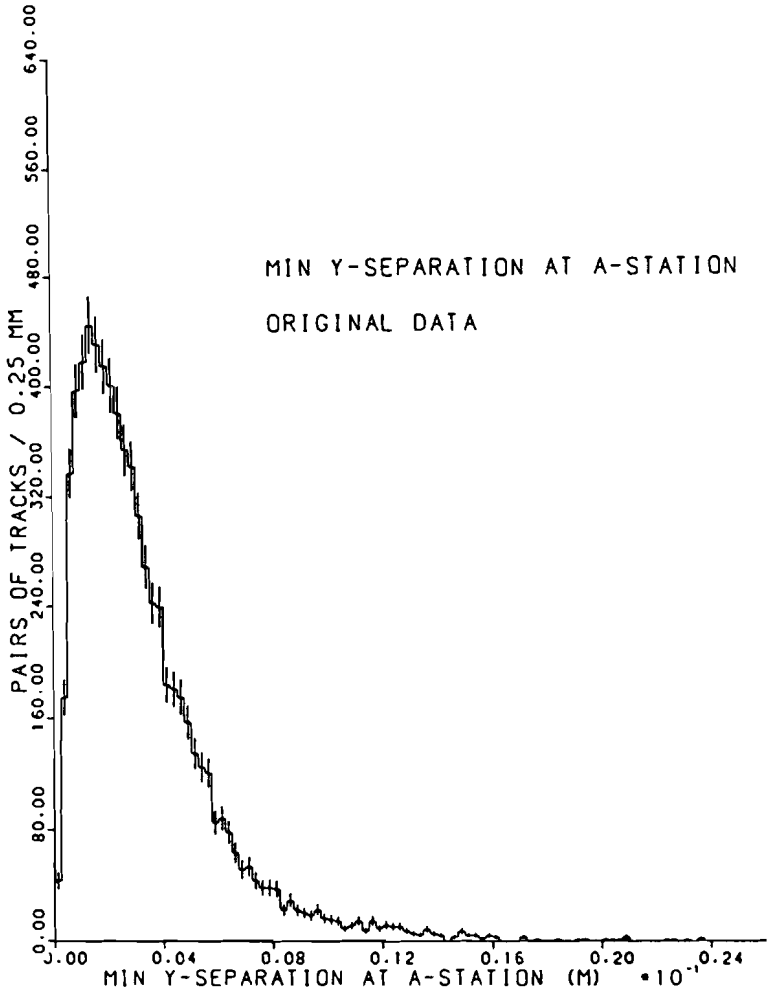

Figure 3.16(b): Minimum y-plane separation of outgoing tracks at the position of the A-station.

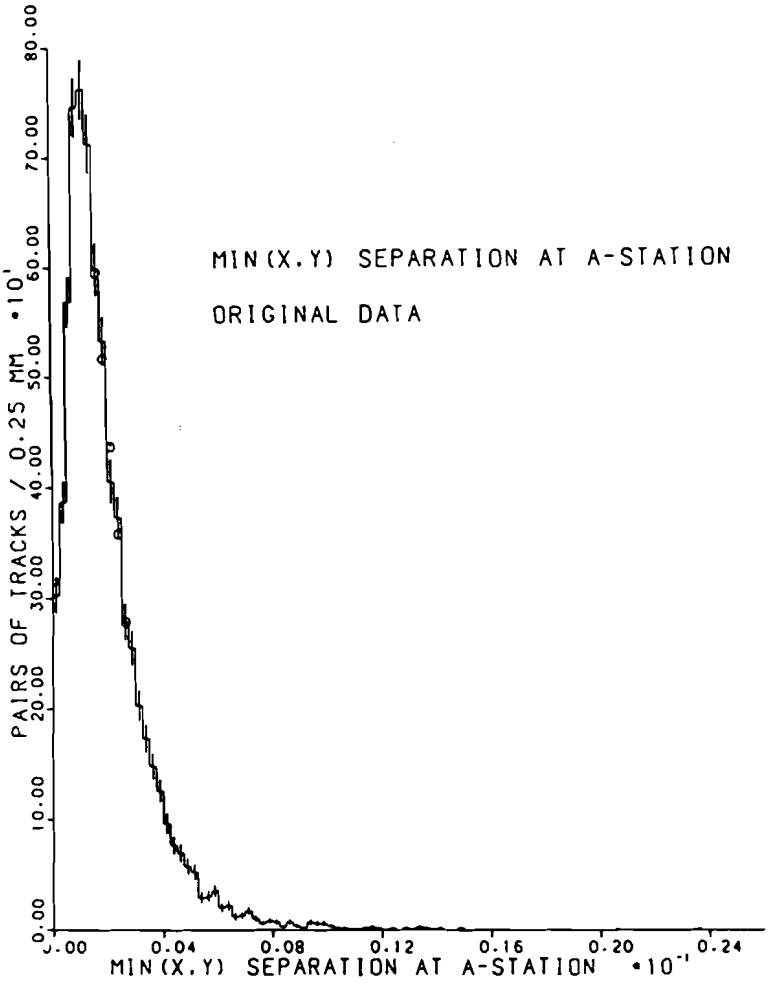

Figure 3.17: Minimum separation, x or y, of outgoing tracks at the position of the A-station. The circles show the straight-line fit done to the data, as explained in the text.

minimum of these for each event, which shall be called Δ. In each case, the binning is 0.25mm, 1/4 of a wire spacing. Note that the effect is most pronounced for $\Delta < 1.0$ mm, which corresponds to one wire spacing.

This behavior may be understood by realizing that these particles were travelling at very high speed, mostly in a forward direction in the lab frame, and had not had a chance to separate very much by the time they had travelled the average 0.727 m from the center of the target to the middle of the A-station, where the wires were spaced 1 mm apart. Thus the trigger would frequently be fooled into thinking that only one particle had passed through the A-station, especially since the trigger logic treated clusters of sparks (adjacent wires lit in a given chamber) as single hits. Up to three adjacent sparks would be treated as a single hit by the trigger (although the TEARS software treated each spark individually). Since the trigger required exactly three hits in two out of the four chambers AU, AV, BU, and BV, missing the trigger condition in one or both of the A-chambers leads to a serious inefficiency.

To correct this problem, the events were, as before, rotated 100 times about the beam axis. From this "unbiased" sample, the Δ were plotted in bins of 0.25 mm, 1/4 of a wire spacing, as shown in Fig. 3.18. These show

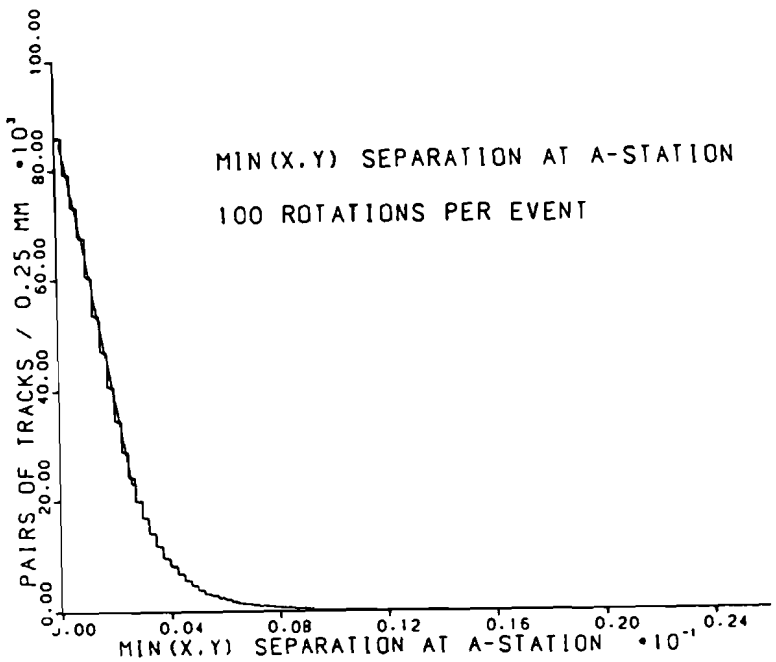

Figure 3.18: Minimum separation, x or y, of outgoing tracks at the position of the A-station, where each event has been rotated about the beam axis 100 times. The straight line shows the fit done to the data, as explained in the text.

that the "ideal" distribution of Δ at the A-station does not dip at $\Delta = 0$, and in fact closely resembles a linear drop in the first ten bins.

Both the unrotated and rotated curves were fit with straight lines of the form $y=A+B*\Delta$. The rotated data was fit in bins 1-10, and the unrotated data was fit in bins 7-11 (as it was determined that bin 6 was spuriously high), so as to keep away from the region where the correction was to be made ($0.0\text{mm} < \Delta < 1.0$ mm).

For the rotated data, the fit yields $A = (89025 \pm 75)$, $B = -(2.56\pm0.01) \times 10^7\ m^{-1}$, with a χ^2/DF of 34.4/8. While this <u>seems</u> like a bad fit, the poor χ^2 can be ascribed to the huge statistics involved. Fig. 3.18 shows the fit line.

For the unrotated data, the fit yields $A = 1111 \pm 59$, $B = -(3.17 \pm 0.26) \times 10^5\ m^{-1}$, with a χ^2/DF of 4.50/3, for a probability of 21%. Fig. 3.17 shows the fit line, as circles.

Normalizing by the data in bins 7-10 yields a factor of 79.5, so that the rotated fit divided by the normalization gives a formula for the "ideal" distribution of

$$No. = 1120 - 3.22 \times 10^5\ (m^{-1}) * \Delta$$

This line is consistent with the fit to the unrotated data

in bins 7-11.

We list the corection bin-by-bin in Table 3.9.

TABLE 3.9

A-STATION CORRECTIONS

Bin	Observed No.	Ideal No.	Efficiency
0.00 mm < Δ < 0.25 mm	303	1080	0.281
0.25 mm < Δ < 0.50 mm	387	999	0.387
0.50 mm < Δ < 0.75 mm	569	919	0.619
0.75 mm < Δ < 1.00 mm	746	838	0.890
1.00 mm < Δ < 1.25 mm	762	758	1.000
1.25 mm < Δ < 1.50 mm	713	677	1.000
1.50 mm < Δ < 1.75 mm	599	597	1.000
1.75 mm < Δ < 2.00 mm	533	516	1.000
2.00 mm < Δ			1.000

Now is is possible to go back to the geometrical acceptance program PIACPT and insert these corrections explicitly. For each event in the rotated sample, one measures Δ, the minimum separation of any pair of tracks, in x or y, at the A-station. According to which bin Δ lies

within, a weight of the appropriate efficiency is given to the event. With this correction, it is found that the geometrical acceptance with A-station correction of the 7205 3π events in this sample is 0.7304.

It is difficult to ascribe an uncertainty to this number, as the statistics of the simulation are so high that statistical errors are negligible, yet the simulation is based on a very rough model of the MPS. The uncertainty of the fits in the A-station corrections is about 8%, but these only affect the portion of the events with low A-station separation. Still, it is the only uncertainty present, so an uncertainty of 8% will be ascribed to the total geometrical efficiency.

The geometrical acceptance calculation has been performed not only for the sample as a whole, but also for individual sub-samples, based on 3π effective mass. These numbers are in Table 3.10, along with the reasons for the chosen binning.

TABLE 3.10

RESULTS OF GEOMETRICAL ACCEPTANCE CALCULATIONS

3π Mass Range (GeV/c^2)	Geom. Accept. w/o A-Station	Geom. Accept. w/ A-Station	Notes
$M(3\pi)<1.10$	0.876	0.609 ± 0.049	Low-mass region
$1.10<M(3\pi)<1.40$	0.896	0.686 ± 0.055	A_1/A_2 region
$1.40<M(3\pi)<1.55$	0.928	0.742 ± 0.059	
$1.55<M(3\pi)<1.80$	0.944	0.785 ± 0.063	A_3 region
$1.80<M(3\pi)$	0.927	0.812 ± 0.069	High-mass region
All $M(3\pi)$	0.913	0.730 ± 0.058	

It may be observed that acceptance based purely on geometry rises steadily with 3π effective mass. Also, the A-station correction goes from small to large, rising faster than pure geometry. This is to be expected, since the A-station correction concerns itself with the spatial spread of the three pions when they reach the z-position of the A-station. As effective mass increases, the particles can be expected to spread out more quickly, leading to less of a correction at large masses. The overall acceptance thus rises with 3π effective mass also.

3.9.6 Event-by-Event Acceptance Corrections

This simulation can be used to calculate an event-by-event acceptance correction. For each real event it is possible to determine a number (between 0.00 and 1.00) corresponding to the fraction of times out of 100 (with each trial having a weight of the A-station efficiency for that trial) it was accepted in the MPS model when rotated. This was done for the entire sample of 7205 events, and the efficiencies stored for later physics analysis.

The reciprocal of each efficiency number was used as the weight of each event, reflecting the idea that, if the MPS was only efficient to a factor eff, then the actual number of events of that type was 1/eff.

3.10 Sensitivity and Cross Sections

In order to calculate a cross section per nucleon for this experiment which may be compared to other experiments, the sensitivity must be calculated. A problem arises in doing so, however, since the target in this experiment consisted primarily of plastic scintillator, composed of carbon and hydrogen, whereas most other experiments have used pure hydrogen in the target. The carbon in the target makes it impossible to quote a cross section in μb/nucleon without taking into account the fact that carbon has 12

nucleons/nucleus, whereas hydrogen has 1 nucleon/nucleus. This would not be a problem except for the observed fact that, for purposes of cross sections, a heavy nucleus with A nucleons tends to behave as though it contains less nucleons than it actually does. Theoretical calculations reveal that the expected behavior goes as $A^{2/3}$ (Pajares 1983). This may be naively explained as follows: If a nucleus contains A nucleons, these may be taken to be uniformly spread over a volume whose radius is proportional to $A^{1/3}$. An incoming beam particle, therefore, "sees" not a sphere, but a circle with area proportional to $A^{2/3}$, and this value is what contributes to the cross section of the interaction.

In practice, $A^{2/3}$ is too simplistic. So how does one model the A-dependance of the cross section? Fortunately, this work has already been done for a similar experiment (Azimov 1982). S.A. Azimov et al in 1982 reported on an experiment using a 200 GeV/c π^- beam on emulsion, and calculated the A-dependence of interactions of various types of nuclei. Their model yields the following results:

$$A_{eff} = \sum_i \rho_i A_i^{\alpha}$$

where

ρ_i is the density of nuclei of the ith type

$\alpha = 0.75^{+0.09}_{-0.14}$.

Taking the target to be composed of polyethylene scintillator with a H/C ratio of 1.10 (PDG 1986), and using atomic weights of hydrogen and carbon of 1 and 12 respectively, we find $\rho_H = 0.084$, $\rho_C = 0.916$, and

$$A_{eff} = 5.99^{+1.48}_{-1.73} \text{ nucleons/nucleus} .$$

To avoid different upper and lower uncertainties, the value

$$A_{eff} = 6.0 \pm 1.6 \text{ nucleons/nucleus}$$

will be used.

The effective atomic weight of the target, again using $\rho_H = 0.084$ and $\rho_C = 0.916$, is

$$A_{targ} = 11.08 \text{ g/mole} .$$

Now the sensitivity may be calculated.

$$S = EB \times \rho t \times N_a \times A_{eff} \times e_{trig} \times e_{recon} \times e_{fid\ cut} / A_{trig} .$$

These numbers are as follows:

$EB = 22.9 \times 10^6$ incident π^- (events)

$\rho t = 15.60 \pm 0.16$ g/cm^2

$N_A = 6.023 \times 10^{23}$ nuclei/mole

$A_{eff} = 6.0 \pm 1.6$ nucleons/nucleus

$e_{trig} = 0.365 \pm 0.029$

$e_{recon} = 0.784 \pm 0.029$

$e_{fid\ cut} = 0.910 \pm 0.003$

$A_{trig} = 11.08$ g/mole

So

$$S = (30.3 \pm 8.5) \times 10^{30} \text{ event-nucleon/cm}^2$$

$$30.3 \pm 8.5 \text{ event-nucleon/}\mu\text{b}$$

where 1 barn = 10^{-24} cm^2, and errors have been added in quadrature.

This number does not take into account the geometrical acceptance calculated for the MPS, and so is to be used whenever data is used which has been weighted on an event-by-event basis to correct for the lack of perfect geometrical acceptance.

The factor for geometrical acceptance, e_{geom}, has been calculated for various mass bins, as well as for the overall sample. The sensitivities for the different mass regions, as well as the overall sensitivity, are in Table 3.11.

TABLE 3.11

SENSITIVITY BY MASS REGION

Mass Region (GeV/c^2)	Sensitivity (Event-nucleon/μb)
$M(3\pi)<1.10$	18.5 ± 5.4
$1.10<M(3\pi)<1.40$	20.8 ± 6.1
$1.40<M(3\pi)<1.55$	22.5 ± 6.6
$1.55<M(3\pi)<1.80$	23.8 ± 6.9
$1.80<M(3\pi)$	24.6 ± 7.2
---	---
All $M(3\pi)$	22.1 ± 6.5

Since there are 7205 events in the final sample, this gives an overall cross section of 326 ± 95 μb/nucleon.

Comparing with other experiments, this value is in fairly good agreement. D. Brick et al (Brick 1983), working with a 150 GeV/c π^- beam in a bubble chamber, get σ_{diff} = 350 ± 30 μb. J. W. Lamsa et al (Lamsa 1978) get a total cross-section $\sigma(\pi^- p \rightarrow \pi^-\pi^-\pi^+ p)$ = 1060 ± 130 μb at 202.5 GeV/c, and estimates that 55% of this is pion single-diffraction, or 580 ± 70 μb.

Further, D. Brick et al in the same paper give a formula which gives the expected cross section at any laboratory momentum, based on world data. It predicts a diffractive cross-section at 200 GeV/c of 360 μb.

Thus the cross section per nucleon obtained here is in general agreement with those obtained in other experiments in the same energy range.

3.11 Resolutions

3.11.1 Momentum Resolution

The momentum resolution for the 3π sample may be estimated from the geometry of the MPS and the known transverse momentum kick of the MPS magnet. The various chambers can have uncertainties in particle position calculated based upon their wire spacing, giving an uncertainty in the angle of the track. The transverse momentum kick of the magnet is known and is 0.696 GeV/c. The formula for momentum uncertainty to be used is:

$$\Delta P/P = (\Delta\theta \ / \ P_{kick})\ P$$

where $\Delta\theta$ is the uncertainty in the change of angle of the track in traversing the magnet, and P is the momentum of a given track.

It can be estimated that $\Delta\theta$ = .00043 mrad, and so

$\Delta P/P = 0.00062\ P$

For P = 100 GeV/c, $\Delta P/P$ = 6.2%.

3.11.2 Resolution of Invariant Quantities

It is important to know the limits within which one knows a given experimental number, yet when plotting thousands of events it is impractical to take into account the uncertainty associated with each number in each event. Therefore, one calculates for various plots a resolution, which is a measure of the average error of the variable being plotted.

The track-reconstruction program KLEENX returned five values for each track: x-slope, x-intercept at front magnet face, y-slope, y-intercept at front magnet face, and 1/p (the reciprocal of the momentum of the track). It also calculated a 5x5 error matrix for each track. These error matrices can be used to calculate the uncertainty (σ) of any quantity calculated from these variables.

For the E580 3π sample, σ has been calculated event-by-event for:

a) $1.10 < M(3\pi) < 1.40$ GeV/c^2 (A_1/A_2 range) (Fig. 3.19)

b) $0.67 < M(\pi^+\pi^-) < 0.87$ GeV/c^2 (ρ^o range) (Fig. 3.20),

c) missing mass squared < 16 (GeV/c^2)^2 (Fig. 3.21),

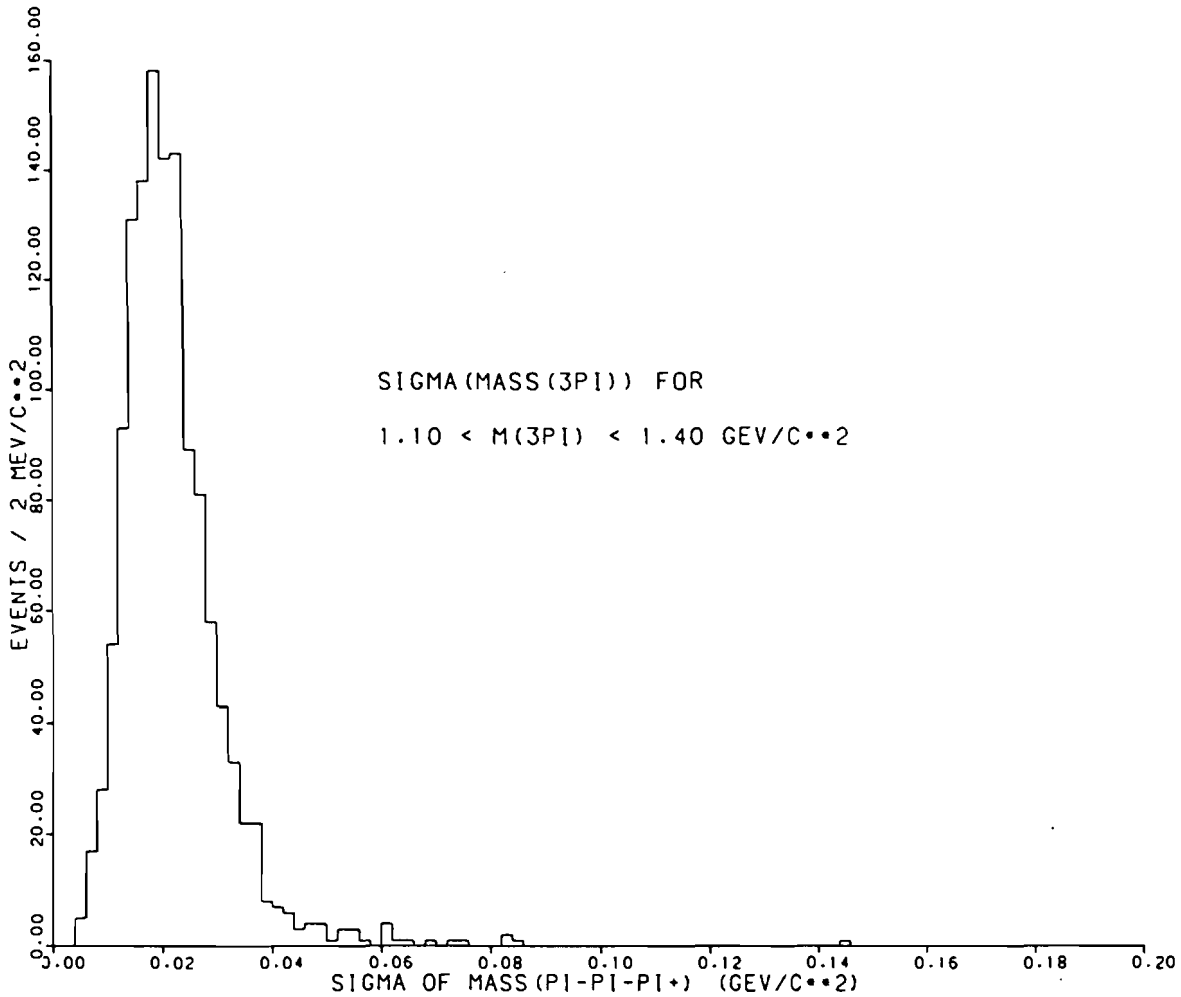

Figure 3.19: Uncertainty in Mass($\pi^-\pi^-\pi^+$), as determined from KLEENX error matrices, for $1.10 < \text{Mass}(\pi^-\pi^-\pi^+) < 1.40\ \text{GeV}/c^2$.

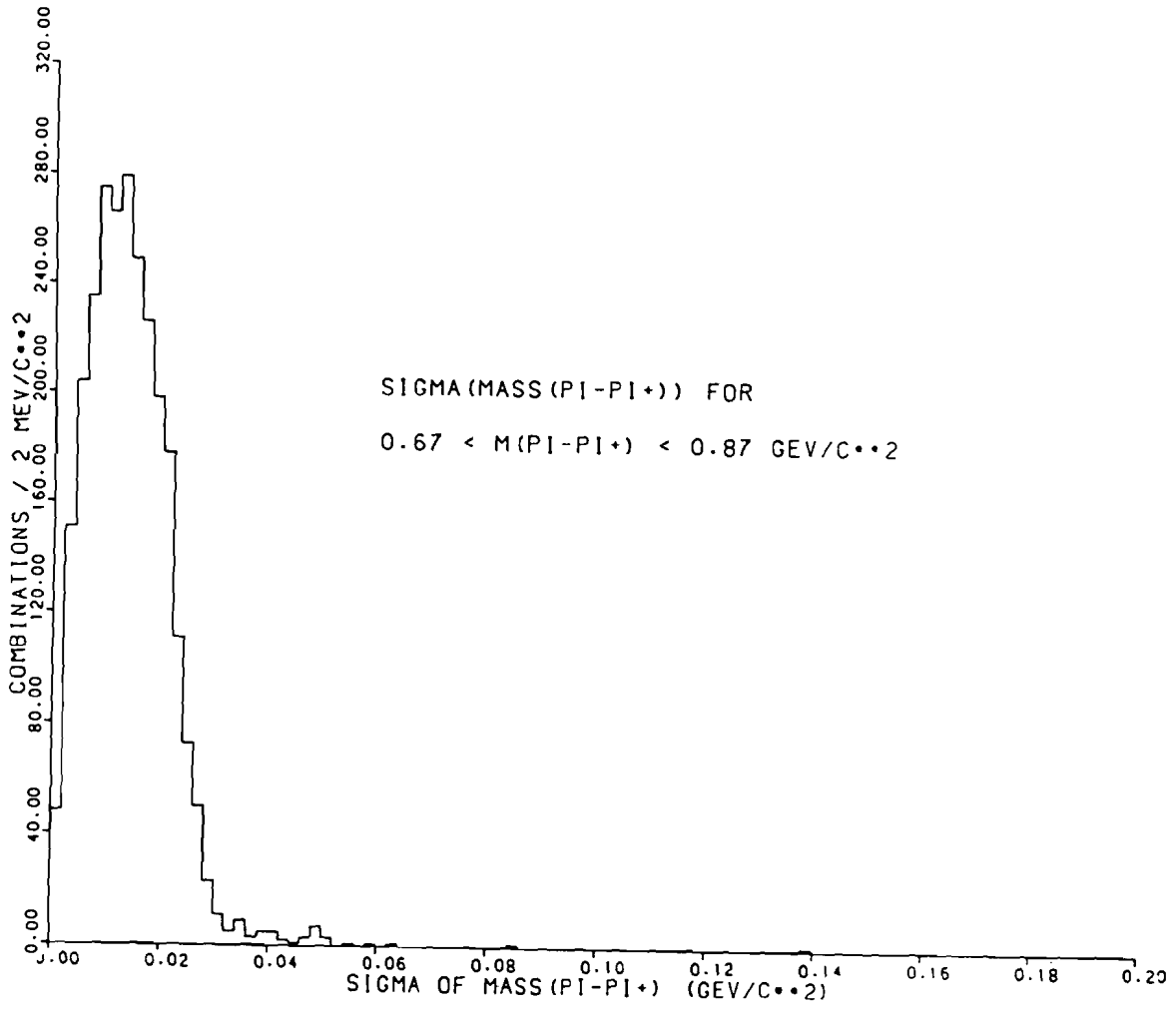

Figure 3.20: Uncertainty in Mass($\pi^-\pi^+$), as determined from KLEENX error matrices, for 0.67 < Mass($\pi^-\pi^+$) < 0.87 GeV/c^2.

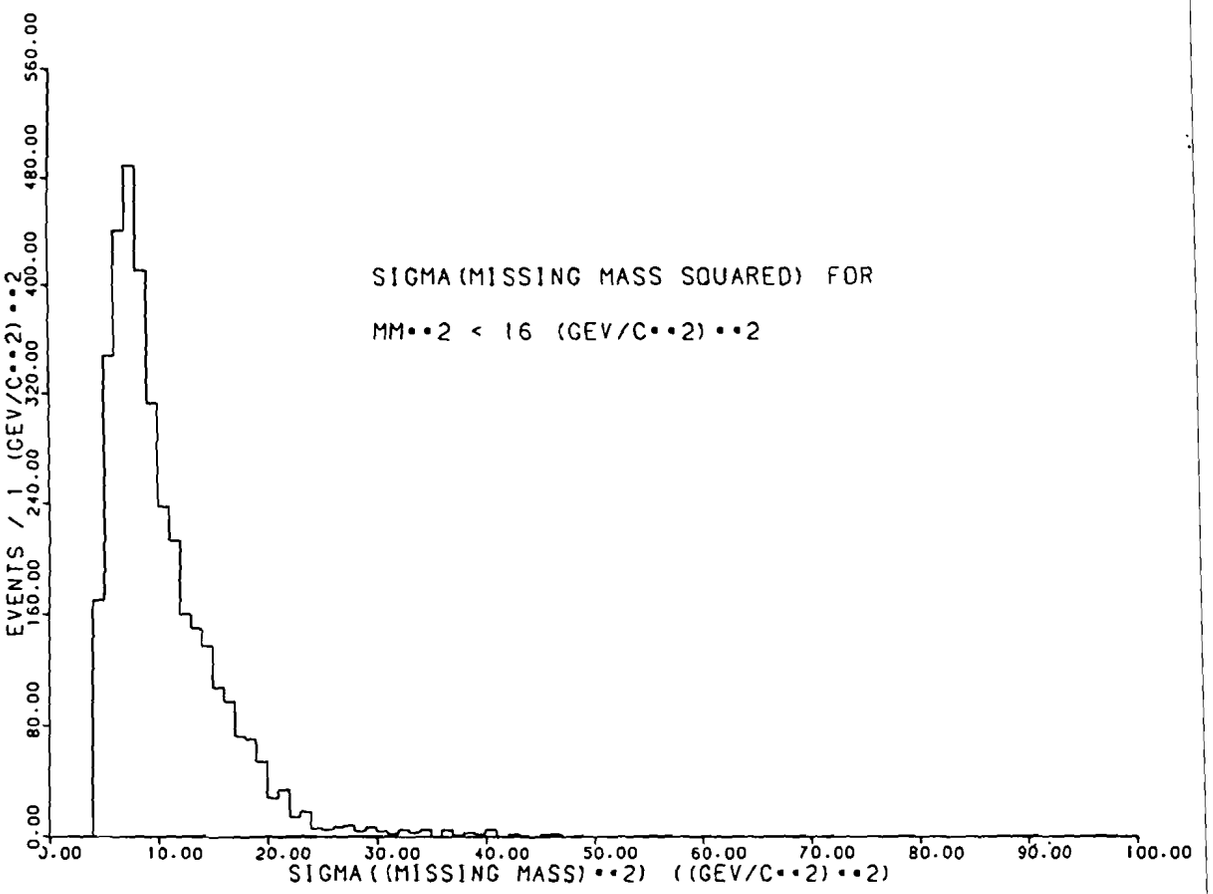

Figure 3.21: Uncertainty in missing mass squared, as determined from KLEENX error matrices, for $MM^2 < 16\ (GeV/c^2)^2$.

d) t' (Fig. 3.22)

e) $t' < 0.02$ $(GeV/c)^2$ (Fig. 3.23)

Once the σ distribution for a given variable is known, one calculates the resolution as follows: for each instance of a given value of σ, one generates N numbers according to a Gaussian distribution centered at zero and with σ equal to that value. One then plots these numbers, and the full width at half maximum (FWHM) of the resulting distribution is the resolution of the original variable.

Resolutions for the above a) - e) are shown in Figs. 3.24 to 3.28, and listed in Table 3.12.

TABLE 3.12

RESOLUTIONS OF INVARIANT QUANTITIES

Distribution	UNITS	FWHM
$1.10<M(3\pi)<1.44$	MeV/c^2	48
$0.67<M(\pi^+\pi^-)<0.87$	MeV/c^2	28
$MM^2<16$	$(GeV/c^2)^2$	20
t'	$(GeV/c)^2$	0.024
$t'<0.02$	$(GeV/c)^2$	0.020

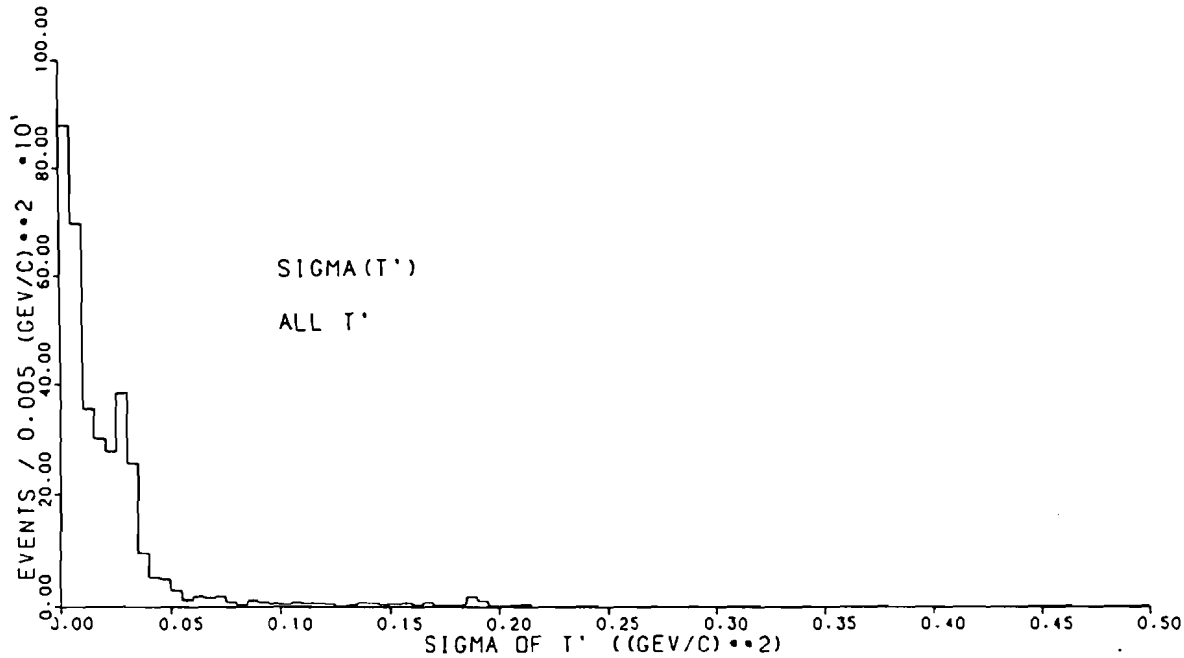

Figure 3.22: Uncertainty in effective momentum transfer t', as determined from KLEENX error matrices, for all values of t'.

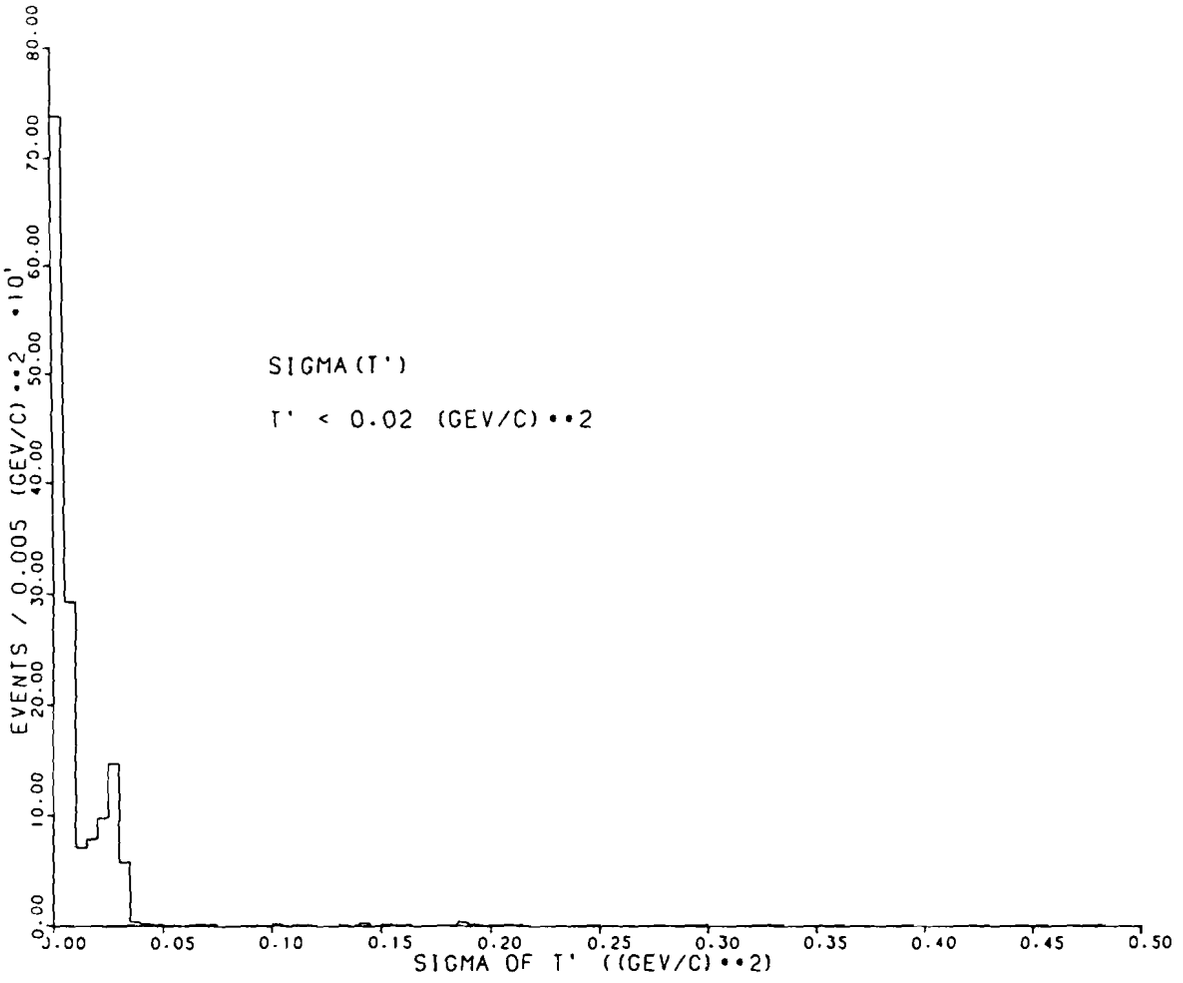

Figure 3.23: Uncertainty in effective momentum transfer t', as determined from KLEENX error matrices, for $t' < 0.02\ (\mathrm{GeV}/c)^{-2}$.

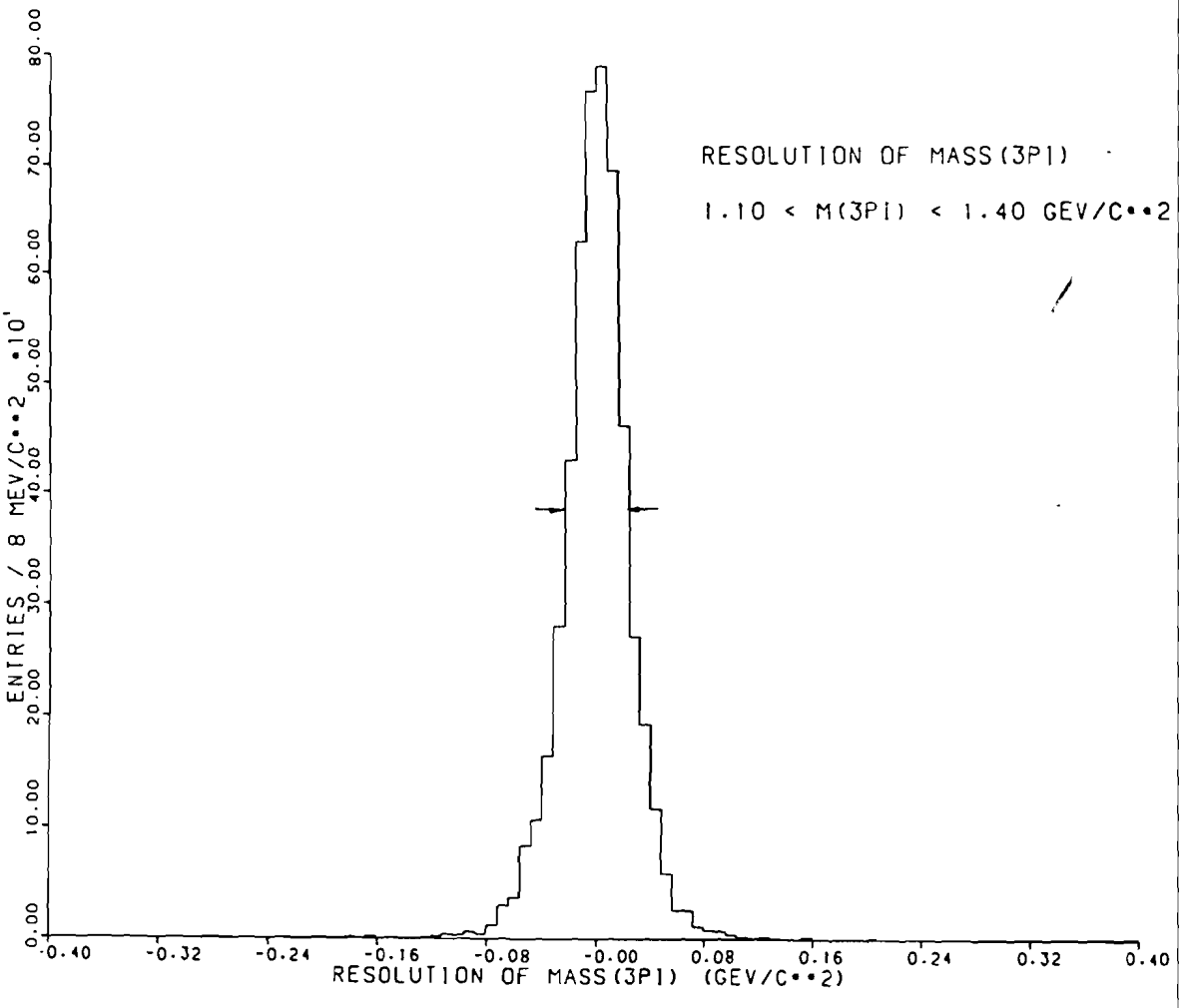

Figure 3.24: Resolution of Mass($\pi^-\pi^-\pi^+$), for $1.10 < \text{Mass}(\pi^-\pi^-\pi^+) < 1.40$ GeV/c^2. Arrows show FWHM of 48 GeV/c^2.

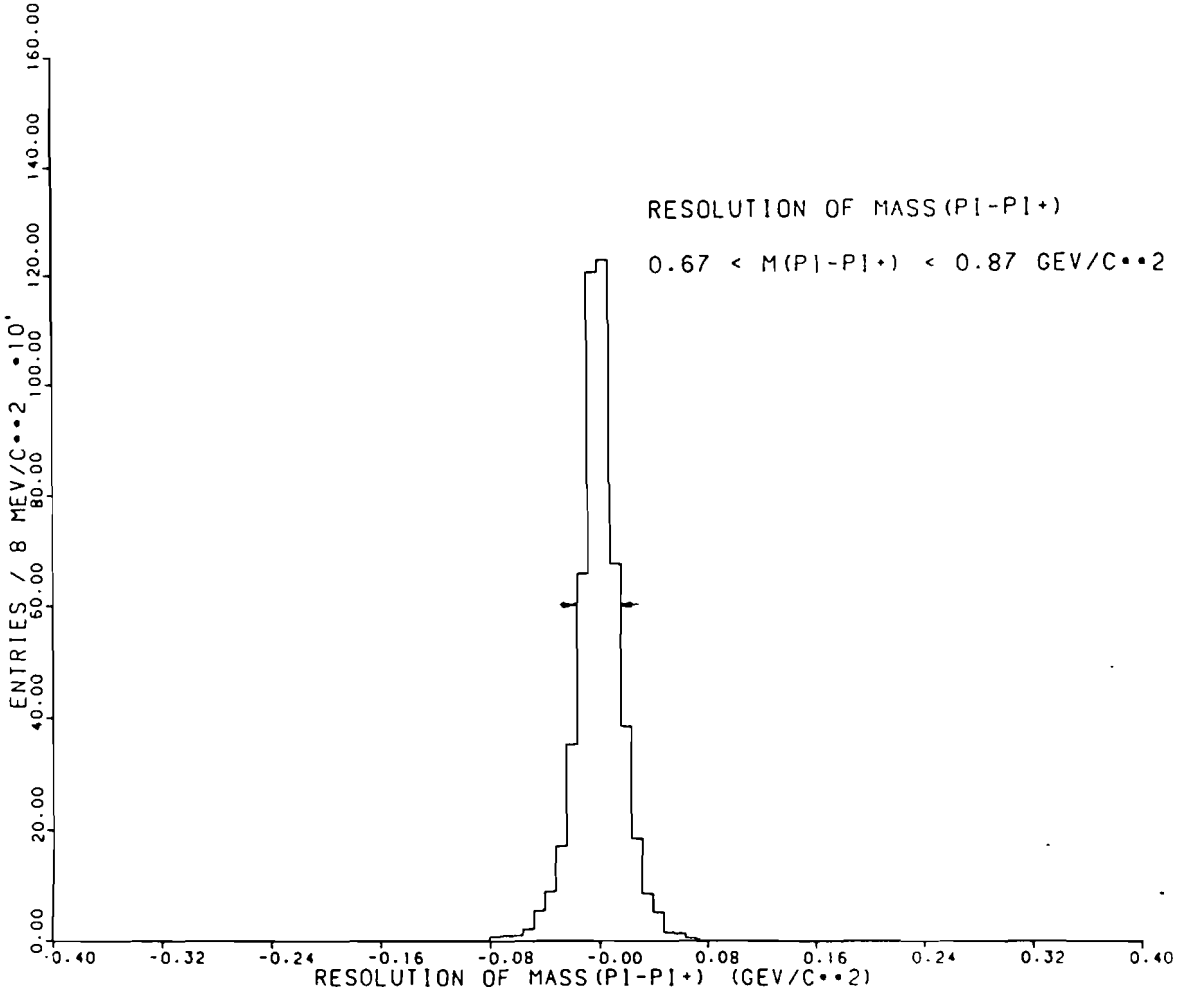

Figure 3.25: Resolution of Mass($\pi^-\pi^+$), for $0.67 < \text{Mass}(\pi^-\pi^+) < 0.87$ GeV/c^2. Arrows show FWHM of 28 GeV/c^2.

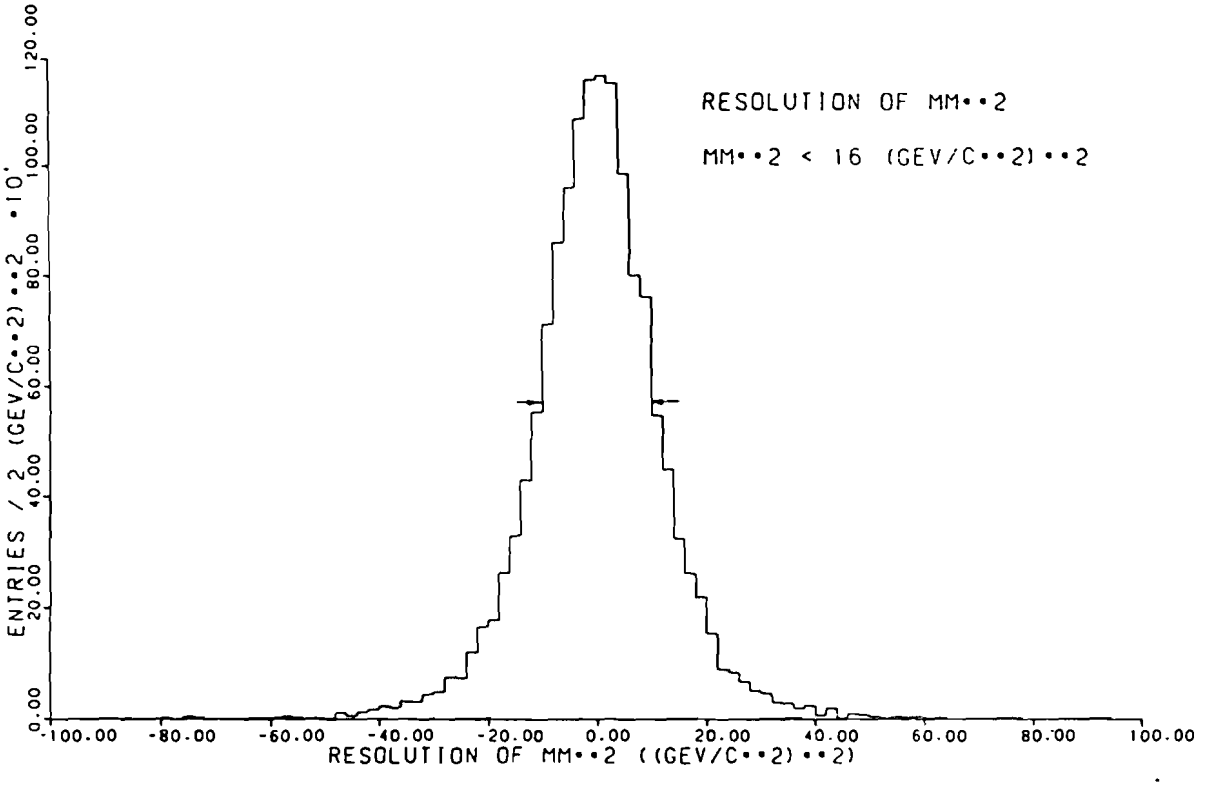

Figure 3.26: Resolution of missing mass squared, for $MM^2 < 16\ (GeV/c^2)^2$.

Arrows show FWHM of 20 $(GeV/c^2)^2$.

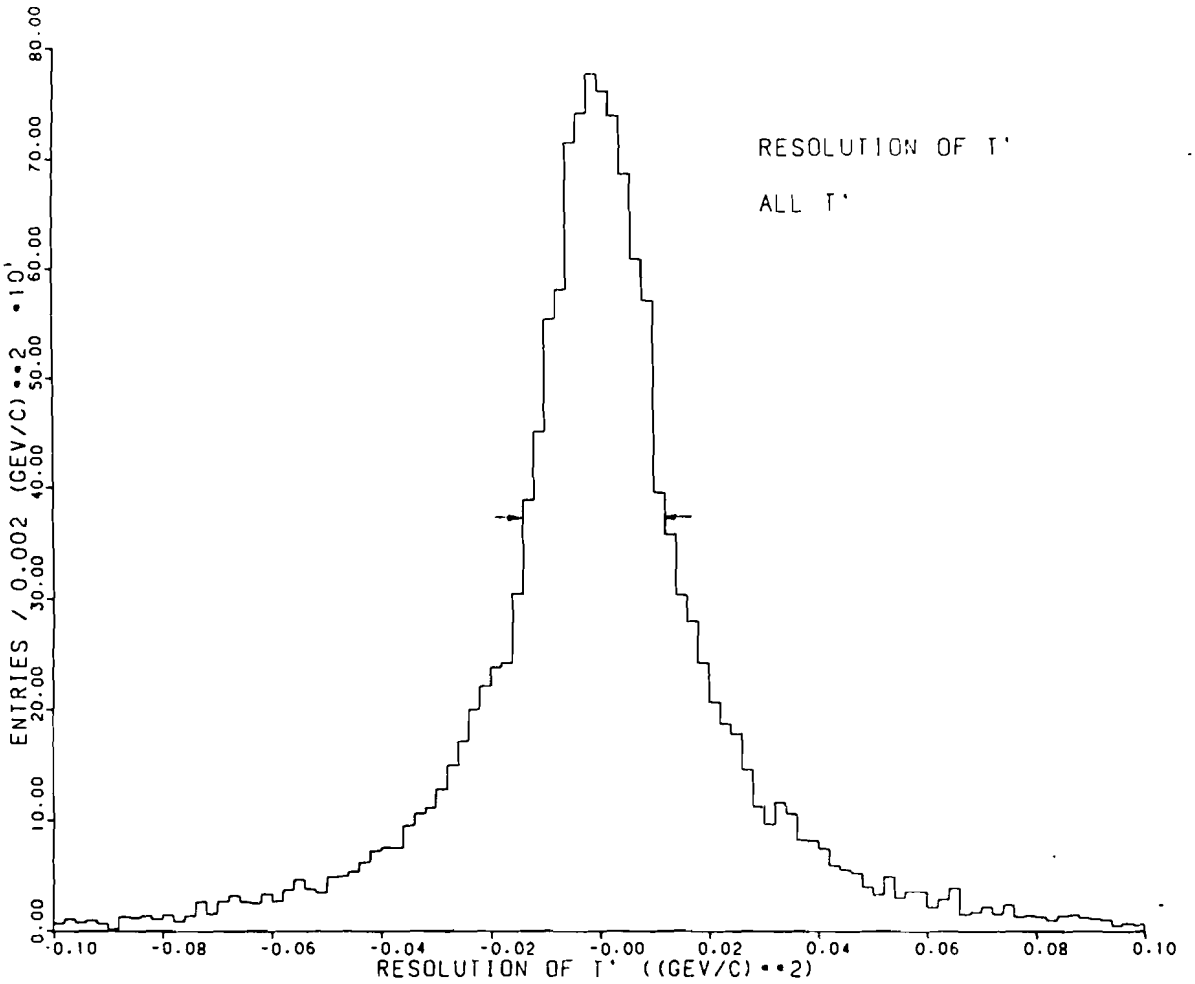

Figure 3.27: Resolution of effective momentum transfer t′, for all values of t′.
Arrows show FWHM of 0.024 $(GeV/c)^{-2}$.

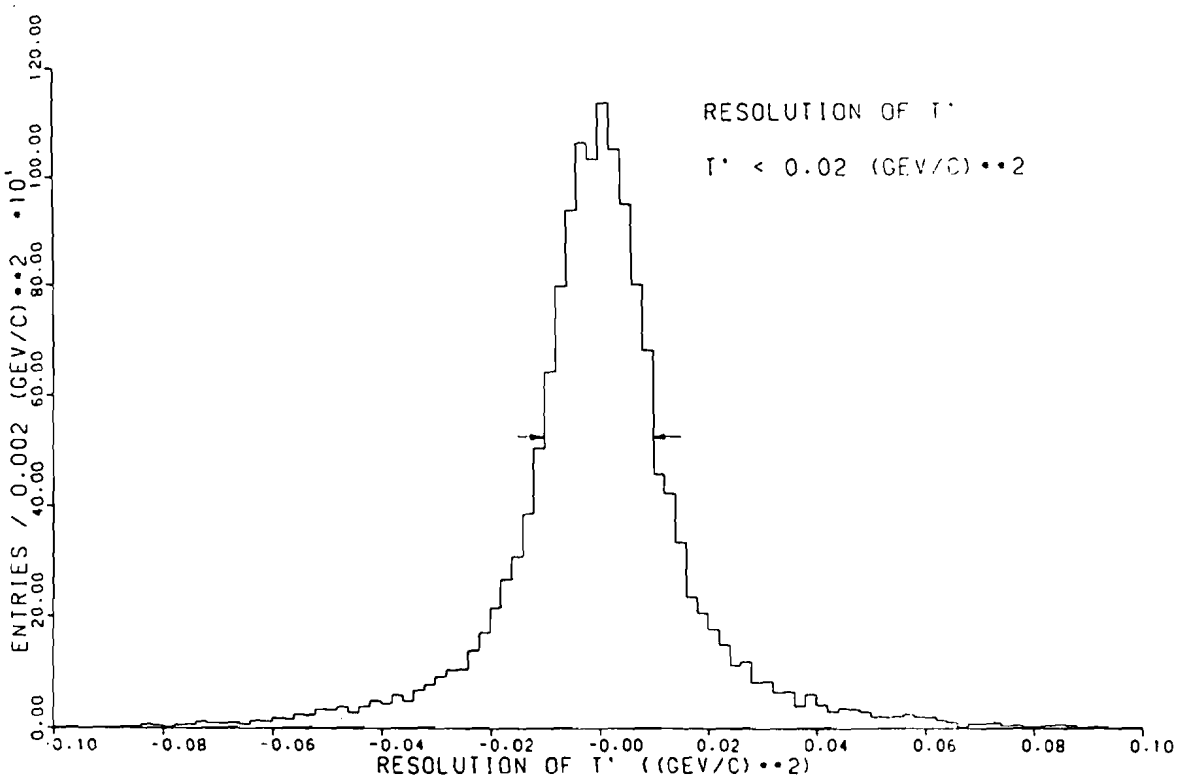

Figure 3.28: Resolution of effective momentum transfer t′, for t′ < 0.02 $(GeV/c)^{-2}$.
Arrows show FWHM of 0.020 $(GeV/c)^{-2}$.

3.11.3 Decay Angle Resolutions

It will be of interest to know the resolution of $\cos\theta$, where θ is a decay angle of some system. There are two such angles used in this analysis. These are:

1) $\cos\theta_J$, where θ_J is the angle in the rest frame of the 3π system between the beam direction and the π^- not considered part of the outgoing $\pi^-\pi^+$ system (Fig. 3.29).

2) $\cos\theta_2$, where θ_2 is the angle in the rest frame of the $\pi^-\pi^+$ system between the decay π^- and the direction of the $\pi^-\pi^+$ system, defined as opposite the direction of the other π^- (figure 3.30).

In order to get an idea of the uncertainty of these quantities, it was decided to treat $\cos\theta$ as a function of the momenta of the three outgoing pions, P(i,j), where i=x,y,z and j=π^+,π^-(slow),π^-(fast). For each event, the uncertainty $\Delta P(i,j)$ of each momentum component of each track was determined from KLEENX output. We make the assumption that the uncertainties due to each momentum component are uncorrelated, and calculate the following:

$$\cos\theta = f(P(1,1),P(2,1),...,P(3,3))$$

$$\cos\theta'(1,1) = f(P(1,1)+\Delta P(1,1),P(2,1),...,P(3,3))$$

$$\cos\theta'(2,1) = f(P(1,1),P(2,1)+\Delta P(2,1),...,P(3,3))$$

. . .

Then

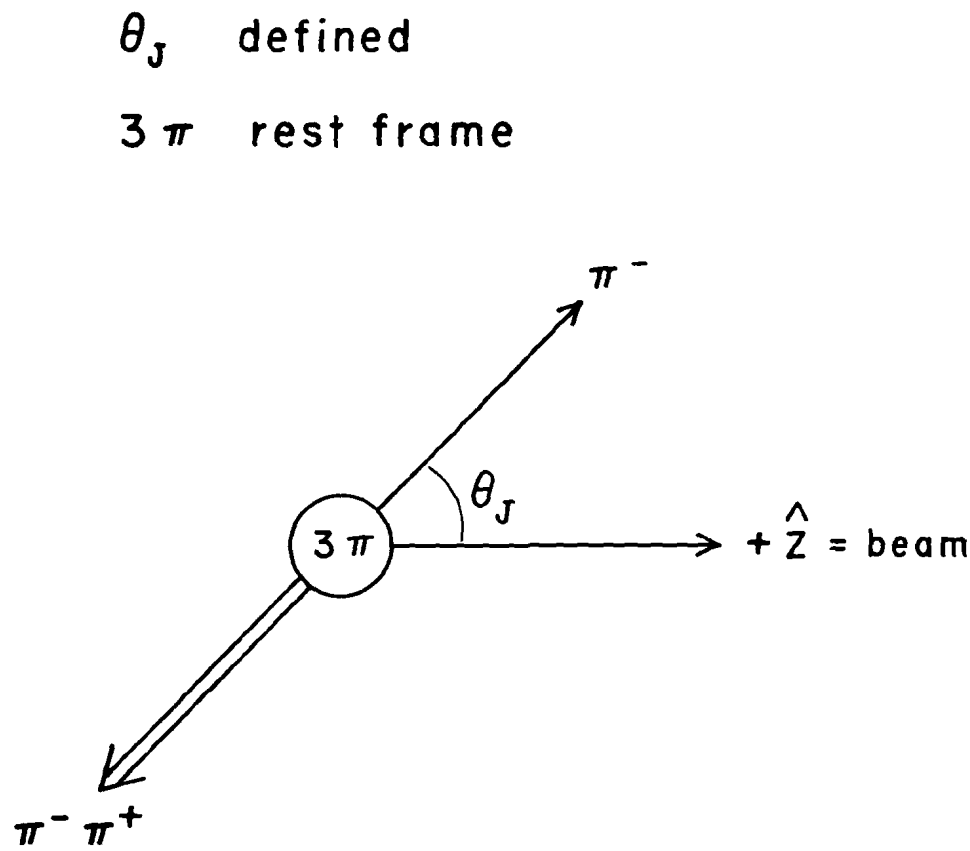

Figure 3.29: Definition of θ_J.

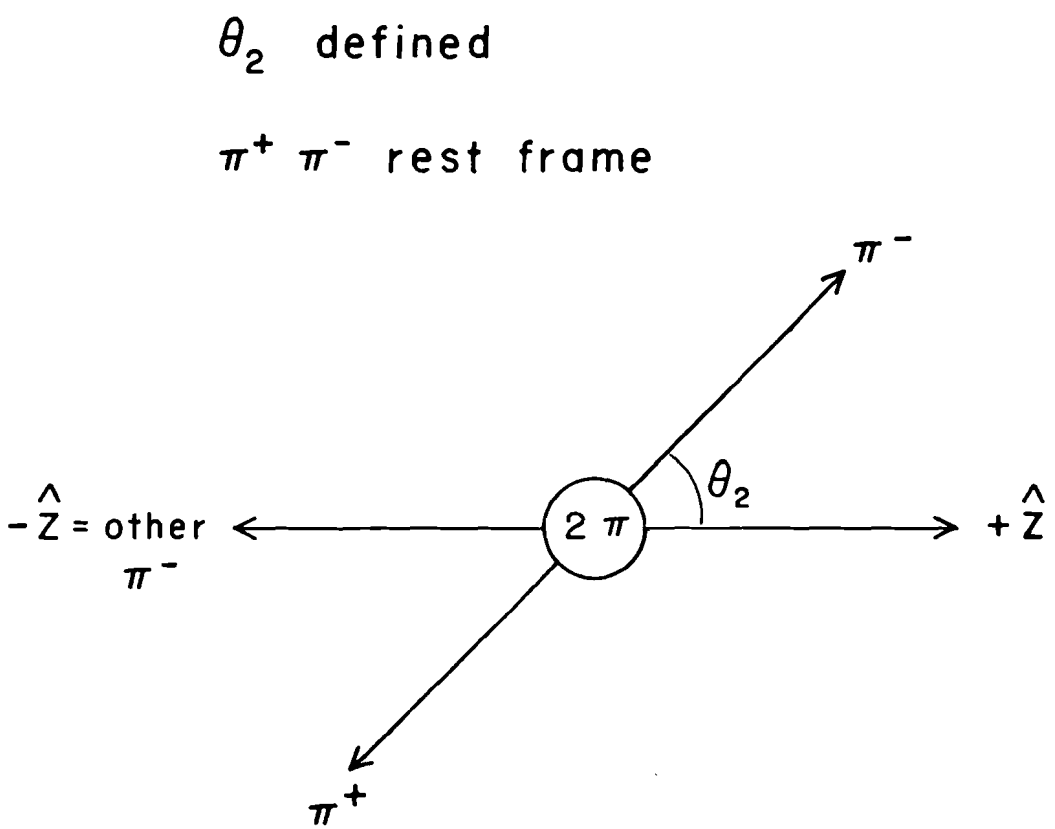

Figure 3.30: Definition of θ_2.

$$\Delta\cos\theta(1,1) = |\cos\theta'(1,1) - \cos\theta|$$

$$\Delta\cos\theta(2,1) = |\cos\theta'(2,1) - \cos\theta|$$

. . .

Finally,

$$\Delta\cos\Theta_{tot} = \mathrm{sqrt}(\Delta\cos\theta(1,1)^2 + \Delta\cos\theta(2,1)^2 + \ldots)$$

It was determined that the resolution of $\cos\theta_J$ as a function of $\cos\theta_J$ was $\Delta\cos\theta_J = 0.001(1-\cos^2\theta_J)$. The resolution of $\cos\theta_2$ was $\Delta\cos\theta_2 = 0.00075(1-\cos^2\theta_2)$

These formulations have been used in calculating error bars for the distributions of moments of spherical harmonics, although it turns out that they are so small that they do not contribute significantly.

CHAPTER 4

PHYSICS ANALYSIS

4.1 Diffraction

Do the 7205 events in the sample display any evidence that they are truly diffractive?

Figure 4.1 shows the distribution of Feynman x (X_F) for the sample, where x_F is defined as $x_F = 2P_L/\mathrm{sqrt}(s)$, where P_L is the momentum component parallel to the beam of the 3π system in the center of mass frame, and sqrt(s) is the energy in the center of mass frame. As can be seen, the data has x_F peaked very sharply forward at +1, indicative of the incident beam π^- dissociating very cleanly into $\pi^-\pi^-\pi^+$, with little loss of forward momentum. The spillover beyond +1 is due to the resolution of x_F. The geometrical acceptance with A-station correction of events below the peak has been calculated using events which did not pass the missing mass squared cut, and found to be 77.1% for events with $0.75 < x_F < 0.85$, so the lack of events below 0.85 cannot be attributed to lack of acceptance.

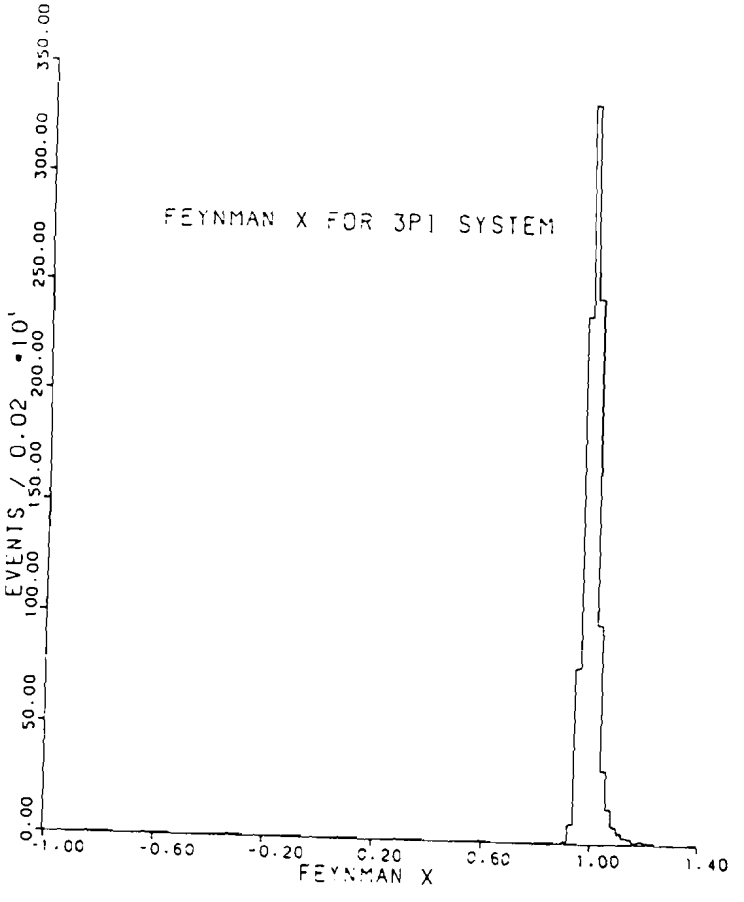

Figure 4.1: Feynman x (x_F) for the $\pi^-\pi^-\pi^+$ system.

A standard feature of diffraction is that the momentum transfer distribution shows a sharp initial slope. By momentum transfer we refer to the Lorentz-invariant quantity t, as defined by

$$t = (p_1 - p_3)^2$$

where p_1 and p_3 are the four-momenta of the incident beam and the outgoing 3π system, respectively.

$$= m_1^2 - 2E_1E_3 + 2\vec{p}_1\cdot\vec{p}_3 + m_3^2$$

For a diffractive sample the t distribution should follow the formula (Abarbanel 1976)

$$N(t)=Ae^{-b|t|}$$

where t is always negative. In practice, plotting t itself is impractical because the value of t depends on the 3π mass, as in Fig. 4.2. So we use a different quantity, t′, given by

$$t' = t_{min} - t \ ,$$

where

$$t_{min} = m_1^2 - 2E_1E_3 + 2|\vec{p}_1|\ |\vec{p}_3| + m_3^2$$

giving

$$t' = 2|\vec{p}_1|\ |\vec{p}_3| - 2\vec{p}_1\cdot\vec{p}_3$$

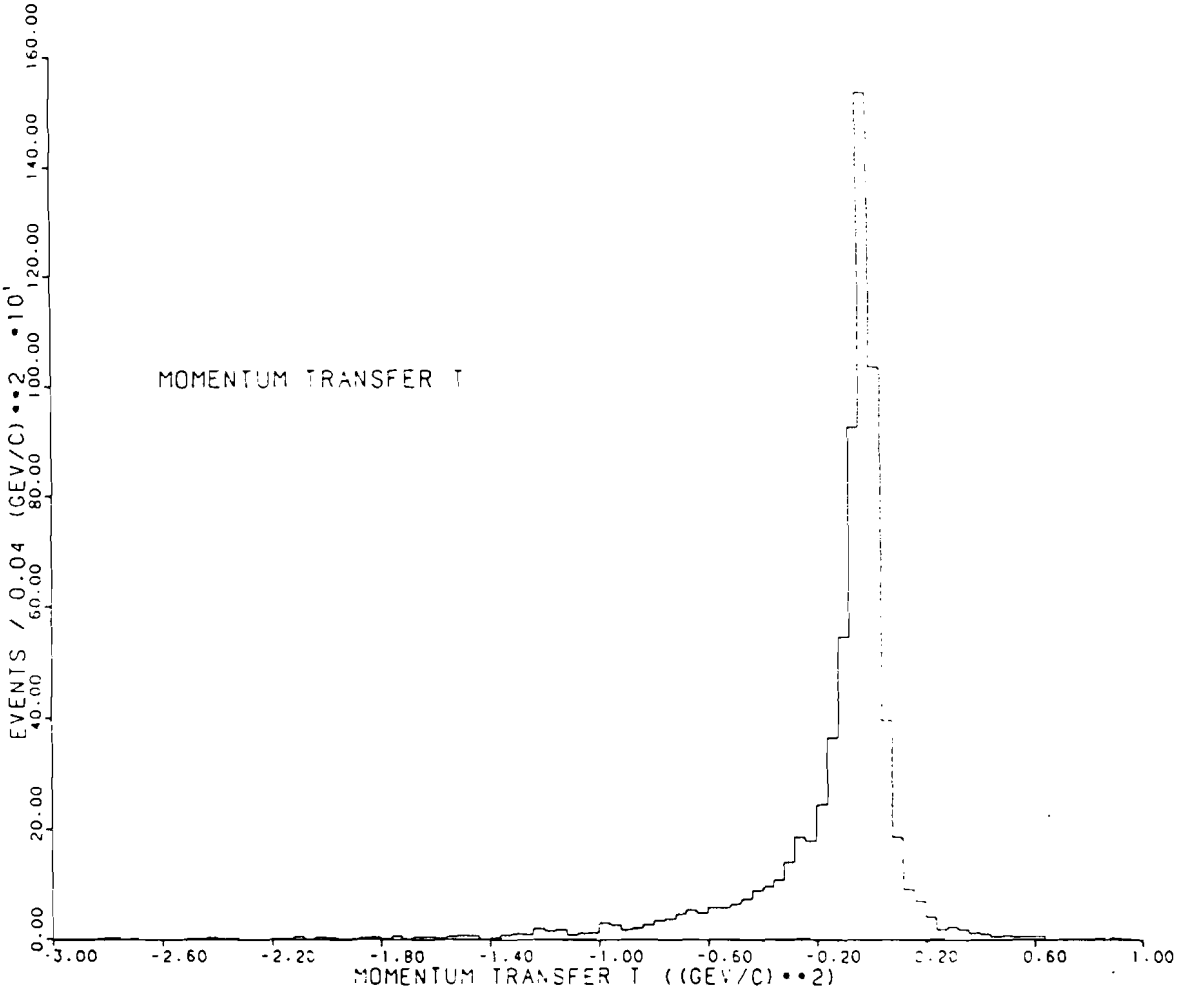

Figure 4.2: Momentum transfer t, for all data.

$$= 2|\vec{p}_1|\ |\vec{p}_3|\ (1 - \cos\theta_{13})$$

where θ_{13} is the angle between momentum vectors, in whatever frame. The variable t′ contains much fewer quantities subject to experimental error, and yet retains the desired feature of giving an exponentially-decaying distribution for diffractive events. t′ now also has the feature of being uniformly non-negative.

In Fig. 4.3 is shown the t′ distribution for our 7205 events, with each event weighted by its own factor of 1/acc, where acc is the geometrical acceptance for that event, including the A-station efficiency. The distribution has a logarithmic scale to show the exponential decrease. There are seen not one or two, but three separate regions of exponential decrease. Fit this distribution to the form

$$N(t') = A_1\exp(-b_1t') + A_2\exp(-b_2t') + A_3\exp(-b_3t') \ .$$

The first region of exponential decrease, for roughly $0.00\ (\mathrm{GeV}/c)^2 < t' < 0.04\ (\mathrm{GeV}/c)^2$, has an exponential slope of $b_1 = 67.8 \pm 4.4\ (\mathrm{GeV}/c)^2$. This corresponds to pions diffracting coherently off of an entire carbon nucleus. The second region, for roughly $0.04\ (\mathrm{GeV}/c)^2 < t' < 0.30\ (\mathrm{GeV}/c)^2$, has slope $b_2 = 11.8 \pm 3.4\ (\mathrm{GeV}/c)^2$, and is attributable to pion diffraction off of hydrogen nuclei, and also from individual nucleons in the carbon nucleus.

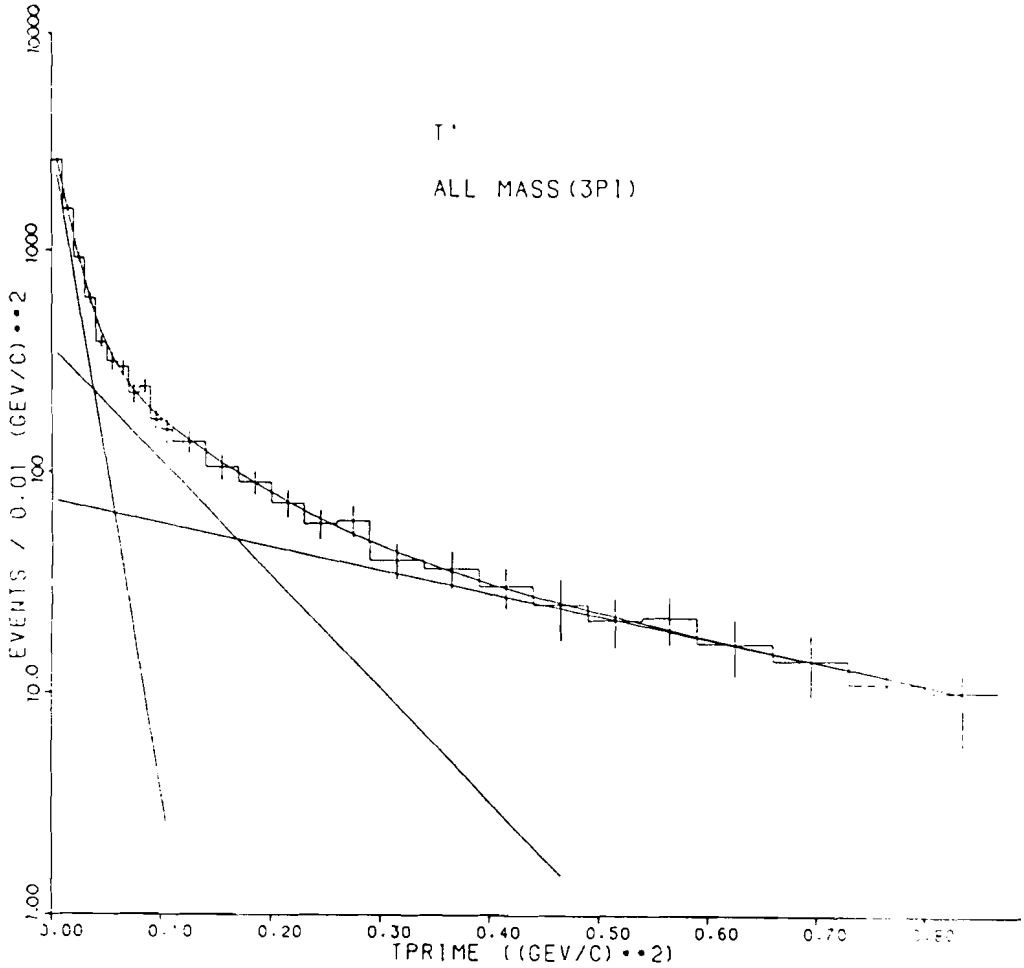

Figure 4.3: Effective momentum transfer t′, for all data. Curves shown are explained in the text.

The third region, for roughly 0.30 $(GeV/c)^2 < t'$, has slope $b_3 = 2.4 \pm 0.9$, and is the expected background (Zotov 1978), which could be called non-diffractive. These curves, plus their sum, are indicated in Fig. 4.3. The fit has a χ^2/DF of 12.2/21. Quoted errors here, as in all these fits, are determined by a change of ±1.0 in the total χ^2.

With this evidence of a sharp exponential slope (actually two: one for the carbon nucleus, and the other for individual nucleons) in hand, we may conclude that we do indeed have diffractive events in our sample.

But this analysis is only preliminary, as a detailed analysis of the t′ spectrum involves looking at t′ in various mass bins. It is observed elsewhere (Antipov 1973a, Antipov 1973b, Bosetti 1975, Daum 1981) that the exponential slope varies as a function of the 3π mass. Thus, it is necessary to fit the above function to the five mass bins, as well as to the complete sample of data, as shown in Figs. 4.3 to 4.8. The results are in Table 4.1.

A number of observations may be made. First, the slope b_2 shows a general decreasing trend with rising 3π effective mass, which has also been observed elsewhere (Antipov 1973a, Antipov 1973b, Bosetti 1975, Daum 1981). Also, the coherent carbon slope b_1 shows a trend to decrease with increasing 3π mass, but not as reliably.

TABLE 4.1

RESULTS OF T′ FITS BY MASS REGION

M(3π) Region (GeV/c^2)	b_1 (GeV/c)$^{-2}$	b_2 (GeV/c)$^{-2}$	b_3 (GeV/c)$^{-2}$	χ^2/DF
M(3π)<1.10	68.2 ± 8.7	12.7 ± 4.9	0.9 ± 2.5	5.7/21
1.10<M(3π)<1.40	63.9 ± 6.0	11.3 ± 6.4	3.0 ± 2.1	14.6/23
1.40<M(3π)<1.55	71.2 ± 9.6	8.8 ± 3.3	0.5 ± 2.9	17.0/21
1.55<M(3π)<1.80	82.6 ±16.2	12.4 ± 6.8	2.2 ± 2.0	8.1/21
1.80<M(3π)	51.1 ± 3.7	4.3 ± 0.4	0.1 ± 0.3	9.0/21
All M(3π)	67.8 ± 4.4	11.8 ± 3.4	2.4 ± 0.9	12.2/21

M(3π) Region (GeV/c^2)	N(Carbon)	N(nucleon)	Total N(wtd)
M(3π)<1.10	1040 ± 330	540 ± 110	1776
1.10<M(3π)<1.40	2020 ± 200	970 ± 480	3812
1.40<M(3π)<1.55	500 ± 60	440 ± 110	1117
1.55<M(3π)<1.80	510 ± 100	430 ± 230	1582
1.80<M(3π)	820 ± 440	1230 ± 80	2483
All M(3π)	4630 ± 330	3100 ± 680	10771

TABLE 4.1 (cont.)

M(3π) Region (GeV/c^2)	Frac(Carbon)	Frac(nucleon)
M(3π)<1.10	0.59 ± 0.19	0.30 ± 0.06
1.10<M(3π)<1.40	0.53 ± 0.05	0.25 ± 0.13
1.40<M(3π)<1.55	0.45 ± 0.05	0.39 ± 0.10
1.55<M(3π)<1.80	0.32 ± 0.06	0.27 ± 0.15
1.80<M(3π)	0.33 ± 0.18	0.50 ± 0.03
All M(3π)	0.43 ± 0.03	0.29 ± 0.06

M(3π) Region (GeV/c^2)	σ(Carbon) (μb/nucleon)	σ(nucleon) (μb/nucleon)	σ(Total) (μb/nucleon)
M(3π)<1.10	34 ± 15	17.8 ± 6.2	59 ± 16
1.10<M(3π)<1.40	67 ± 20	32 ± 18	126 ± 35
1.40<M(3π)<1.55	16.5 ± 5.0	14.5 ± 5.5	37 ± 10
1.55<M(3π)<1.80	16.8 ± 5.8	14.2 ± 8.6	52 ± 15
1.80<M(3π)	27 ± 16	41 ± 12	82 ± 23
All M(3π)	153 ± 44	102 ± 36	326 ± 95

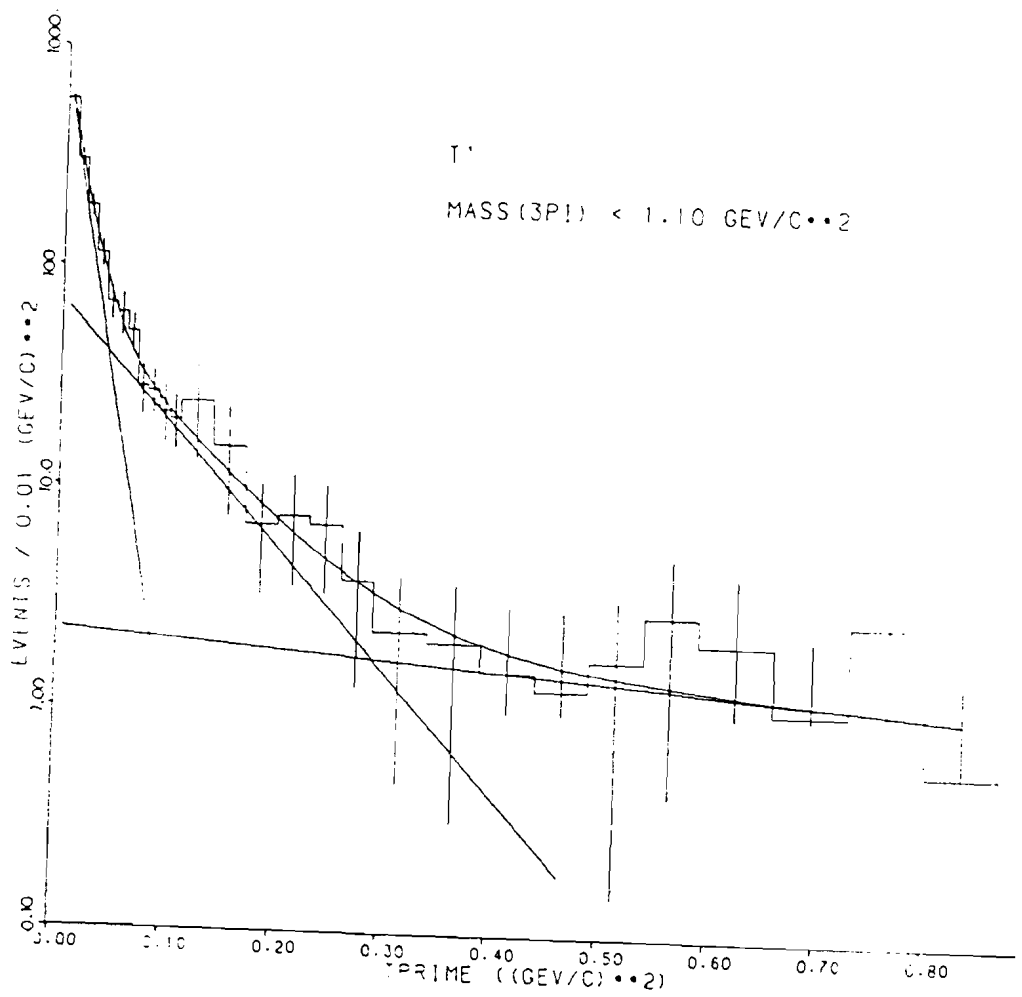

Figure 4.4: Effective momentum transfer t′, for Mass($\pi^-\pi^-\pi^+$) < 1.10 GeV/c^2. Curves shown are explained in the text.

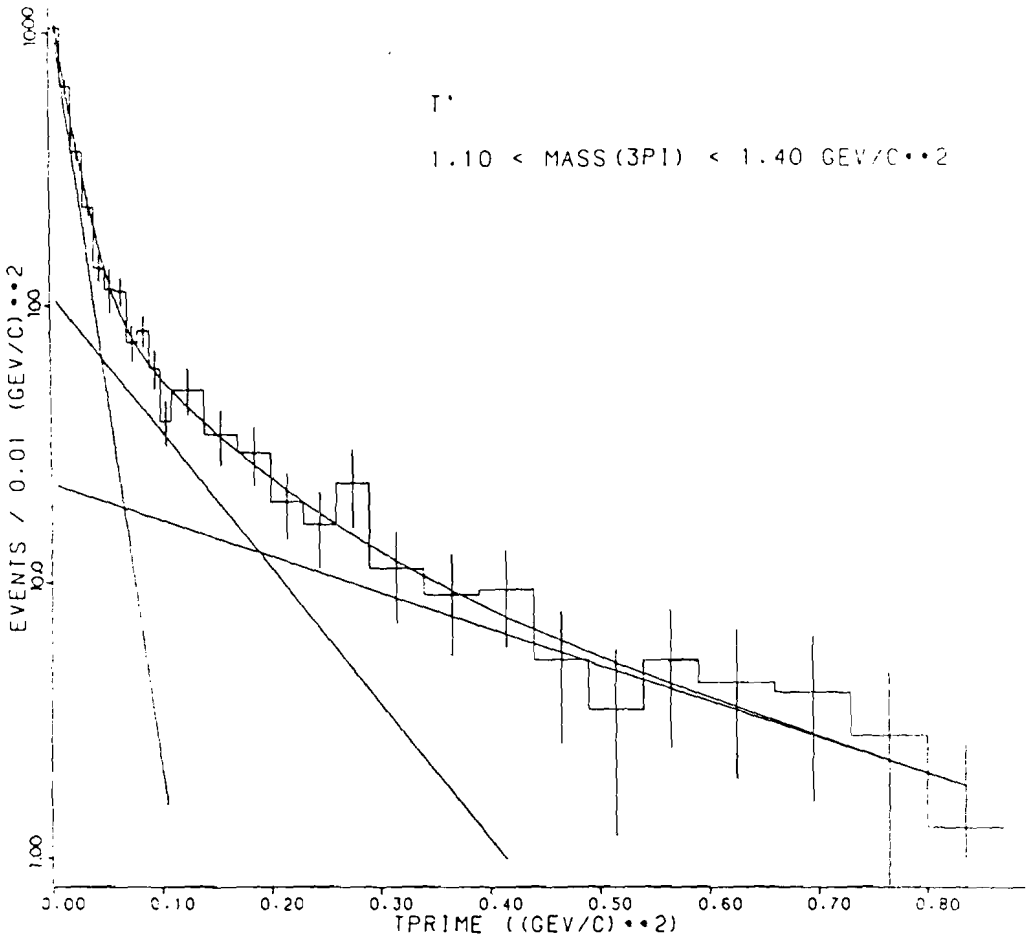

Figure 4.5: Effective momentum transfer t', for $1.10 < \mathrm{Mass}(\pi^-\pi^-\pi^+) < 1.40\ \mathrm{GeV}/c^2$. Curves shown are explained in the text.

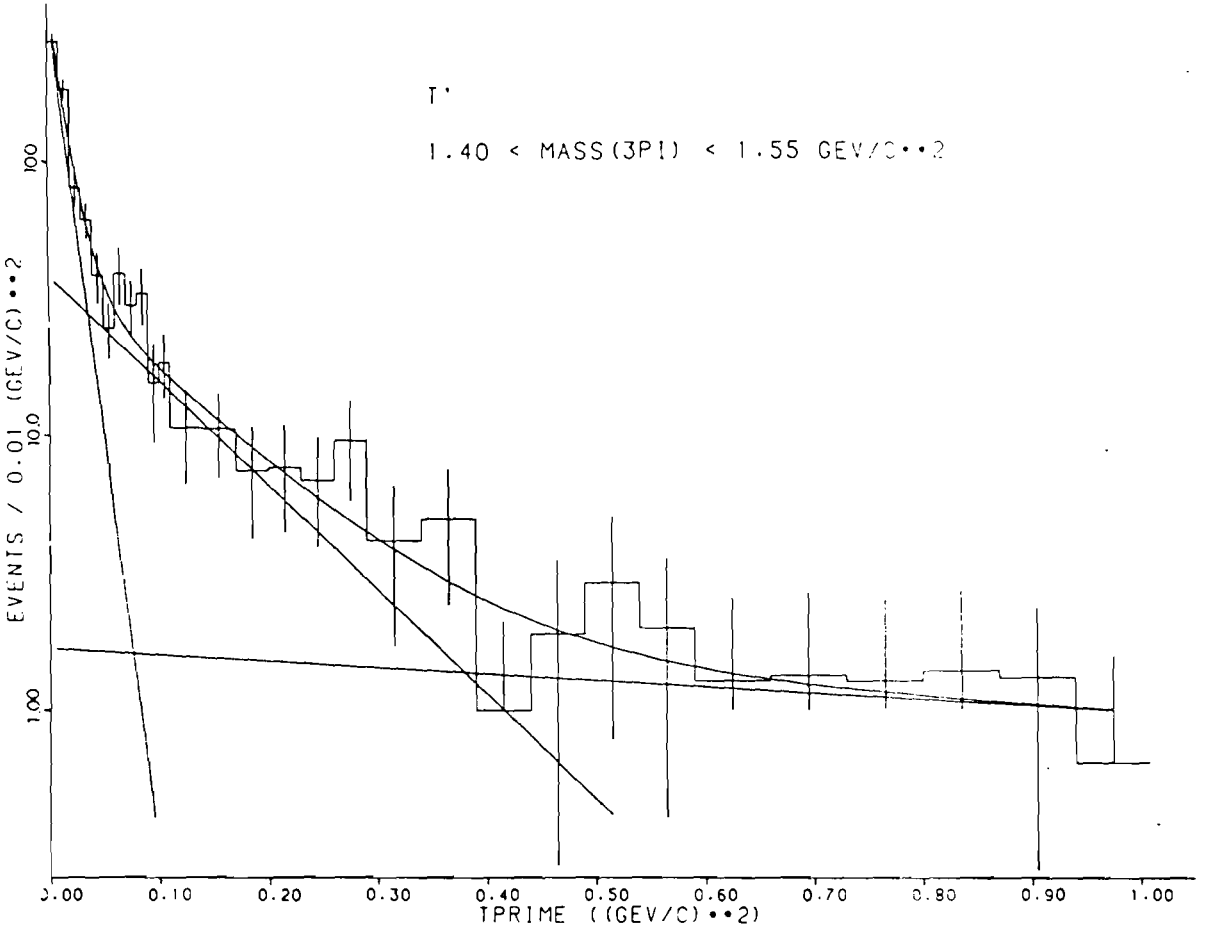

Figure 4.6: Effective momentum transfer t', for $1.40 < \mathrm{Mass}(\pi^-\pi^-\pi^+) < 1.55\ \mathrm{GeV}/c^2$. Curves shown are explained in the text.

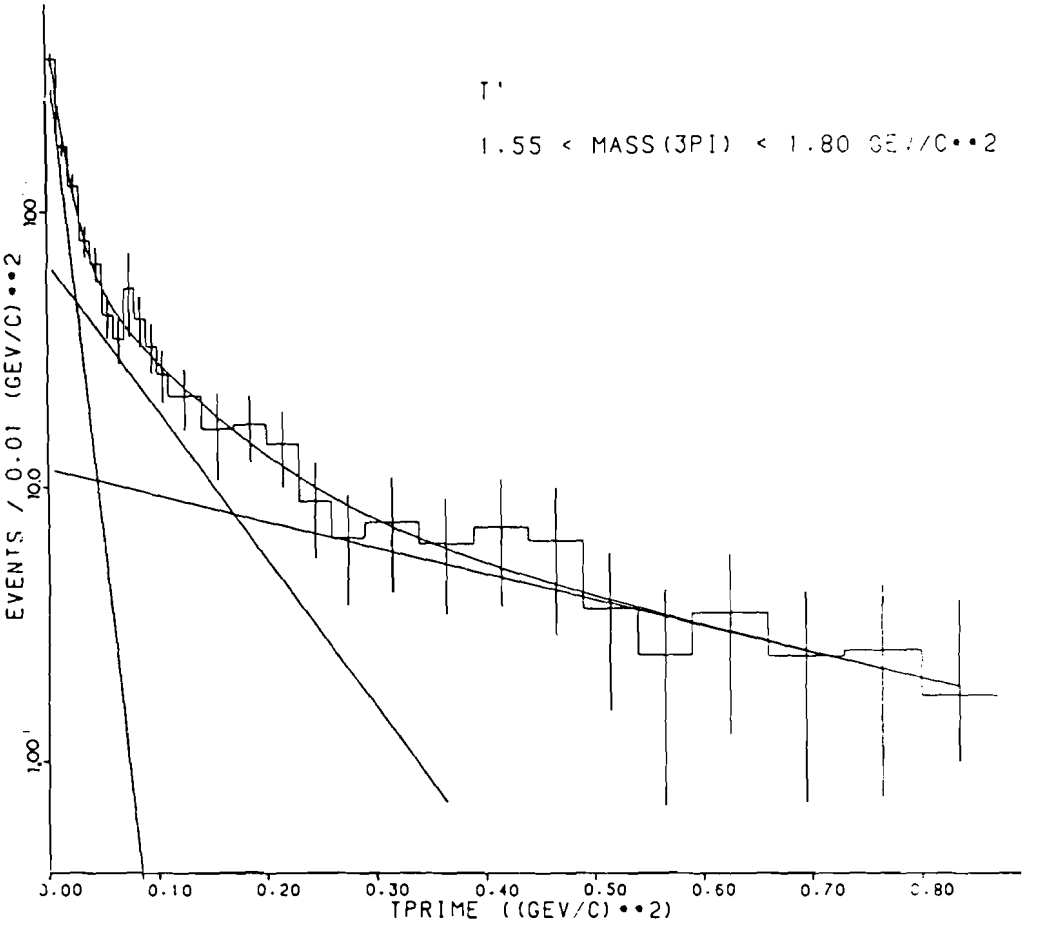

Figure 4.7: Effective momentum transfer t', for $1.55 < \mathrm{Mass}(\pi^-\pi^-\pi^+) < 1.80\ \mathrm{GeV}/c^2$. Curves shown are explained in the text.

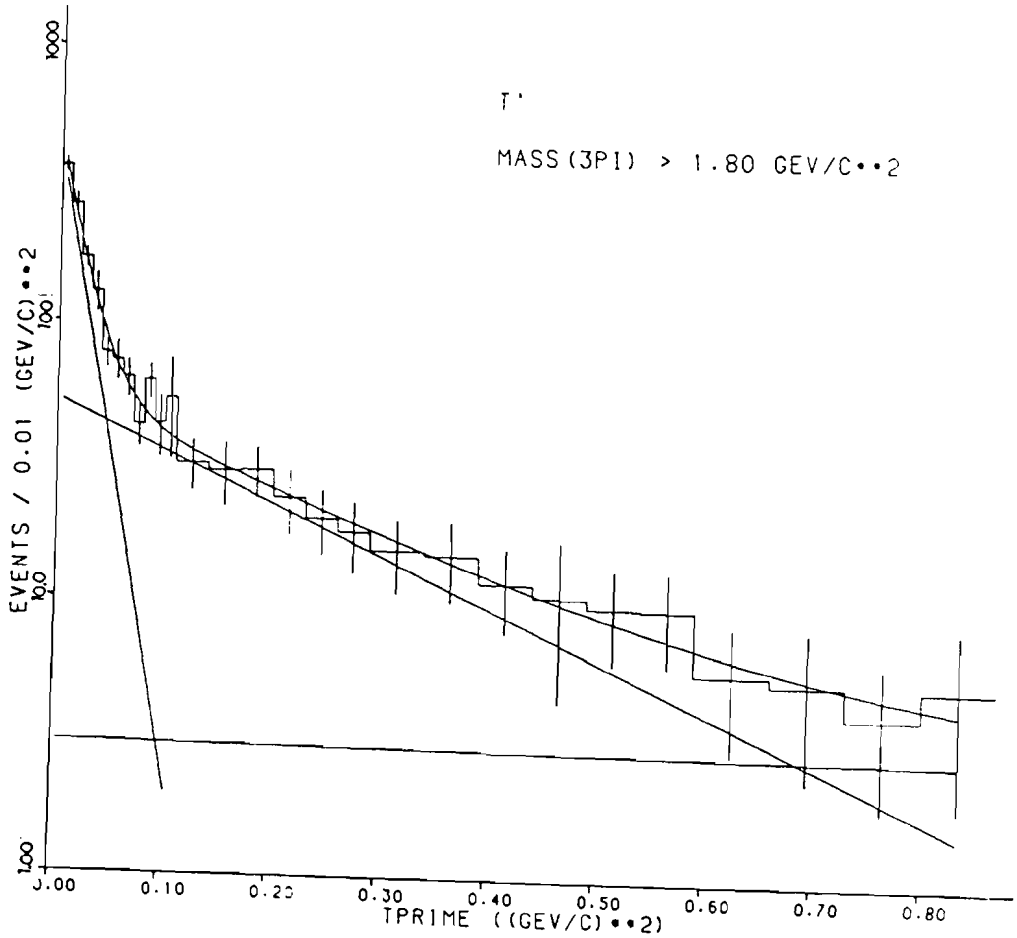

Figure 4.8: Effective momentum transfer t′, for $1.80 < \mathrm{Mass}(\pi^-\pi^-\pi^+)$.

Curves shown are explained in the text.

Also of note is the fact that the ratio of coherent carbon events to single-nucleon events, taken as N(carbon)/N(nucleon), decreases with rising 3π mass. At low mass ($M(3\pi) < 1.40$ GeV/c^2) this ratio is about 2:1, decreasing to about 1:1 at medium ($1.40 < M(3\pi) < 1.80$ GeV/c^2) mass, and <1:1 at high ($M(3\pi) > 1.80$ GeV/c^2) mass. This shows that coherent diffraction has more of a tendency to produce low-mass states than single-nucleon diffraction, and has also been observed by J. Pernegr et al (Pernegr 1982).

More insight into this phenomenon may be gained by looking at a Chew-Low plot of $M(3\pi)$ vs. t, as in Fig. 4.9. The distribution of low mass events is heaviest at low t, and the t distribution is heavier at low 3π mass, reflecting more events at the low mass.

The overall cross section for this sample is 326 ± 95 μb/nucleon. This compares with a diffractive cross section obtained in the E580 $K^o_s K^o_s \pi^-$ sample of 3.4 ± 1.1 μb/nucleon (Chen 1983), and in the E580 $K^o_s K^o_s \pi^+ \pi^- \pi^-$ sample of 1.6 ± 0.7 μb/nucleon (Chang 1984). These numbers are consistent with expectations that heavy flavor (in this case strangeness) production leads to a large drop in cross section.

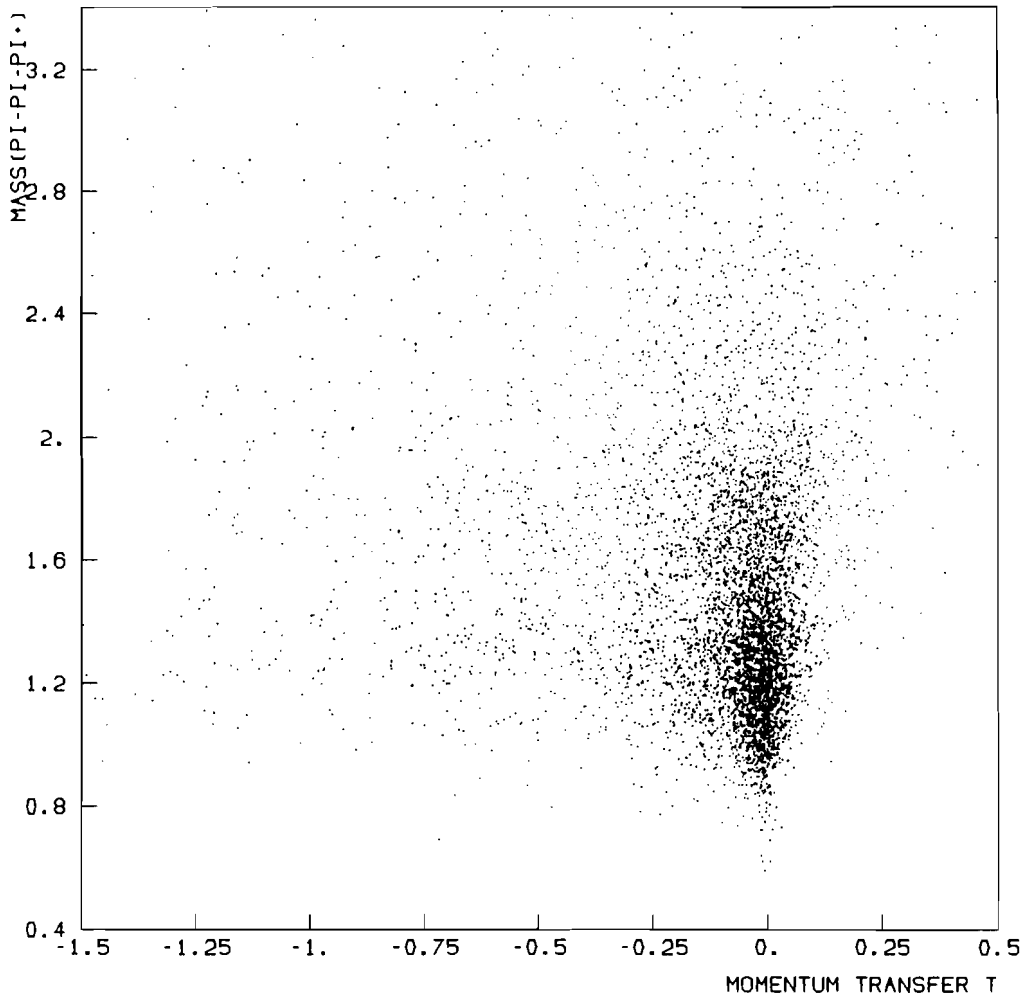

Figure 4.9: Scatterplot of Mass($\pi^-\pi^-\pi^+$) vs. t, for $0 < t < 1.0$ $(GeV/c)^2$.

The presence of a distinct number of coherent carbon diffraction events makes it possible to calculate the A^{α} behavior of this sample. If the assumption is made that the coherent carbon events are the only result of any A^{α} behavior (if $\alpha \neq 1$), then using the model of Azimov et al (Asimov 1982), as explained in Section 3.10, and the numbers $\rho_H = 0.084$ and $\rho_C = 0.916$, a value of $\alpha = 0.74 \pm 0.05$ is obtained. This is consistent with the value obtained by Azimov et al with 200 GeV/c π^- on emulsion.

The value of b_2 (diffraction off of nucleons) for the overall sample is 11.8 ± 3.4 $(GeV/c)^{-2}$. This may be compared to the value obtained in the analysis of the $K^o_s K^o_s \pi^-$ sample of 992 diffractive events from E580 (Chen 1983). These events were defined as being diffractive, as here, by making an identical cut in the missing mass squared distribution, requiring $MM^2 < 16$ $(GeV/c^2)^2$. The exponential slope obtained for the $K^o_s K^o_s \pi^-$ sample was 9.6 ± 1.9 $(GeV/c)^{-2}$, slightly smaller than that for the 3π sample. Also, in the 392 diffractive events of the E580 $K^o_s K^o_s \pi^+ \pi^- \pi^-$ sample, the observed exponential slope was 5.4 ± 0.7 $(GeV/c)^{-2}$ (Chang 1984). This is consistent with observations made by P. Bosetti et al (Bosetti 1975), both that slope tends to decrease with increasing mass, and that the slope decreases in going from a 3π system to a $KK\pi$ system.

4.2 Two Pion Data Sample

4.2.1 $\pi^-\pi^-$ Mass Spectrum

Fig. 4.10 shows the invariant effective mass of all $\pi^-\pi^-$ pairs of the 7205 events, in 30 MeV/c^2 bins in accordance with resolution, and weighted for acceptance. The distribution is generally featureless, as predicted by the simple $q\bar{q}$ quark model: in order to have a meson resonance which decays into $2\pi^-$, one would need a $q\bar{q}$ pair in which the sum of the charges of q and $\bar{q}$ is -2. This is impossible under the quark model, since the largest charge on any quark is 2/3.

The $\pi^-\pi^-$ distribution has been fit to a function of the form

$$F(M) = A(M-M_T)^{\alpha}\exp(-\beta M-\gamma M^2) \ ,$$

where $M_T = 2M_{\pi^-} = 2(0.1395\ \mathrm{GeV}/c^2) = 0.2790\ \mathrm{GeV}/c^2$.

The fit resulted in a χ^2/DF of 56.2/49, for a probablility of 22.3%. The resultant parameters were as follows:

$A = 15050 \pm 180$

$\alpha = 0.968 \pm 0.013$

$\beta = 4.282 \pm 0.012$

$\gamma = -0.264 \pm 0.011$

Errors here, as in all fits, correspond to a change of ±1.0

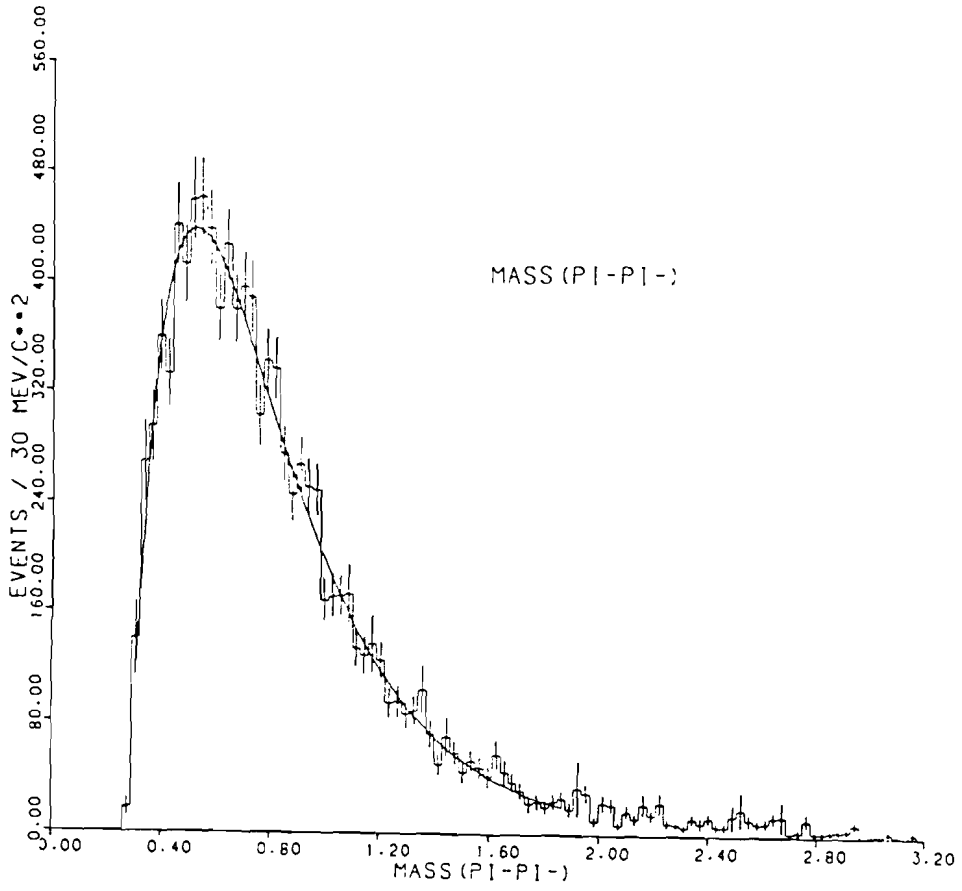

Figure 4.10: Effective mass of all $\pi^-\pi^-$ pairs, one entry per event.

in the total χ^2. The results of the fit are shown in Figure 4.10.

The good results of this fit give us confidence in using this formulation for the background of other effective mass plots.

4.2.2 $\pi^-\pi^+$ Mass Spectrum

Figure 4.11 shows the invariant effective mass of all $\pi^-\pi^+$ combinations, two per event, in 30 MeV/c^2 bins, weighted for acceptance. We observe a very strong signal peaking around 770 MeV/c^2, which we will take to be the $\rho^0(770)$, and a lesser enhancement around 1270 MeV/c^2, which may be taken to be the $f^0(1270)$, both of which have strong decay modes into $\pi^-\pi^+$ (PDG 1986). A fit was done to this distribution, consisting of the above parameterization for the background, plus two Breit-Wigner resonance terms, one of spin 1 constrained to lie within the mass region of the ρ^0, the other of spin 2 constrained to lie within the mass region of the f^0. See Appendix C for the form of the Breit-Wigner resonance functions. The results of the fit are as follows:

$M(\rho^0)$ = 773 ± 1 MeV/c^2 (PDG value 770 ± 3 MeV/c^2)

$\Gamma(\rho^0)$ = 169 ± 49 M3V/c^2 (PDG value 153 ± 2 MeV/c^2)

$N(\rho^0)$ = 8510 ± 670 events

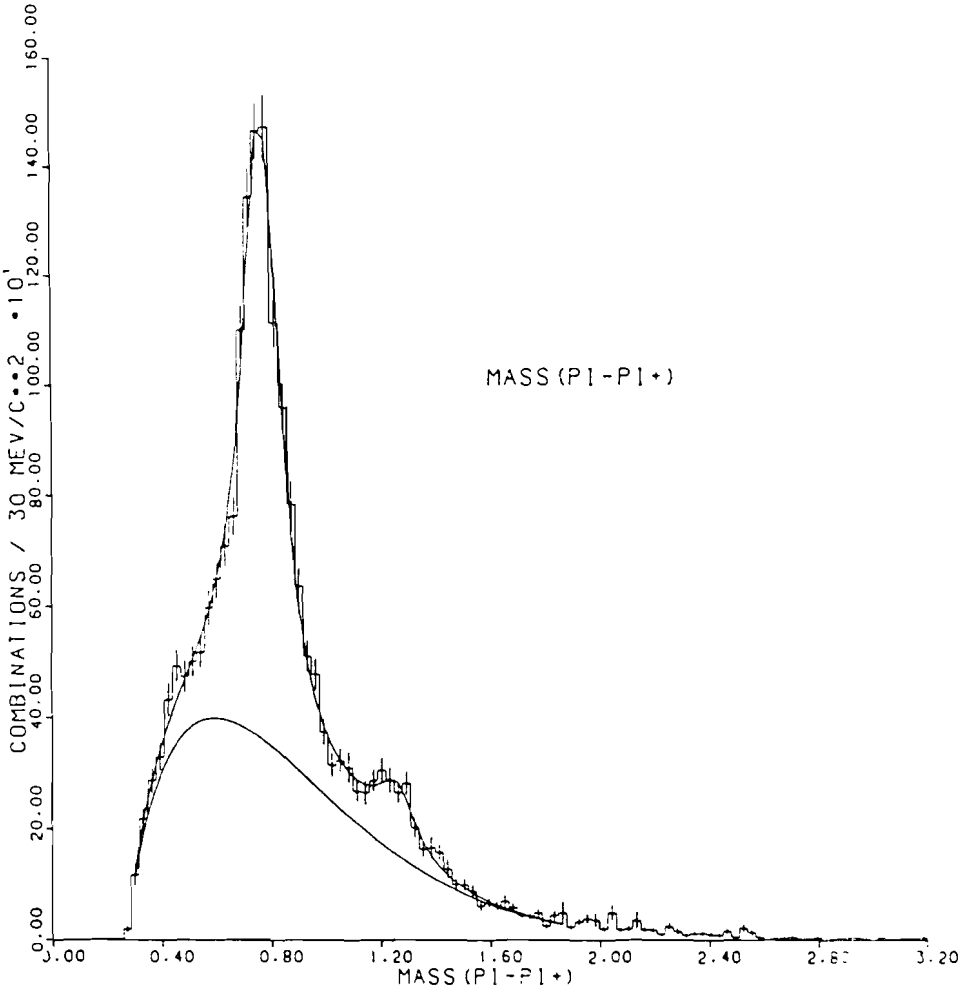

Figure 4.11: Effective mass of all $\pi^-\pi^+$ pairs, two entries per event. Curves shown are explained in the text.

$M(f^o) = 1268 \pm 9$ MeV/c^2 (PDG value 1274 ± 5 MeV/c^2)

$\Gamma(f^o) = 178 \pm 27$ MeV/c^2 (PDG value 176 ± 20 MeV/c^2)

$N(f^o) = 1090 \pm 120$ events

N(Total) = 20926.3 combinations (weighted)

$A = 3200 \pm 400$

$\alpha = 0.744 \pm 0.048$

$\beta = 1.758 \pm 0.010$

$\gamma = 0.512 \pm 0.050$

$\chi^2/DF = 57.1/43$

The results of the fit are shown in Figure 4.11. As may be readily seen, these values for mass and width of the ρ^o and f^o are quite consistent with the accepted values. It must be borne in mind that there are two $\pi^-\pi^+$ combinations per event, and the individual events are weighted according to acceptance.

It is observed that the ρ^o and f^o comprise $81.3 \pm 6.4\%$ and $10.4 \pm 1.1\%$ of the total data, an observation consistent with that of C. Baltay et al (Baltay 1978).

Based on our sensitivity of 30.3 ± 8.5 weighted events/μb, we obtain the following cross-sections per nucleon for the ρ^o and f^o:

$\sigma(\rho^o \rightarrow \pi^-\pi^+) = 208 \pm 65$ μb/nucleon

$\sigma(f^o \rightarrow \pi^-\pi^+) = 26.6 \pm 8.3$ μb/nucleon

4.2.3 $\pi^-\pi^+$ Spin Analysis

It is of interest to see if it is possible to ascertain whether the observed enhancements exhibit behaviour consistent with our assumption that the π^o and f^o are spin 1 and spin 2, respectively. Figure 4.12(a-h) shows $\langle Y_L^o \rangle$, L = 1 to 8, vs. Mass($\pi^-\pi^+$), where the $\langle Y_L^o \rangle$ are moments of spherical harmonic functions, defined as follows:

$$\langle Y_L^o \rangle = \sum^N (2L+1)/4\pi * P_L^0(\cos\theta_2) * \text{weight},$$

where

The summation is over all events,

P_L^0 are Associated LeGendre Polynomials (See App. A)

θ_2 is the angle between the two π^-'s in the rest frame of a $\pi^-\pi^+$ combination (Fig. 3.23), and is the decay angle of the $\pi^-\pi^+$ combination.

weight is a correction for acceptance, as explained in Section 3.9.6.

Since there are two $\pi^-\pi^+$ combinations per event, there are two entries per event in the distributions of the $\langle Y_L^o \rangle$. Error bars are based on both the estimated uncertainty of $\cos\theta_2$, as explained in Section 3.11.3, and on statistics, which turns out to be the dominant source of uncertainty.

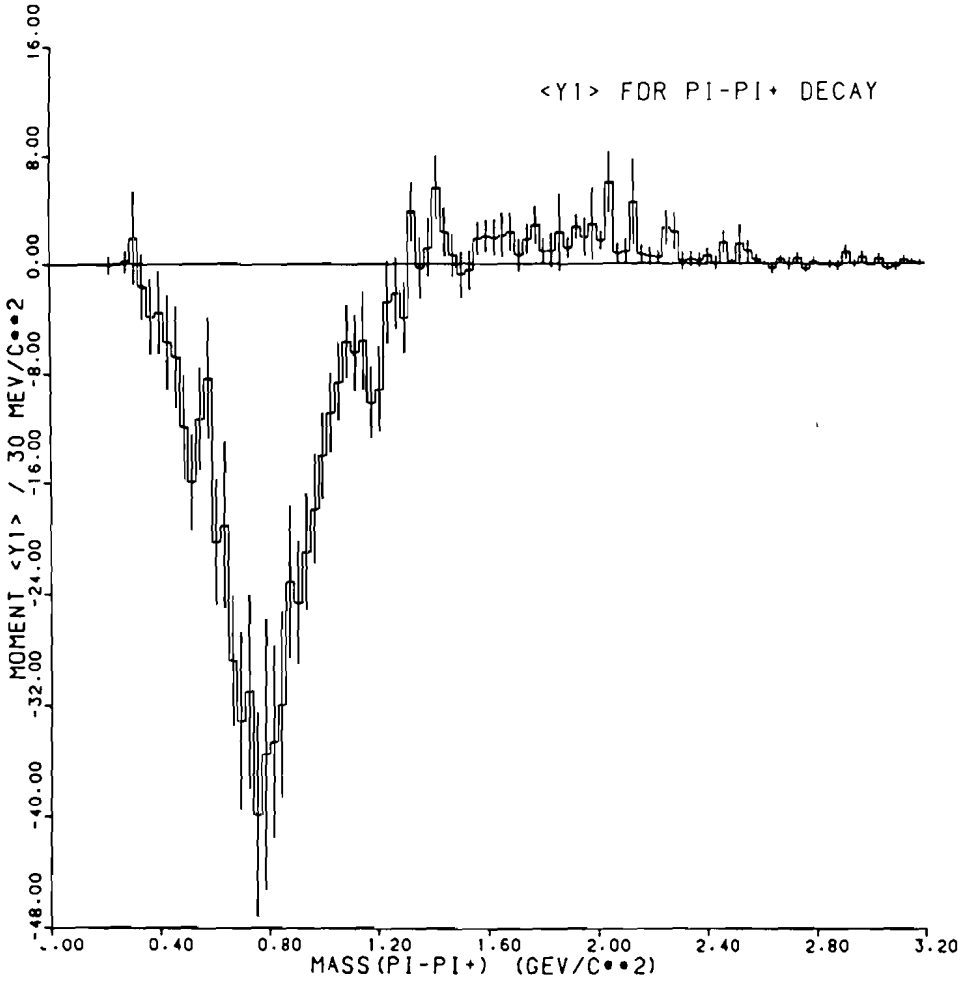

Figure 4.12(a): Moments of spherical harmonic Y_1^0 vs. Mass($\pi^-\pi^+$). Two entries per event.

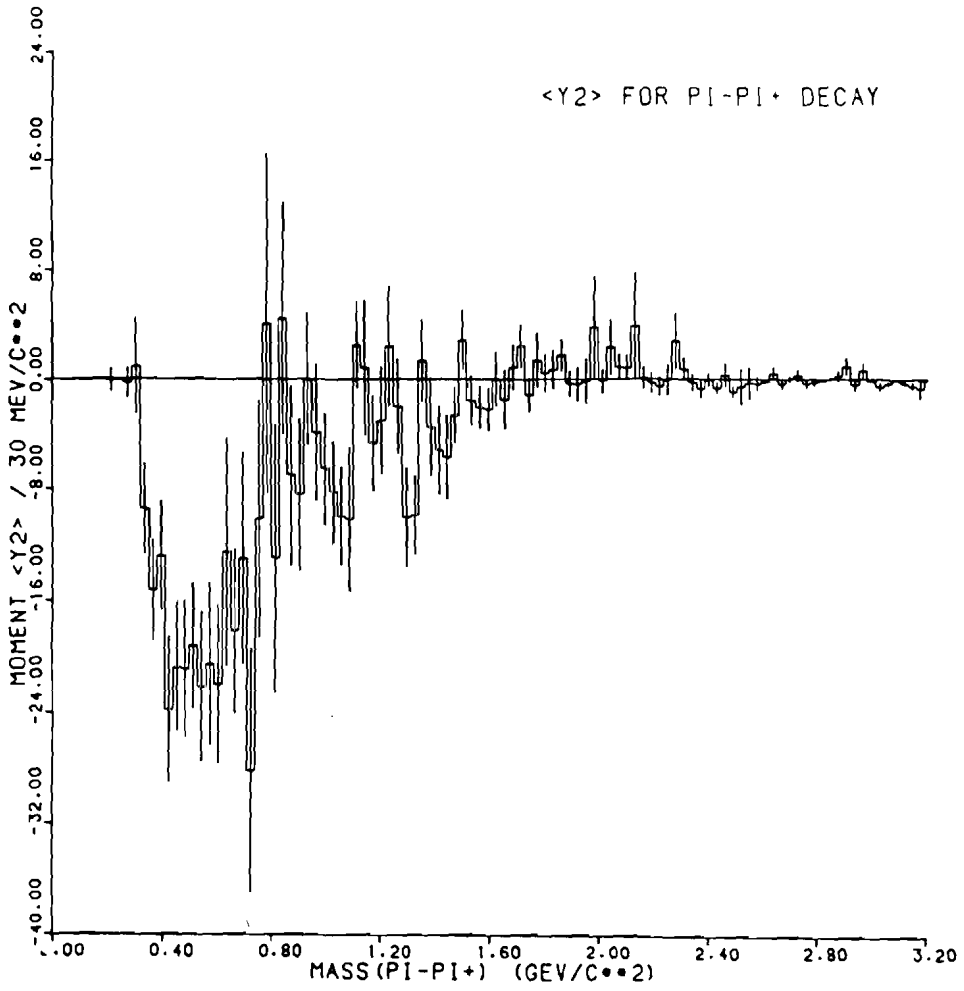

Figure 4.12(b): Moments of spherical harmonic Y_2^0 vs. Mass($\pi^-\pi^+$). Two entries per event.

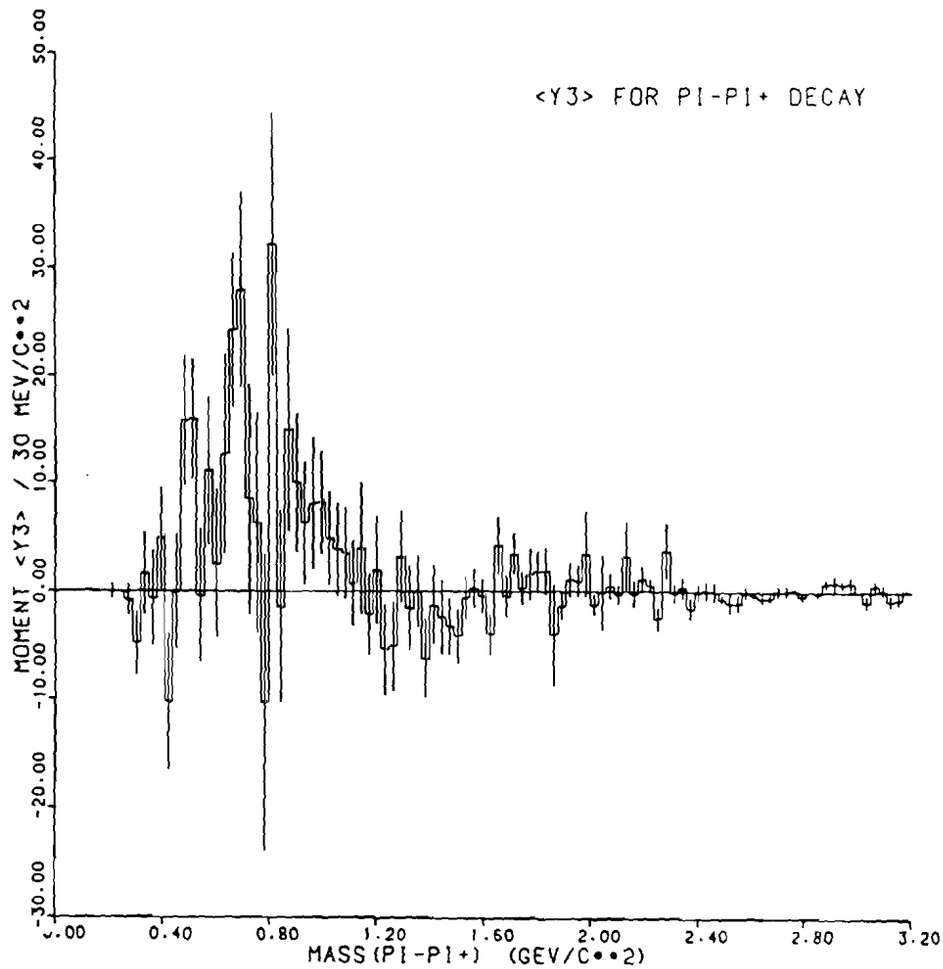

Figure 4.12(c): Moments of spherical harmonic Y_3^0 vs. Mass($\pi^-\pi^+$). Two entries per event.

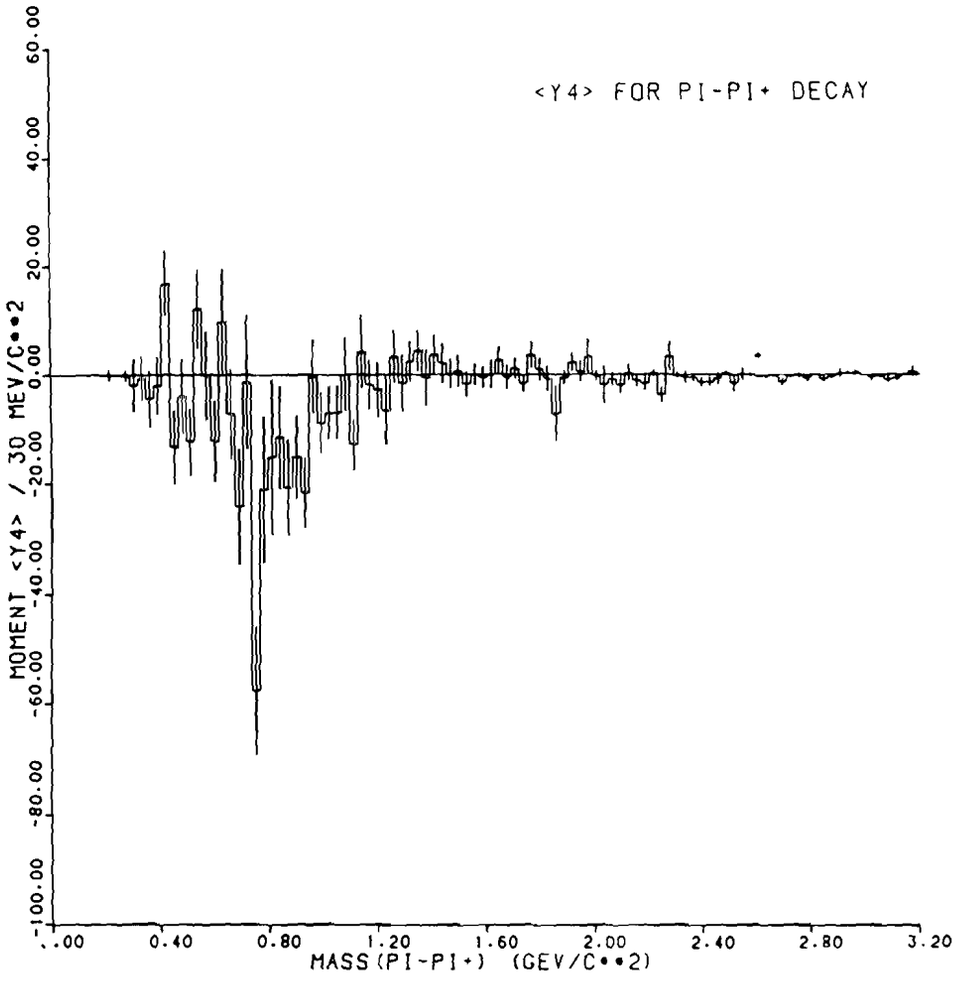

Figure 4.12(d): Moments of spherical harmonic Y_4^0 vs. Mass($\pi^-\pi^+$). Two entries per event.

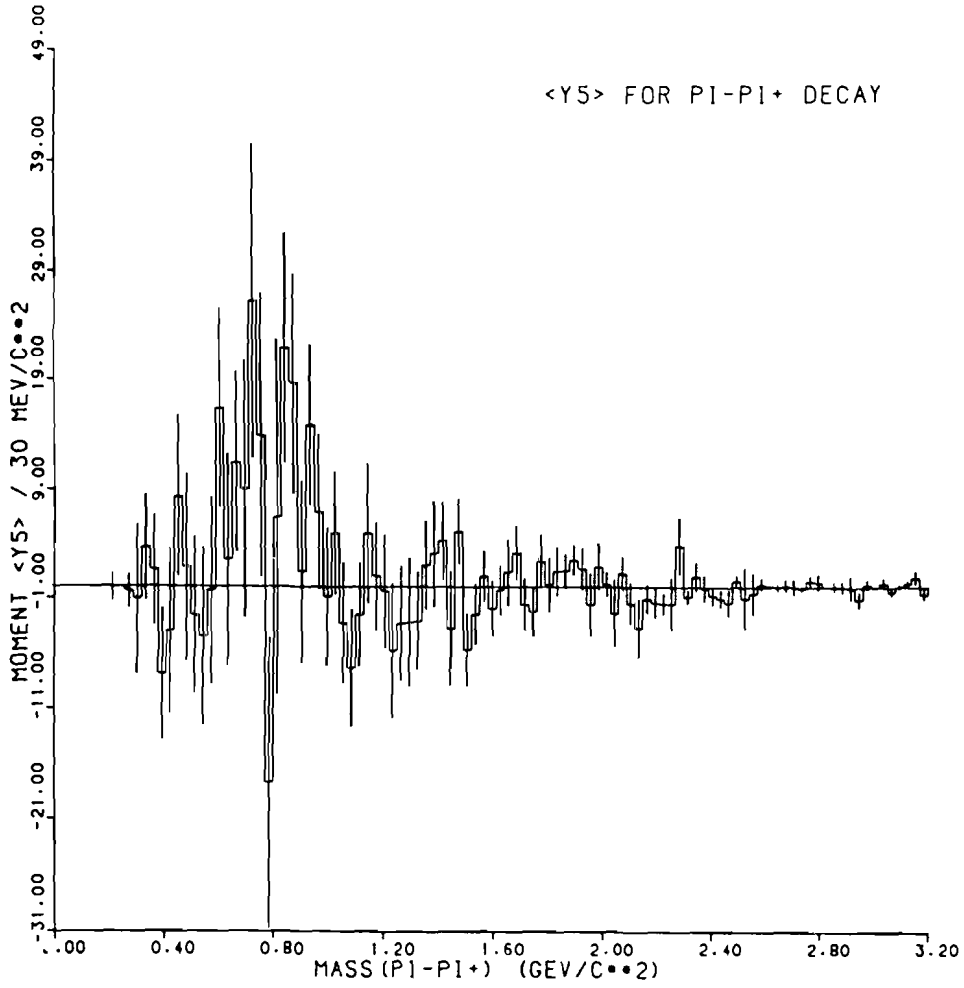

Figure 4.12(e): Moments of spherical harmonic Y_5^0 vs. Mass($\pi^-\pi^+$). Two entries per event.

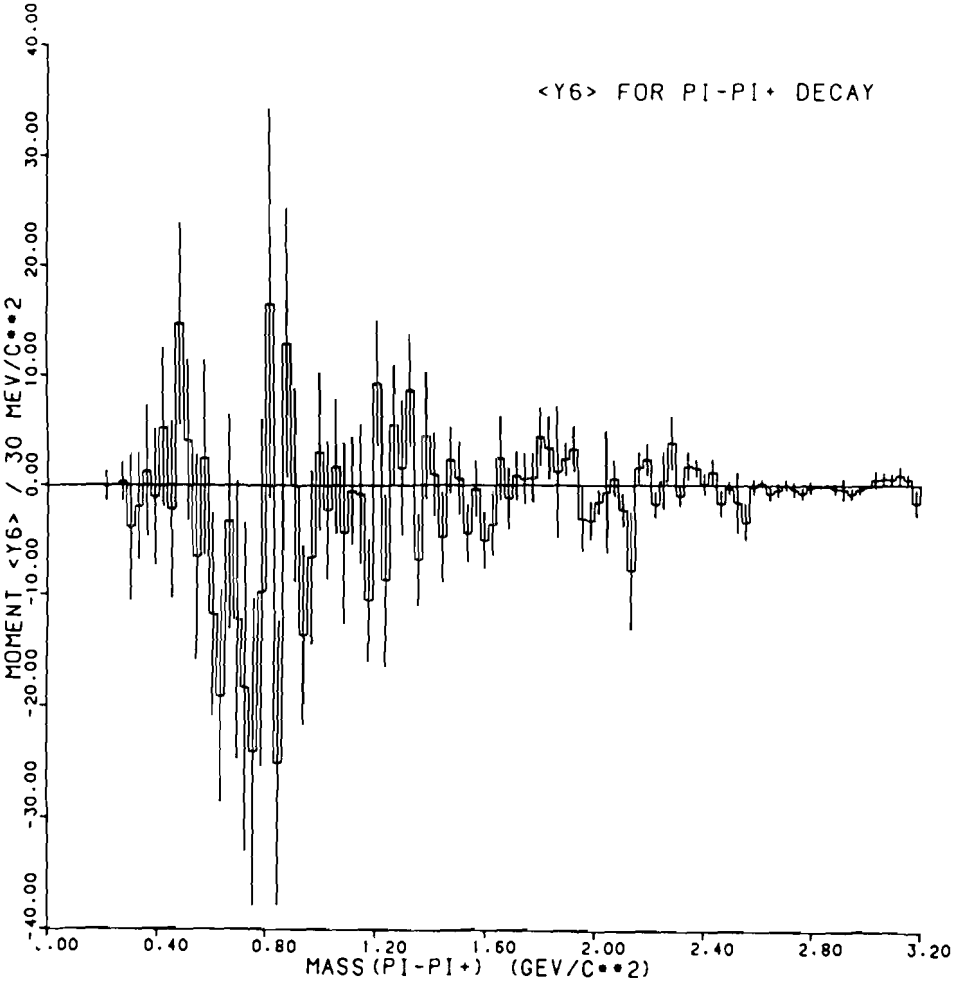

Figure 4.12(f): Moments of spherical harmonic Y_6^0 vs. Mass($\pi^-\pi^+$). Two entries per event.

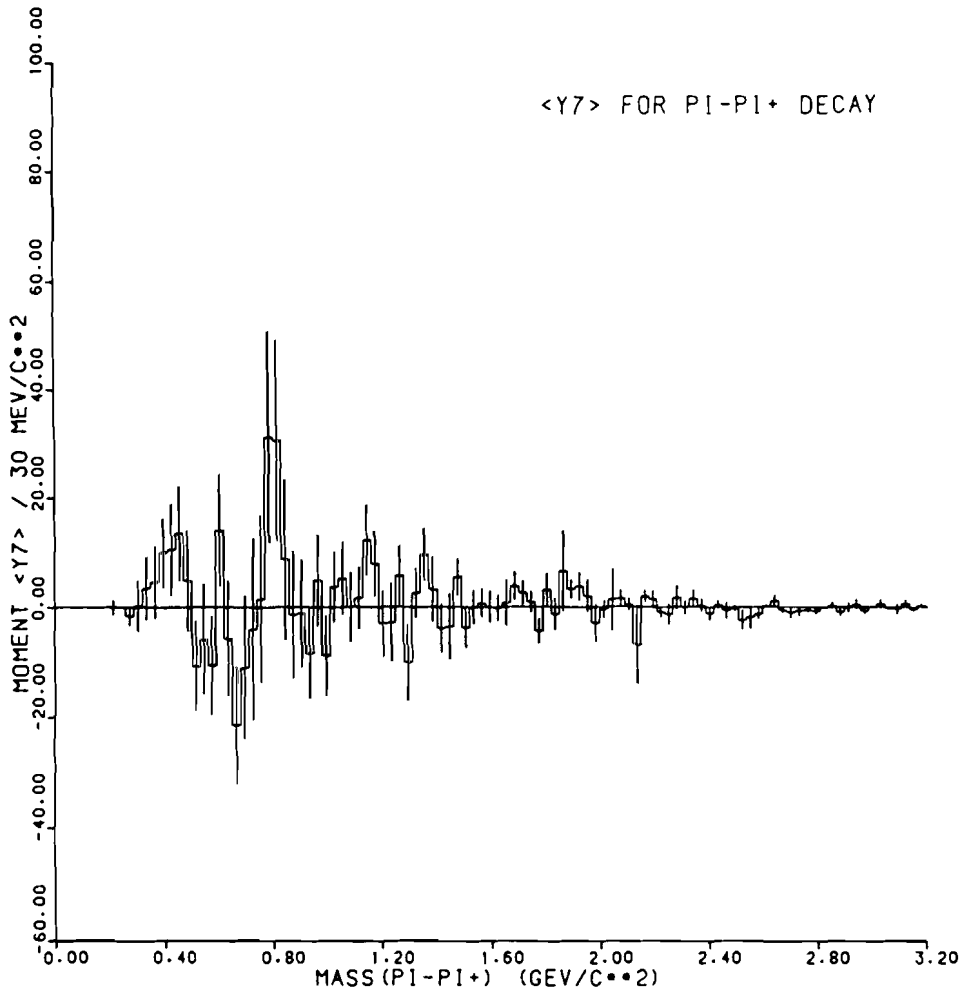

Figure 4.12(g): Moments of spherical harmonic Y_7^0 vs. Mass($\pi^-\pi^+$). Two entries per event.

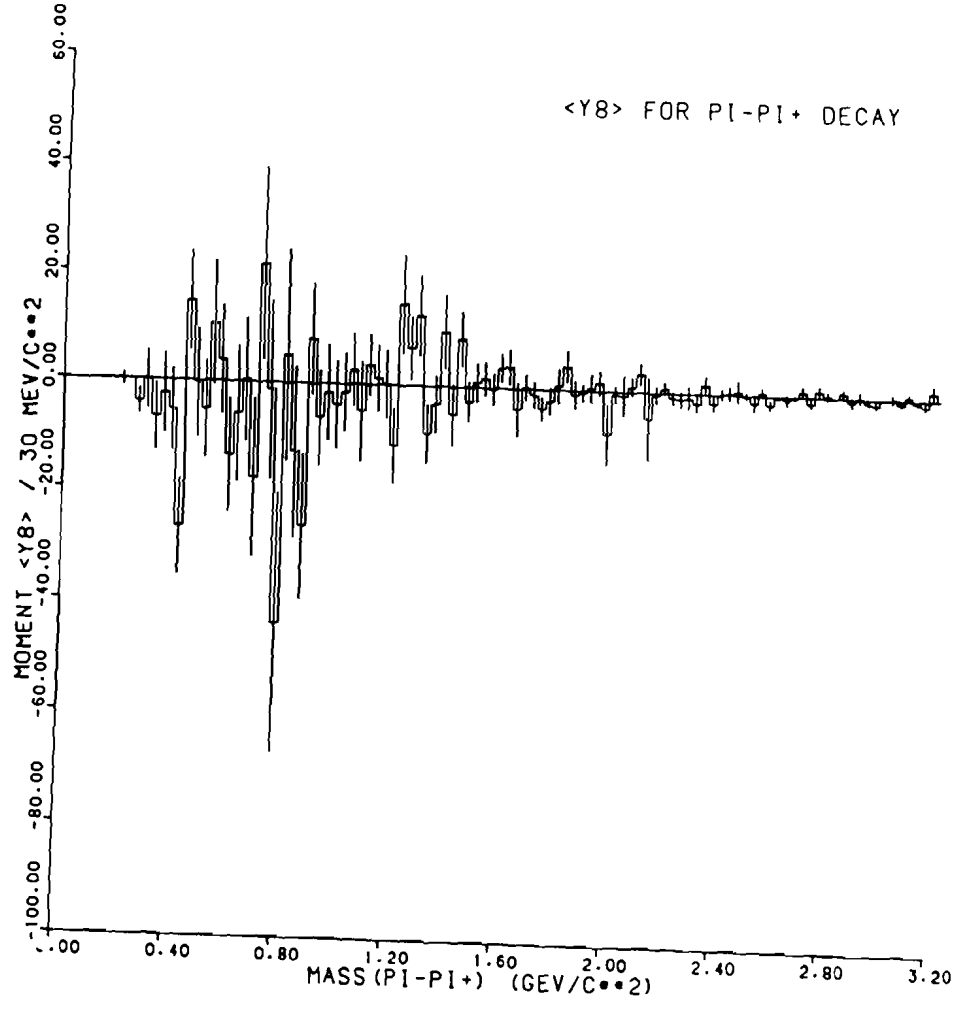

Figure 4.12(h): Moments of spherical harmonic Y_8^0 vs. Mass($\pi^-\pi^+$). Two entries per event.

It should be noted that Y_0^0 is a constant function, and so plotting moments of Y_0^0 is the same as merely plotting the effective mass.

$\langle Y_1^0 \rangle$ shows clear activity (a signal inconsistent with zero over several bins) between about 470 and 1130 MeV/c^2, and $\langle Y_2^0 \rangle$ shows activity between about 320 and 770 MeV/c^2, with indications of activity going up to 1100 MeV/c^2. This could be taken as evidence of an object of nonzero spin in that mass region. $\langle Y_3^0 \rangle$ and all higher moments show no clear activity in any mass region, so we may conclude that there is an object of spin greater than 0 and consistent with 1 roughly in the region between 470 and 1100 MeV/c^2, which would be the ρ^0. There is no evidence in the f^0 region for a spin 2 object.

4.2.4 ρ^0 and f^0 Cuts

It is desirable for purposes of later analysis to have a well-defined cut for each of the ρ^0 and f^0. Specifically, one needs to define a mass region corresponding to the ρ^0 and the f^0, and also determine which $\pi^-\pi^+$ pair to use if both combinations happen to lie within the appropriate mass region. This is to avoid having double entries for some events and not others. In practice, this is only used in plotting moments of

$Y_L(\cos\theta_J)$ of the 3π system with a p cut, and only 20% of the events containing ρ^o's have them for both $\pi^-\pi^+$ combinations.

To define mass regions for the ρ^o and f^o, we refer to previous papers on the subject, and choose numbers which are both consistent with our values here and with previous work, to invite comparison.

Common choices for a ρ^o region are 660 to 860 MeV/c^2 (Brick 1983, Kitagaki 1982, Thompson 1974b), 665 to 865 MeV/c^2 (Ascoli 1973, Beketov 1978), and 670 to 870 MeV/c^2 (Brick 1980). All are consistent with these results of the mass and width of the ρ^o, the latter most so. Thus, the ρ^o is defined to be a $\pi^-\pi^+$ combination with an effective mass lying between 670 and 870 MeV/c^2.

The most common choice for an f^o mass region, as best as can be determined, is 1140 to 1360 MeV/c^2 (Ascoli 1973, Thompson 1974b). As this is consistent with our findings of the f^o mass and width, we choose to adopt it.

Now we must choose a criterion for deciding which $\pi^-\pi^+$ combination is a ρ^o or an f^o, should both combinations fall into the correct mass region. To decide this, we look in Fig. 4.13 at a Dalitz plot of $\pi^-(\text{fast})\pi^+$ vs. $\pi^-(\text{slow})\pi^+$, where $\pi^-(\text{fast})$ is the π^- with the larger laboratory momentum, and $\pi^-(\text{slow})$ the other π^-. It may be seen from

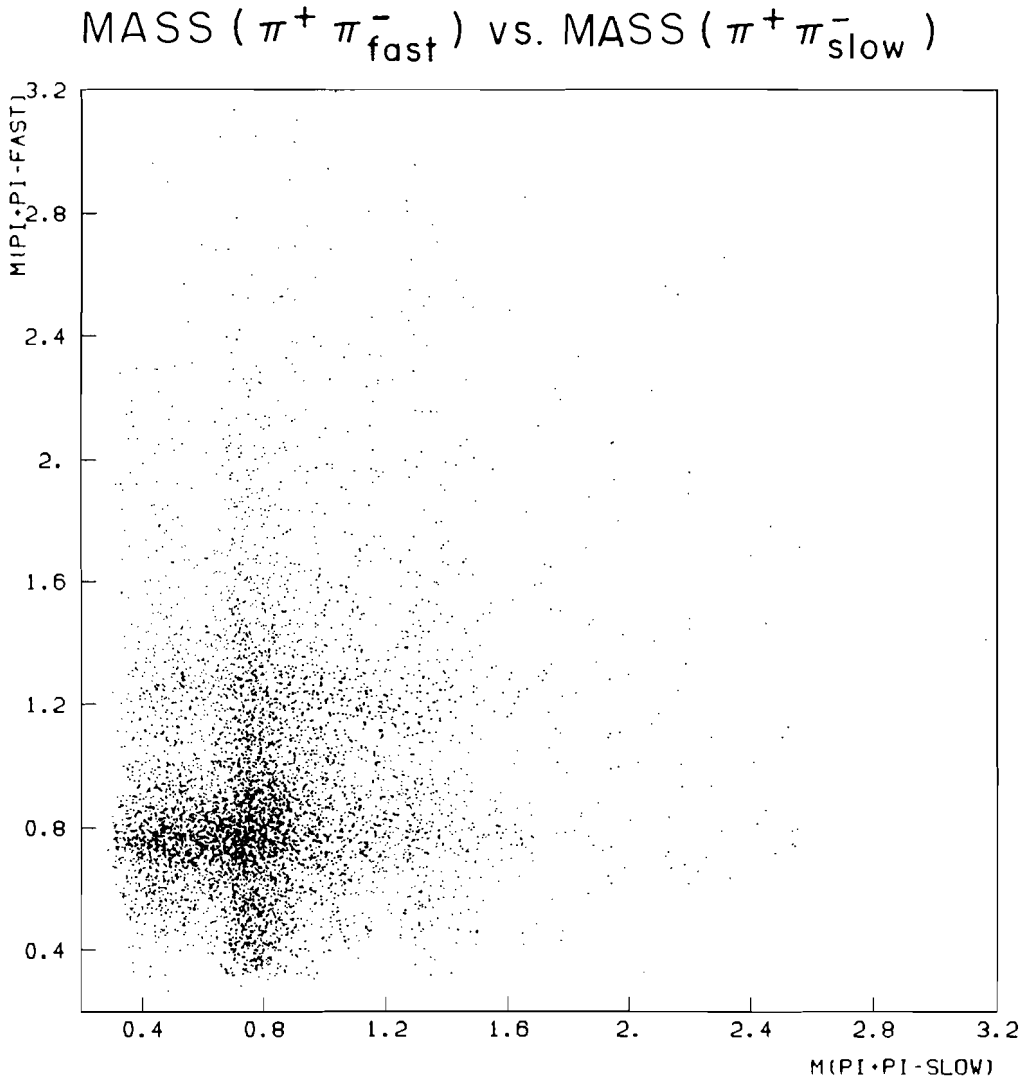

Figure 4.13: Dalitz plot of Mass(π^-(fast)) vs. Mass(π^-(slow)).

Fig. 4.13 and its projections in Fig. 4.14(a-b) that the f^o appears mostly in the π^-(fast)π^+ spectrum. The ρ^o band in π^-(fast)π^+ stops at roughly 900 MeV/c^2 in π^-(slow)π^+, while the ρ^o band in π^-(slow)π^+ extends to high masses in π^-(fast)π^+. Further, the $\rho^o\rho^o$ intersection region appears to be roughly the sum of the intersecting ρ^o bands. Based on these observations, especially the apparent absence of f^o in π^-(slow)π^+ and a desire to have the same cut criteria for both ρ^o and f^o, it is chosen that, in the case of both $\pi^-\pi^+$ combinations lying in the appropriate mass region, the one to be chosen will be the one from the π^-(fast)π^+ combination.

4.3 Three Pion Data Sample

Fig. 4.15 shows the invariant effective mass of $\pi^-\pi^-\pi^+$ for the 7205 events, in 50 MeV/c^2 bins in accordance with resolution, and weighted for acceptance. We see a clear enhancement in the region 950 to 1550 MeV/c^2, with a smaller enhancement in the region 1550 to 1900 MeV/c^2. These may be termed the A_1/A_2 and A_3 regions, respectively.

As was discussed in the Sec. 1.2, the A_1 and A_3, while well-established resonances, are <u>not</u> purely Breit-Wigner, but rather a Breit-Wigner interfering with a Drell-Hiida-Deck background. The A_2 <u>is</u> a normal

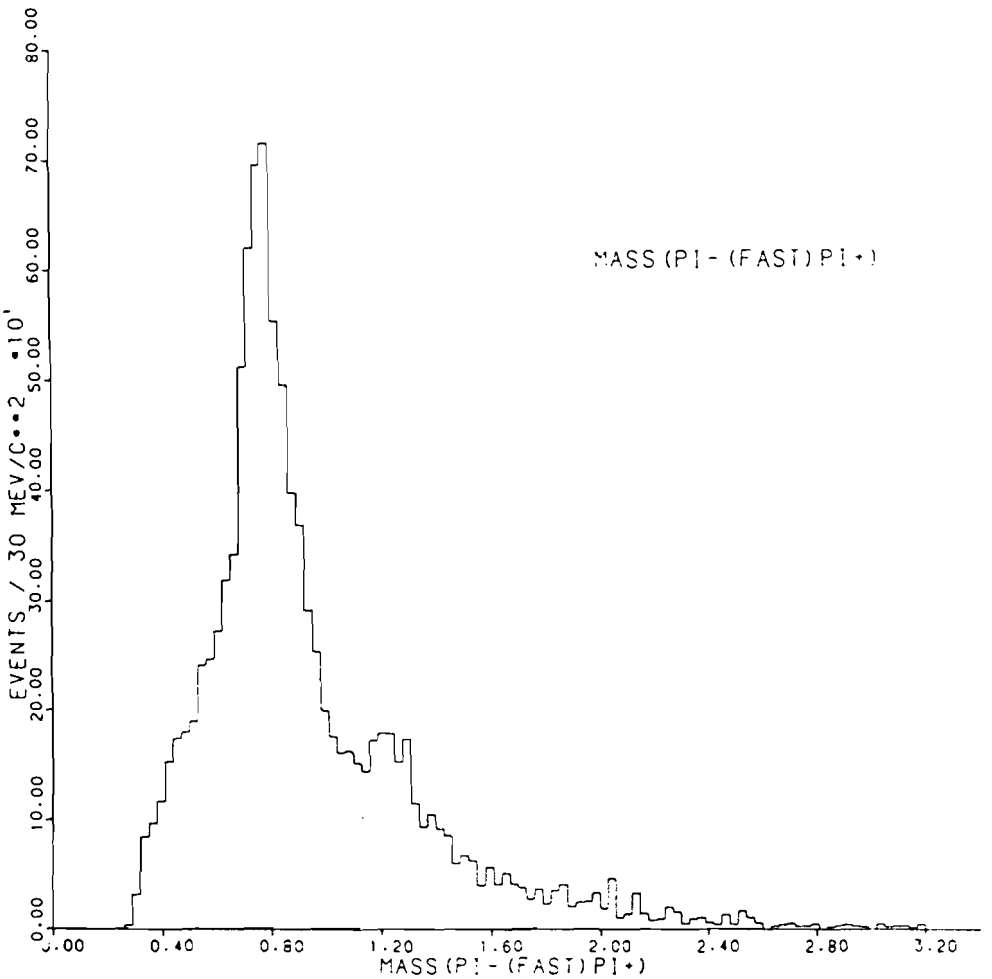

Figure 4.14(a): Effective mass of π^-(fast)π^+ combinations. One entry per event.

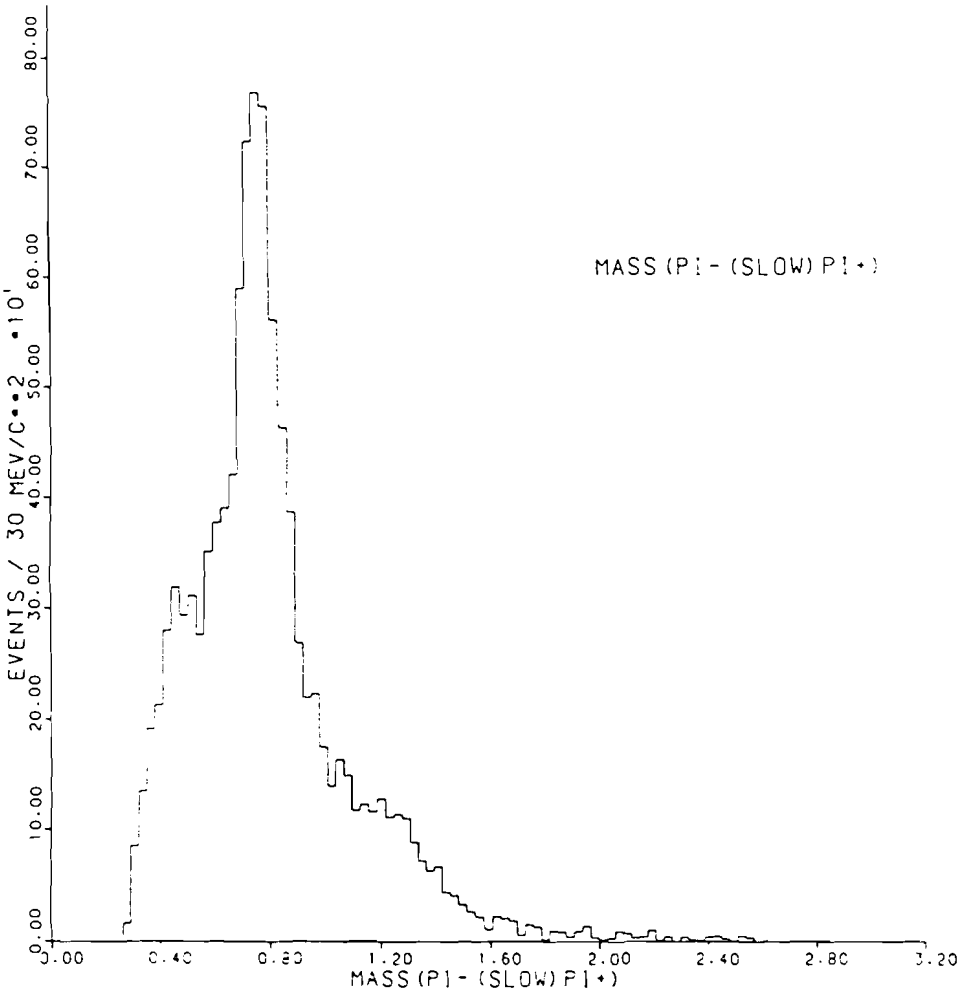

Figure 4.14(b): Effective mass of π^-(slow)π^+ combinations. One entry per event.

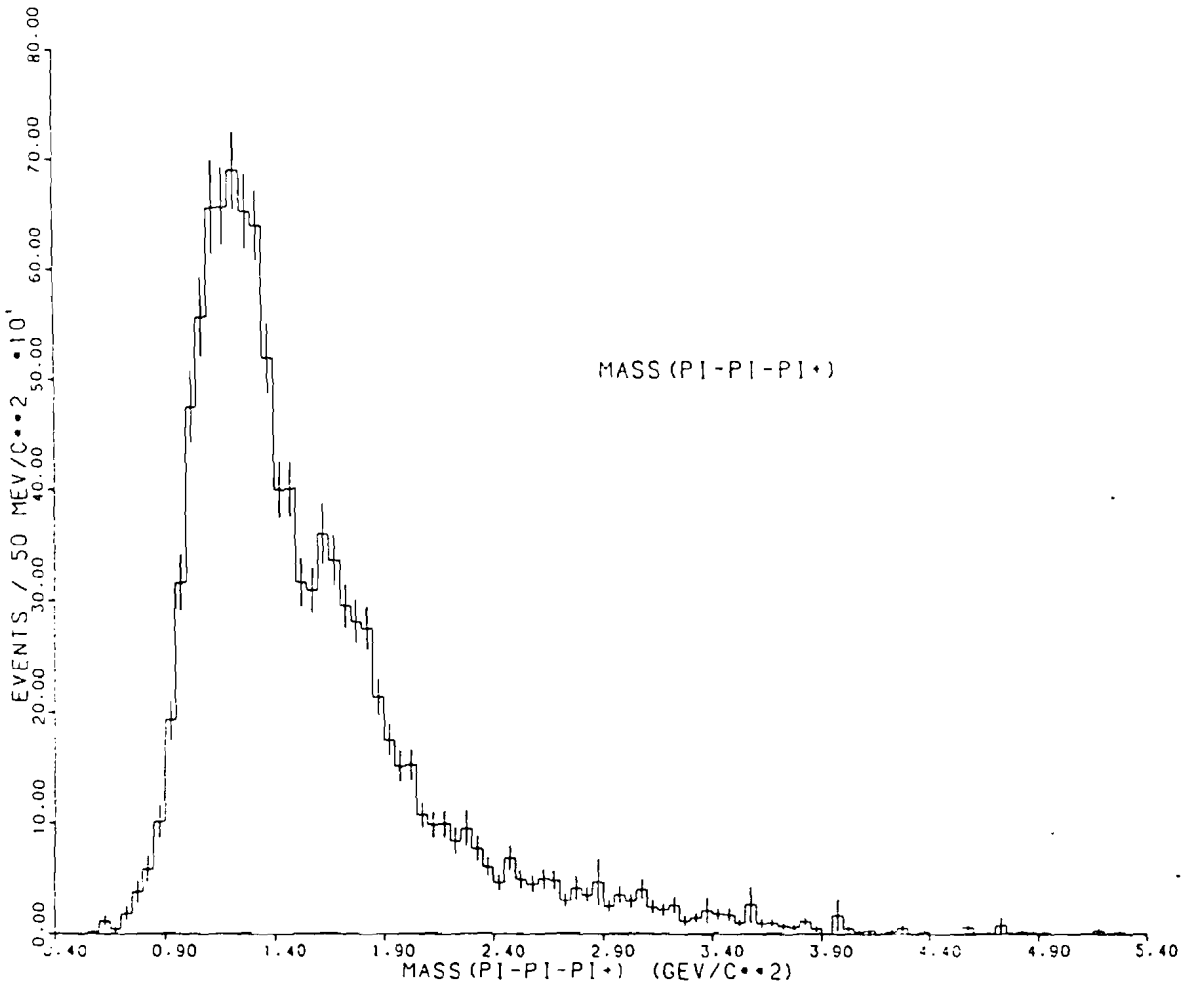

Figure 4.15: Effective Mass of $\pi^-\pi^-\pi^+$ combinations.

One entry per event.

Breit-Wigner resonance, but it is buried at the high end of the A_1 mass region. Thus, it is not possible to merely fit the 3π mass spectrum to a background plus three Breit-Wigner resonance terms.

4.3.1 M(3π) Spectrum with f^o Cut

The simplest structure to look at here is the A_3. It has been established that the A_3^- has a branching fraction to $f^o\pi^-$ of 53 ± 5% (PDG 1986), whereas the A_1 and A_2 do not decay to $f^o\pi^-$ (PDG 1986). Thus, if a cut is made on the f^o in the $\pi^-\pi^+$ mass, specifically that $1140 < M(\pi^-\pi^+) < 1360$ MeV/c^2, we can presumably isolate the A_3^-. Figure 4.16 shows this distribution, using acceptance-weighted events. If, in spite of the fact that the A_3 is not purely a Breit-Wigner resonance, we fit the distribution to a background plus a Breit-Wigner of spin 2 (as would be expected of the A_3), we get good results.

The background function is similar to that used for the 2π fits, except that the M_T term is allowed to float. It has the form

$$F_{back}(M) = A(M-M_T)^{\alpha}\exp(-\beta M-\gamma M^2)$$

The fit results are as follows:

$$M(A_3^-) = 1688 \pm 17 \text{ MeV}/c^2$$

(Book value 1680 ± 30 MeV/c^2)

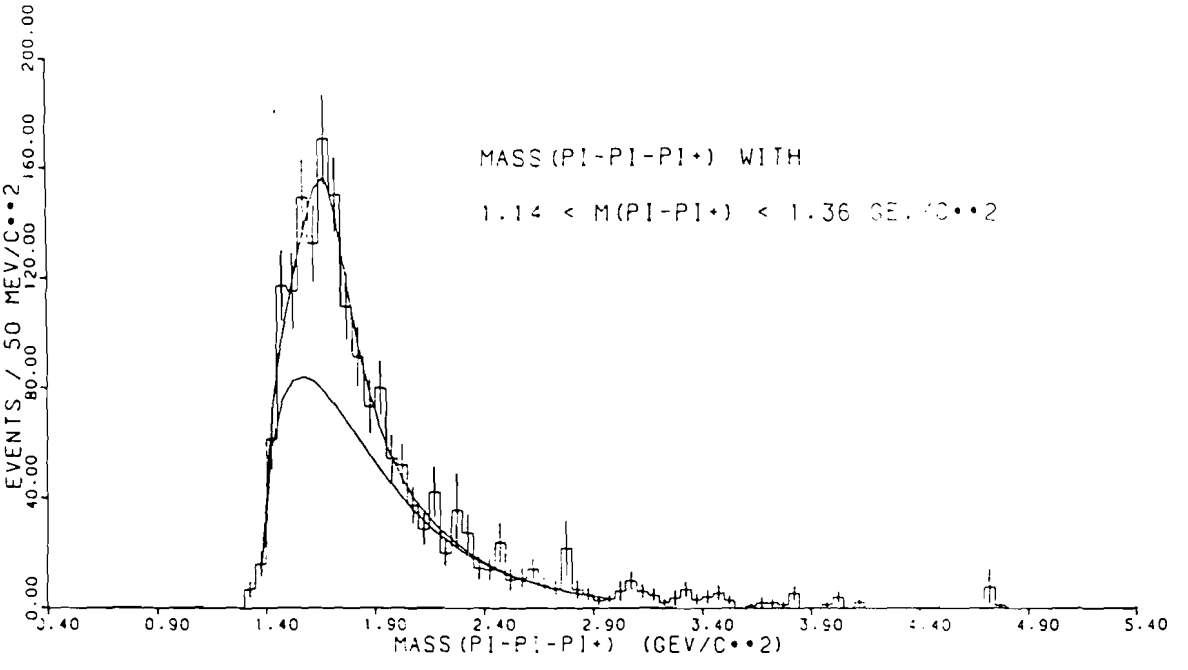

Figure 4.16: Effective Mass of $\pi^-\pi^-\pi^+$ combinations, with 1.14 < Mass($\pi^-\pi^+$) < 1.36 GeV/c^2 (f^0 cut). One entry per event.

$\Gamma(A_3^-) = 293 \pm 39$ MeV/c^2 (Book Value 250 ± 50 MeV/c^2)

$N(A_3^-) = 500 \pm 40$ weighted events

$M_T = 1370 \pm 2$

$A = 70800 \pm 4300$

$\alpha = 0.669 \pm 0.021$

$\beta = 3.789 \pm 0.016$

$\gamma = -0.1187 \pm 0.0066$

$\chi^2/DF = 23.9/25$

This fit has been superimposed on Figure 4.16. Quoted uncertainties correspond to a change of ±1.0 in the total χ^2.

The values for the mass and width of the A_3^- are in good agreement with the established values (PDG 1986). However, we have fit a Breit-Wigner to an object which is known to not be one, so we shall adopt an arbitrary systematic error of 20%. Thus,

$N(A_3^-) = 500 \pm 40 \pm 100$ weighted events

Using the known sensitivity for weighted events of 30.3 ± 8.5 events/μb, we find that

$\sigma(A_3^- \rightarrow f^0\pi^- \rightarrow \pi^-\pi^-\pi^+) =$

16.5 ± 4.8 (stat.) ± 5.7 (syst.) μb/nucleon .

4.3.2 M(3π) Spectrum

Figure 4.17 is a scatterplot of M(3π) vs. $M(\pi^-\pi^+)$, with two combinations per event. We observe a heavy concentration of events at the ρ^0-A_1/A_2 intersection, and also at the ρ^0-A_3 intersection, indicating that both the A_1/A_2 and A_3 enhancements have decay modes which include the ρ^0. There is a slight concentration at the f^0-A_3^- intersection, showing that the A_3^- does indeed decay into $f^0\pi^-$, as discussed above.

Figure 4.15 shows the M(3π) distribution with weighted events, and Figure 4.18 shows M(3π) with a cut on the ρ^0 mass in $M(\pi^-\pi^+)$, requiring $670 < M(\pi^-\pi^+) < 870$ MeV/c^2. In the former distribution both the A_1/A_2 and A_3 enhancements are evident, while in the latter only the A_1/A_2 enhancements is readily apparent, presumably due to the low (34 ± 6%) branching fraction of $A_3^- \rightarrow \rho^0\pi^-$ (PDG 1986). Numerous fits have been attempted to these distributions, consisting of both background plus two Breit-Wigners (A_1/A_2 and A_3) and background plus three Breit-Wigners (a separate Breit-Wigner for each 3π enhancement). These fits turn out to be very sensitive to the precise limits placed upon the mass and width of the A_1, and return a number of events in the A_1/A_2 peak ranging from 370 (with limits very tight) to 5900 (with loose limits, in which the A_1/A_2 Breit-Wigner attempts to account for the entire peak). Clearly, it is

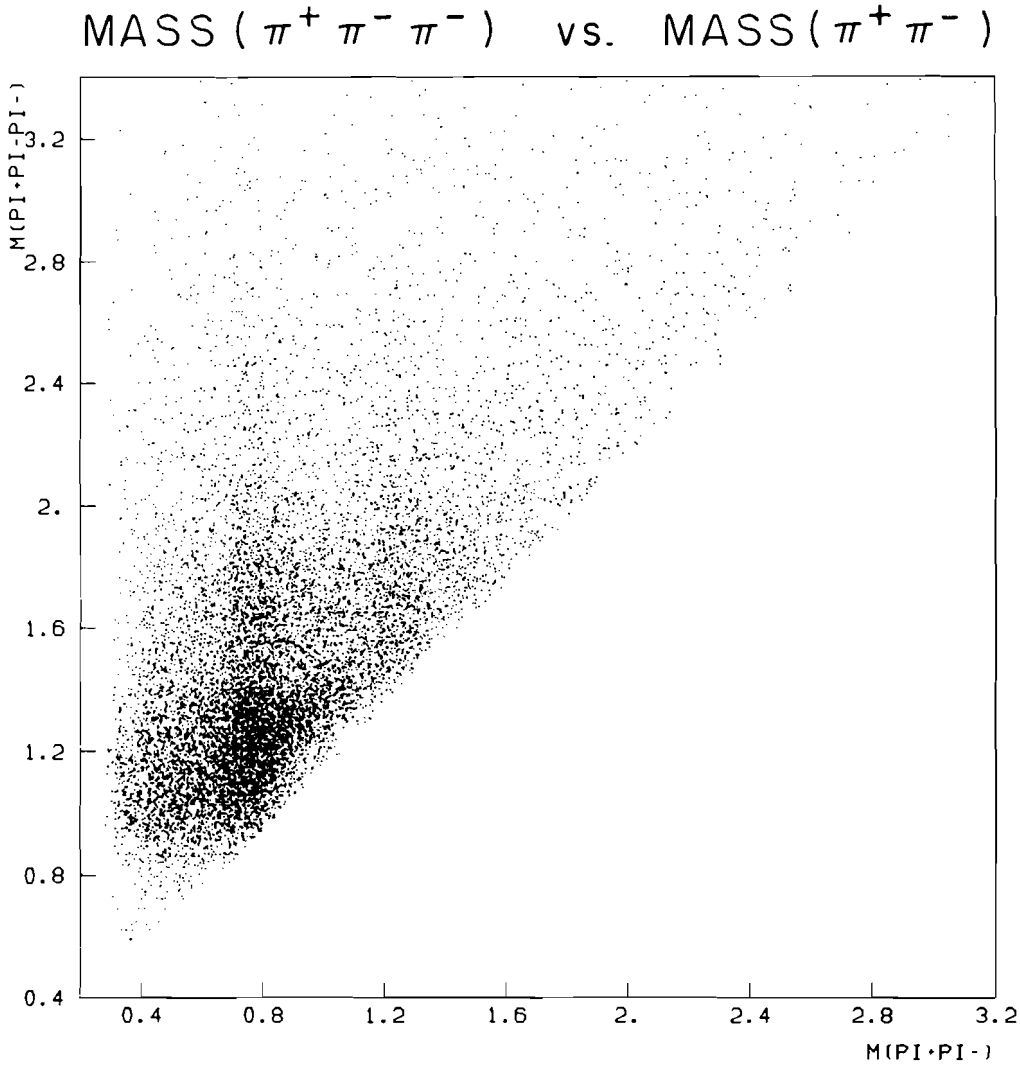

Figure 4.17: Scatterplot of Mass($\pi^-\pi^-\pi^+$) vs. Mass($\pi^-\pi^+$).

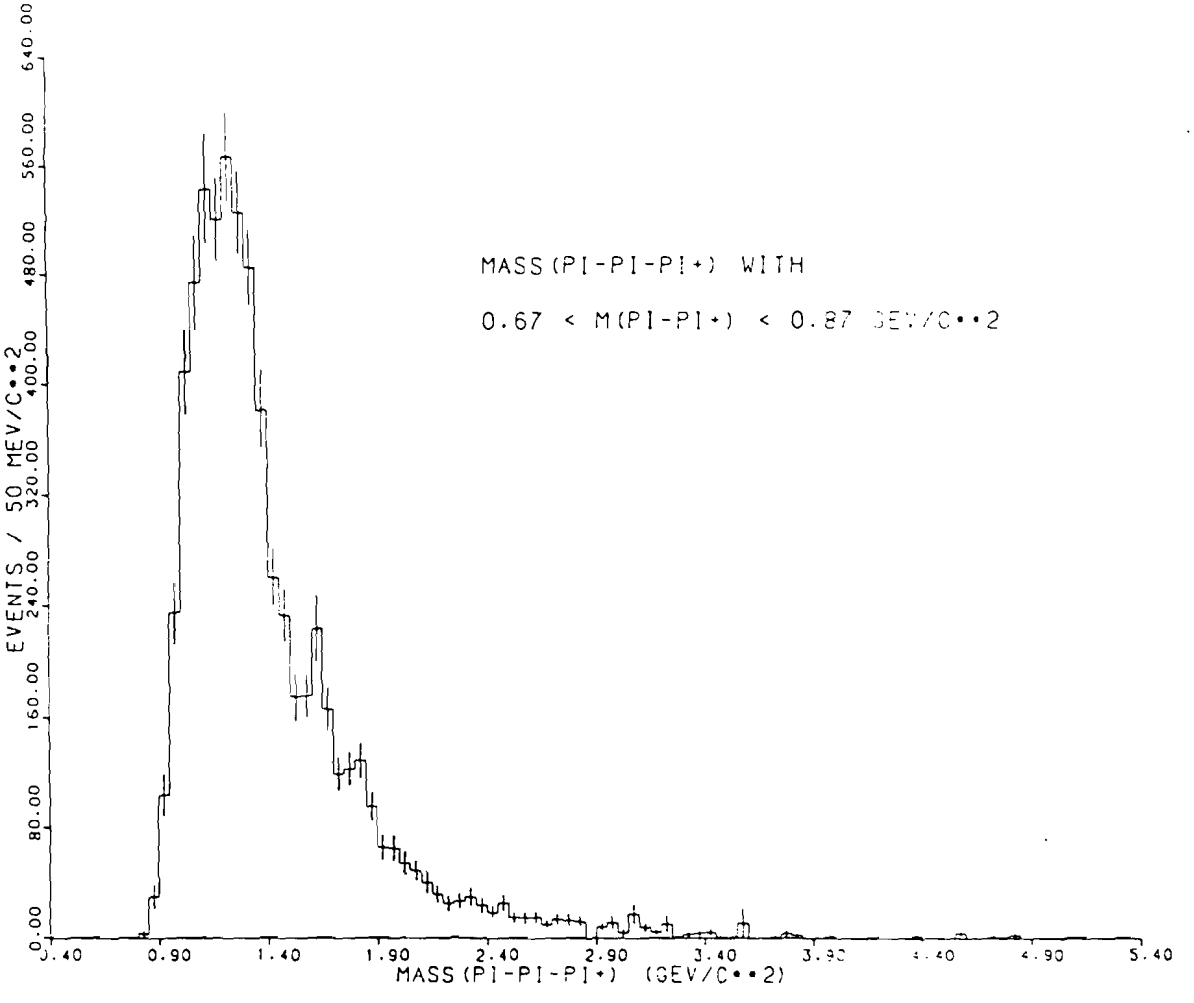

Figure 4.18: Effective Mass of $\pi^-\pi^-\pi^+$ combinations, with $0.67 < \mathrm{Mass}(\pi^-\pi^+) < 0.87$ GeV/c^2 (ρ^0 cut). One entry per event.

not possible to pin down precise values for the number of A_1 and A_2 events in the sample, save to give cross section numbers per nucleon for various mass bins, as done in Section 4.1.

4.3.3 3π Spin Analysis

Since it is not possible to pin down precise values for the number of events in the A_1/A_2 enhancements, is it possible to at least determine that the enhancements contain objects of the correct spin? The A_1 is known to be a $J^P = 1^+$ object, and the A_2 and A_3 are 2^+ and 2^-, respectively.

Fig. 4.19(a-h) shows the moments of the first eight spherical harmonics $\langle Y_L^0 \rangle$ vs. $M(3\pi)$ for $M(3\pi)$ without any cuts, and Fig. 4.20(a-h) shows $\langle Y_L^0 \rangle$ vs. $M(3\pi)$ for $670 < M(\pi^-\pi^+) < 870$ MeV/c^2. $\langle Y_L^0 \rangle$ is defined as follows:

$$\langle Y_L^0 \rangle = \Sigma\ (2L+1)/4\pi \times P_L^0(\cos(\theta_J)) \times \text{weight},$$

where

the summation is over all events,

the P_L^0 are Associated Legendre Polynomials (see App. A),

weight is based on the acceptance of the individual event,

θ_J is the angle in the 3π rest frame between a π^- and

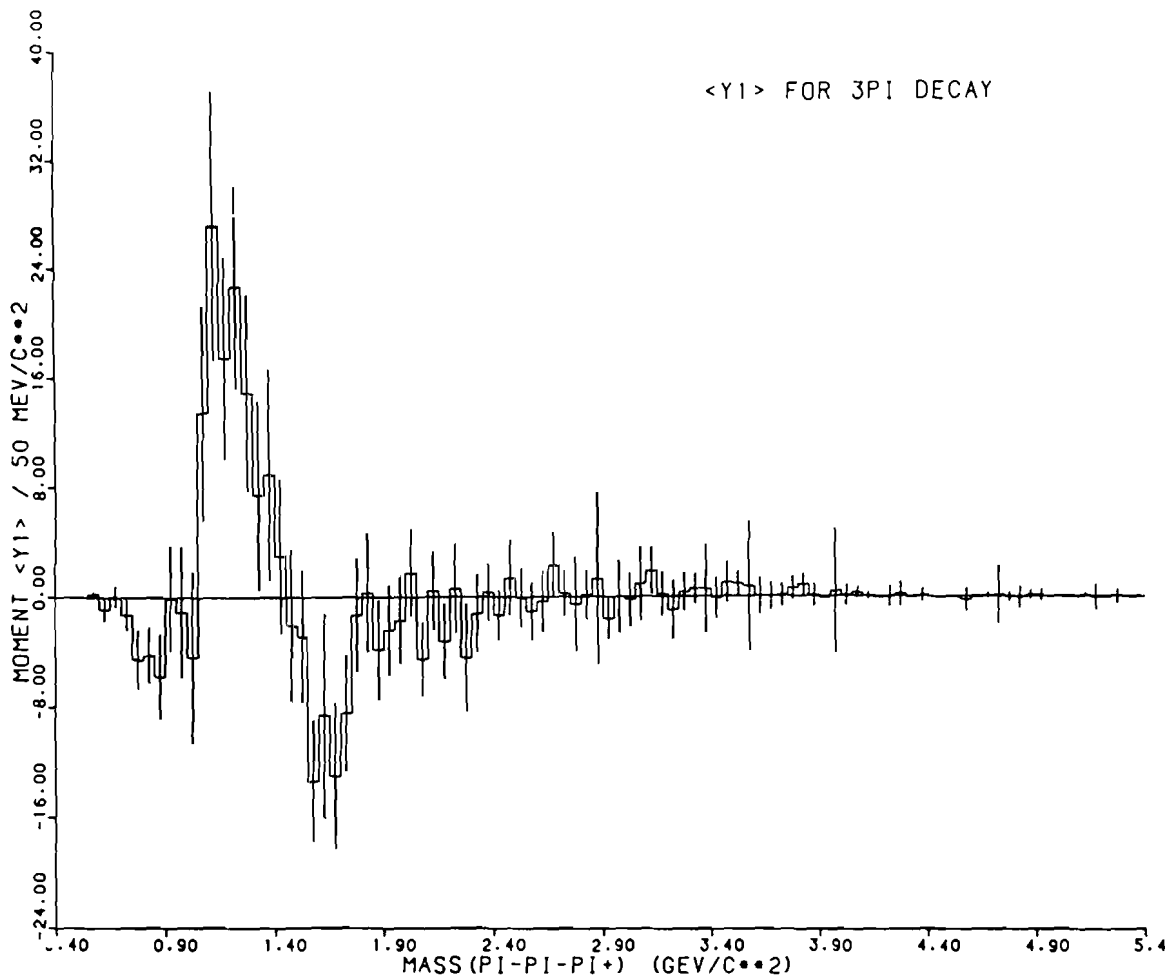

Figure 4.19(a): Moments of spherical harmonic Y_1^0 vs. Mass($\pi^-\pi^-\pi^+$). Two entries per event.

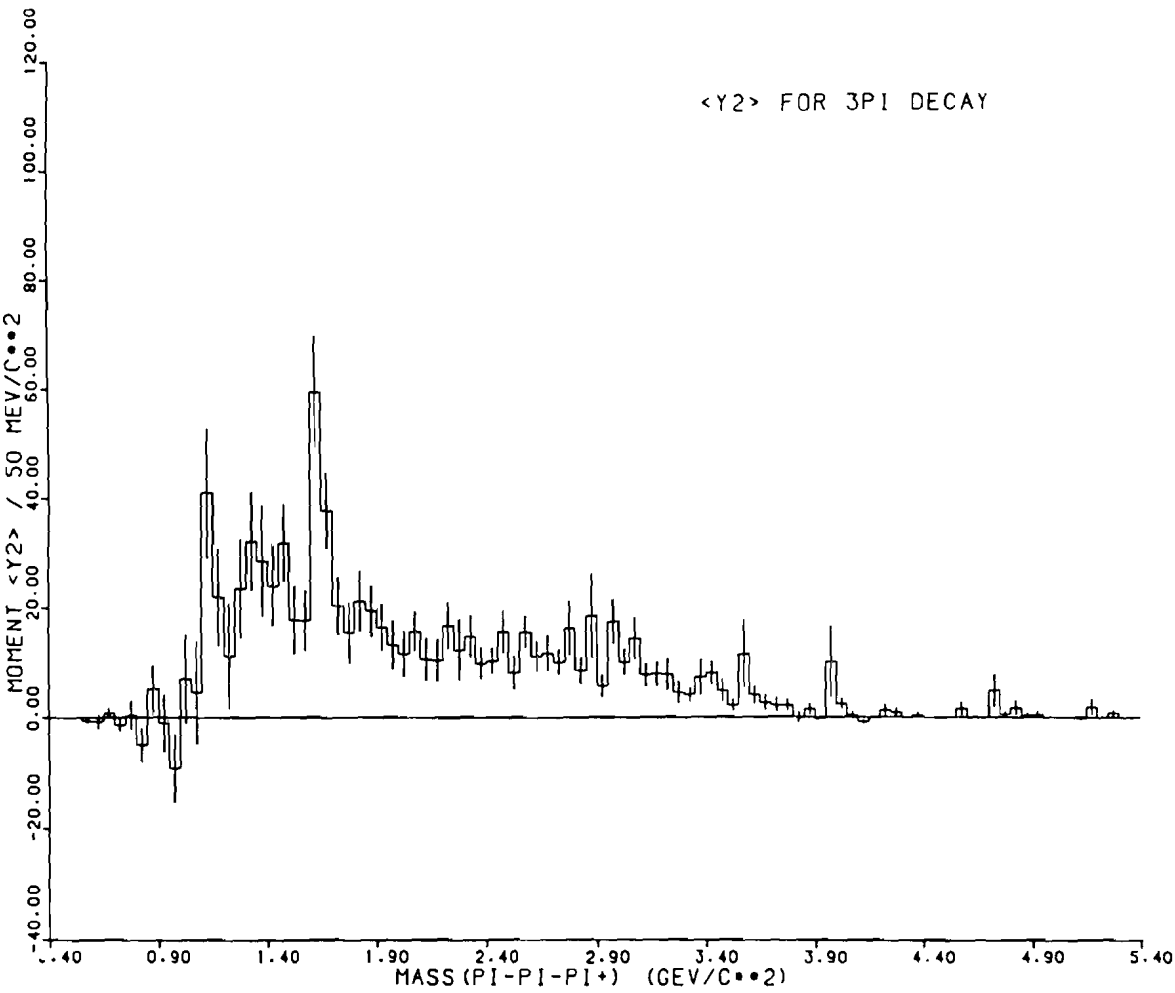

Figure 4.19(b): Moments of spherical harmonic Y_2^0 vs. Mass($\pi^-\pi^-\pi^+$). Two entries per event.

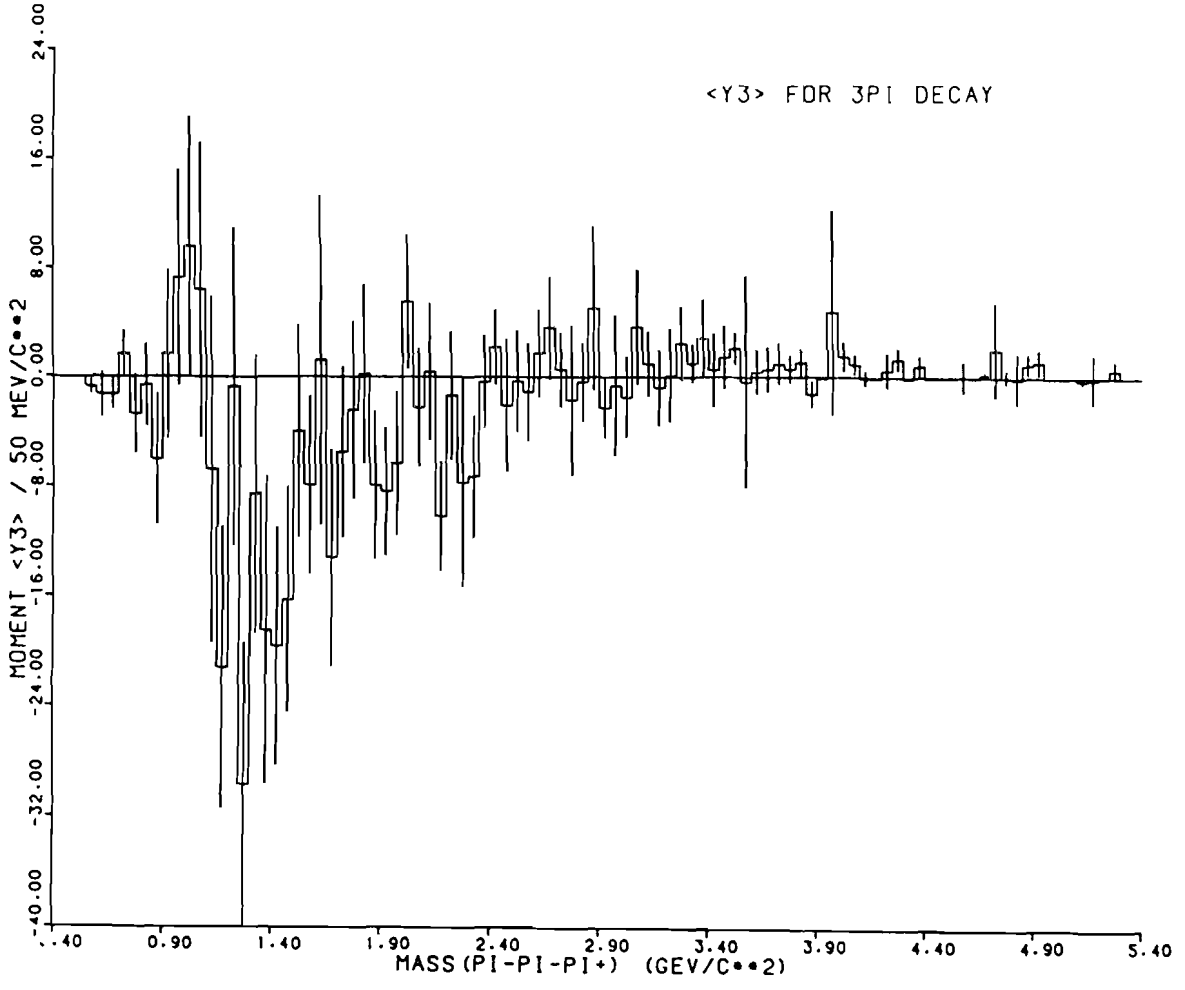

Figure 4.19(c): Moments of spherical harmonic Y_3^0 vs. Mass($\pi^-\pi^-\pi^+$). Two entries per event.

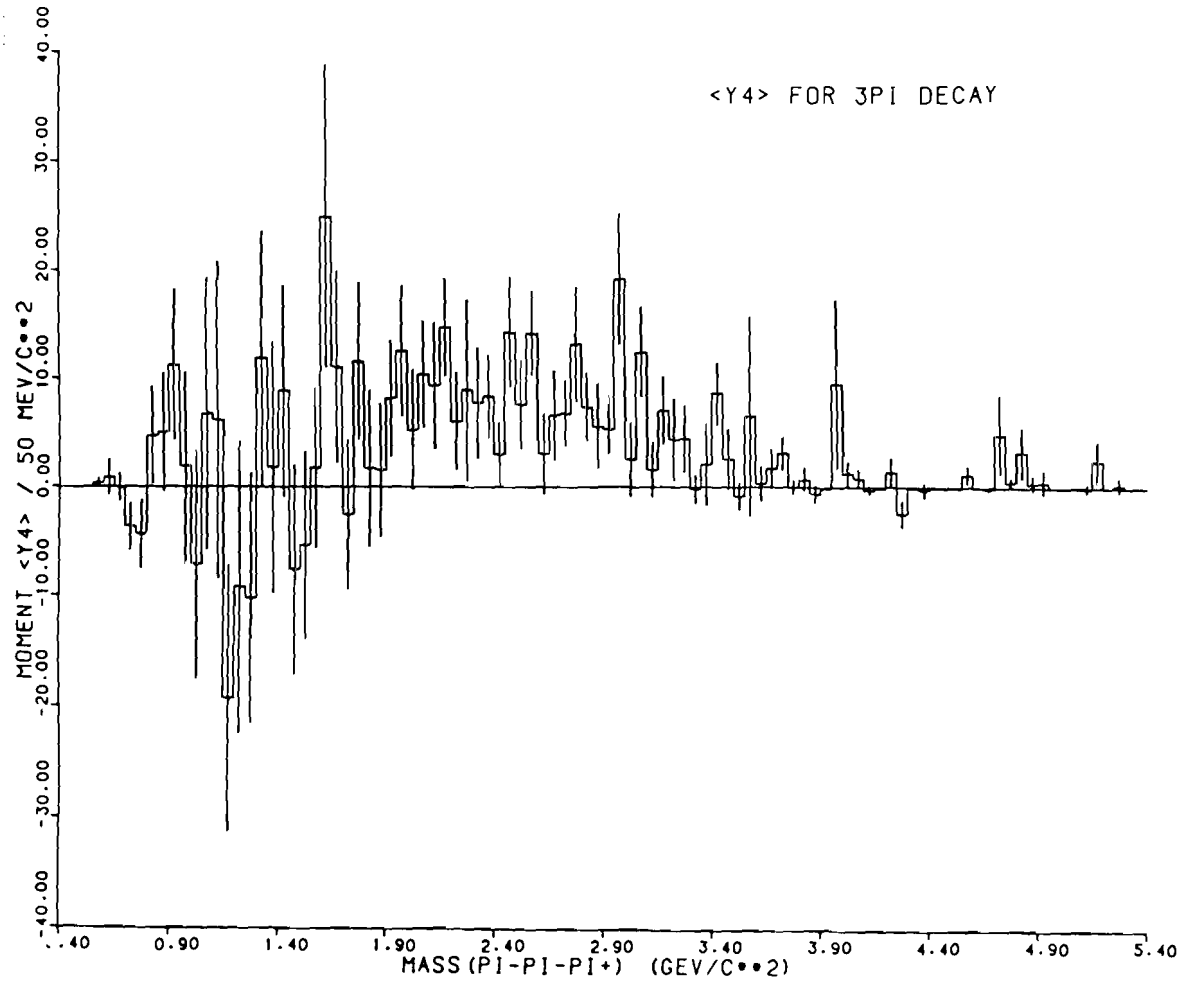

Figure 4.19(d): Moments of spherical harmonic Y_4^0 vs. Mass($\pi^-\pi^-\pi^+$). Two entries per event.

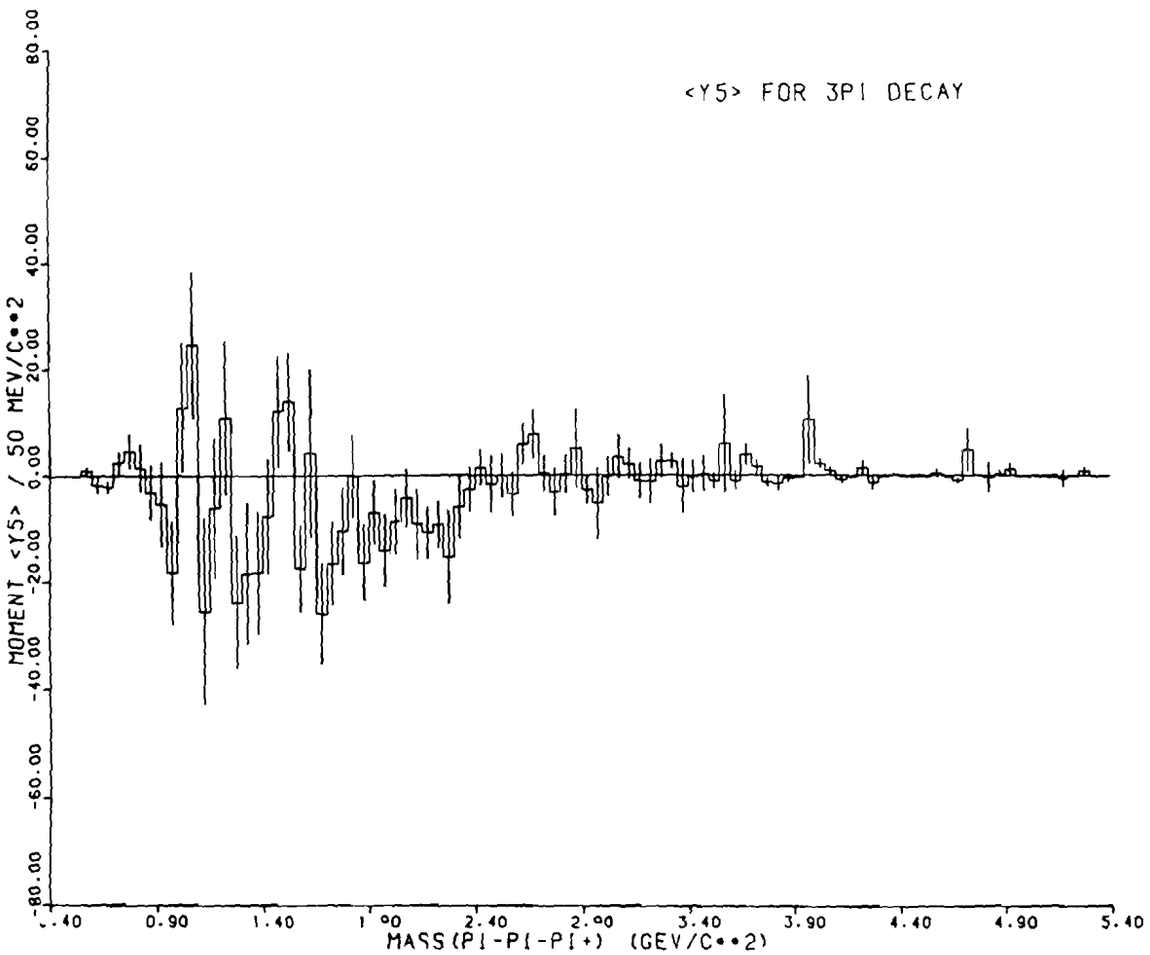

Figure 4.19(e): Moments of spherical harmonic Y_5^0 vs. Mass($\pi^-\pi^-\pi^+$). Two entries per event.

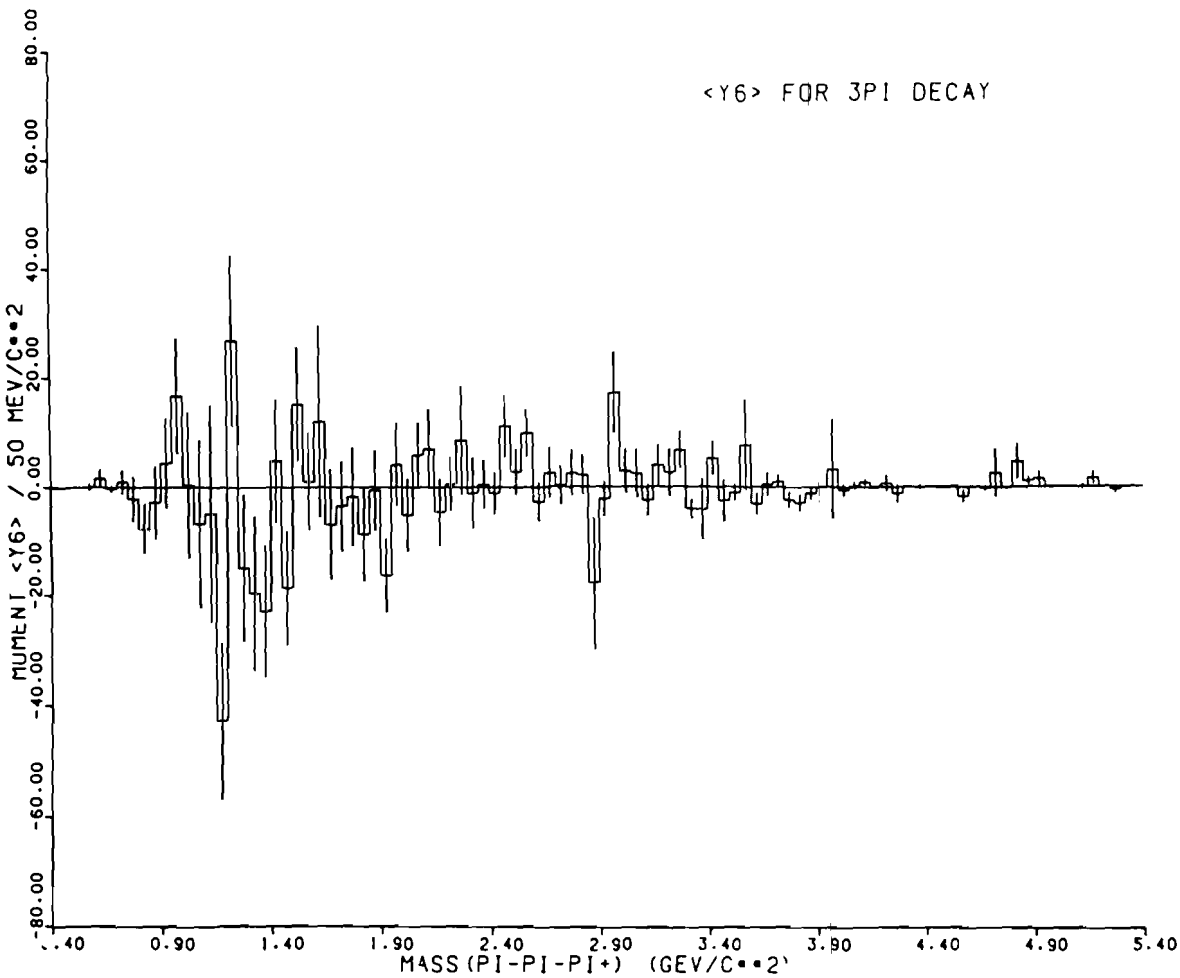

Figure 4.19(f): Moments of spherical harmonic Y_6^0 vs. Mass($\pi^-\pi^-\pi^+$). Two entries per event.

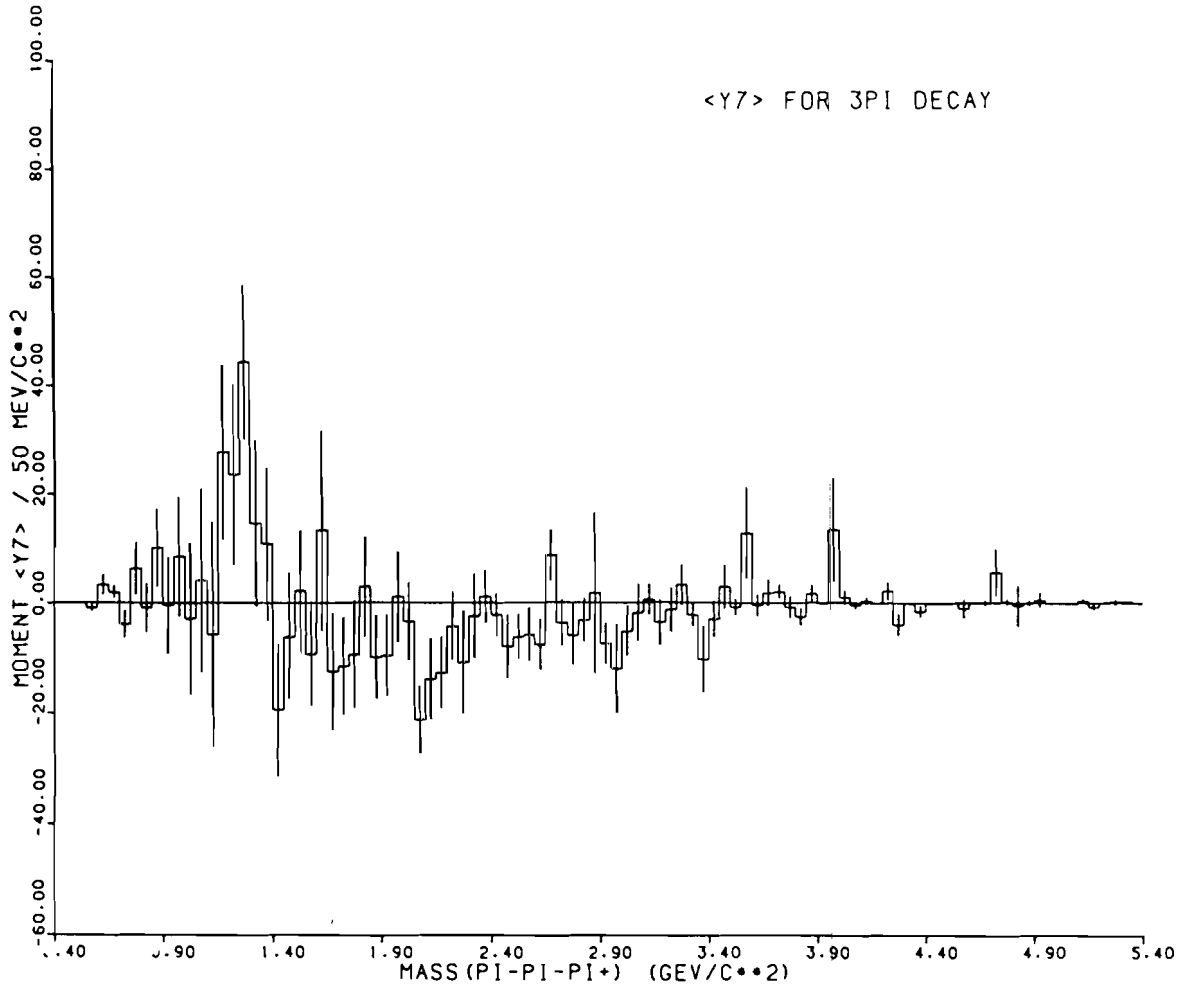

Figure 4.19(g): Moments of spherical harmonic Y_7^0 vs. Mass($\pi^-\pi^-\pi^+$). Two entries per event.

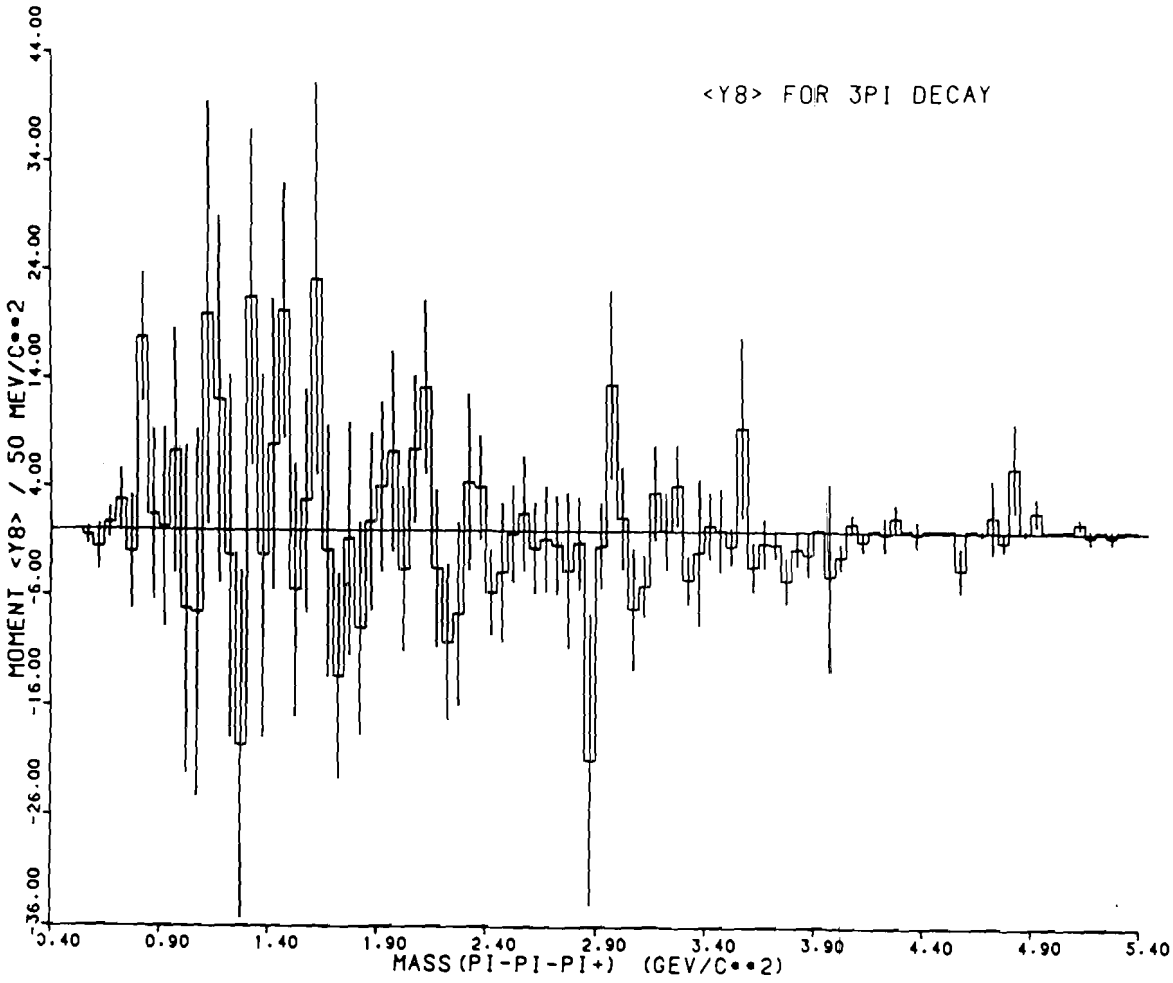

Figure 4.19(h): Moments of spherical harmonic Y_8^0 vs. Mass($\pi^-\pi^-\pi^+$). Two entries per event.

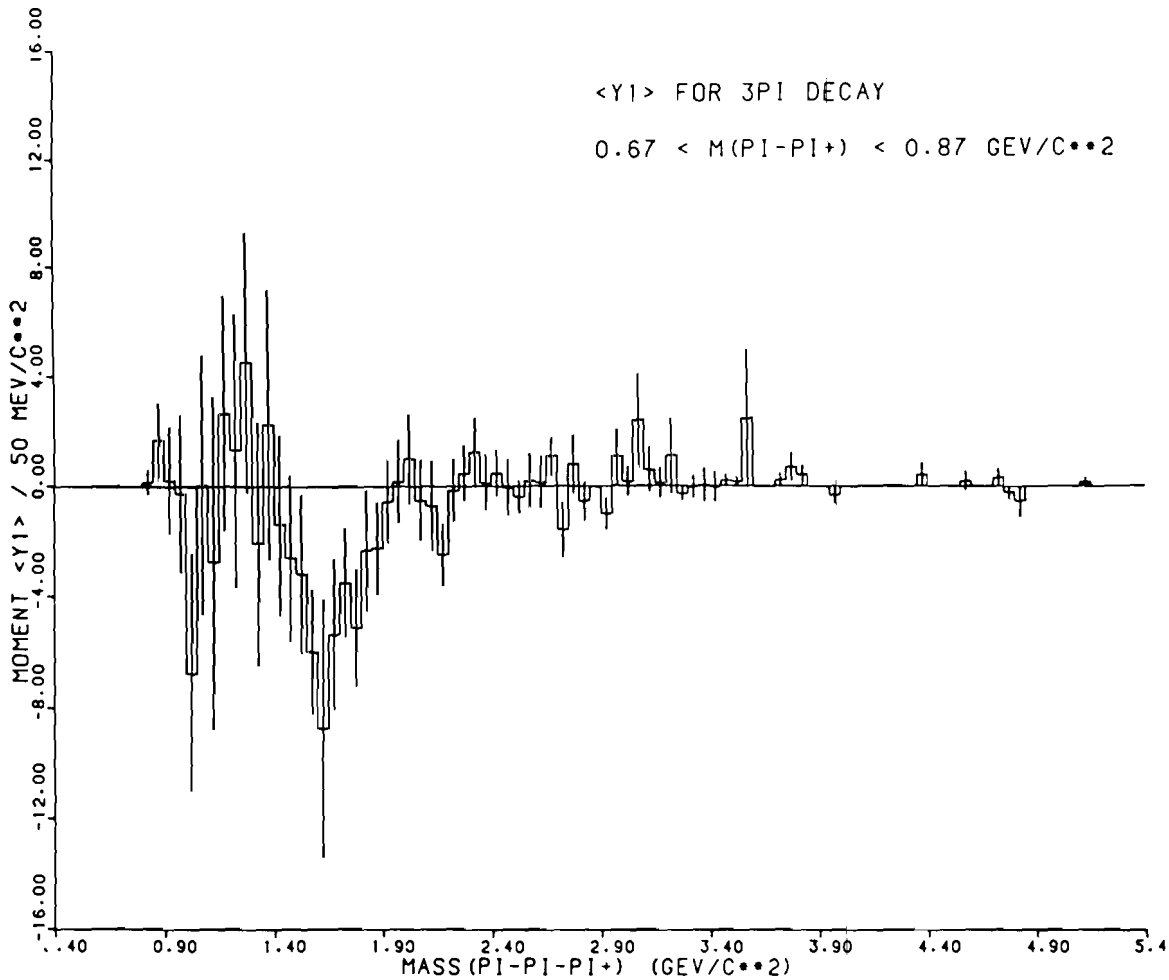

Figure 4.20(a): Moments of spherical harmonic Y_1^0 vs. Mass($\pi^-\pi^-\pi^+$), with $0.67 < \text{Mass}(\pi^-\pi^+) < 0.87$ GeV/c^2. One entry per event.

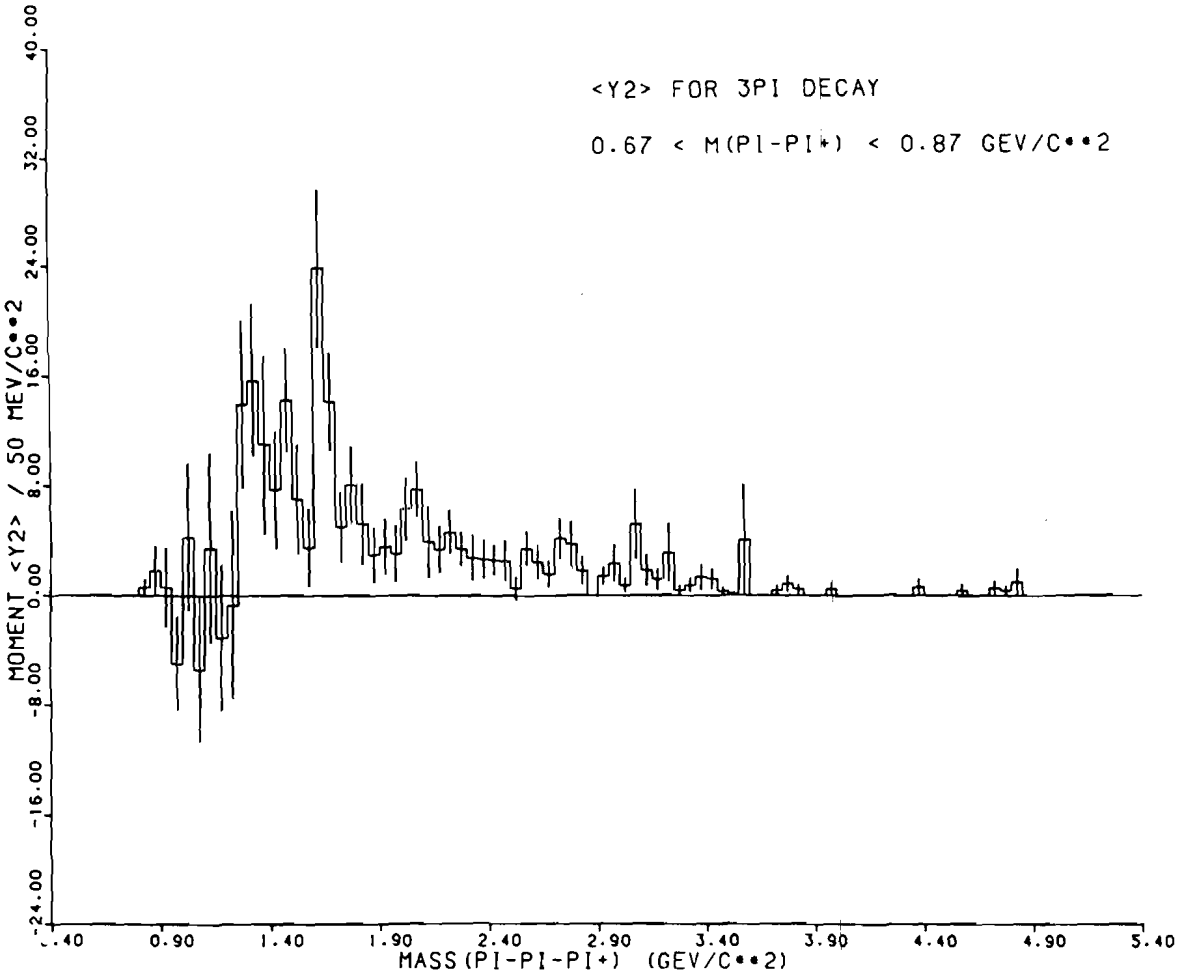

Figure 4.20(b): Moments of spherical harmonic Y_2^0 vs. Mass($\pi^-\pi^-\pi^+$), with $0.67 < \text{Mass}(\pi^-\pi^+) < 0.87$ GeV/c^2. One entry per event.

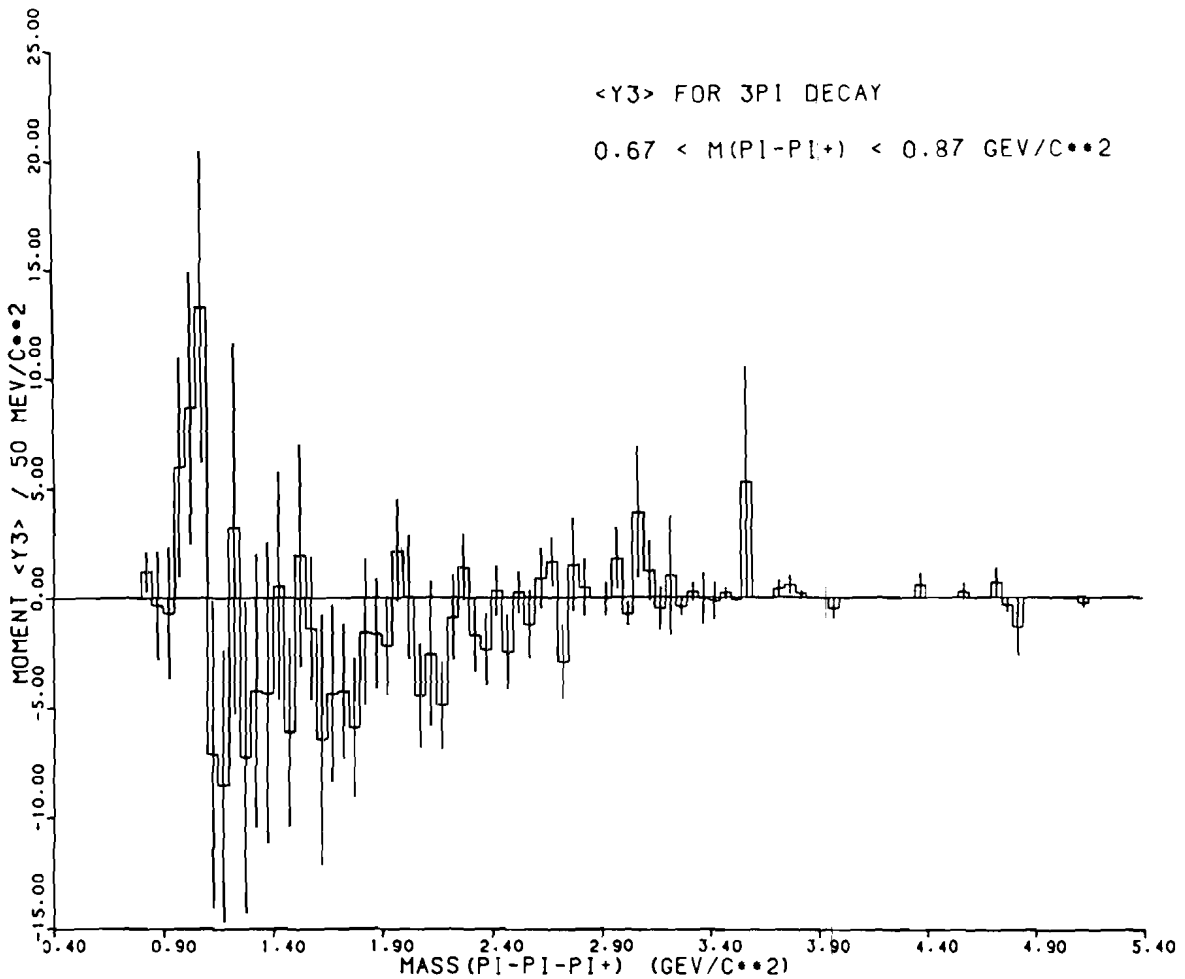

Figure 4.20(c): Moments of spherical harmonic Y_3^0 vs. Mass($\pi^-\pi^-\pi^+$), with $0.67 < \text{Mass}(\pi^-\pi^+) < 0.87$ GeV/c^2. One entry per event.

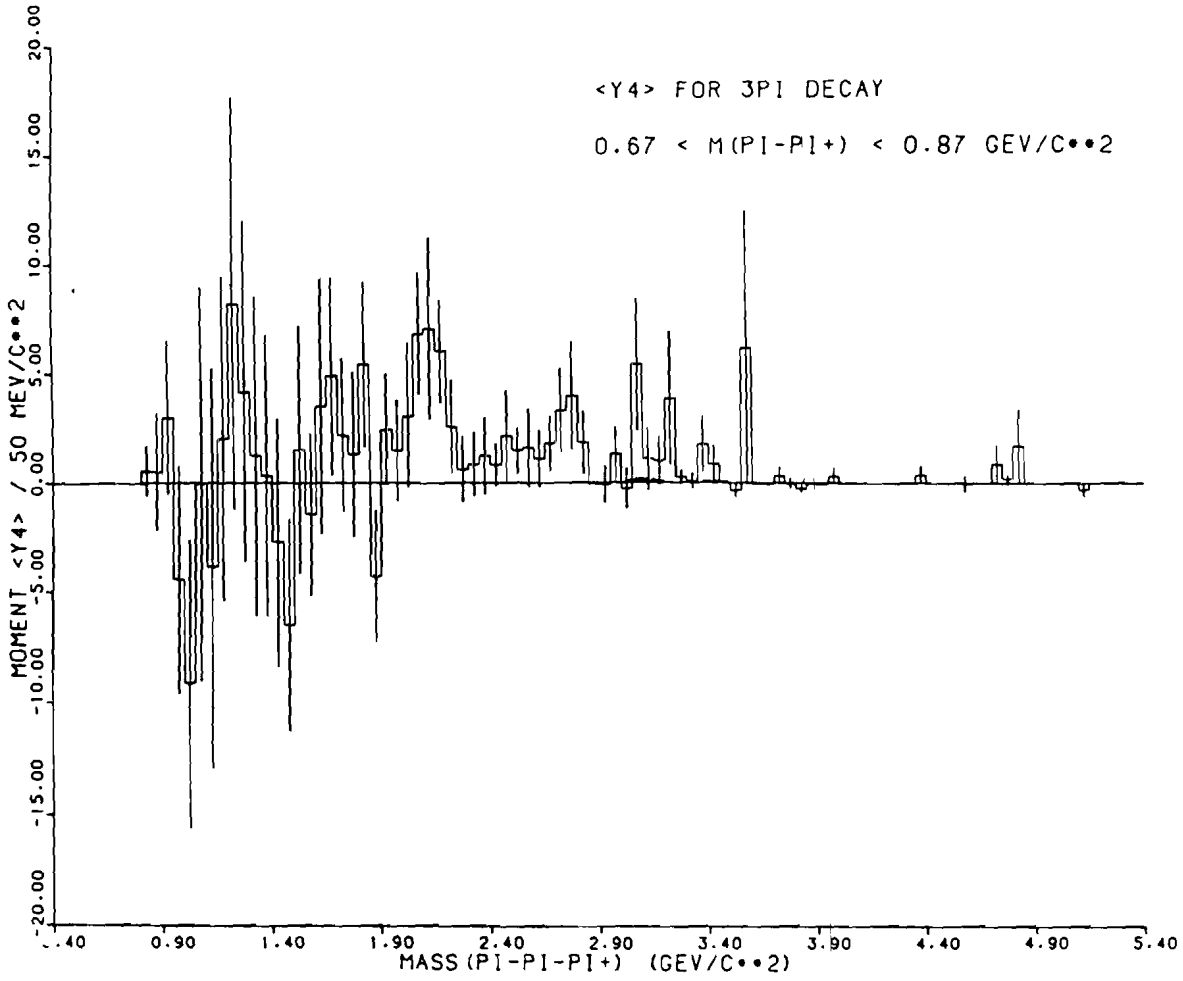

Figure 4.20(d): Moments of spherical harmonic Y_4^0 vs. Mass($\pi^-\pi^-\pi^+$), with $0.67 < \text{Mass}(\pi^-\pi^+) < 0.87$ GeV/c^2. One entry per event.

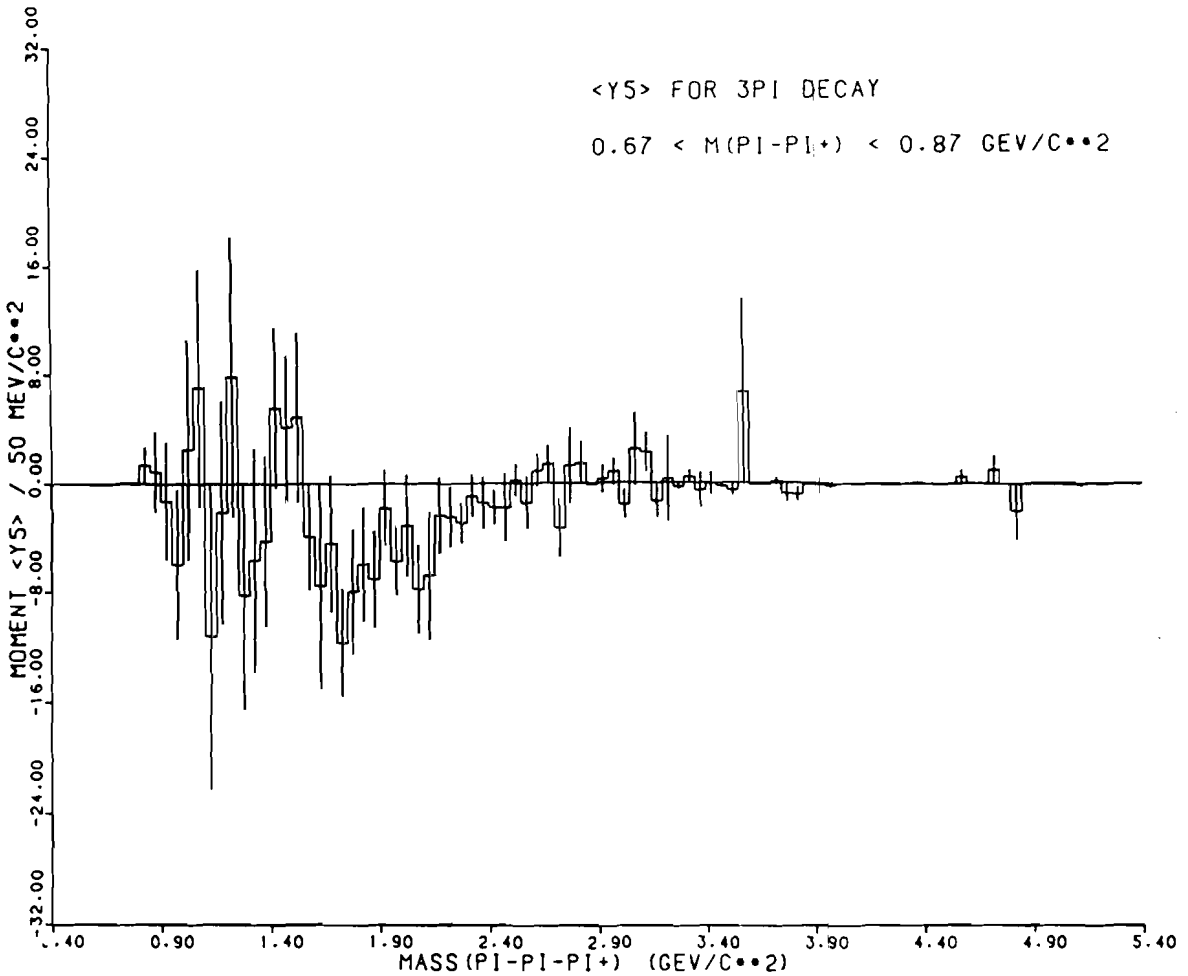

Figure 4.20(e): Moments of spherical harmonic Y_5^0 vs. Mass($\pi^-\pi^-\pi^+$), with $0.67 < \text{Mass}(\pi^-\pi^+) < 0.87$ GeV/c^2. One entry per event.

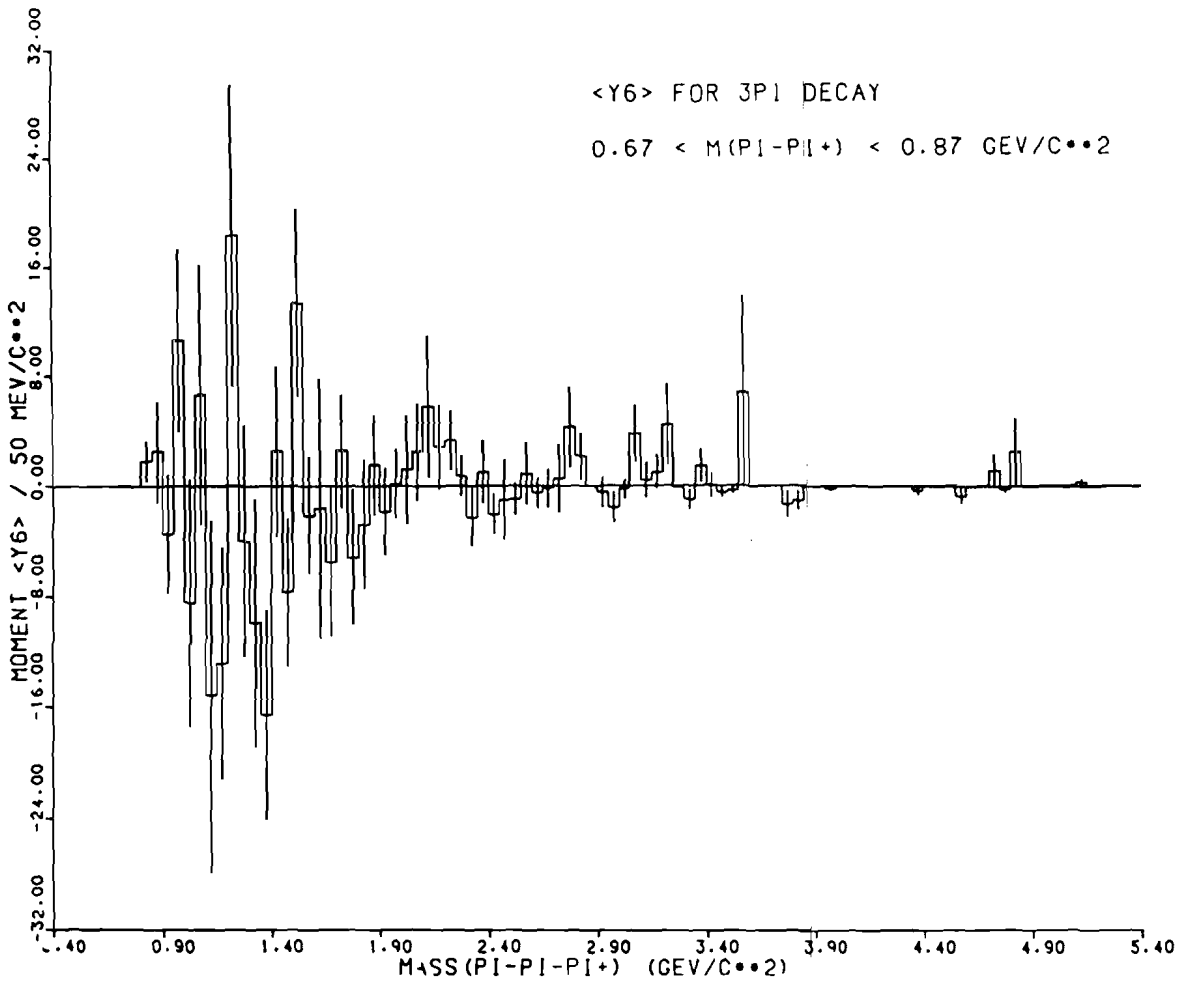

Figure 4.20(f): Moments of spherical harmonic Y_6^0 vs. Mass($\pi^-\pi^-\pi^+$), with $0.67 < \text{Mass}(\pi^-\pi^+) < 0.87$ GeV/c^2. One entry per event.

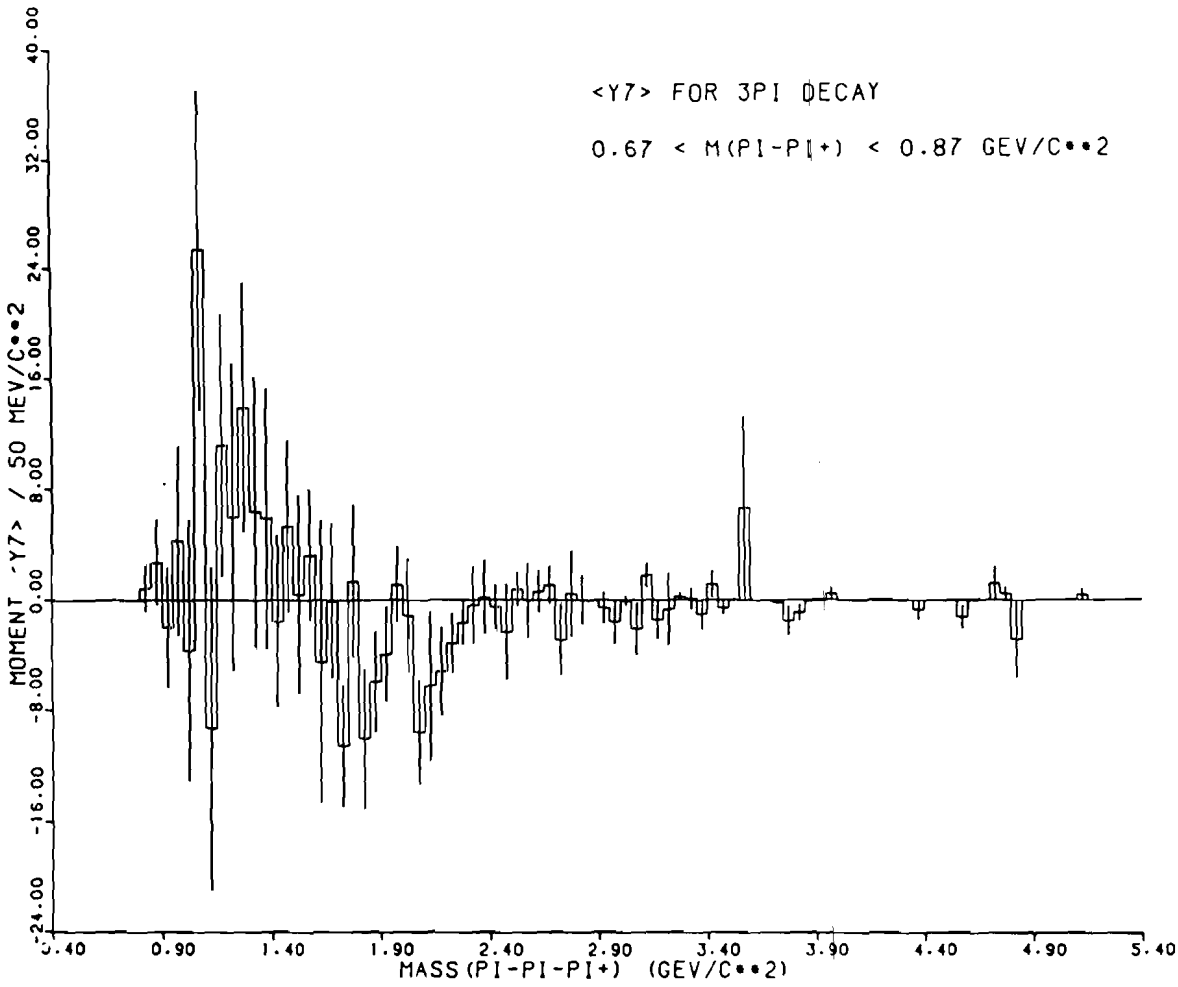

Figure 4.20(g): Moments of spherical harmonic Y_7^0 vs. Mass($\pi^-\pi^-\pi^+$), with $0.67 < \text{Mass}(\pi^-\pi^+) < 0.87$ GeV/c^2. One entry per event.

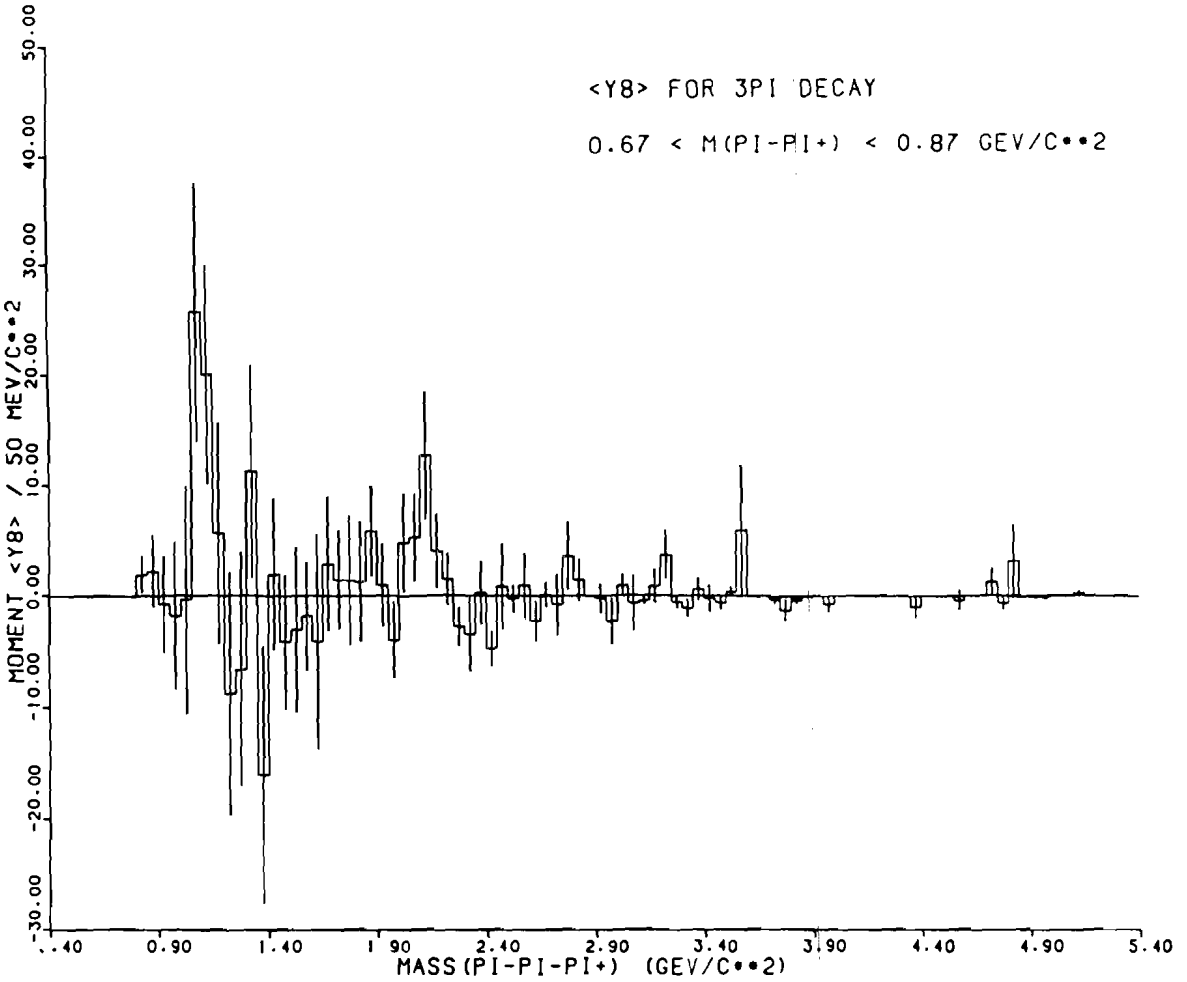

Figure 4.20(h): Moments of spherical harmonic Y_8^0 vs. Mass($\pi^-\pi^-\pi^+$), with 0.67 < Mass($\pi^-\pi^+$) < 0.87 GeV/c^2. One entry per event.

the beam direction (Fig 3.32).

In Fig. 4.19(a-h) there are two entries per event. For these plots without cuts, $\langle Y_1^0 \rangle$ for 3π shows clear activity for $1000 < M(3\pi) < 1450$ MeV/c^2. $\langle Y_2^0 \rangle$ for 3π without cuts shows clear activity for the entire region $1100 < M(3\pi) < 3800$ MeV/c^2. $\langle Y_3^0 \rangle$ for 3π without cuts shows ragged activity in the $1000 < M(3\pi) < 1500$ MeV/c^2 region. $\langle Y_L^0 \rangle$, L = 4-8 shows no clear activity. If any conclusion may be drawn from this, it is that there is at least one object of nonzero spin in the region $1000 < M(3\pi) < 1450$ MeV/c^2. This is consistent with the established spins of the A_1 and A_2. No comment may be made on the spin of the A_3 enhancement.

In Fig. 4.20(a-h) the π^- used in the definition of θ_J is the one not used in the $\pi^-\pi^+$ combination in the ρ^0 mass region. In the events of both $\pi^-\pi^+$ combinations falling in the ρ^0 mass region, the one from π^-(fast)π^+ is used, as explained in Section 4.2.4. Fig. 4.20 thus has one entry per event.

$\langle Y_1^0 \rangle$ for 3π without cuts shows clear activity for $1000 < M(3\pi) < 1450$ MeV/c^2. $\langle Y_2^0 \rangle$ for 3π without cuts shows clear activity for the entire region $1100 < M(3\pi) < 3800$ MeV/c^2. $\langle Y_3^0 \rangle$ for 3π without cuts shows ragged activity in the $1000 < M(3\pi) < 1500$ MeV/c^2 region. $\langle Y_L^0 \rangle$, L = 4-8 shows no clear activity. If any conclusion

may be drawn from this, it is that there is a spin 1 object in the region $1000 < M(3\pi) < 1450$ MeV/c^2, interfering with a spin 2 object. While not a strong statement, and certainly not unambiguous, this is at least consistent with the established spins of the A_1 and A_2. No comment may be made on the spin of the A_3 enhancement.

$\langle Y_1^0 \rangle$ for 3π with the ρ^o cut shows activity in the region $1400 < M(3\pi) < 1900$ MeV/c^2, while $\langle Y_1^0 \rangle$ for 3π with the ρ^o cut shows ragged activity for $1250 < M(3\pi) < 2500$ MeV/c^2. $\langle Y_L^0 \rangle$, L = 3-8 show no clear activity. No unambiguous conclusions may be drawn from this, except perhaps that there may be a spin 1 object somewhere in the region $1400 < M(3\pi) < 1900$ MeV/c^2.

The process of looking at $\langle Y_L^o \rangle$ moments is by no means conclusive, but is at least consistent with the established fact that the A_1 is a spin 1 object.

4.4 Conclusions and Summary

Fermilab experiment E580 ran in Spring of 1980. Among its triggers was $\pi^- N \rightarrow \pi^- \pi^- \pi^+ N$, with an effective beam of 22.9M incident pions. 48657 useful events were written to tape, and analyzed at Notre Dame. After various data-quality cuts the sample was reduced to 18933 events.

A cut on missing-mass squared ($MM^2 < 16\ (GeV/c^2)^2$) was made to eliminate unseen particles except the target object. This further reduced the sample to 7563 events, which were deemed "diffractive". Finally, a fiducial volume cut to eliminate events with low acceptance brought the final sample to 7205 events. Sensitivity was calculated to be 30.3 ± 8.5 events/μb, giving an overall cross section of 296 ± 95 μb/nucleon. Cross-sections per nucleon are reported for various sub-regions of the 3π effective mass spectrum.

The distribution of x_F for the 3π system shows almost all events residing in the peak at +1, indicating that the sample very cleanly consists of events in which the incident π^- dissociates into 3π, with minimal loss of momentum.

A look at t′ distributions, both for the overall sample and for various regions of the 3π mass, reveals that the distributions are the sum of three decaying exponential functions. The first is coherent production off of carbon nuclei in the plastic target, and is very steep (slope around 70 $(GeV/c)^{-2}$). The second is from diffraction off of individual nucleons, and has a slope around 12 $(GeV/c)^{-2}$. The third is background, and extends to large t′ with a very shallow slope (around 2 $(GeV/c)^{-2}$). The diffractive exponential slopes show indications of

decreasing with increasing 3π effective mass, as has been observed elsewhere. The coherent carbon diffraction favors low values of 3π effective mass, decreasing in proportion to nucleon diffraction as the mass rises. This also has been elsewhere observed. A^{α} dependence of the cross section has been calculated to be 0.74 ± 0.04, consistent with other observations.

The $\pi^-\pi^-$ effective mass spectrum is featureless, as is expected from a simple quark model.

The $\pi^-\pi^+$ effective mass spectrum shows copious production of the $\rho^o(770)$, and lesser production of the $f^o(1270)$. Numbers for mass and width of these resonances are well within established values. Cross sections are as follows:

$\sigma(\rho^o) = 280 \pm 82$ μb/nucleon

$\sigma(f^o) = 36 \pm 11$ μb/nucleon

Plotting of spherical harmonic moments of $\cos\theta_2$, the decay angle of the ρ^o or f^o shows some indication that the ρ^o is a spin 1 object.

The 3π effective mass spectrum clearly shows enhancements corresponding to the A_1^-/A_2^- and A_3^-. By means of a cut on the f^o mass, the A_3^- can be isolated and fit. The results for mass and width are consistent with established values, and the cross section is calculated as:

$\sigma(A_3^-) = 16.5 \pm 4.8(\text{stat.}) \pm 5.7(\text{syst.})$ μb/nucleon,

where a 20% systematic uncertainty in number of events has been adopted due to the fact that the A_3 is not a pure Breit-Wigner resonance.

Values for mass, width, and cross section for the A_1^- and A_2^- were not extracted, both due to their overlap and also the fact that the A_1^- is not a normal Breit-Wigner resonance. Plotting the spherical harmonic moments of $\cos\theta_J$, the decay angle of the 3π system, gives weak indications of a an object or objects on nonzero spin in the A_1^-/A_2^- region.

This paper is the first to look in detail at momentum transfer distributions and cross sections per nucleon in the 3π system at an energy of 200 GeV/c. The data is comparatively clean, and where comparison with other data is possible, proves consistent with others' results.

APPENDIX A

SPHERICAL HARMONIC MOMENTS

Moments of the first eight spherical harmonics are used in analyzing the spins of observed mass enhancements. These are defined as follows:

$$\langle Y_L^0(M)\rangle = \Sigma\ Y_L^0(\cos\theta)$$

where the summation is over all events, and the $\langle Y_1^0\rangle$ are binned according to effective mass of the 3π system.

The Y_L^0 are the Spherical Harmonic functions, and are defined as follows:

$$Y_L^0(\cos\theta) = [(2L+1)/4\pi] \star P_L^0(\cos\theta)$$

where the P_L^0 are Associated LeGendre Polynomials, as follows:

$$P_1^0(x) = x$$

$$P_2^0(x) = (1/2)\star(3x^2-1)$$

$$P_3^0(x) = (1/2)\star(5x^3-3x)$$

$$P_4^0(x) = (1/8)\star(35x^4-30x^2+3)$$

$$P_5^0(x) = (1/8)\star(63x^5-70x^3+15x)$$

$$P_6^0(x) = (1/16)\star(231x^6-315x^4+105x^2-5)$$

$$P_7^0(x) = (1/16)\star(429x^7-693x^5+315x^3-35x)$$

$$P_8^0(x) = (1/128)\star(6435x^8-12012x^6+6930x^4-1260x^2+35)$$

APPENDIX B

HISTOGRAM PLOTTING PACKAGE

The histograms in this paper were done with HBOOK, a FORTRAN histogram package developed at CERN. A program was devised to take data directly from HBOOK histograms, and plot it on the HEP-B CALCOMP Model 1039 plotter, although the package is sufficiently general to work on any graphic device using CALCOMP instructions.

The program is called HISTPLOT, and runs interactively at a terminal, sending directions directly to the CALCOMP plotter. It asks of the user the following questions:
1) What is the name of the file containing the histogram data to be plotted?

A correct response is a valid name of a VAX file. The name file.PLT has been adopted as a convention for files to be plotted. The file must contain the following information:

NPTS = Number of data points

XARRAY(i), i=1,NPTS = Left edge of each bin

YARRAY(i), i=1,NPTS = Value of each bin

BINSIZE(i), i=1,NPTS = Width of each bin

ERROR(i), i=1,NPTS = Error bar of each bin
(optional: see below)

A FORTRAN subroutine called HISTSAVE exists in system libraries to automatically save histograms in this format. The call is:

```
CALL HISTSAVE(id,'file.PLT',iflag)
```

where

id = HBOOK identification number of the histogram to be saved

iflag = 0 if no errors to be saved
1 if errors are to be saved

2) What is the x-axis length in inches?

Any positive number will do as a response. The CALCOMP software gives axis values at each inch, choosing "nice" numbers, and scales the histogram so as to fit within the given size.

3) What is the y-axis length in inches?

See 2) above.

4) Enter label of the x-axis (40 char max):

Any character string will be accepted.

5) Enter label of the y-axis (40 char max):

See 4) above.

6) Do you want a title? (y/n)

If YES, then

6a) Enter 1st line of title (40 char max):

Any character string will be accepted.

6b) Enter x,y,height of 1st line (inches):

x and y are positioned relative to the origin of the plot, which have already been specified. The height of the characters is important, as the plotter allocates a square field for each character, so height * (no. of characters) = length of title.

6c) Enter 2nd line of title (40 char max):

Same as 6a). If left blank, 6d) is not asked.

6d) Enter x,y,height of 2nd line (inches):

Same as 6b).

7) Do you want to set the x-scale by hand?

If YES, then

7a) Enter minimum, increment for x:

A detailed understanding of the CALCOMP scaling procedure is needed to give good values for these numbers, and experience has shown that it is generally easiest to let the automatic scaling routines do their job.

8) Do you want to set the y-scale by hand?

If YES, then

8a) Enter minimum, increment for y:

Same as 7a).

9) Do you want log scaling?

If YES, then

9a) Log scaling of x-axis?

If YES, then all the x-axis data will have $\log_{10}(x)$ plotted instead of x. Unfortunately, due to a lack of the appropriate CALCOMP subroutines on our VAX computer, this is not true logarithmic plotting, but rather a plotting of the logarithm of each value. The axes are labelled with the value of the logarithm, rather than with the actual value.

9b) Log scaling of y-axis?

Same as 9a). If both 9a) and 9b) are answered with NO, no error occurs.

10) Do you want error bars?

If YES, then each point is plotted with a vertical error bar in the center of the bin. The input file must contain values for ERROR(i), or a fatal error will occur. If logarithmic scaling of the y-axis has been chosen, the error bars are scaled accordingly, and a check is made to prevent a fatal error in case the bin value minus the error value is negative.

11) Do you want to plot a function?

If YES, then

11a) What is the name of the file containing the function(s) to be plotted?

A correct response is a valid name of a VAX file. The name file.FNC has been adopted as a convention for files to be plotted. The file must contain the following information:

NFNC = Number of functions to be plotted

DO i=1,NFNC Loop over all the functions

NPTS = Number of points in ith function

XARRAY(j), j=1,NPTS = x coordinate of jth point of ith function

YARRAY(j), j=1,NPTS = y coordinate of jth point of ith function

END DO

11b) Do you want unbroken lines?

If YES, then all NFNC functions will be plotted by a connect-the-dots procedure, without special symbols at the given points. This is fine except for places where a function changes sharply, giving a jagged look to the plot. If NO, then

11c) Enter the symbol number you want:

This is a request for the code number for a CALCOMP-defined special symbol to be plotted at the function data points. There are 126 symbols defined, including about a dozen ideally suited for plotting. If this option is chosen, then the function(s) will be plotted by placing the specified symbol at each function data point, with no connecting lines.

This paper uses the HISTPLOT package for almost all of its histograms, except that in some cases the plots have been slightly modified by hand, such as correctly labelling the logarithmic scales.

APPENDIX C

BREIT-WIGNER RESONANCE FUNCTIONS

The functional form used for the Breit-Wigner resonances in this paper come from a FORTRAN subroutine written by Gina Galtieri in 1965. Let

L = Spin of resonance

M = Experimental effective mass of decaying particles

M0 = Mass of resonance (to be determined)

G0 = Width of resonance (to be determined)

MD1 = Experimental mass of 1st daughter particle

MD2 = Experimental mass of 2nd daughter particle

MD01 = Actual mass of 1st daughter

MD02 = Actual Mass of 2nd daughter

Then

$$Q = \mathrm{sqrt}[\ (M^2-(MD1+MD2)^2)*(M^2-(MD1-MD2)^2)\ /\ 2M\ ]$$

$$Q0 = \mathrm{sqrt}[\ (M0^2-(MD01+MD02)^2)*(M0^2-(MD01-MD02)^2)\ /\ 2M0\ ]$$

$$G = G0*(Q/Q0)^{2L+1}$$

and the weight BW of the event is

$$BW = M*M0*G*G0*Q0\ /\ [\ Q*(M0^2-M^2)^2+(M0*G)^2)\ ]$$

Basically, this is a Breit-Wigner resonance with angular momentum considerations fully taken into account.

REFERENCES

Aaron: R. Aaron, R.S. Longacre, Phys. Rev. D24 (1981)
1981 p. 1207-1217

Abarbanel: H.D.I. Abarbanel, Rev. Of Modern Physics 48
1976 (1976) p. 435-465

Alberi: G. Alberi, G. Goggi, Phys. Rep. 74 (1981)
1981 p. 1-207

Antipov: Yu. M. Antipov et al, Nucl. Phys. B63
1973a (1973) p. 141-152

Antipov: Yu. M. Antipov et al, Nucl. Phys. B63
1973b (1973) p. 153-174

Arenton: M. Arenton et al, Nucl. Phys. B274
1986 (1986) p. 707-713

Ascoli: G. Ascoli et al, Phys. Rev. D7 (1973)
1973 p. 669-686

Azimov: S.A. Azimov et al, Yad. Fiz. 35 (1982)
1982 p. 950-959, English translation in
Sov. J. Nucl. Phys. 35 (1982) p.552-557

Baltay: C. Baltay, C.V. Cautis, M. Kalelkar,
1977 Phys. Rev. Lett. 39 (1977) p. 591-594

Baltay: C. Baltay et al, Phys. Rev. D17 (1978)
1978 p. 62-82

Beketov: G.V. Beketov et al, Yad. Fiz. 28 (1978)
1978 p. 1266-1274, English Translation in
Sov. J. Nucl. Phys. 28 (1978) p. 653-656

Berger: E.L. Berger et al, Phys. Rev. D19 (1979)
1979 p. 2595-2606

Bonesini: M. Bonesini et al, Phys. Lett. 103B
1981 (1981) p. 75-78

Bossetti: P. Bosetti et al, Nucl. Phys. B101
1975 (1975) p. 304-332

Brick: D. Brick et al, Phys. Rev. D21 (1980)
1980 p. 1726-1743

Brick: D. Brick et al, Z. Phys. C19 (1983)
1983 p. 1-9

Chabaud: V. Chabaud et al, Nucl. Phys. B178
1981 (1981) p. 401-420

Chang: C.C. Chang et al, Phys. Rev. D29 (1984)
1984 p. 1888-1894

Chen: T.Y. Chen et al, Phys. Rev. D28 (1983)
1983 p. 2304-2307

Daum: C. Daum et al, Nucl. Phys. B182 (1981)
1981 p. 269-336

Dzierba: A. Dzierba, E. Malamud, D. McLeod,
1977 "Multiparticle Spectrometer at Fermilab",
prepared for MPS Workshop, March 4-5, 1977,
available through Fermilab library

Fenker: H. Fenker et al, Phys. Rev. D30 (1984)
1984 p. 872-876

Gaidos: J.A. Gaidos, W.L. Yen, Phys. Rev. D19
1979 (1979) p. 22-42

Kaidalov: A.B. Kaidalov, Phys. Reports 50 (1979)
1979 p. 157-226

Kitagaki: T. Kitagaki et al, Phys. Rev. D26
1982 (1982) p. 1554-1571

Lamsa: J.W. Lamsa et al, Phys. Rev. D18 (1978)
1978 p.3933-3938

Malamud: E. Malamud, "The M6 Beam Line" (1977)
1977 Available through Fermilab library

Mikocki: S. Mikocki, "Inclusive Resonance Production
1985a in Single-Vee Events in π^-N Interactions
at 200 GeV", Ph.D. dissertation, Visginia
Polytechnic Institute and State University
(1985)

Mikocki: S. Mikocki et al, Fermilab-Pub-85/132-E
1985b (1985)

Napier: A. Napier et al, Phys. Lett. 149B
1984a (1984) p. 514-518

Napier: A. Napier, Private Communications (May 5 1984,
1984b June 26 1984, April 11 1985, April 17 1985)

Otter: G. Otter et al, Nucl. Phys. B80 (1974)
1974 p. 1-11

Pajares: C. Pajares, A.V. Ramallo, Lett. Nuovo Cimento
1983 (1983) p. 354-358

PDG : Particle Data Group, Phys. Lett. 170B (1986)
1986 p. 1-350

Pernegr: J. Pernegr et al, Nucl. Phys. B134
1978 (1978) p.436-462

Pernegr: J. Pernegr, XII International
1982 Symposium on Multiparticle Dynamics,
ed. by W.D. Shephard _V.P. Kenney
(1982) p. 119-127

Poirier: J.A. Poirier, XII International
1982 Symposium on Multiparticle Dynamics,
ed. by W.D. Shephard _V.P. Kenney
(1982) p. 153-160

Saleem: M. Saleem, H. Rashid, F. Aleem,
1984 Prog. Theor. Phys. 71 (1984) p. 659-662

Stampke: S.R. Stampke, "Pion-Pion Decay Distributions
1982 for $\pi^- \to \pi^+ \pi^- n$ at 100 and 175 GeV/c",
Ph.D. dissertation, California Institute of
Technology, CALT-68-936 (1982)

Thompson: G. Thompson et al, Phys. Rev. D9
1974a (1974) p. 560-565

Thompson: G. Thompson et al, Nucl. Phys. B69
1974b (1974) p. 381-398

URA : Universities Research Association, National
1968 Accelerator Laboratory Design Report,
U.S. Atomic Energy Commission (1968)

Williams: E.G.H. Williams et al, Phys. Rev. D30,
1984 (1984) p. 877-883

Yung: K.W. Yung, "Study of Hadronic Jets Produced by
1979 Charged Pion and Proton Beams Incident on Hydrogen and Aluminum Targets", Ph.D. dissertation, California Institute of Technology, CALT-68-743 (1979)

Zachariasen: F. Zachariasen, Phys. Reports (1971)
1971 p. 1-75

Zielinski: M. Zielinski et al, Phys. Rev. D30
1984 (1984) p. 1855-1860

Zotov: N.P. Zotov, V.A. Tsarev, Fiz. Elem. Chastits
1978 i At. Yadra 9 (1978) p. 650-709, English translation in Sov. J. Part. and Nucl. 9 (1978) p. 266-290